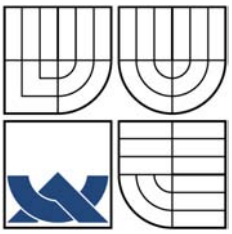

VYSOKÉ UČENÍ TECHNICKÉ V BRNĚ
BRNO UNIVERSITY OF TECHNOLOGY

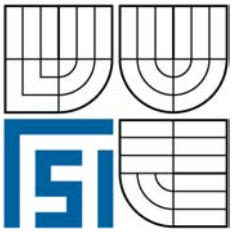

FAKULTA STROJNÍHO INŽENÝRSTVÍ
ÚSTAV FYZIKÁLNÍHO INŽENÝRSTVÍ
FACULTY OF MECHANICAL ENGINEERING
INSTITUTE OF PHYSICAL ENGINEERING

CURRENT INDUCED MAGNETIZATION DYNAMICS IN NANOSTRUCTURES

DYNAMIKA MAGNETIZACE V NANOSTRUKTURÁCH VYVOLANÁ ELEKTRICKÝM PROUDEM

DIZERTAČNÍ PRÁCE
DOCTORAL THESIS

AUTOR PRÁCE
AUTHOR
Ing. VOJTĚCH UHLíŘ

VEDOUCÍ PRÁCE
SUPERVISOR
prof. RNDr. TOMÁŠ ŠIKOLA, CSc.

ŠKOLITEL SPECIALISTA
CO-SUPERVISOR
STEFANIA PIZZINI, PhD.
Institut Néel, CNRS Grenoble

BRNO 2010

Université de Grenoble

Vysoké učení technické v Brně

Thèse de doctorat

présentée par

Vojtěch Uhlíř

pour obtenir le grade de

Docteur de l'Université de Grenoble
Spécialité Physique des Matériaux

Doktor
Spécialité Génie Physique et des Matériaux

Current Induced Magnetization Dynamics in Nanostructures

présentée le 29 octobre 2010

Composition du jury:

Dafiné Ravelosona	Rapporteur
André Thiaville	Rapporteur
Roman Antoš	Examinateur
Alain Fontaine	Examinateur
Stefania Pizzini	Directrice de thèse
Tomáš Šikola	Directeur de thèse

Thèse préparée à l'Institut Néel à Grenoble
et à l'Institut du Génie Physique à Brno

Dedicated to my family

Věnováno mé rodině

Abstrakt

Předkládaná dizertační práce pojednává o problematice pohybu doménových stěn (DS) vyvolaného spinově polarizovaným proudem v magnetických nanodrátech na bázi spinového ventilu NiFe/Cu/Co. Jedná se o tzv. efekt přenosu spinového momentu. Multivrstevnatý systém NiFe/Cu/Co, kde se doménová stěna pohybuje ve vrstvě NiFe, vykazuje velmi vysokou účinnost přenosu spinového momentu, což bylo v literatuře potvrzeno na základě magnetotransportních měření. Tato práce má za cíl pozorovat stav DS během jejich pohybu, pomocí fotoelektronové mikroskopie kombinované s kruhovým magnetickým dichroismem. Tato technika využívá synchrotronové záření, které svým časovým rozlišením umožňuje sledovat dynamickou odezvu magnetizace na elektrický proud.

Podstatnou částí řešení byla optimizace růstu vrstev NiFe/Cu/Co kvůli snížení magnetické dipolární interakce mezi vrstvami. V práci je také řešen způsob přípravy nanodrátů litografickými metodami. Byly provedeny dva módy měření: i) kvazistatický, tj. pozorování DS před a po injekci proudu do nanodrátu a ii) dynamické měření, kde je DS sledována během působení proudového pulzu. S využitím kvazistatickém módu byla vypracována rozsáhlá statistika pohybu DS: i) byly naměřeny jejich vysoké rychlosti přesahující 600 m/s za působení průměrné proudové hustoty nutné k posuvu doménové stěny - 5×10^{11} A/m^2; ii) DS jsou v systému NiFe/Cu/Co velmi silně zachycovány dipolární interakcí mezi NiFe a Co způsobenou nehomogenitou krystalové struktury ve vrstvě Co. V dynamickém módu bylo odhaleno, že působením Oerstedovského pole kolmého na nanodráty v rovině vzorku se magnetizace ve vrstvě NiFe silně natáčí. Tento efekt přispívá k vysokým rychlostem DS pozorovaných v nanodrátech NiFe/Cu/Co.

Abstract

This thesis deals with the study of current-induced magnetization dynamics and domain wall (DW) motion in NiFe/Cu/Co nanowires, induced by the so-called spin-transfer torque effect. Prior to this work, transport measurements had proven that in this trilayer system, DWs in NiFe can be moved with relatively low current densities, suggesting a particularly high spin-torque efficiency. The aim of this study has been to use photoemission electron microscopy combined with x-ray magnetic circular dichroism at synchrotron radiation sources to observe directly the magnetic configurations in the trilayers and their evolution during and after the application of nanosecond current pulses. An important step of the work has been to optimize the growth of the NiFe/Cu/Co layers, in the view of increasing interface quality and minimize interlayer coupling. The process of nanowire patterning by e-beam lithography has also been optimized. Two kinds of measurements have been carried out: i) quasi static measurements, where the domain configuration is observed before and after the application of current pulses and ii) dynamic measurements, where the magnetic configuration has been observed during the application of current pulses. The first measurements have allowed us to study the statistical behaviour of DWs under the application of current pulses: on one hand, the domain wall velocities reach extremely high values for relatively low current densities (up to 600 m/s for 5×10^{11} A/m^2). On the other hand, DW motion over distances larger than 2-3 μm is strongly hindered by pinning. We have identified the pinning of DWs

in the NiFe layer as being due to crystallographic inhomogeneities of the Co layers, via magnetic dipolar effects. Time-resolved measurements during the current pulses, carried out for the first time by our team, have allowed us to demonstrate that the NiFe magnetization is strongly tilted in the direction transverse to the nanowire direction, due to the presence of a transverse Oersted field. This effect might contribute to the enhancement of DW velocities in the NiFe layers.

Klíčová slova
přenos spinového momentu, doménová stěna, dynamika magnetizace, magnetické nanodráty, pohyb doménové stěny vyvolaný elektrickým proudem, spinový ventil

Keywords
spin-transfer torque, domain wall, magnetization dynamics, magnetic nanowires, current-induced domain wall motion, spin-valve multilayers

UHLíŘ, V., *Current Induced Magnetization Dynamicsin Nanostructures*, Brno, Vysoké učení technické v Brně, Fakulta strojního inženýrství, 2010, 239 s., Vedoucí dizertační práce prof. RNDr. Tomáš Šikola, CSc.

Prohlašuji, že jsem předloženou dizertační práci vypracoval samostatně za odborného vedení prof. RNDr. Tomáše Šikoly, CSc. a Stefanie Pizzini, PhD. Dále prohlašuji, že veškeré podklady, ze kterých jsem čerpal, jsou uvedeny v seznamu použité literatury.

CONTENTS

INTRODUCTION

Nanotechnology has become an integral part of contemporary technology and in many fields (science, electronics, industry, medicine) it leads the innovation processes. This pursuit for improving performance of recent devices brings attention to novel fields like spintronics which upgrades the standard electronics by incorporating the spin of electrons in the electrical transport properties of materials, thus opening new horizons not only for applications, but also for enriching the basic research by investigation of mutual interaction of electrical current and magnetization.

Nowadays, magnetic materials and magnetic devices are the basic means for data storage. Hence, the findings in the spintronics field are important for applications, as they provide essential technological advances for the electronics and information technology industry. The rapidly increasing data storage capacity of harddisks is a consequence of one of the spintronics products – the giant magnetoresistance (GMR). It enabled development of harddisk read-head sensors so that they can record smaller and smaller fields of decreasing magnetic clusters where the data is stored. Since the discovery of GMR in 1988 the development has speeded up considerably, at the moment offering a large number of possible revolutionary applications in electronics. To recognize this substantial progress, the main inventers of GMR, Albert Fert and Peter Grünberg, were awarded the Nobel prize in physics in 2007.

At the end of the 1990's it was shown that a spin-polarized current excites the magnetization state and might eventually lead to the magnetization reversal. One of the most interesting consequences is the possibility to manipulate domain walls (DWs) in nanowires solely by an electric current. However, this idea is not new, the concept has been evolving since the 1950's, but it is above all the nanotechnology, in particular the lithography techniques and novel methods for observing magnetization, which gave the important impetus to the advent of investigation of current-induced domain wall motion (CIDWM). The advantage of electric current with respect to the effect of magnetic field is that it drives the domain walls in the direction of electron flow, whereas the magnetic field tends to increase or shrink domains of opposite magnetizations. This is convenient for designing magnetic storage devices based on a shift register. However, the current density required for inducing DW motion is of the order of $10^{11} - 10^{12}\,\mathrm{A/m^2}$ which justifies the need for nanowires with as small cross-sections as possible, to minimize the injected current.

The CIDWM provides a path to the design and construction of nonvolatile high-performance memories and logic systems that could take the lead over the semiconductor-based technology. However, for successful application, further optimization of systems featuring CIDWM has to be done. In particular, the critical current density has to be minimized, the DW velocity has to be maximized and to assure reproducible and reliable DW motion, pinning of DWs along the nanowire has to be

controlled.

The goal of this thesis is to carry out time-resolved observation of magnetization dynamics induced by spin-polarized current. Direct imaging of CIDWM is of a high interest as it is expected to provide a key insight on the response of DW magnetization to current, allowing one to compare it to the recent theoretical predictions. The chosen system is a NiFe/Cu/Co spin-valve stack, since, as will be described in Section 2.3.5, this multilayer configuration is a promising candidate for devices based on CIDWM.

The presented manuscript summarizes the results of a joint thesis between the Institut Néel (IN) in Grenoble, France, and the Institute of Physical Engineering (IPE) at the Brno University of Technology, Czech Republic. The author profited of the joint-thesis PhD fellowship of the French government to spend 18 months in total at the IN.

The manuscript is organized as follows. In Chapter 1 I give a theoretical background in nanomagnetism and spin-polarized transport. On this basis, Chapter 2 describes the DW motion induced by magnetic field and electric current. It briefly covers also the theoretical and experimental state-of-the-art and open questions.

Part II is devoted to the sample fabrication and optimization of material properties. In particular, Chapter 3 summarizes the improvements of the multilayer system which were carried out at the IPE. Chapter 4 deals with patterning of the multilayers into nanowires. Besides the standard electron-beam lithography, the patterning by focused ion beam is introduced.

Part III is mainly devoted to the experimental investigation of CIDWM and magnetization dynamics carried out at the IN. Chapter 5 introduces photoemission electron microscopy combined with x-ray circular magnetic dichroism (XMCD-PEEM), a technique used to study both the quasistatic and dynamic behavior of magnetization in NiFe/Cu/Co nanowires. The description of the experimental setup is given as well.

Finally, Chapter 6 covers the experimental results of quasi-static and dynamic measurements and a discussion on general aspects influencing the DW motion in spin-valve nanowires.

Part I

THEORETICAL BACKGROUND AND STATE-OF-THE-ART

Chapter 1

CONCEPTS OF THIN FILM MAGNETISM AND SPINTRONICS

The aim of the two introductory chapters is to establish a theoretical background and a state-of-the-art context required for understanding of the current-induced domain wall motion in spin-valve nanowires, a topic which will be addressed theoretically in Chapter 2 and experimentally in Part III.

1.1 Magnetism Basics

1.1.1 Energies in Magnetism

The magnetic state of an object reaches equilibrium, if it minimizes the sum of all applicable energies. In this section we list the most relevant energies which are important for the following explanations and discussions.

Zeeman Energy

If an external magnetic field H_a acts on a magnetic moment, it aligns the moment in the field direction. If however a misalignment is present, the system has a Zeeman energy

$$E_\mathrm{Z} = \int_V -\mathbf{M}\mathbf{H}_\mathrm{a}\mathrm{d}V \tag{1.1}$$

where $\mathbf{M}$ is the magnetization per volume unit.

Exchange Energy

The exchange interaction arises from the Coulomb interaction between electrons and the symmetrization postulate [1]. It tends to align spins parallel or antiparallel, depending on a particular material. The exchange interaction is described by the Heisenberg hamiltonian [2]:

$$\mathcal{H}_\mathrm{ex} = -\sum_{i \neq j} \mathrm{J}_{ij}\mathbf{S}_i\mathbf{S}_j \tag{1.2}$$

where J_{ij} is the exchange constant (or exchange integral [1, 3]) between the $\mathbf{S}_i$ and $\mathbf{S}_j$ spins. J_{ij} is positive for ferromagnetic ordering and negative for antiferromagnetic

ordering. The exchange interaction is extremely short-range (it is based on wave function overlap and Pauli exclusion principle), so one often takes into account only the interaction between nearest neighbor spins.

For an approximation of a magnetic continuum, in particular for micromagnetic simulations, one uses the exchange energy formula exploiting the exchange energy density which is a function of gradients of direction cosines of magnetic moments:

$$E_{\mathrm{ex}} = \int_V A \left[(\nabla \mathbf{m}_x)^2 + (\nabla \mathbf{m}_y)^2 + (\nabla \mathbf{m}_z)^2 \right] \mathrm{d}V. \tag{1.3}$$

A is an exchange stiffness constant dependent on the crystal symmetry.

Magnetocrystalline Energy

Magnetocrystalline energy arises from the orientation of magnetization with respect to the crystallographic axes of the system. In the case of uniaxial anisotropy, the first term of the magnetocrystalline energy reads

$$E_{\mathrm{K}} = \int_V K \sin^2\theta \mathrm{d}V \tag{1.4}$$

where θ is the angle between the magnetization and the easy magnetization axis, and K is an anisotropy constant dependent on the crystal symmetry.

Magnetic Dipolar Energy

Magnetic dipolar energy arises from the interaction of ordered magnetic dipoles. It can be written as

$$E_{\mathrm{d}} = -\frac{1}{2} \int_V \mathbf{H}_{\mathrm{d}} \mathbf{M} \mathrm{d}V. \tag{1.5}$$

The demagnetizing field H_{d} opposes the magnetization which creates it and reads

$$\mathbf{H}_{\mathrm{d}} = -N\mathbf{M} \tag{1.6}$$

where N is a demagnetizing factor, or more generally a demagnetizing tensor. Minimizing the magnetic dipolar energy means limiting the accumulation of magnetic charges. Although in reality the existence of magnetic charges has not been proven, it is a convenient auxiliary construction which facilitates the description of micromagnetic problems. We might define the density of volume charges:

$$\rho_{\mathrm{m}} = -\mathrm{div}\, \mathbf{M} \tag{1.7}$$

and of surface charges:

$$\sigma_{\mathrm{m}} = \mathbf{n} \cdot \mathbf{M} \tag{1.8}$$

where $\mathbf{n}$ is the unit vector of a surface normal.

1.1.2 Magnetization Dynamics, Landau-Lifshits-Gilbert Equation

The behavior of a magnetic moment submitted to an external field is described by the Landau-Lifshits-Gilbert (LLG) equation [4]. The first term represents Larmor precession of the magnetic moment in the magnetic field. Gilbert [5] introduced the second, damping term, which ensures relaxation of the magnetic moment in the direction of the field (see Fig. 1.1). The equation reads

$$\frac{\partial \mathbf{m}}{\partial t} = \gamma_0 \mathbf{H}_{\text{eff}} \times \mathbf{m} + \alpha \mathbf{m} \times \frac{\partial \mathbf{m}}{\partial t} \tag{1.9}$$

where $\mathbf{m}$ is a magnetization unit vector defined as $\mathbf{m} = \mathbf{M}/M_{\text{S}}$. α is a phenomenological damping parameter, it is a measure of magnetic moment susceptibility to readjusting its direction along the effective field $\mathbf{H}_{\text{eff}}$ which is defined as

$$\mathbf{H}_{\text{eff}} = -\frac{1}{\mu_0 M_{\text{S}}} \frac{\delta E}{\delta \mathbf{m}} \tag{1.10}$$

where E is the total energy of the system.

Sometimes one uses the equation in the form originally proposed by Landau and Lifshits [4]:

$$\frac{\partial \mathbf{m}}{\partial t} = \gamma^* \mathbf{H}_{\text{eff}} \times \mathbf{m} + \lambda \mathbf{m} \times \mathbf{H}_{\text{eff}} \times \mathbf{m} \tag{1.11}$$

where $\lambda = \alpha\gamma^* = \alpha\gamma_0/(1+\alpha^2)$. The difference in the two damping forms is schematically shown in Fig. 1.1. As both equations are equivalent and describe the same dynamics, the trajectory is the same for both forms. The equivalence is accomplished by renormalizing the gyration constant γ_0 and the damping constant α in the Landau-Lifshits form. The Gilbert damping form can be decomposed into a radial component and a friction-like component, which slows down the precession. Typical values of α in NiFe films are close to 0.01 [6, 7, 8].

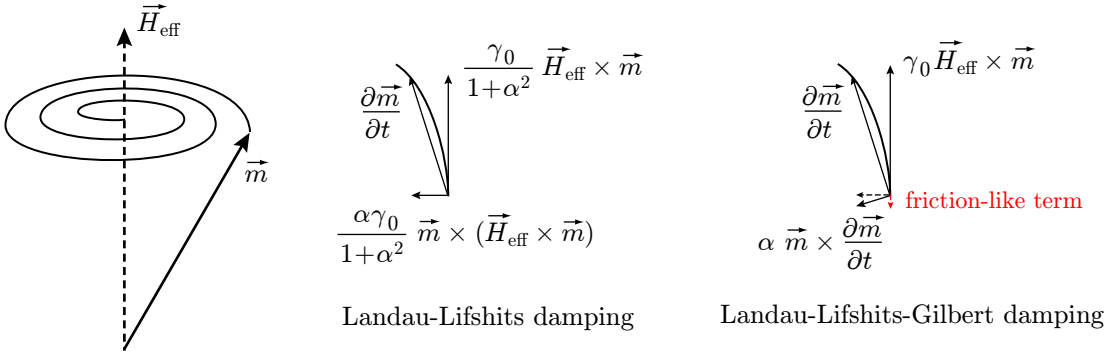

Fig. 1.1: Damped precession of a magnetic moment in an effective magnetic field. Schematic top views of the Landau-Lifshits and Landau-Lifshits-Gilbert scenarios are shown.

1.1.3 Ferromagnetic Ordering in Metals

Ferromagnetism is a property of materials which show a spontaneous magnetization in the absence of an external magnetic field. In an insolated atom, Hund's rules describe filling of the levels by electrons [3]. Hence, maximizing the spin leads to a non-zero magnetic moment of atoms with partially filled orbitals.

However, in solids the crystalline environment can modify the building-up of the electronic structure as the crystal field breaks the spherical symmetry. Also, in solids the electronic states of the individual atoms become hybridized and form energy bands. Spontaneous spin polarization would lead to a cost of kinetic energy for promoting the electrons to unoccupied states.

There are two simplified models which are useful for explaining ferromagnetism in metals [9]. The *Stoner model* assumes both spin-up and spin-down electron bands to have a free electron dispersion. A relative shift Δ_{xc}, the ferromagnetic exchange splitting of energy bands (see Fig. 1.2), will only appear if the exchange interaction is strong enough to balance the cost in the kinetic energy [10, 11]. This condition requires a sufficiently high density of states at the Fermi level [3].

The *s-d model* could be adapted for transition metal ferromagnets like Fe, Co and Ni. It describes the s electrons as delocalized ones (lower effective mass), responsible for conduction, and d electrons as localized ones (higher effective mass). The s and d bands are weakly coupled by the exchange interaction. The d band is spin-split and is responsible for the spontaneous magnetization. Splitting of the s band is negligible [1]. As the definition of spin-up and spin-down electrons depends on the quantization axis, i.e. on the magnetization direction, the two electron populations will be addressed as minority and majority ones in the following (see Fig. 1.2).

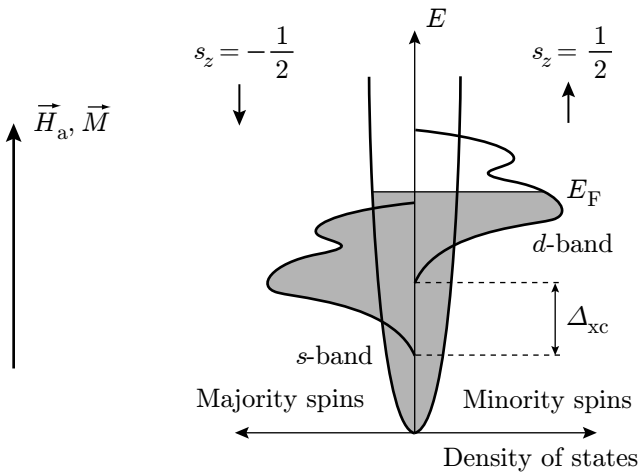

Fig. 1.2: Schematic of the ferromagnetic exchange splitting in transition metals. Magnetization defines the quantization axis, i.e. the minority spins point in the magnetization direction which is determined by the majority magnetic moments. Figure adapted from [1].

In real systems, the electron-electron interaction and the effect of the exchange interaction on electron motion cannot be neglected. An approach to deal with these

many-body interactions is called *density functional theory* (DFT, see e.g. [9, 3] and references therein). It finds the ground energy state of the electron system as a functional of the electron density. An approach taking into account the inhomogeneities of the electron gas density and the effects of spin-polarization is called *local spin-density approximation* (LSDA).

For the qualitative description in the following we will limit ourselves to the free-electron model.

1.2 Magnetic Thin Films, Nanowires and Domain Walls

Reducing dimensions of materials from bulk (3D) to thin films (2D) and nanowires (1D) leads to a substantial modification of their physical properties, for instance electric transport, crystalline lattice, mechanical, optical and indeed magnetic properties. Low-dimensionality changes the band structure and the density of states at the Fermi level, which may transform some materials, nonmagnetic in bulk, into ferromagnetic ones [3]. Some constants, e.g. the Curie temperature T_C, are strongly dependent on the thin film thickness. In this section we will show some of the properties of magnetic multilayers, in particular interlayer coupling, and domain wall (DW) types in thin films and nanowires.

1.2.1 Interlayer Coupling

Magnetic layers incorporated in complex multilayers may interact with each other in various ways. If they are directly in contact, the exchange interaction dominates. However, the magnetic layers may be separated by nonmagnetic spacers. Also in this case a direct exchange interaction can play a role, in particular if the nonmagnetic layer is discontinuous and contains pinholes. For continuous thin metallic spacers, the exchange interaction is mediated by the conduction electrons. For spacers thicker than 3-5 nm, dipolar interactions become more important. In the following we discuss these cases.

Orange Peel Coupling

This type of coupling is based on magnetic dipolar interactions and may be found in a system of two ferromagnetic layers separated by a nonmagnetic spacer. If the interfacial roughness is reproduced at both interfaces (see Fig. 1.3), the magnetization will form magnetic charges at the interfaces such that there will be a positive coupling between the layers.

Such a situation is often present in realistic multilayers. A model for the quantitative description of the effect was proposed by L. Néel in 1962 [12]. Later, it was compared to experimental observations and a good agreement was found [13, 14].

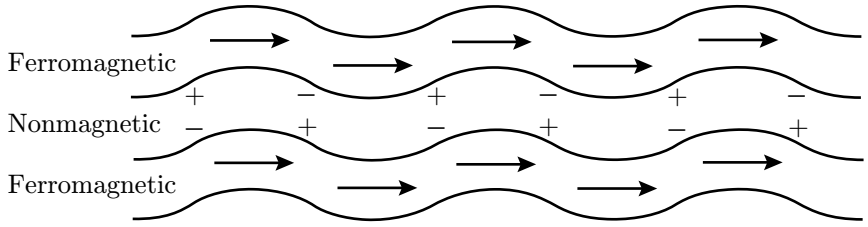

Fig. 1.3: Schematic of the formation of charges at rough interfaces. The resulting dipolar interaction is called the orange-peel coupling.

Indirect Exchange in Metals

Conduction electrons in metals can mediate the exchange interaction between magnetic ions. The magnetic ions first spin-polarize the conduction electrons and these consequently act on the neighboring ions. This indirect interaction decreases quickly[1] with the distance between the magnetic ions (layers) and is oscillatory in space, i.e. it can have both ferromagnetic or antiferromagnetic character depending on the separation between the magnetic layers. The oscillation period is determined by the conduction electron wavevector at the Fermi level. This interaction is also called RKKY according to the scientists who discovered this effect – Ruderman, Kittel, Kasuya and Yoshida.

Direct Exchange Coupling – Exchange Bias

Exchange bias (EB), or exchange anisotropy, is based on an interfacial exchange interaction between an antiferromagnetic layer (AF) and a ferromagnetic layer (FM). The unidirectional exchange field acts in superposition with an applied field and for this reason it causes a typical shift of a hysteresis loop with respect to zero field. Besides the shift, the AF also causes an important coercivity enhancement of the FM. Exchange bias was discovered by Meiklejohn and Bean [18] on Co nanoparticles with CoO shells as a new type of magnetic anisotropy.

An important condition for EB is that the *Curie temperature* T_C of the FM has to be larger than the ordering *Néel temperature* T_N of the AF. The exchange anisotropy is induced by heating the system above T_N, applying a large magnetic field ($\sim$1 T) to saturate the system in a given direction and cooling it below T_N while the field is still applied (field cooling). More details on EB systems can be found for instance in the review by Nogués and Schuller [17].

The range of thermal stability of an EB system is limited by the *blocking temperature* T_B of the AF layer. It can be determined for instance by measuring the temperature dependence of the hysteresis loop. This shift extrapolates to zero at T_B. Venus and Hunte [28] showed that exchange bias persists up to T_N, but is greatly reduced.

Below the blocking temperature, antiferromagnetic order is present at a long-range scale, and thermal activation is not sufficient to switch all the AF moments upon

[1] The exchange coupling of magnetic layers through a nonmagnetic metallic spacer becomes negligible at approximately 5 nm [15, 16, 47].

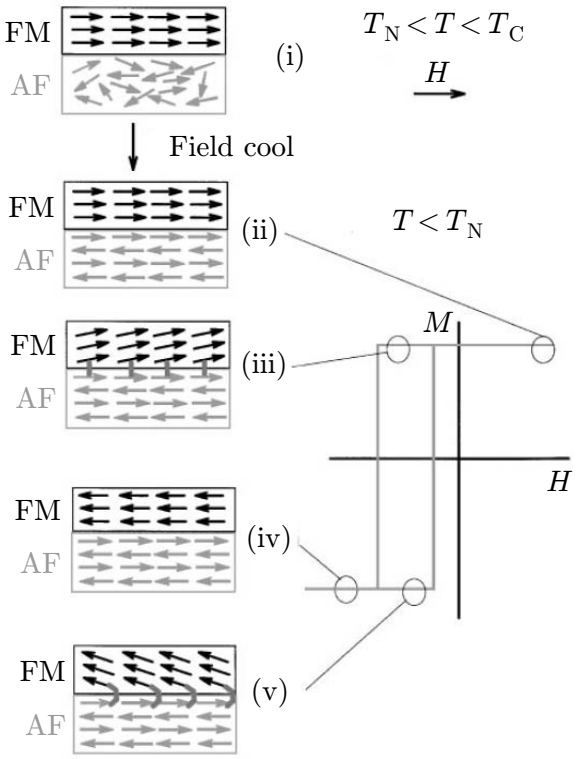

Fig. 1.4: Schematic of field cooling and exchange biasing for an AF/FM system. While sweeping the applied magnetic field below T_N, the spins in the AF remain fixed and induce a bias field acting on the FM. Figure reproduced from [17].

switching the FM layer. The "frozen" magnetic structure within the AF layer, together with the exchange coupling at the AF/FM interface, will lead to a shift of the FM hysteresis loop. In the region $T_B < T < T_N$ long-range AF order is still present, but thermal activation can lead to switching of the complete AF layer upon FM reversal (training effect). In that case, only an increase of coercivity in the FM is measured, due to temperature dependent relaxation effects in the AF. In general, both loop shift and increase in coercivity are present, due to a distribution of AF grain sizes that leads to a distribution of blocking temperatures.

In this study, we are particularly interested in the Co/CoO system. The CoO layer was intended to increase the coercivity of the Co layer and hence to assure independent switching of the Co and NiFe layers in the NiFe/Cu/Co trilayers. A discussion about the transition temperatures in the Co/CoO system follows.

Blocking and Néel Temperatures of CoO_x Layers

Finite-size effects play a very important role in magnetic properties of thin films. The transition temperatures depend on the strength of the exchange interaction and the number of neighboring atoms. Hence the Néel temperature T_N, similarly to T_C of thin films and nanoparticles [19], decreases with the layer thickness or the grain size. Thermal fluctuations disturbing the magnetic order can be introduced to obtain empirical

models of thickness dependence of T_N [21, 20]. These cited works directly compare the model to experimental results on CoO layers [23, 24] and yield a very good agreement with the experiment.

For measuring the transition temperatures, specific heat [25, 24] and neutron scattering [26] techniques are often employed, because these measure average properties of the spin system [24]. Note that using other techniques, such as the susceptibility measurement [23], may lead to ambiguous results in the case of very thin AFM films, as the uncompensated spins at the surfaces and interfaces intervene importantly in the measurement [27]. The magnetic moment associated to these spins can be quantified by measuring the thermoremanent moment obtained by aligning the uncompensated spins by field cooling. Subsequently, by increasing the temperature, one may find the maximum blocking temperature T_B^{max} at which the thermoremanent moment vanishes [24, 27].

Tang et al. [24] showed that reducing the thickness of CoO from 10 nm to 2 nm leads to a T_N decrease from 275 K to 220 K. One has to also consider the structure and the growth conditions which may affect the thickness dependence, in particular very thin CoO layers[2] (below 2 nm) were found amorphous [24].

A different situation arises if the CoO layer forms a bilayer with antiferromagnetic NiO [25] or ferromagnetic Fe_3O_4 [26]. In case of NiO, the exchange coupling enhances the ordering temperature T_N in thin CoO layers (determined from specific-heat measurements). By decreasing the total thickness of the CoO/NiO bilayer, it was shown [25] that the intrinsic magnetic correlation length for this system was between 1.3 and 2.5 nm. The bilayer of a thickness below this length presents only one phase transition at a common T_N. The T_N of CoO was substantially enhanced by exchange coupling to NiO, while AF ordering was suppressed when decreasing the thickness of an isolated CoO layer [25].

A similar behavior was found in Fe_3O_4/CoO exchange-biased systems [26] where the ordering temperature T_N of CoO (determined from neutron diffraction experiments) was found larger for small thicknesses than the bulk value. It was enhanced by the exchange coupling to a 10 nm thick Fe_3O_4 layer and for very thin layers of CoO (down to 1 ML) it extrapolates to T_C of Fe_3O_4. However, the blocking temperature (determined from the bias shifts of hysteresis loops) decreased with the CoO thickness (see Fig. 1.5). These dependencies were also modeled by Lang et al. [22, 21].

[2]Prepared by dc magnetron sputtering on Si(100) substrates in the presence of Ar and O_2.

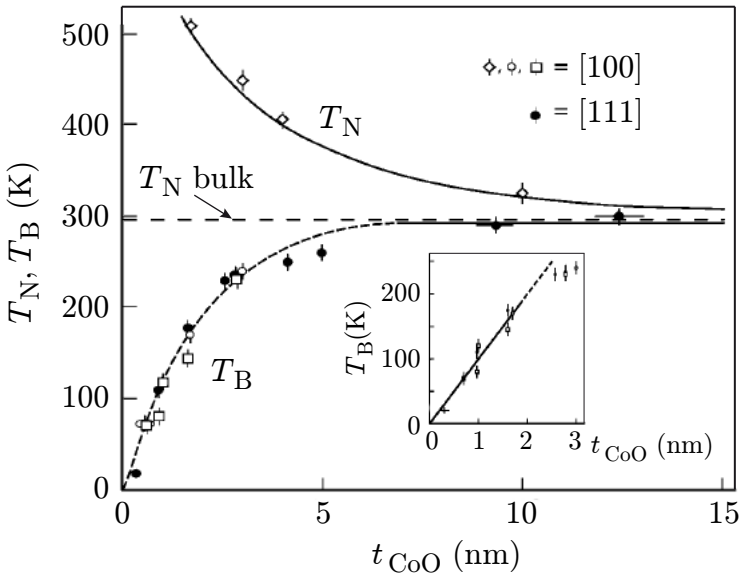

Fig. 1.5: The ordering temperatures T_N and T_B of a Fe_3O_4/CoO exchange biased system as a function of CoO thickness. In the inset a detail for small thicknesses is shown. The system was grown epitaxially on different substrates – orientation [111] was obtained for Al_2O_3 (0001) substrates and [100] for $SrTiO_3$ and MgO (100) substrates. Figure reproduced from [26].

1.2.2 Domain Walls in Magnetic Nanowires

Domains in ferromagnetic materials are separated by DWs. Basically they can be distinguished according to the angle between the magnetization in the two domains. A 90° DW separates domains having their magnetization perpendicular to each other, a 180° DW domains with an antiparallel alignment of their magnetizations [3]. In long and narrow magnetic nanowires made of magnetically soft materials, where shape anisotropy dominates, the magnetization lies usually along the nanowires and 180° DWs are formed.

DWs consist of continuously rotating magnetization due to the strong short-range exchange interaction. In zero applied field, the DW shape and width is a compromise between the exchange energy and the anisotropy energy (including shape anisotropy arising from dipolar effects) [33].

If the DW magnetization rotates in the plane parallel to the DW, it represents a so called *Bloch wall* [Fig. 1.6(a)]. In the case of a *Néel wall*, the magnetization rotates in the plane perpendicular to the DW [Fig. 1.6(b)]. In nanowires of in-plane[3] anisotropy and rectangular cross-sections[4] one can find transverse DWs (TWs) [Fig. 1.6(c)] and vortex DWs (VWs) [Fig. 1.6(d)]. The TW features a continuous rotation of magnetization, thus minimizing the exchange energy at the expense of the magnetic dipolar energy. On the contrary, the VW represents a magnetization circulating about a so called *vortex core*. In this case, the dipolar energy is minimized and the exchange energy increased. The TW is a typical DW type for narrow and thin nanowires, as the

[3]In the plane of the nanowire.
[4]Sometimes also called *nanostripes*.

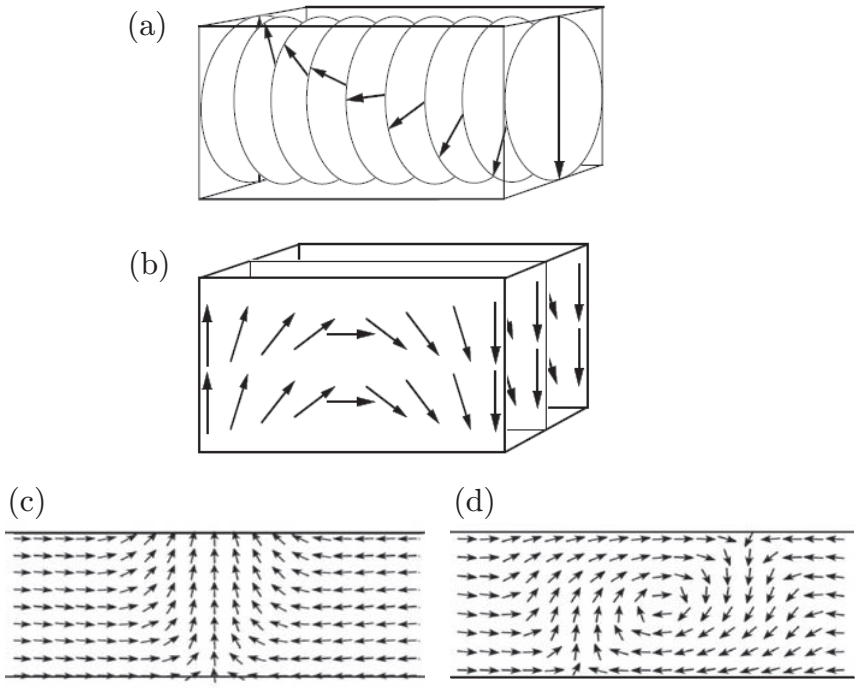

Fig. 1.6: Examples of a Bloch DW (a) and a Néel DW (b). In nanowires VWs and TWs can be found. (c) represents the top view of a TW, (d) of a VW. (a) and (b) were reproduced from [33], (c) and (d) from [37].

TW has the lowest energy here. For wider and thicker nanowires the VW becomes an energetically favorable configuration.

By comparing the energies of the TWs and VWs for cross-sections of different width and thickness, one can construct a phase diagram of DW stability. McMichael and Donahue [34] and Thiaville and Nakatani [35] carried out micromagnetic simulations to find the phase boundary between regions of stable TWs and VWs in NiFe nanowires. The calculated phase diagram was compared to experimental results in Co and NiFe rings by M. Kläui et al. [36, 37].

DW Phase Diagram in Spin-Valve Nanowires

We have carried out micromagnetic simulations using OOMMF to determine the phase diagram of the DW structure in the NiFe layer of a NiFe/Cu/Co nanowire, as a function of the nanowire width and NiFe thickness. The thickness of the Co and Cu layers was fixed to 5 nm. The length of the considered nanowires was 6 μm. Further details on simulations can be found in Appendix A.

The initial simulations aimed on reproducing the border line between TW and VW stability regions presented in Ref. [35]. After successful verification the phase diagram was constructed for the NiFe/Cu/Co system (see Fig. 1.7). The border line between the TW and VW stability regions for NiFe in the NiFe/Cu/Co system is shifted in favor of TWs with respect to single NiFe nanowires [35]. Moreover, the presence of a single-

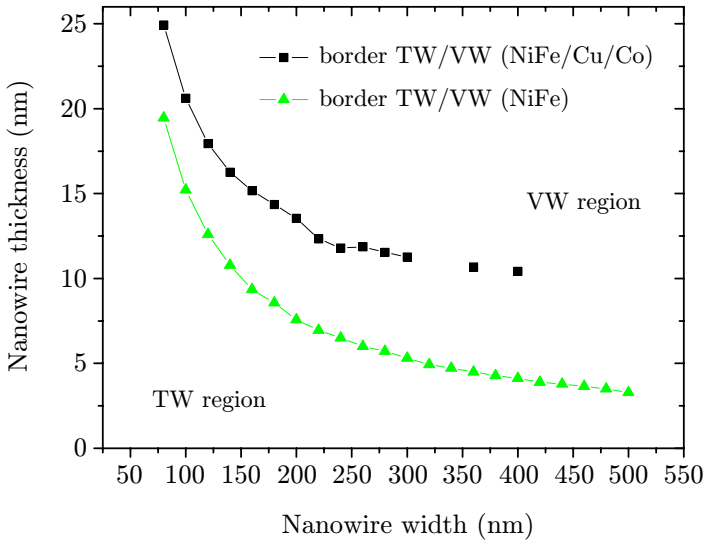

Fig. 1.7: Phase diagram of VW and TW stability in single NiFe nanowires and in NiFe layers of NiFe/Cu/Co nanowires. The green curve was reproduced from Ref. [35].

domain Co layer breaks the symmetry of the system and makes the TWs asymmetric due to the dipolar interaction with the tilted magnetization in the Co layer [38].

Given the size of the nanowire cross-sections we use (thickness 5 nm, width 200-400 nm) in our experimental studies, we can claim that in our system we deal with TWs. For this reason in the following sections we will focus on the description of the TW behavior under magnetic field or electric current.

1.3 Spin-Dependent Transport and Magnetoresistance

The resistivity of metals originates from scattering of electrons on defects, impurities (principal source at low temperatures) and on thermal lattice vibrations (principal source at high temperatures, even at room temperature). In the independent and free electron approximation, the resistivity might be described by the models of Drude and Sommerfeld (a detailed treatment can be found in [39]).

The scattering probability per unit of time is given as $1/\tau$ where τ is a mean relaxation time between the scattering events. In the Sommerfeld model, the relaxation approximation assumes that the collisions of the conduction electrons lead the system to a local thermodynamic equilibrium described by the Fermi-Dirac distribution

$$f(E) = \frac{1}{\mathrm{e}^{\frac{E-\mu_\mathrm{c}}{k_\mathrm{B}T}} + 1} \tag{1.12}$$

where μ_c is the chemical potential. The scattering events take place for electrons with energies close to the Fermi level, with a spread given by the thermal energy $k_\mathrm{B}T$.

Conductivity is described by the Drude formula

$$\sigma = \frac{ne^2\tau}{m_\mathrm{e}}. \tag{1.13}$$

where n is the electron density. For electrons with energies close to the Fermi level we can define the *mean free path* as

$$\ell = \tau v_\mathrm{F} = \tau\sqrt{\frac{2E_\mathrm{F}}{m_\mathrm{e}}}, \tag{1.14}$$

i.e. a mean path between two subsequent collisions. If one is interested in electronic transport in a structure with a characteristic length smaller than ℓ, one talks about the *ballistic regime*, as the electron collisions can be neglected. If the characteristic length is much larger than ℓ, then by passing the structure the electron experiences several scattering events and one deals with the *diffusive regime*.

For the spin dependent transport, one defines a so-called *spin diffusion length* ℓ_sf – a mean path between two collisions reversing the spin. Typical values are approximately 50 nm for a ferromagnetic and 1 μm for a non-magnetic material at liquid He temperatures [1]. ℓ_sf is mostly larger than the mean free path ℓ, as not all collisions reverse the spin. However, the exact values depend largely on a particular material and the temperature of measurement. Details can be found in a review [40].

According to the Matthiessen's rule, the resistivities associated with individual scattering contributions can be simply added. As shown in Section 1.1.3, in transition metal ferromagnets the electrons at the Fermi level are located in both the s and d bands. These represent two conduction channels, i.e. the resistivities add in parallel and the total conductivity then reads [1]

$$\sigma = \frac{n_s e^2\tau_s}{m_s^*} + \frac{n_d e^2\tau_d}{m_d^*}. \tag{1.15}$$

The effective mass m_d^* of d-electrons is much higher than for the light and mobile s-electrons. Hence, the latter ones are dominantly responsible for conductivity [41].

Mott [42, 43] suggested that the conduction s-electrons are mainly scattered to the d states and assumed that spin-flip events are negligible at low temperatures. This explains why Cu is a better conductor than the ferromagnetic transition metals – as there are nearly no available d states at the Fermi level in Cu, the relaxation time τ is longer. If only spin-conserving collisions take place, then the conduction is governed through independent channels of spin-up and spin-down electrons. This is a base for the *two current model*, introduced by Fert and Campbell [44, 45].

Moreover, Fe, Co and Ni exhibit largely different populations of majority and minority electrons at the Fermi level (see Fig. 1.2). This leads to an asymmetry in scattering of majority and minority electrons and consequently the electric current becomes po-

larized according to the majority electrons[5]. We may define *spin polarization*

$$P = \left| \frac{n^{\mathrm{maj}} - n^{\mathrm{min}}}{n^{\mathrm{maj}} + n^{\mathrm{min}}} \right| \tag{1.16}$$

where n^{maj} and n^{min} are the majority and minority electron densities at the Fermi level, respectively. Experimentally, the value of P for NiFe can be most often found in the range of $0.3 - 0.4$ [8, 46], depending on the measurement technique.

1.3.1 Magnetoresistance

Magnetoresistance is generally a change of resistance $\Delta R/R$ of a material under an applied magnetic field H_{a}:

$$\frac{\Delta R}{R} = \frac{R(H_{\mathrm{a}}) - R(0)}{R(0)}. \tag{1.17}$$

Here we list some of the important magnetoresistance types:

- Cyclotron magnetoresistance
  Effect on conduction electrons which bend their trajectories under applied field giving rise to a precession at a cyclotron frequency $\omega_{\mathrm{C}} = \frac{qB}{2m^*}$. The increase of resistivity takes values up to 1%. This is an intrinsic effect (effect of the inner magnetic field). It occurs in both non-magnetic and magnetic materials, but is the dominant effect in non-magnetic materials.

- Anisotropic magnetoresistance (AMR)
  Change of resistance when the electric current is perpendicular or parallel to the internal magnetization. This effect was first discovered by William Thomson (Lord Kelvin) in 1856. It is connected to the spin-orbit interaction and its influence on *s-d* scattering [3]. This is also an intrinsic effect and takes values up to 2% for permalloy (NiFe) and 3% for NiCo alloys. The dependence of AMR on the parallel and perpendicular orientations of the current density $\mathbf{j}$ and magnetization $\mathbf{M}$ reads
  $$R = R_{\perp} + (R_{\parallel} - R_{\perp}) \cos^2(\mathbf{j}, \mathbf{M}). \tag{1.18}$$

- Giant magnetoresistance (GMR)
  Extrinsic effect, it is directly connected to the action of the external field. It is a property of two magnetic layers separated by a nonmagnetic metallic spacer [47] and depends on the angle between the two magnetizations.

- Tunnel magnetoresistance (TMR)
  The system exhibiting TMR consists of two magnetic layers, similarly to GMR, separated by a nonmagnetic insulating spacer [48]. It is based on spin-dependent tunnelling [49, 50, 51] due to the asymmetry in the density of states of the majority and minority spins at the Fermi level. For a parallel configuration there

[5] Strictly speaking according to the *d*-band with less available states at the Fermi level.

is a maximum match between the number of occupied states in the magnetic electrodes, i.e. the resistance is minimum. For the antiparallel configuration the tunnelling takes place between the majority states in the first magnetic layer and corresponding minority states in the second magnetic layer, giving rise to a higher resistance. The TMR was discovered in alumina-based tunnel junctions. However, the highest TMR values exceeding 600% at room temperature were reported for MgO-based junctions [52].

1.3.2 Giant Magnetoresistance

The spintronics boom was triggered by the GMR discovery in 1988, simultaneously by the groups of Albert Fert [53] and Peter Grünberg [54]. For this work they were awarded a Nobel prize in physics in 2007. It was discovered that a parallel alignment of ferromagnetic (FM) layers separated by a nonmagnetic (NM) spacer features a drastically lower resistance than the antiparallel alignment. The GMR ratio is usually defined as

$$GMR = \frac{R_{\mathrm{AP}} - R_{\mathrm{P}}}{R_{\mathrm{P}}} \tag{1.19}$$

where R_{P} is the resistance of the parallel state at the maximum applied field and R_{AP} the maximum resistance of the antiparallel state. The effect is more pronounced in the case of multilayers (multiple repetition of the basic feature) or at low temperatures where the spin-flips do not play a major role.

Effectively two geometries can be established:

- Current-In-Plane (CIP)
  The current flows parallel to the layers. The NM layer thickness should be less than the mean free path ℓ, otherwise the conduction electrons will not transfer the spin information between the layers.

- Current-Perpendicular-to-Plane (CPP)
  The current flows perpendicular to the layers. Here the thickness of the NM spacer is determined by the spin diffusion length ℓ_{sf} [55]. The CPP geometry gives higher values of GMR, because conduction electrons are forced to go through all the interfaces and there is no current shunting through the nonmagnetic metal.

The technological aspects and experimental arrangements are described in Section 3.2 in more detail. From a fundamental point of view, the CPP GMR is less complex than the CIP equivalent, because of the high symmetry of the former [55]. Some advantages of this geometry for determining the fundamental quantities underlying spin-polarized transport were shown in [56].

The essential condition for the GMR effect is that the probability of electron scattering either in the bulk of the FM layers or at the FM/NM interfaces has to be spin-dependent [57, 58]. Following the two current model, the mean free path ℓ^{maj} of majority electrons is longer than that of minority electrons and therefore the resistance r for majority electrons is lower than R for minority electrons (see Fig. 1.8). For an

opposite magnetization, the situation reverses. Thus assuming two independent spin channels we can find the total resistances $R_{\mathrm{P}} = 2rR/(r+R)$ and $R_{\mathrm{AP}} = (r+R)/2$.

Note that even in the absence of current, there is a spin accumulation of majority electrons in the NM layer (and spin depletion in the FM layer) near the FM/NM interface. It is caused by different ℓ for majority and minority electrons in the FM layer. Far from the interface in the NM layer the electron populations become unpolarized again.

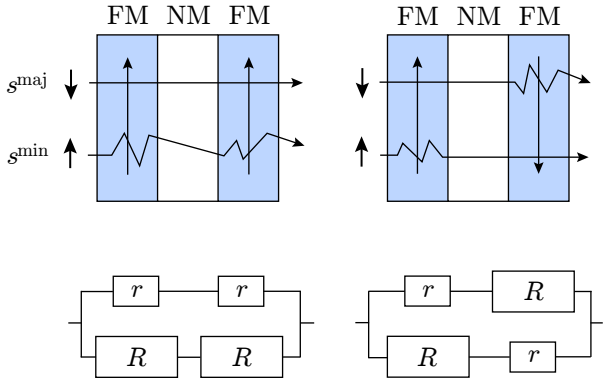

Fig. 1.8: Schematic illustration of the GMR effect in the CPP geometry. In the parallel magnetization configuration the majority electrons are less diffused and the minority ones more diffused, giving rise to a lower total resistance than in the antiparallel configuration where for each spin direction the resistivity is higher in one layer than in the other.

Chapter 2

SPIN-TRANSFER TORQUE AND DOMAIN-WALL MOTION

2.1 Field-Induced Domain-Wall Motion

Applying a magnetic field to a system containing a DW will modify the energy landscape and, if there is not a remaining potential barrier, it will lead to a displacement of the DW to an energetically more favorable position. The effect of a magnetic field on DWs is a relatively old subject. DW motion in bulk ferromagnetic bodies in low applied fields was first described by Landau and Lifshits [4], followed by Döring [59] who introduced the DW mass concept in 1948. The first analytical solution of field-induced DW motion in uniaxial bulk material was derived by Thiele [60] and Schryer and Walker [61]. The latter study identified two regimes of DW motion - a steady-state regime with a high DW mobility[1] at low fields and a precessional regime with a lower mobility at high fields. The critical field separating these two regimes was later called the Walker breakdown field, H_{W}.

Later, Slonczewski and Malozemoff [62, 63, 64] studied DW dynamics of magnetic bubble domains in orthoferrite perpendicular-anisotropy systems in view of introducing magnetic bubble memories. They started with a 1D model to describe DW dynamics in nanowires. 1D model represents a chain of magnetic moments along say x direction with no variation in y and z directions. The moments of the chain can point in any direction. This model is valid for narrow and thin nanowires with the transverse size comparable to the exchange length.

Slonczewski described the DW dynamics by using the LLG equation, where generalized coordinates q, ϕ, θ and Δ were introduced (see Fig. 2.1) [62]. q represents the DW position, ϕ the out-of-plane angle, θ the azimuth angle and Δ the DW width parameter. Δ was obtained from the magnetization profile of a 1D Bloch wall:

$$\theta(x) = 2 \arctan\left(\mathrm{e}^{\frac{x}{\Delta}}\right). \tag{2.1}$$

The magnetization profile of a 1D TW might be fitted with (2.1) and the wall width

[1] Defined as $\mu_{\mathrm{w}} = v/H_{\mathrm{a}}$, where v is the DW velocity and H_{a} the applied field.

parameter is then approximated by [65, 66]

$$\Delta = \sqrt{\frac{A}{K_0 + K\sin^2\phi}} = \frac{\Delta_0}{\sqrt{1 + \frac{K}{K_0}\sin^2\phi}}. \tag{2.2}$$

K_0 is a uniaxial anisotropy constant and K is a uniaxial transverse term describing wires with a non-circular cross-section, thus accounting for the transverse anisotropy. $\Delta_0 = \sqrt{A/K_0}$ is the Bloch wall width defined for thick layers where only the magnetocrystalline anisotropy is taken into account.

Consider a magnetic nanowire with a magnetization direction parallel to the nanowire, containing a TW. The effect of a field H_a applied along the nanowire might be schematically described as follows [67]. First, H_a exerts a torque on the TW magnetization which cants the magnetic moments out of the plane [Fig. 2.1(a)]. The resulting demagnetizing field exerts an additional torque $\mathbf{H}_\mathrm{d} \times \mathbf{M}$ that drives the DW in the H_a direction [Fig. 2.1(b)]. The applied field alone is not so efficient in moving the DW along x, because the damping term dragging the magnetization towards the field is small.

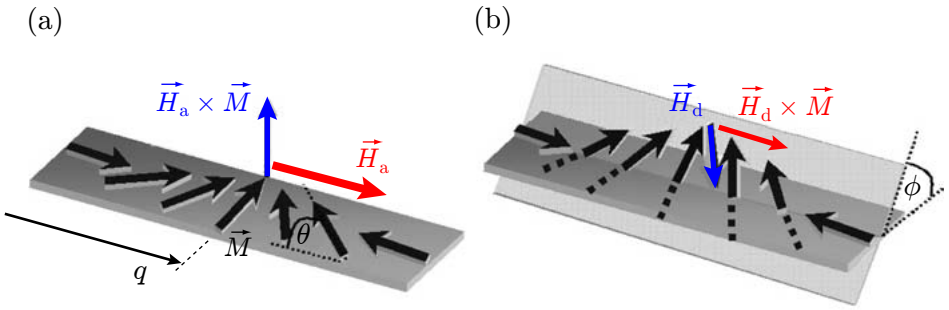

Fig. 2.1: Effect of an applied field on TW dynamics. (a) The torque of the applied field cants the magnetic moments out of the plane, thus creating a perpendicular demagnetizing field (b) which drives the DW forward. The generalized coordinates q, ϕ and θ are indicated. Images taken from [67].

Although the DW dynamics in experimentally realistic nanowires can be satisfactorily modeled only using 2D and 3D simulations, in the following the dynamics will be first described within the 1D model, as the findings give a good qualitative insight on the DW dynamics in wider nanowires.

Analytical Model

The dynamic equations for the parameters q and ϕ were first derived by Slonczewski [62] and together with the expression for Δ might be obtained by solving the Lagrangian formulation of the problem [66]. They read:

$$\frac{\alpha}{\Delta}\frac{\partial q}{\partial t} + \frac{\partial \phi}{\partial t} = \gamma_0 H_\mathrm{a}, \tag{2.3}$$

$$\frac{1}{\Delta}\frac{\partial q}{\partial t} - \alpha\frac{\partial \phi}{\partial t} = \gamma_0 H_\mathrm{K} \sin\phi \cos\phi, \tag{2.4}$$

$$\frac{\partial \Delta}{\partial t} = \frac{12\gamma_0}{\alpha\mu_0 M_\mathrm{S}\pi^2}\left[\frac{A}{\Delta} - (K_0 + K\sin^2\phi)\Delta\right]. \tag{2.5}$$

For a given ϕ Δ relaxes towards its equilibrium[2] value:

$$\Delta^* = \sqrt{\frac{A}{K_0 + K\sin^2\phi}}. \tag{2.6}$$

The DW width adapts according to the instantaneous ϕ angle which evolves differently in the low-field and high-field regimes. From (2.3) and (2.4) we obtain

$$\frac{\partial \phi}{\partial t} = \frac{\gamma_0}{1+\alpha^2}(H_\mathrm{a} - \frac{\alpha}{2}H_\mathrm{K}\sin 2\phi). \tag{2.7}$$

Most of the important properties of 1D DW dynamics are encoded in this equation. Assuming zero transverse anisotropy first, i.e. $H_\mathrm{K} = 0$, the DW magnetization rotates uniformly around the wire axis:

$$\phi = \frac{\gamma_0 H_\mathrm{a} t}{1+\alpha^2} \tag{2.8}$$

and the corresponding DW velocity reads

$$\frac{\partial q}{\partial t} = \gamma_0 \Delta_0 H_\mathrm{a}\frac{\alpha}{1+\alpha^2}. \tag{2.9}$$

In this case, the α parameter is crucial for DW motion along the nanowire, as relaxation of the DW magnetization towards the applied field is necessary.

If some shape anisotropy in the wire cross-section is present, i.e. the aspect ratio is different from 1, the solution of (2.7) splits into two cases. If H_a is inferior to the so-called *Walker field* [see Fig. 2.2(a)]

$$H_\mathrm{W} = \frac{\alpha H_\mathrm{K}}{2}, \tag{2.10}$$

a stationary solution of (2.7) exists and an equilibrium value ϕ^* can be determined from

$$\sin 2\phi^* = \frac{H_\mathrm{a}}{H_\mathrm{W}}. \tag{2.11}$$

[2] $\partial\Delta/\partial t = 0$.

This regime is characterized by a steady-state DW motion at a constant velocity

$$\frac{\partial q}{\partial t} = \frac{\gamma_0 \Delta^* H_\mathrm{a}}{\alpha} \tag{2.12}$$

where Δ^* is the relaxed DW width at ϕ^*. The energy stored in the magnetization tilt ϕ and subsequent distortion of the width Δ during the DW motion led Döring [59] to introduce the concept of DW kinetic energy and DW mass. The DW velocity is approximately α^{-2} times higher than in the zero transverse anisotropy case for the same applied field and hence this configuration is more promising for applications.

The velocity increases linearly up to the H_W value, reaching a maximum

$$v_\mathrm{W} = \frac{\gamma_0 \Delta_0}{\alpha} H_\mathrm{W} = \frac{\gamma_0 \Delta_0}{2} H_\mathrm{K}. \tag{2.13}$$

If K/K_0 is not small, the maximum velocity is reached below H_W [see Fig. 2.2(b)] and reads [66]

$$v_\mathrm{max} = 2 v_\mathrm{W} \frac{K_0 \left(\sqrt{1 + \frac{K}{K_0}} - 1 \right)}{K}. \tag{2.14}$$

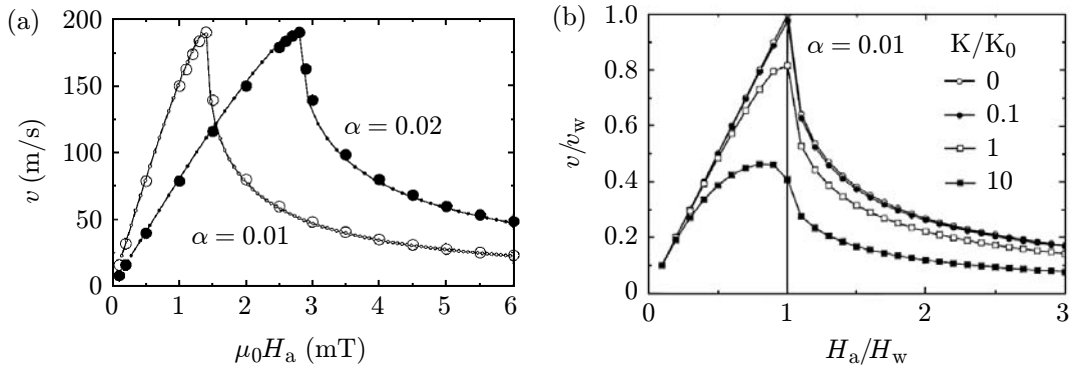

Fig. 2.2: (a) Effect of α on DW mobility for non-zero H_K. The velocity increases linearly at low fields and is inversely proportional to the damping constant α. (b) Effect of the transverse anisotropy K on H_W and v_W. Images taken from [66].

Above the Walker breakdown, ϕ does not retain its equilibrium value and the magnetization precesses around the wire axis. The precession is non-uniform because of the transverse anisotropy term. Also the DW width expands and shrinks periodically and one can only obtain a relation of the average DW velocity during one oscillation period [65, 66]:

$$\left\langle \frac{v}{\Delta} \right\rangle = \frac{\gamma_0}{\alpha} \left(H_\mathrm{a} - \frac{\sqrt{H_\mathrm{a}^2 - H_\mathrm{W}^2}}{1 + \alpha^2} \right). \tag{2.15}$$

For $H_\mathrm{a} \gg H_\mathrm{W}$ the DW *mobility* can be approximated by

$$\mu_\mathrm{w} = \gamma_0 \Delta \frac{\alpha}{1 + \alpha^2}. \tag{2.16}$$

Numerical simulations [66, 68] showed a very good agreement with the conclusions predicted by the analytical 1D model. Simulations of DW dynamics in strip-like nanowires in the same work also confirmed the viability of the above-described characteristics for wider nanowires. The DW velocity in the steady-state regime increases linearly up to H_{W} which is proportional to α and the transverse anisotropy, while the maximum velocity is α-independent and is determined by the nanowire geometry. However, the 1D model fails to provide precise values of the H_{W} and v_{w} quantities.

Beyond the Walker field the DWs experience periodic transformations which are slowing down the DW progression. In case of a TW, an antivortex core nucleates at one edge of the nanowire and propagates to the other edge, thus forming a TW of an opposite magnetization [66]. The process could be viewed also as a rotation of the antivortex core around the nanowire axis. In case of a VW, the vortex core follows a similar spiral trajectory. The transformations take place between a VW and two opposite configurations of a TW.

An analytical solution of field-driven DW dynamics in strip-like nanowires taking into account demagnetizing factors was derived by Porter and Donahue [69]. However, the formula for the Walker field is similar to the presented 1D solution. It reads

$$H_{\mathrm{W}} = \frac{\alpha}{2} M_{\mathrm{S}} (N_z - N_y) \tag{2.17}$$

where N_z and N_y are the perpendicular and transverse demagnetizing factors, respectively.

2.1.1 Experiments

Except for the pioneering work of Sixtus and Tonks (circular wires of Ni or Armco-Fe alloy, 380 μm diameter) [70, 71] and Slonczewski and Malozemoff [62], most of the experimental studies dealing with DW dynamics have focused on Permalloy.

Field-induced DW dynamics in nanowires was studied by several groups. Ono et al. [72] measured DW velocities in NiFe/Cu/NiFe trilayers using the GMR effect at low temperatures. The DW mobility they reported was very low, 260 $\mathrm{ms^{-1}T^{-1}}$ in 500 nm wide nanowires.

A following study was carried out by Atkinson et al. [73] on 200 nm wide NiFe nanowires. Using MOKE magnetometry at room temperature, they measured the time needed to switch the nanowire magnetization as a funcition of field. They found a substantially higher DW mobility exceeding 3000 $\mathrm{ms^{-1}T^{-1}}$.

A substantial advance was made by Beach et al. [74] who managed to experimentally observe both steady-state and precessional regimes of DW motion. The experimental method was again MOKE magnetometry carried out on 600 nm wide and 20 nm thick NiFe nanowires. As they pointed out, the previous studies by Ono and Atkinson were not necessarily contradictory, as they studied different regimes of DW motion.

The precessional DW motion beyond the Walker threshold was observed by Hayashi et al. [75, 76]. They employed time-resolved AMR measurements to follow DW transformations in 200 nm or 300 nm wide and 10 nm thick NiFe nanowires. The correspon-

dence of discrete resistance levels and different DW structures was verified by Magnetic Force Microscopy (MFM). They found an excellent agreement of the oscillation frequency of DW transformations with the theoretical prediction of the 1D model.

Dynamical aspects induced by the shape of field pulses were studied by Weerts et al. [77] in NiFe nanowires. They measured an average DW velocity dependent on the pulse risetime by time-resolved MOKE. It was found that the velocity (maximum $\sim$600 m/s in 750 nm wide wires) decreases with increasing the pulse risetime. This was confirmed by micromagnetic simulations which showed that fast-rising pulses cause the injection of VW-TW pairs from a nucleation pad. The complex structures propagated more quickly than simple TWs created in case of long risetimes.

2.1.2 Effect of Roughness

It can be expected that in real structures there is always extrinsic DW pinning which implies a non-zero depinning field H_{dep}[3] needed for DW propagation. The pinning sites might originate from rugged edges of the sample, roughness of the surface, magnetic impurities, local defects in anisotropy, grain boundaries, etc. The pinning strength generally depends on the proportion of the DW width and the lateral size of the potential well associated with a particular pinning site. For this reason pinning is more important for perpendicular anisotropy systems featuring narrow DWs (in the order of $\sim$ 10 nm for nanowires [78]) than for in-plane anisotropy systems (e.g. NiFe, DW width $\sim$ 100 nm). Also, pinning is often induced by coercivity fluctuations which have a larger effect in systems with a high anisotropy.

Reaching the depinning field H_{dep} for DW propagation is required only at zero temperature, i.e. the DW can be moved even for fields below H_{dep} due to thermal activation. In this case the DW moves in a Barkhausen-like manner [79] by jumps from one pinning site to another. This situation is called the *creep regime* [80]. The average DW velocity reads

$$v = v_0 \left[-\left(\frac{T_{\mathrm{dep}}}{T}\right)\left(\frac{H_{\mathrm{dep}}}{H}\right)^{\eta} \right]. \tag{2.18}$$

T_{dep} is the depinning temperature given by $U_{\mathrm{C}}/k_{\mathrm{B}}$, where U_{C} is related to the height of the DW pinning energy barrier, H_{dep} is the depinning field, v_0 is a numerical prefactor, and η is a universal dynamic exponent equal to 1/4 for a one-dimensional interface moving in a two-dimensional weakly disordered medium [81]. The value of η was experimentally confirmed in a study of creep DW motion in Pt/Co/Pt films [82, 83].

If $H > H_{\mathrm{dep}}$, the pinning becomes less relevant and the DW motion passes to the so-called *flow (viscous) regime*, where the pinning sites act only as a source of dissipation [81].

Depending on the magnitude of H_{dep} with respect to H_{W}, the flow regime might correspond to either the linear or precessional regimes found for DW motion without pinning [83]. Fig. 2.3 schematically shows these situations.

[3] Sometimes called a propagation field.

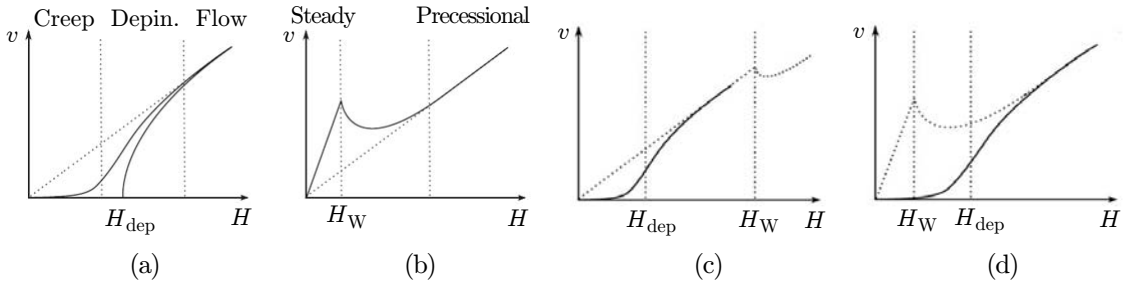

Fig. 2.3: Effect of pinning on DW mobility. (a) Creep, depinning and flow regimes of a DW submitted to an applied field in a weakly disordered medium. (b) In a system with zero pinning, the steady-state and precessional regimes of DW motion can be found. If the Walker breakdown is not observed, it can mean either that the applied field was not high enough (c) or that the depinning field is higher than H_W (d). Images taken from [83].

The creep regime has been experimentally measured in perpendicular-anisotropy systems [82, 83], also for driving forces different from magnetic field [84, 85], but it was not observed in low anisotropy systems with wide DWs, such as NiFe [74]. Cayssol et al. [78] studied the creep regime in Pt/Co/Pt nanowires and found that the depinning field scales with the reciprocal wire width. It turned out that the roughness becomes more important in case of narrower nanowires.

The edge roughness has an important impact on the DW dynamics, as the DW transformations beyond H_W are initiated at the sides of nanowires. On the basis of micromagnetic simulations it has been shown that introducing defects as small as 6 or 7 nm leads to suppression of DW transformations in NiFe nanowires [86]. A similar effect was achieved by using perpendicularly magnetized FePt underlayers [87].

2.1.3 Effect of Transverse Field on DW Propagation

Applying a field transverse to a nanowire represents another means of modifying DW depinning and dynamics [88, 89]. A transverse field H_{tr} parallel to the magnetization of a TW increases its width and makes the TW more mobile (Δ increases) and less sensitive to local variations of structure topography or magnetic anisotropy. Glathe et al. [88] controlled the frequency of DW oscillations behind the Walker-breakdown by varying the applied field H_{tr}. The Walker breakdown could be even completely suppressed for sufficiently high fields. Recently a similar effect induced by an out-of-plane field was reported [90].

Bryan [92, 93] simulated the DW velocity in 100 nm wide nanowires submitted to H_{tr}. Below H_W, a transverse field applied parallel (antiparallel) to the DW magnetization increased (decreased) the maximum velocity v_W. Bryan et al. [92] pointed out that this is not only due to the DW widening, as the relative change in Δ is 3× smaller than the velocity enhancement. By adapting the approach developed by Sobolev et al. [94, 95, 96] one should also take into account the azimuth angle θ of the magnetization

canted by H_{tr} and neighboring to the DW. Below H_{W} the DW velocity then reads [92]

$$v = \left[\frac{2\,\cos\theta}{2-(\pi-2\theta)\tan\theta}\right]\frac{\gamma_0\Delta}{\alpha}H_x. \tag{2.19}$$

Additionally, in [92] it was found that H_{tr} applied parallel (antiparallel) to the DW magnetization decreases (increases) H_{W}. In a subsequent study, Glathe et al. [91] reported an experimental DW velocity of 4500 m/s, obtained for quite a low longitudinal field (approx. 2 mT) and high transverse field (approx. 60 mT) in 160 nm wide NiFe/CoFe/Cu/CoFe GMR nanowires. This DW velocity, found well below H_{W}, could not be explained by a 1D model approximation (2.19).

Finally we note that applying a nonuniform transverse field has also been proposed as another means of driving DWs [97, 98].

2.2 Dawn of Spin-Transfer Torque

The GMR effect relies on the spin polarization of an electric current induced by magnetic electrodes. In 1996, it was theoretically proposed that a reciprocal effect, i.e. a modification of the magnetization state of the electrode by the act of spin-polarized current, is possible [99, 100]. This effect was experimentally verified soon after [101, 102]. Zhang, Levy and Fert [103] have theoretically shown that the exchange interaction between the localized magnetic moments and the conduction electrons flowing through a magnetic multilayer results in two new terms in the LLG equation – an effective field-like term and a spin-torque term.

A schematic model is shown in Fig. 2.4(a). It represents a Co/Cu/Co pillar structure. F_1 is a thick layer which is either pinned to an AF or supposed to have much higher coercivity than F_2. The electrons passing F_1 become spin-polarized along the direction of F_1 magnetization. The misalignment between the magnetization directions of F_1 and F_2 will cause the conduction electrons to lose the transverse component of their spin momentum. This momentum is transferred to the local F_2 magnetization because of total angular momentum conservation.

The loss of transverse spin momentum happens over a very short distance (around 1 nm), i.e. the torque is an interfacial effect, more efficient on thin layers [103, 104, 105]. If the current exceeds a critical current density of the order of $10^{10}\,\mathrm{A/m^2} - 10^{12}\,\mathrm{A/m^2}$, the magnetization in F_2 might be switched to the spin direction of the incoming electrons. For this reason it is important to design the pillar structures to a lateral size of the order of 100 nm, to decrease the total injected current. The effect of spin torque was also proven in magnetic tunnel junctions (MTJ) with an insulating instead of a conducting spacer [106, 107].

Fig. 2.4(b) shows switching of the free magnetic layer F_2 in a Co/Cu/Co pillar back and forth solely by the action of an electric current. The electrons flowing from F_1 to F_2 tend to align the two magnetizations parallel to each other. For the opposite electron flow, the effective torque acting on the free F_2 layer will favor an antiparallel alignment. This is a consequence of spin accumulation [58] of the minority electrons

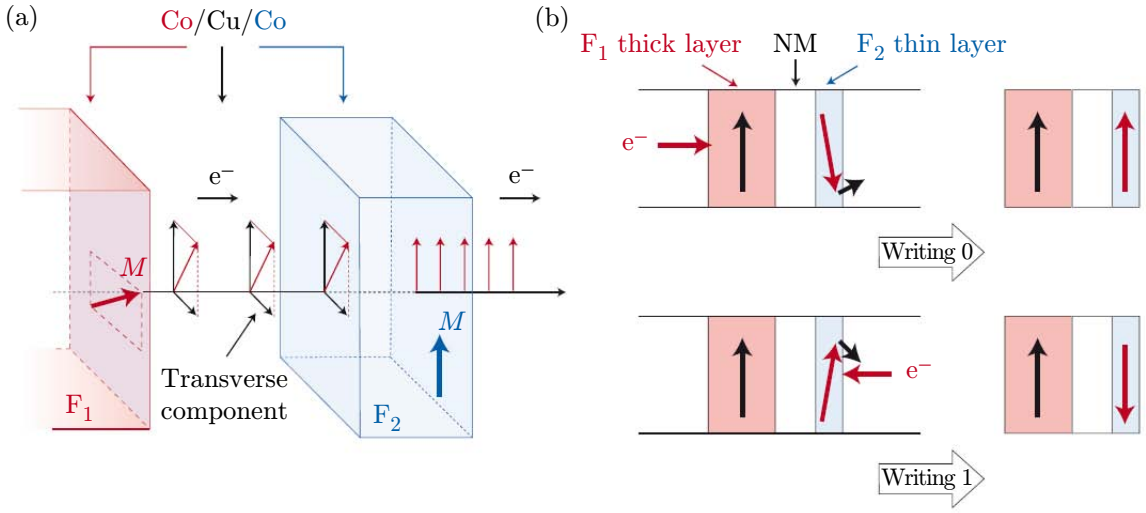

Fig. 2.4: Magnetization switching in FM/NM/FM pillars induced by spin-transfer torque. (a) The electrons become spin-polarized in the pinned F_1 layer and transfer their momenta to the misaligned magnetization in the successive free layer F_2. (b) Switching of the free F_2 layer back and forth by an electric current of opposite polarity. Figure taken from [104].

reflected at the F_1/NM interface which oppose the magnetization in F_2. A detailed treatment of this effect requires to consider carefully spin-dependent transmission and reflection at FM/NM interfaces and spin accumulation [108, 9].

The presented means of switching might be successfully exploited in numerous applications [109, 110]. One of the most promising is the spin-torque-transfer magnetoresistive random-access memory (STT-MRAM) [111, 112], a successor to field-induced magnetic switching MRAM [113].

In the micromagnetic approach, the spin-transfer term can be regarded as opposing the damping term. By tuning the amplitudes of the applied magnetic field and current such that the spin-transfer term compensates the damping, one can achieve stable and frequency-tunable magnetization oscillations [114, 115]. This high frequency precession is intensively investigated in view of nanoscale GHz radiation sources operating on a chip. However, there are still many challenges of both scientific and technological character to be reached before these devices can be industrially realized [102].

2.3 Current-Driven Domain-Wall Motion

The interaction of electric currents and magnetization has been a subject of interest since the 1950's (see e.g. the review by L. Thomas [116] and references therein). However, the most important contribution to the early understanding of this effect was brought by L. Berger during the 1970's and 80's. He focused on the interaction between electric current and DWs. In his first papers [117, 118, 119] he proposed a mechanism called *hydromagnetic DW drag*. He suggested that a DW traversed by a current modifies the current flow because of the Hall effect or magnetoresistance. This

inhomogeneous flow would then produce a magnetic field exerting a net force on the DW itself. The effect would be dominant for film thicknesses larger than 100 nm [120].

In the case of thinner wires, another mechanism, *s-d exchange interaction*, was proposed [121, 122]. This time the model also took into account the spin of the electrons and was based on the interaction between the conduction electron spins and the localized magnetic moments.

Further research in this field received a strong impetus by the papers of J. C. Slonczewski [99] and L. Berger [100] dealing with spin momentum transfer in magnetic multilayers and further developing the existing theories of Berger. In these works it was generally assumed that the magnetization is homogeneous in the individual layers. Soon after publication of the spin-torque effect in pillars, several studies appeared that generalized the spin torque term in the LLG equation for continuously varying magnetization [123, 124, 126]. The modified equation reads

$$\frac{\partial \mathbf{m}}{\partial t} = \gamma_0 \mathbf{H}_{\text{eff}} \times \mathbf{m} + \alpha \mathbf{m} \times \frac{\partial \mathbf{m}}{\partial t} - (\mathbf{u}\nabla)\,\mathbf{m}. \tag{2.20}$$

$\mathbf{u}$ represents a vector oriented along the direction of electron motion which incorporates its current density j and spin polarization P:

$$\mathbf{u} = \frac{\mathbf{j} P g \mu_{\text{B}}}{2 e M_{\text{s}}}. \tag{2.21}$$

u can be interpreted as an effective spin current drift velocity. Importantly, this additional term is derived under adiabatic conditions – the spin-polarization axis adiabatically follows the local magnetization direction. This is fulfilled for a large exchange field in the material and for the magnetization varying slowly in space. In the literature, the DW width is often compared to the Fermi wavelength [124, 151], Larmor length [147] or spin diffusion length [103, 149] to test this criterion.

By exploiting numerical simulations it has been shown [125, 126, 127] that CIDWM is not sustainable solely by the action of the adiabatic term. The DW moves during the current pulse onset and then it stops. This gives rise to a non-zero threshold current, higher than the experimental values [182], even in perfect nanowires without roughness. It turned out that a new term, called non-adiabatic, had to be introduced to reproduce the experimental results.

Thiaville et al. [128] introduced such a nonadiabatic term, characterized by a parameter β[4], in the LLG equation and showed that even a small β parameter comparable to α results in an important correction to the adiabatic current effect. The equation reads:

$$\frac{\partial \mathbf{m}}{\partial t} = \gamma_0 \mathbf{H}_{\text{eff}} \times \mathbf{m} + \alpha \mathbf{m} \times \frac{\partial \mathbf{m}}{\partial t} - (\mathbf{u}\nabla)\,\mathbf{m} + \beta \mathbf{m} \times [(\mathbf{u}\nabla)\,\mathbf{m}] \tag{2.22}$$

The action of the adiabatic and nonadiabatic torques on a TW is schematically shown in Fig. 2.5. The adiabatic torque tends to cant the magnetization so that the TW would be displaced in the direction of the electron flow. However, if the nonadiabatic torque is

[4]The β parameter represents the ratio of the nonadiabatic and adiabatic torques.

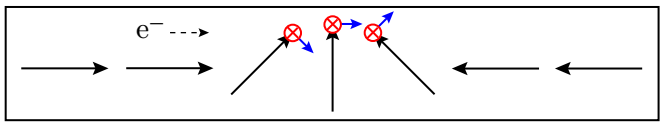

Fig. 2.5: Schematic of the action of adiabatic and nonadiabatic torques on a TW magnetization.

not present, the TW will be just distorted and a transient displacement will be induced ($\sim 100\,\mathrm{nm}$) [127]. The nonadiabatic torque acts similarly to an applied magnetic field, i.e. it tilts the magnetization out-of-plane and the torque of the demagnetizing field drives the TW forward.

For moderate driving currents and not too strong transverse dynamics, one can employ the 1D model. As described in Section 2.1, the idea is to simplify the description of the DW motion by two parameters: displacement of the DW center and a net distortion of the TW structure [128]:

$$\frac{\alpha}{\Delta}\frac{\partial q}{\partial t} + \frac{\partial \phi}{\partial t} = \gamma_0 H_\mathrm{a} + \frac{\beta}{\Delta}u, \tag{2.23}$$

$$\frac{1}{\Delta}\frac{\partial q}{\partial t} - \alpha\frac{\partial \phi}{\partial t} = \gamma_0 H_\mathrm{K}\sin\phi\,\cos\phi + \frac{u}{\Delta}. \tag{2.24}$$

At zero applied field one gets [128]

$$\frac{\partial q}{\partial t} = \frac{\beta}{\alpha}u - \frac{\Delta}{\alpha}\frac{\partial \phi}{\partial t}, \tag{2.25}$$

$$\frac{\partial \phi}{\partial t} = \frac{\alpha}{1+\alpha^2}\left[\frac{\beta-\alpha}{\alpha}\frac{u}{\Delta} - \frac{\gamma_0 H_\mathrm{K}}{2}\sin 2\phi\right]. \tag{2.26}$$

The DW width parameter is identical to (2.2).

Fig. 2.6 shows micromagnetic simulations of the TW velocity as a function of injected current density in 120 nm wide and 5 nm thick NiFe nanowires. The DW behavior depends on the value of the β parameter. For $\beta = 0$, a high critical current density j_c is observed. Once the TW moves, then slightly above the threshold it propagates at a velocity proportional to $\sqrt{j^2 - j_\mathrm{c}^2}$ [151], reaching the limit case $v = u$ for high current densities.

If $\beta < \alpha$, the TW velocity increases linearly up to a threshold current and then again converges to u (not shown in Fig. 2.6, see the 1D model results in the original paper [128]).

If $\beta > \alpha$, two regimes of TW motion can be found – a stationary and a precessional regime. Below the Walker threshold, the TW is driven solely by the nonadiabatic term [129]. The velocity reads $v = \beta u/\alpha$ and the ratio β/α can be interpreted as a spin-transfer efficiency from the current density to the DW motion.

Beyond the critical value of j_c no solution with a constant angle ϕ and a constant velocity v exists. In this precessional regime, the adiabatic torque starts to increase the

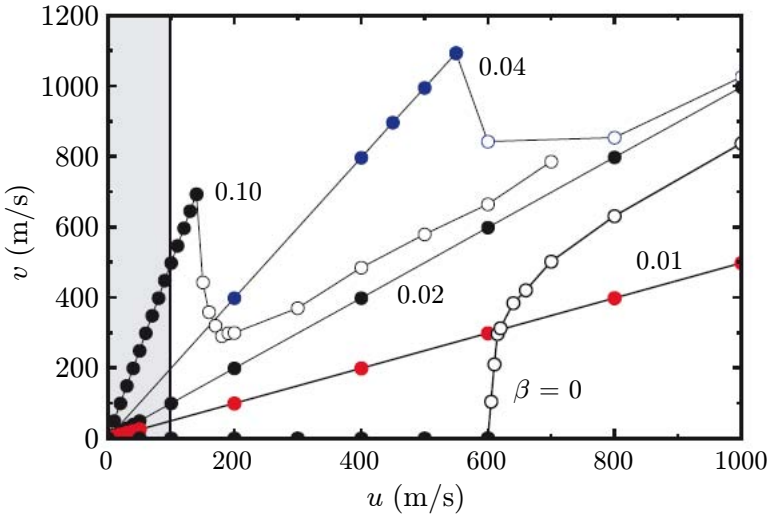

Fig. 2.6: TW velocity as a function of the effective spin current drift velocity u for different values of the parameter β. The α parameter was set to 0.02 [86]. The shaded area approximately shows the range of u used in experiments. $u = 100\,\mathrm{m/s}$ corresponds to a current density of $3.6 \times 10^{12}\,\mathrm{A/m^2}$, assuming $P = 0.4$. Figure taken from [128].

TW velocity. There is an analogy with DWs in nanowires with negligible transverse anisotropy described for the field-driven case [eq. (2.9)]. The time-averaged velocity reads [130]

$$\langle v \rangle = \frac{1 + \alpha\beta}{1 + \alpha^2} u. \tag{2.27}$$

In all the mentioned cases the TW velocity v converges to u for large applied currents.

Finally, if $\alpha = \beta$, the TW moves as a rigid body without deformation and the Walker field becomes infinite.

Analytical calculations of the DW velocity and Walker breakdown in magnetic nanowires were carried out by Mougin et al. [130]. They present the DW behavior under both magnetic field and current and take into account the reduced dimensions of the nanowires, i.e. the transverse and perpendicular demagnetizing factors.

Although the qualitative description of DW dynamics can be applied to a VW as well, its behavior under current cannot be simply described by the 1D model. In addition, the description of a VW state requires a coordinate for the transverse position of a vortex core. An alternative equation for describing VW motion was developed by Thiele [60]. The idea is to transform the torques on individual spins into effective forces acting on the spin structure [67]. Several models were presented to simply describe the VW internal structure [132] and its dynamics [133]. In particular, Ref. [133] introduces a 2D model for describing the DW structure and reproduces the transverse motion of the vortex core upon application of a field or current.

Detailed numerical simulations of TW and VW motion under field, current and a combined action of both were carried out by Thiaville and Nakatani [134].

2.3.1 Landau-Lifshits or Landau-Lifshits-Gilbert damping?

For the special case of $\alpha = \beta$ eq. (2.22) can be rewritten (by multiplying it by $1 + \alpha\mathbf{m}\times$ on the left) [135, 136]:

$$\frac{\partial \mathbf{m}}{\partial t} = \gamma^* \mathbf{H}_{\text{eff}} \times \mathbf{m} + \alpha\gamma^* \mathbf{m} \times \mathbf{H}_{\text{eff}} \times \mathbf{m} - (\mathbf{u}\nabla)\,\mathbf{m}, \tag{2.28}$$

where $\gamma^* = \gamma_0/(1+\alpha^2)$. As pointed out by Barnes and Maekawa [137], in this situation the Galilean invariance of the system would be possible, i.e. $\alpha = \beta$ implies the existence of *inertial* solutions $\tilde{m}(\mathbf{r} - \mathbf{v}t)$, where $\tilde{m}$ represents a static DW configuration and $\mathbf{v}$ an arbitrary velocity which is equal to $\mathbf{u}$.

Tserkovnyak [135] deduced that a situation of $\alpha = \beta$ is not likely, first as the presence of spin-orbit coupling and magnetic disorder might microscopically modify the α and β parameters, second as the *s-d* model of transition-metal ferromagnetism itself implies breaking of the Galilean invariance – the scattering times for minority and majority electrons are different, so that the DW velocity is not equal to the average drift velocity.

The early experimental works [139, 138, 140] found approximately $\alpha = \beta$. Later, however, very high DW velocities exceeding the spin-transfer rate u in NiFe were found [141, 142]. This indicates that the β/α ratio might be generally material- and structure-dependent.

The form of Landau-Lifshitz and Gilbert damping has motivated M. D. Stiles [143] to show that (2.28) rather than (2.22) incorporates a more natural form of damping which reduces the free magnetic energy in the presence of spin-transfer torque. An intensive discussion about this discrepancy was raised. For instance, Tserkovnyak [135] pointed out that there are simple models for which the LL [144] or the LLG form [145] arises more naturally. Moreover, the LLG and LL forms of damping can be easily transformed in the equations (2.22) and (2.28), as mentioned above. We recall that it is only in the situation of $\alpha = \beta$ where the β parameter does not appear in eq. (2.28). This shows that numerical studies of DW motion described by the LL and LLG equations with $\beta = 0$, i.e. adiabatic torques [143], cannot be effectively compared. A further discussion on this topic can be found in [146].

2.3.2 Microscopic origin of the β parameter

As follows from the previous discussion, the origin and magnitude of the β parameter is a hot subject of current research and a general consensus has not been reached yet. In the following we will summarize the main published ideas.

Waintal and Viret [147] and Vanhaverbeke and Viret [148] based their model on Larmor precession of a conduction electron about a local *s-d* exchange field. Both the adiabatic and nonadiabatic terms can be recovered. A characteristic length to be compared to the DW width to separate the two terms in this approach is the Larmor wavelength[5]. Initially, the spins are aligned with local magnetization, but after entering the DW the spin direction deviates from the magnetization direction due to the spin

[5] A distance the electron passes during one period of Larmor precession around the exchange field.

precession. At the end of one period the spins and magnetization become aligned again. The nonadiabatic term arising from this mistracking is spatially non-local, but otherwise it has the same form of β as in the models of Zhang or Tatara which whill be discussed in the following.

Zhang and Li [149] computed the response of conduction electrons to a spatial and time varying magnetization. Subsequently the reciprocal effect of spin torque on magnetization was derived. They found an additional spin-torque term, connected to the mistracking between the conduction electron spins and the local magnetization direction. This leads to a nonequilibrium spin accumulation in the DW which is relaxed mainly by spin-flip scattering. On the contrary, the adiabatic torque is connected to the instantaneous reorientation of the spins of conduction electrons along the magnetization direction and is completely absorbed by the distortion of a DW. The nonequilibrium spin density induces the nonadiabatic torque, described by the coefficient

$$\beta = \frac{\tau_{\mathrm{ex}}}{\tau_{\mathrm{sf}}} \tag{2.29}$$

where τ_{ex} is the period of Larmor precession around the exchange field and τ_{sf} is the spin relaxation time. With respect to eq. (2.22), there is a factor of $1/(1+\beta^2)$ at both the adiabatic and nonadiabatic terms. For typical transition-metal ferromagnets eq. (2.29) leads to β values of 0.01-0.04 [149, 128] and thus this factor brings only a small correction.

The nonequilibrium spin density also leads to a modification of the precession and damping terms in the LLG equation – the gyromagnetic ratio and the α damping parameter have to be renormalized. However, the correction is about two orders of magnitude smaller than the nominal values.

Xiao, Zangwill and Stiles [150] argued that the spin of the conduction electrons follows the local magnetization adiabatically, even in the presence of spin-flip relaxation, except for very narrow DWs ($\sim$nm).

Tatara and Kohno [151] studied the DW motion in two limiting cases. For wide DWs, much longer than the Fermi wavelength, they derived a spin-tranfer torque identical to the adiabatic torque of eq. (2.22). For narrow DWs a momentum-transfer term was found. It acts on the DW as an effective force and is proportional to the current density j and DW resistivity[6] [151]. The nonadiabatic term remains valid for wider DWs in some proportion, but decreases strongly with the DW width. The connection between the nonadiabatic spin-torque and DW resistance was studied by Berger [156].

Magnon emission has been also found as a contribution to the nonadiabatic spin torque [157, 158]. If magnons provided the only relaxation possibility, the DW velocity would adapt to the spin-current velocity u, i.e. $\alpha = \beta$ [158]. However, this is not valid for real systems with magnetic inhomogeneities and defects.

Duine at al. [160] have calculated α and β for a model ferromagnet, showing that a nonzero parameter α implies a nonzero nonadiabatic spin-transfer torque. Kohno, Tatara and Shibata [161] have shown that both β and α arise from spin-relaxation

[6] DW resistivity is connected to the reflection of electrons on the spatial varying magnetization [152, 153, 154, 155].

processes and generally $\alpha \neq \beta$.

The formula (2.22) holds well in case $\hbar\omega \ll \Delta_{\mathrm{xc}}$, where ω is a ferromagnetic-resonance (FMR) angular frequency and Δ_{xc} is the ferromagnetic exchange splitting, and for smooth walls and moderate applied currents [135]. A dynamic correction for β was introduced in Refs. [144, 159]. This correction becomes important for high currents.

The uncertainty in the β/α ratio, which in different predictions range from lower than 1 to close to 1 or even much larger than 1, motivated Garate et al. [162] to derive the β parameter directly from the band structure of real materials. They identified two sources of nonadiabatic spin-transfer torque – the first for which the magnetization change is too fast and the electrons do not follow the local magnetization direction, the second is related to the change of magnetization damping due to the excitation of electron bands by electric current. Their result can be used for calculating β for different materials from first principles. It turns out that "α and β have the same qualitative dependence on disorder, although their ratio depends on the details of the band structure", in particular the spin-orbit interactions [162].

Recently, a new concept of efficient DW manipulation was introduced – the Rashba spin-orbit interaction [163]. It arises from the motion of conduction electrons in an asymmetric crystal-field potential. In its rest frame the electron feels a magnetic field which couples to the electron's spin and causes its precession. This Rashba field has an effect similar to the field-like β term. Its influence was demonstrated for instance in the $Pt/Co/AlO_x$ system [164] where high current-induced DW velocities were observed and β was found to be as high as 1 [165].

Tatara et al. [151, 170] identified different regimes of DW pinning and argued that in case of a nonzero β no intrinsic pinning exists. The DW threshold current depends on the extrinsic pinning, caused by various defects. Duine and Morais Smith [171] studied both the extrinsic and intrinsic pinning and obtained results for the DW velocity as a function of current for various regimes of pinning. In particular, "they found that the exponent characterizing the creep regime strongly depends on the presence of a dissipative spin-transfer torque."

Thermal activation effects were studied theoretically for instance by [166, 167, 168, 169]. Generally it was found that at nonzero temperature the DW moves even before reaching the current threshold. In the model presented by Duine, Núñez and MacDonald [168] the velocity of a rigid DW increases linearly with current even in the absence of the β term.

J.-V. Kim and C. Burrowes [172] studied the viscous regime of CIDWM and found how the adiabatic and non-adiabatic torques influence the DW depinning driven by thermal activation. The effective energy barrier was lowered by current, but the transition rate was still governed by the Arrhenius law. They found that the variation in the effective energy barrier depended only on the nonadiabatic parameter β. These findings were exploited in a following experimental study [173] of viscous DW motion in nanowires based on perpendicular-anisotropy Co/Ni multilayers and FePt thin films. The determined β values were $\beta_{\mathrm{CoNi}} = 0.022$ and $\beta_{\mathrm{FePt}} = 0.06$[7] which were close to the

[7] β_{FePt} was determined with an uncertainty of 50%.

known Gilbert damping constants in these materials [173].

A similar approach was chosen by Eltschka et al. [174] to determine the β parameter for NiFe. They found values of 0.01 for a TW and 0.073 for a VW. The value of β for a TW is very close to the α damping parameter. This seems to be in line with the concepts mentioned above, that the α and β parameters do not have very different values for most materials, as long as they have a related origin.

It has been shown for a VW, but it could be accepted as a general feature, that the effective damping constant α found for a given structure depends strongly on disorder (impurities, grain structure, defects) and internal DW dynamics. Hence, such an α value determined from DW-motion or vortex-gyration experiments should not be a priori considered as the intrinsic α [175].

2.3.3 Experiments

Moving magnetic domain walls (further DWs) by spin-polarized current has attracted a considerable worldwide interest and the number of experimental studies on this topic is increasing exponentially [67, 116]. Here we will mention some of the relevant achievements in the experimental confirmation of the spin torque effect on DWs. Other important papers will be mentioned in the introduction and discussion of the experimental Part III as a comparison to the results of our study.

The effect of electric current on a DW was first tested already in the 1980's [120, 177, 178]. Because of the high current densities needed for DW motion and a multidomain structure in wide wires [179], subsequent experimental studies on single DWs were carried out only when the evolution of lithography techniques allowed narrow nanowires to be produced.

The majority of studies were carried out for single NiFe nanowires featuring in-plane magnetic anisotropy [116]. The first experiments with applying only current were however carried out by J. Grollier et al. [180] on spin-valve NiFe/Cu/Co structures. Later on, Grollier at al. [181] showed back and forth switching of the NiFe layer by current-induced DW motion with the assistance of a 0.3 mT magnetic field. The spin-valve-based nanowires will be addressed in more detail in Section 2.3.5.

Further verification of the effect came with the works of Vernier et al. [182] and Tsoi, Fontana and Parkin [183]. Vernier et al. studied CIDWM in NiFe nanowires by magneto-optical Kerr effect (MOKE). Tsoi, Fontana and Parkin employed the magnetic force microscopy (MFM) and AMR techniques to identify DW motion between two constrictions in CoFe nanowires.

Yamaguchi et al. [184] provided the first experimental determination of a current-induced DW velocity. They studied DW displacements in L-shaped NiFe nanowires by MFM. Two effects were found: the DW displacement scaled linearly with the current pulse duration, indicating DW propagation at a constant velocity during the pulse; the DW velocity increased with the applied current density. The DW moved along the direction of the electron motion at a velocity of approximately 3 m/s for current densities close to the threshold of 6.7×10^{11} A/m^2 (value corrected for nanowire heating [185]).

Kläui et al. [186] observed continuous transformation of a VW to a TW after application of several current pulses to 500 nm wide and 10 nm thick NiFe nanowires. This was the first experimental evidence of DW transformations due to current. The employed observation technique was scanning electron microscopy with polarization analysis (SEMPA). The recorded DW velocities were quite low, 0.3 m/s for 10-μs pulses of 2.2×10^{12} A/m^2. In a subsequent study of the same group [187], the magnetization configuration of 1 μm wide NiFe wires was imaged by X-ray magnetic circular dichroism photoemission electron microscopy (XMCD-PEEM). Using consecutive pulses they nucleated and annihilated vortices due to the spin-torque effect. The velocity of these complex micromagnetic objects decreased with the number of present vortices.

One of the highest DW velocities in NiFe was reported by Hayashi et al. [141] – 110 m/s in zero field. Similar DW velocities of 130 m/s induced by 3-ns current pulses of 4×10^{12} A/m^2 were recently found by Heyne et al. [142] in NiFe nanowires. They attribute the high velocities to very short pulse risetimes (approx. 100 ps) which are faster than the magnetization damping time and more efficient than the pinning field [188]. The DW velocity v was very close to the spin-transfer effective rate u which would also mean that α is close to β in their system.

Note that the current densities needed for such a rapid DW motion are elevated much above 1×10^{12} A/m^2 at zero applied magnetic field. At such high current densities DW transformations may take place [186], thus lowering the DW velocity.

Heyne et al. [189] used XMCD-PEEM to visualize magnetic DWs in 1.5 μm wide and 8 nm thick NiFe wires. They observed DW transformations from TWs to VWs upon a current pulse and back to TWs upon a further current injection. Importantly, the VWs featured the same chirality at each transformation, as well as the same direction of the vortex core motion, which is a signature of spin-torque effects [133] rather than thermal activation. The transformations indicate that $\alpha \neq \beta$. The critical current densities[8] for TWs and VWs were slightly different, 9×10^{11} A/m^2 and 7.5×10^{11} A/m^2, respectively.

Experiments on a combined action of field and current were carried out by Beach et al. [138] and Hayashi et al. [139]. In particular, they explored field-driven DW motion assisted by dc current. The DW velocity could be enhanced or suppressed depending on the mutual magnitude and orientation of the field and current. The velocity enhancement was dependent on the field range. Generally the mobilities in the linear and precessional regimes were not strongly influenced, there was just a velocity offset. As mentioned in the previous section, both studies deduced that β was comparable to α.

As shown already in the theoretical section, although a large number of papers deal with the determination of the nonadiabatic spin-torque contribution, the ratio β/α for different materials remains an open question. Besides the approach to measure the β parameter from the variation of the energy barrier in the creep regime, a method based on vortex core displacement was recently proposed [190]. "The scheme allows one to distinguish between the displacements of the vortex core due to the nonadiabatic spin torque, the adiabatic spin torque and the Oersted field, independently of the exact direction of the current flow" [190].

[8] A minimum current density for which a DW displacement is detectable.

The relationship between α and β has been tested by Moore et al. [191]. NiFe wires were doped with Ho in order to engineer the α damping constant. α was measured by FMR and subsequently the β/α ratio was determined from the DW velocity in the linear regime. Up to 4% of Ho the two parameters scale and in this range the β/α ratio was found to be 16. This indicates that the nonadiabatic spin torque originates from the same mechanism as the Gilbert damping [191].

The *thermal effects* play an important role in CIDWM. Increasing temperature leads to a decrease of magnetization and pinning strength [192], but also to a decrease in spin polarization of the current [193]. This change naturally becomes even more important close to the Curie temperature [194]. Laufenberg et al.[195] observed a decrease in the spin-transfer efficiency, which is proportional to β, when the temperature varied between 4 K and 300 K. The critical current density increased by 40%, but the critical field in the field-driven case decreased. Although the reason was not clear, the authors suggested that this variation might be due to thermally excited spin waves.

A large interest has been recently devoted to the systems with *perpendicular magnetic anisotropy* (PMA). The nanowires contain very narrow Bloch walls which are convenient to explore the nonadiabatic limit [192]. Ravelosona et al. [192] studied DW motion in a CoPt/Cu/CoPt multilayer and found quite a high spin transfer efficiency, as the DWs were displaced with a current density as low as $10^{11}\,\mathrm{A/m^2}$. Due to a large pinning, the DWs moved over small distances ($\sim$10 nm) which were recorded by the extraordinary Hall effect (EHE).

Some systems with PMA, like $\mathrm{Pt/Co/AlO_x}$ [84], exhibit larger DW velocities than NiFe, up to 400 m/s [196]. The current densities required for reaching these velocities exceeded $1 \times 10^{12}\,\mathrm{A/m^2}$ at zero applied magnetic field.

Recently, a lot of papers investigating CIDWM in PMA systems of different materials, from FePt [173], to Co/Ni [173, 197, 198, 199, 200], Co/Pt [201, 202], CoCrPt [203], $\mathrm{Pt/Co/AlO_x}$ [84, 165], TbFeCo [204] and $\mathrm{SrRu0_3}$ (with a threshold current of the order of $10^{10}\,\mathrm{A/m^2}$ [205]) have been published. Describing them in detail is out of the scope of this chapter. Some of the important results were already mentioned previously in the text.

Very low critical current densities for CIDWM, of the order of $10^9\,\mathrm{A/m^2}$ [85, 206, 207], were found in *magnetic semiconductors*, in particular GaMnAs. This was attributed to the low spontaneous magnetization and high-carrier spin polarization of GaMnAs [208]. Yamanouchi et al. [85, 207] observed thermal creep of DWs in GaMnAs for low applied current densities. The maximum observed velocities reached 20 m/s [85]. The obstacle for employing this material in devices is that it is not ferromagnetic at room temperature (T_C is 110 K [209]). Recently, the β parameter has been derived from the dependence of DW velocity on injected current [210]. It reads 0.25, i.e. it is identical to the effective α found for GaMnAs [206].

2.3.4 Pinning and Dynamics

The problem of DW pinning by defects is one of the main issues in almost every studied system today [140, 201, 211, 212]. Hence, avoiding or controlling the pinning

is an essential point for future exploitation of magnetization switching by DW motion in reliable electronic devices.

Current-induced depinning of DWs is often studied for a single defect, which in most cases consists of an artificially introduced, lithographically prepared notch of different shapes [183, 213, 214, 215]. Another artificial means of DW pinning is to use L-shaped nanowires with a curvature radius comparable to the DW width [216]. In most cases, a highly stochastic DW depinning probability is found for both field [217, 218] and current [140] pulses. Recently it has been shown that the DW depinning threshold current depends on the shape of the pinning profile [219] as well as the temporal shape of the current pulse [188]. The pinning is also different for a DW that moves across a notch (dynamic pinning) than for one that is trapped there (static pinning) [220].

Considerable pinning might also be induced by natural defects in both straight and curved nanowires [140, 211, 221] without artificial pinning sites. The DWs can usually be depinned by applying current densities above a certain threshold value. Particularly, in Ref. [211] after reaching the threshold current density, DWs in single NiFe nanowires (100 nm - 1 μm wide and 12-24 nm thick) jumped from one pinning site to the next, indicating that in this system the depinning current densities had similar values for different natural defects.

Thomas et al. [222] showed that depinning of DWs driven by nanosecond-long pulses is very sensitive to the exact pulse length. This is due to the current-induced oscillatory motion of the DW in a particular potential well. After the end of the pulse, if the DW is in a phase where it can overcome the pinning potential, it will be depinned. The direction of the initial DW motion can thus be both with/against the electron flow.

A very interesting experiment aiming to determine the DW mass was carried out by Saitoh et al. [223]. They studied resonant oscillations of a DW confined in a U-shaped NiFe nanowire. The potential well was determined by an applied field and the excitation was provided by a small ac current ($10^{10}\,\mathrm{A/m^2}$). They obtained a DW mass of approximately $6.6 \times 10^{-23}\,\mathrm{kg}$. Moreover, the resonant excitation allowed μm displacements to be achieved.

Observation of oscillatory DW depinning further motivated the studies of DW oscillations in a pinning potential. This phenomenon has been extensively studied both theoretically [224, 225] and experimentally [226, 227, 228, 229].

2.3.5 Effects in Spin-Valve Nanowires

For spin-valve NiFe/Cu/Co nanowires, critical current densities as low as $8 \times 10^{10}\,\mathrm{A/m^2}$ were found, assuming a uniform current flow in the trilayer [181, 213]. The critical current density can be further lowered to $1 \times 10^{10}\,\mathrm{A/m^2}$ by employing CoFeB as a soft magnetic layer instead of NiFe [230]. High DW velocities in this system were suggested by Lim et al. [213], who observed a 20 μm DW displacement induced by a 0.5 ns current pulse. However, besides the intriguing value of the DW velocity, many open questions arised in this work — the DW displacement did not scale with the current pulse duration and a reversal of the direction of DW motion was observed at high current densities.

We will show in Part III that in spin-valve nanowires DW velocities above 600 m/s and more could be achieved using relatively low current densities below 5×10^{11} A/m^2.

A theoretical work on spin injection in spin-valve systems containing DWs was carried out by Khvalkovskiy et al. [231]. They considered a spin valve system consisting of a ferromagnetic layer with a single DW, a metal spacer and a second ferromagnetic layer that is a planar (magnetization in-plane) or vertical polarizer (magnetization out-of-plane). This situation was compared to a single ferromagnetic layer. It was found that spin accumulation inside the Cu spacer layer in the region of a DW gives rise to a spin current injected vertically in the DW. This additional channel for the spin transfer from the current to the magnetic moments inside the DW might improve the spin transfer efficiency leading to a significant reduction of the critical currents. The better efficiency of spin torque has been predicted for a perfect vertical injection of the current [231]. In case of an in-plane polarizer, the DW moved at a velocity of 100 m/s at 10^{11} A/m^2.

An experimental proof of the large effect of perpendicular spin currents in spin valve systems was given by Boone et al. [232]. The authors investigated the DW motion in the NiFe layer of NiFe/Cu/$Co_{50}Fe_{50}$ spin-valve nanowires. The DW motion was driven by a resonant excitation of the DW in a potential well. Very high DW velocities of about 800 m/s at current densities as low as 9×10^{10} A/m^2 were found [232].

These advantageous results for spin-valve nanowires are very promising for the application of CIDWM. The combination of different magnetic and nonmagnetic layers might however be problematic because of a large number of free parameters to investigate [116]. Particularly the growth of the individual layers may lead to interface roughness resulting in DW pinning and the dipolar interaction between the magnetic layers is also significant. These issues will be addressed in Chapter 3.

2.3.6 Application Concepts

Besides the fundamental investigation of the interaction of current and magnetization, the research in DW motion is motivated mainly by two applications:

- Magnetic Logic Devices
  As proposed originally by Allwood et al. [233], these devices work with field-induced DW motion. On the basis of the proposed essential logic circuits like NOT [234] and AND, any more complicated logic systems might be realized.

- Racetrack Memory
  This memory was proposed as a direct competitor to harddisks and random-access memories and has become almost a Holy Grail in the CIDWM community. The father of this idea, S. S. P. Parkin, introduced the concept of a cheap, fast, non-volatile and low-consumption memory [235, 236]. The racetrack in Fig. 2.7(a),(b) represents a nanowire with notches where the information is stored in the DWs separating domains of opposite magnetizations. Unlike magnetic field, upon applying current pulses the domain wall set moves as a whole in one direction over a read (c) and write (d) head.

The racetrack memory does not have any rotating mechanical parts as harddisks, i.e. it is as fast as solid-state memories, but the information can be written an infinite number of times (with respect to FLASH disks which have a limited number of cell overwritings) and is preserved after the computer is powered down. The energy consumption is very low as there are no coils for production of magnetic field. The storage density is limited by the lithography state-of-the-art, in any case the 3D ordering offers a huge reserve for the expansion of the memory size [see Fig. 2.7(e)].

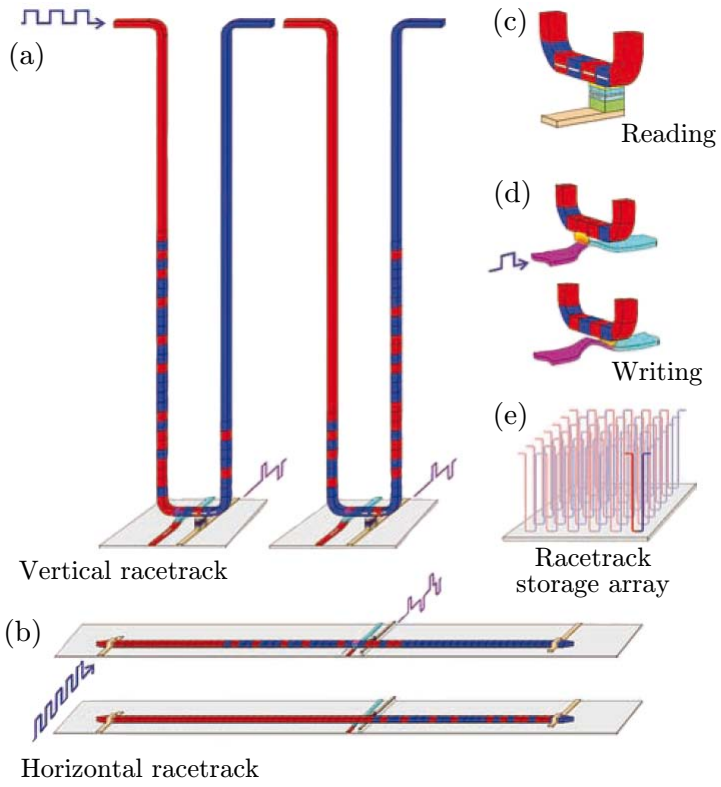

Fig. 2.7: The concept of the racetrack memory. (a) vertical racetrack, (b) horizontal racetrack. (c) reading data from the stored bit can be done by reading the resistance of a magnetic tunnel junction in contact with the racetrack. (d) writing of the information bit is performed by the stray field of a domain below the magnetic bit. The polarity of the "writing domain" can be altered by current injection as well. (e) concept of the racetrack array. Figure taken from [236].

Part II

OPTIMIZATION OF SPIN-VALVE MULTILAYERS AND NANOWIRE PATTERNING

Chapter 3

CONTINUOUS SPIN-VALVE FILMS

In Section 2.3.5 we suggested that the patterned spin-valve systems are promising candidates for devices based on current-induced domain-wall motion. From the fundamental point of view, the spin torque in spin valves and the GMR effect are closely connected. Hence, it is likely that the system optimized in terms of GMR will also feature high-efficiency spin transfer in case of the DW motion. In the chosen NiFe/Cu/Co multilayer, we investigate the DW motion in the NiFe layer.

The choice of materials was influenced by technological aspects and requirements for the synchrotron-based magnetic imaging technique selected for observation of the CIDWM – XMCD-PEEM. Its elemental selectivity enables one to probe the magnetization in each layer separately and to investigate their mutual interaction. However, for this purpose each magnetic layer needs to have a different elemental composition. Moreover, because of surface sensitivity of the technique, the NiFe layer has to be at the top. More details will be given in Chapter 5.

A system featuring GMR is also attractive because one can indirectly follow the DW motion on the basis of transport measurements [237, 181]. However, it has been shown [238] that the DW motion in NiFe/Cu/Co nanowires is largely influenced by pinning of various origins. It is clear that a multilayer system will be more sensitive in this aspect and an optimization in terms of the layer growth, interfacial roughness and interlayer coupling will be necessary. It is also essential to ensure that switching of the NiFe layer is independent of the magnetization state in the Co layer.

In this chapter we address mostly material issues and while optimizing the multilayer parameters we also analyze physical and chemical processes like oxidation, corrosion and thin film growth. A review of the used analytical techniques is given in Appendix B.

3.1 Deposition Methods and Thin Film Growth

In the early stage of exploration of GMR systems, Parkin et al. [15] showed that magnetic multilayers prepared by magnetron sputtering could feature higher GMR than those made by Molecular Beam Epitaxy (MBE). The reason is probably connected to the imperfections of specific MBE-prepared multilayers [239]. In the following we describe properties of some commonly used deposition methods and give reasons for the final choice of the deposition method.

3.1.1 Thin Film Growth

The thin film growth is based on thermodynamic and kinetic laws governing the interaction of a deposited material with a substrate. The widely used deposition techniques of metal thin films, for instance sputtering (Section 3.1.2), represent off-equilibrium processes of thin-film deposition. Before describing them in more detail, epitaxial growth modes under equilibrium conditions will be mentioned (see Fig. 3.1):

- Frank-van der Merve mode
  This mode represents a *layer by layer* 2D growth. Each monolayer (ML) begins to grow after the previous one is finished. In this case the interaction between the atoms of the deposited material and the substrate is stronger than that between the atoms of the deposited material. This is valid for the epitaxial growth of materials with similar lattice and material parameters (crystallographic orientation, small lattice mismatch, chemical bonds) as the substrate.

- Vollmer-Weber mode
  In this case the interaction between the atoms of the deposited material is stronger than that between the deposited material and the substrate and this results in an *island* 3D growth. This mode is highly influenced by the surface diffusion of the deposited material. A continuous layer is formed by coalescence of the individual islands.

- Stranski-Krastanov mode
  This mode, also called the *layer-plus-island* mode, is an intermediate case. After formation of one ML, or sometimes several complete MLs, an island formation occurs [240]. The critical layer thickness before island formation is influenced by chemical and physical properties, like the surface energy and lattice constants of the substrate and deposited material (i.e. strain).

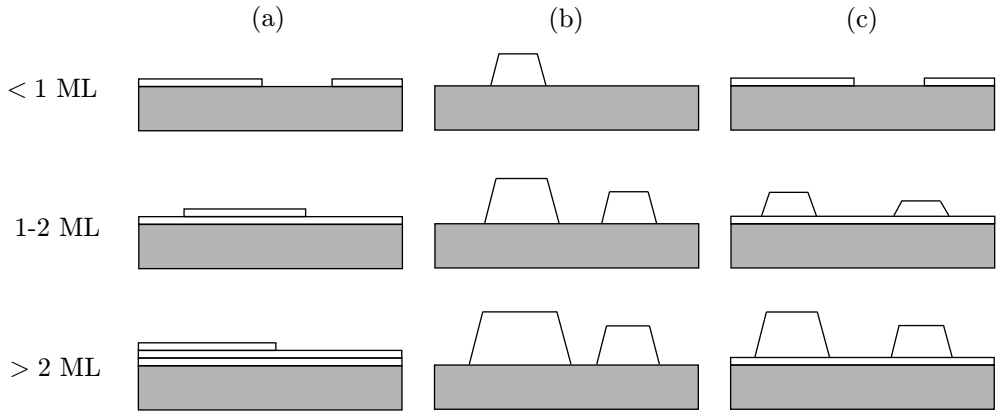

Fig. 3.1: Schematic representation of the three growth modes for different coverages (in monolayers, ML): (a) Frank-van der Merve, layer-by-layer growth; (b) Vollmer-Weber, island growth; (c) Stranski-Krastanov, layer-plus-island growth. Adapted from [240].

The deposition of a material on a substrate is controlled by an interplay of thermodynamics and kinetics. An atom arriving at the surface might be [241]:

1. re-evaporated, if the substrate temperature is high enough,
2. captured by existing clusters or at defect sites such as steps,
3. combined with another atom to form a cluster.

A small cluster is metastable and might decay before reaching a so-called critical island size at which the cluster becomes stable. The deposited atoms are incorporated into these clusters by *surface diffusion*. During this process the atom transfers its energy to the substrate. This process is highly dependent on the substrate temperature. The diffusion rate D standing for the number of unit cells visited by the atom per unit time reads [242]

$$D = \frac{1}{2d_{\mathrm{m}}}\nu_0 \exp\left(\frac{E_{\mathrm{d}}}{k_{\mathrm{B}}T}\right), \tag{3.1}$$

where d_{m} is the dimension of the motion (according to the substrate lattice), ν_0 is the attempt frequency, E_{d} is the activation energy of the surface diffusion, k_{B} the Boltzmann constant and T is the substrate temperature. The atom diffuses with the rate D until it meets a second (diffusing) atom or a cluster. The key parameter, besides the diffusion coefficient, is also the particle flux F. The ratio D/F characterizes the kinetics of the deposition, namely it determines the average distance the atom covers before it joins another atom or cluster. For a deposition slower than the diffusion (large D/F) the atoms have enough time to find a minimum energy configuration (the growth is lead by thermodynamics, see Fig. 3.2) and this situation might favor an island or layer-plus-island growth. For a fast deposition (small D/F) the growth is lead by kinetics and metastable structures are preferably formed [243].

The growth mode is also influenced by the substrate flatness, modified for instance in case of step-like vicinal surfaces, adsorbates on the surface, etc.

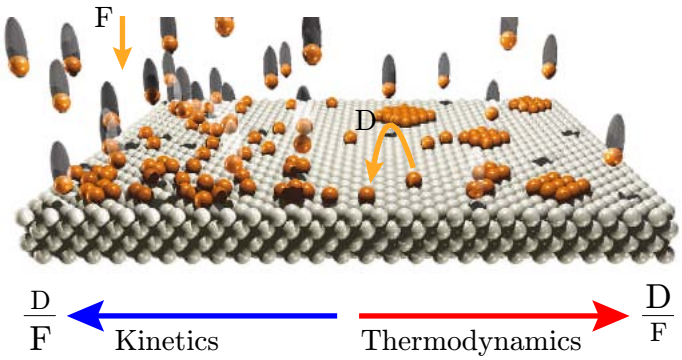

Fig. 3.2: Atomic-scale view of growth processes at surfaces. The type of growth is largely determined by the ratio between diffusion rate D and deposition flux F. Image taken from [243].

3.1.2 Deposition Methods

Various deposition methods differ in the energy of deposited atoms and in other parameters determining the growth process.

- Evaporation/Molecular Beam Epitaxy
  This technique is based on heating a material in a Knudsen effusion cell until it starts to sublimate. The evaporated atoms then condense on a substrate. The energy of the deposited atoms is defined just by their thermal energy. Hence, we can control the D/F ratio by varying the substrate temperature (by modifying D) and particle flux F. Note that the deposition necessarily takes place in ultra-high vacuum (UHV, approx. 10^{-8} Pa) to avoid surface contamination, as the deposition rates are often quite low with respect to sputtering techniques (0.01-1 Å/s). However, higher deposition rates of (1-20) Å/s are also used. The conditions for the layer-by-layer growth also vary according to the given combination of the layer and substrate material and lattice parameters.

- Magnetron Sputtering
  This technique relies on the sputtering of a target (cathode) by ions of a sputtering gas. Magnetic field is used to confine the plasma to the proximity of the target. The sputtered material is consequently deposited on a substrate. Magnetron sputtering varies from MBE growth techniques due to the different kinetic energy of deposited atoms [244]. The energy of sputtered atoms depends on many factors – on the masses of sputtering gas atoms, target atoms, the product of the gas pressure (typically 3×10^{-1} Pa) and the target-to-substrate distance (Paschen's law). Surface diffusion can be controlled by varying the pressure (increasing pressure means slowing down the atom diffusion) and the substrate temperature. The weak point is a close spatial proximity of discharge plasma and substrates together with relatively high pressure in this region. Hence unwanted interactions between the plasma and the growing film cannot be avoided [246].

- Ion-Beam Sputtering
  In ion-beam sputtering (IBS), on the contrary to the magnetron sputtering, the basic processes as ion generation (usually Ar ions) and acceleration on one hand and target interaction and film formation on the other hand are widely separated. The gas discharge is confined to an ion-beam source. This enables an independent control of ion energy and ion current density over a wide range [246]. The angle of ion-beam incidence can be chosen arbitrarily.

  The energy of the sputtered particles, two orders of magnitude higher than in the MBE case, results in their high diffusivity. The energy spread is lower than in the case of magnetron sputtering. When the sputtered particles hit the surface they also induce defects [247] and form dangling bonds [240] which increase the density of cluster nucleation. This effect is even more pronounced by the Ar ions scattered from the target surface and impinging on the substrate (see also Fig. 3.3). The higher density of nucleation sites ensures a more homogenenous coverage of the substrate, together with the high diffusion rate that helps the

system to reach the equilibrium configuration. This stands behind the higher smoothness of layers deposited by ion-beam sputtering.

For the GMR multilayer optimization we chose the IBS/IBAD[1] technique (available at the IPE), mainly because of the good control and variability of the deposition parameters. Another advantages with respect to the magnetron sputtering results from the lower pressure during deposition (leading to lower contamination) and higher directionality of the particles incoming on the surface. The deposition rates were controlled by quartz measurements.

The ion-beam sputtering facility constructed at the IPE is shown in Fig. 3.3. It consists of a vacuum chamber, two Kaufman ion-beam sources, a target manipulator and a substrate holder. Before deposition, the system is pumped down in two steps: first by a rotary pump and then by a cryopump, reaching a base pressure of 1-5$\times 10^{-5}$ Pa. Afterwards, the Ar gas is introduced through the discharge chamber of the ion-beam source and the work pressure in the main vacuum chamber is kept at approximately 1×10^{-2} Pa. After the ignition of a dc plasma discharge in the main ion source the Ar ions can be extracted and accelerated against the target, thus sputtering off the selected target material. The simulated distribution of sputtered particles from the point A is indicated by the blue polar diagram in Fig. 3.3(c). Their mean energies are spread between 5 and 15 eV. The red polar diagram indicates the simulated distribution of scattered primary ions. In the direction of the highest intensity of deposition their mean energy reaches 47 eV for 600-eV primary ions. The corresponding ion-to-atom ratio is 1:50.

When placing the sample at the position indicated by a black arrow in Fig. 3.3(c), which is the point of the maximum deposition rate, a thickness homogeneity of 95% is reached at the circumference of a circle with a 5-cm diameter and a center at the arrow position.

- Ion-Beam Assisted Deposition
  In case of Ion-Beam Assisted Deposition a secondary Kaufman ion-beam source is employed to simultaneously bombard the growing layer with Ar ions of energies between 0 and 100 eV. This way the energy of atoms diffusing on the surface is enhanced, but the number of defects and dangling bonds increases as well. The intermixing between different atomic species, which is dependent on the ion energy, becomes more significant as the assisting ions increase both the surface and the volume diffusivity. As the ion energy increases, the interfaces are less sharply defined and a mixed zone of approx. 1 nm occurs. A diffusive interface can be found also for materials which do not mix under equilibrium conditions, e.g. Co and Cu. In this case the interface quality may be improved by annealing (see Section 3.6).

  Fig. 3.4 shows different interfacial structures dependent on the atom mobility at the surface and in the bulk. Intermixing is related to the assisting ions bombardment, while the roughness is usually a consequence of limited atom mobility

[1] Ion-Beam Assisted Deposition.

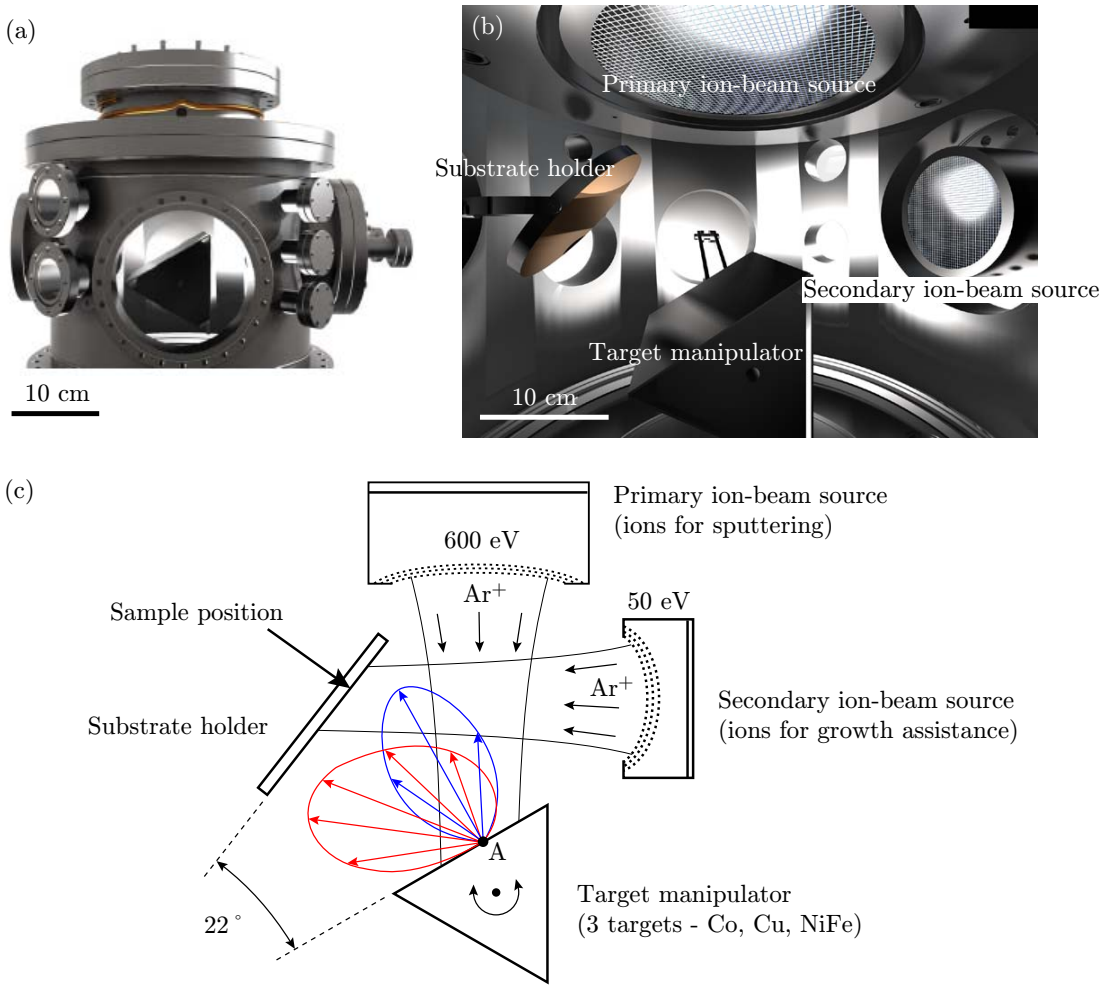

Fig. 3.3: (a) shows the deposition apparatus for ion-beam sputtering and IBAD. (b) inside view of the deposition apparatus with two Kaufman ion-beam sources, the target manipulator and the substrate holder. The 3D model was created by J. Neuman. (c) Sketch of the deposition process. The blue polar diagram indicates the material sputtered from the point A. The red one represents the reflected Ar ions and atoms. The distance of a point on the curve from the point A represents a relative intensity in that particular direction. The angular distributions were calculated by T. Matlocha.

on the growing surface. A low substrate temperature and no ion irradiation during the growth will minimize interdiffusion and intermixing [245]. Such conditions may lead to a kinetically limited growth with accumulating roughness as illustrated in Fig. 3.4(a). Increasing the substrate temperature or assisting bombardment at higher ion energies ($\geq$ 100 eV) activates bulk diffusion across the interfaces, as illustrated in Fig. 3.4(c). Therefore, it is necessary to find a balance between the layer smoothness and the interface intermixing by tuning the assisting ions energy, ideally leading to an interface structure as illustrated in Fig. 3.4(b).

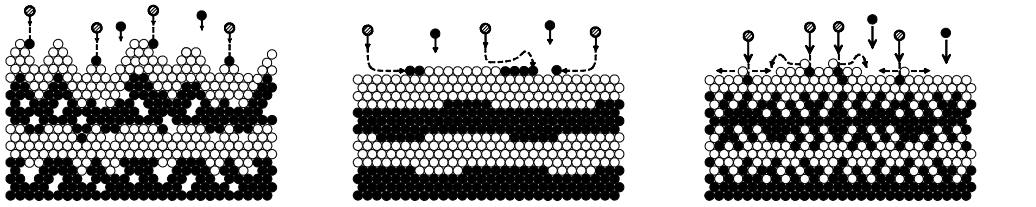

Fig. 3.4: Schematic view of different interfacial structures depending on relative mobilities of atoms at the surface and in the bulk of the multilayers. From [245].

3.2 Experimental Aspects of GMR Systems

Due to the high application interest when studying GMR systems, most of the studies presented in the literature are devoted to multilayered structures with a high repetition number of the (FM/NM) feature providing the largest possible GMR effect. There are different types of GMR structures differing in the way the antiparallel state of the layer magnetizations is achieved [57]:

- Antiferromagnetically coupled multilayers
  The magnetic layers are coupled via the non-magnetic spacer by the RKKY interaction (see Section 1.2.1). The high-resistance state can be found at zero magnetic field, whereas a high-enough field brings the system into the parallel orientation and a low-resistance state. Typical systems are Fe/Cr (for this type of samples the GMR was discovered [54]) and Cu/Co multilayers with maximum GMR (at 4.2 K) of 150% [248] and 115% [249], respectively. Note that the amplitude of the effect is a characteristic of the pair of ferromagnetic transition metal/non-magnetic metal and not of each metal considered separately [57]. In Fe/Cu or Co/Cr multilayers much lower GMR is observed.

- Spin-valve[2] sandwiches
  The system comprises two identical magnetic layers separated by a non-magnetic spacer where one of the magnetic layers is pinned by an antiferromagnet (exchange-bias interaction) [262]. In practice, the pinned layer is not switched by an external field, just the free layer. In NiFe-based spin valves, very high sensitivity of the free layer was found – a change of resistivity exceeding 20%/mT is obtained [251].

- Multilayers comprising ferromagnetic layers of different coercivities
  Here, an independent switching of the layers is assured by two magnetic layers of different coercivities – either of different thicknesses or materials (e.g. NiFe/Cu/Co) [252]. This kind of system is sometimes called pseudo spin-valve. The term spin valve is regularly associated with the system described in the item

[2]The term "magnetic valve" or "spin valve" was first introduced by J. Slonczewski [250].

above. However, for this work the division is irrelevant and we will stick to the term spin valve also in this case. We restrict ourselves just to one repetition of the NiFe/Cu/Co feature, providing a model system for current-induced DW motion in patterned nanowires of this sandwich structure (see Section 2.3.5).

Let us recall that two main factors are essential for GMR in the FM/NM/FM system. First, the probability of electron scattering either in the bulk of the FM layers or at the FM/NM interfaces has to be spin-dependent. Second, the conduction electrons have to be able to visit both FM layers successively.

- Bulk versus interfacial spin-dependent scattering
  The location and nature of the scattering centers that give rise to the spin-dependent scattering are specific for each material combination and thus are important for the spin-valve optimization [57]. There are different approaches to determine the bulk/interface principal contribution. These two contributions can be better separated in the CPP geometry where the current flows perpendicular to the interfaces [58, 255], although a direct comparison of the parameters obtained in CPP and CIP geometries may not be applicable. A very strong interfacial spin-dependent scattering has been found at the Co/Cu [256], Co/Ag and Fe/Cr interfaces.

  When the ferromagnetic material is an alloy instead of a pure element (e.g. NiFe), the bulk spin-dependent scattering seems to dominate the interface one [57]. The importance of the respective contributions can be tailored by modifying the interfaces [257]. By adding thin Co layers (just 2.5 Å) at the NiFe/Cu interfaces of a NiFe/Cu/NiFe/FeMn stack the giant magnetoresistance is doubled, confirming the large spin-dependent scattering at the Co/Cu interface. Later theoretical studies aimed at resolving the question of major contributors to the spin-dependent scattering process and the analysis of the interface states showed that the interface scattering is favored [253, 254].

- Layer thicknesses
  It is expected that the most important parameter is the thickness of the spacer which has to be smaller than the electron mean free path (typically a few nm). A monotonic decrease in the GMR amplitude is observed when increasing the spacer thickness [258]. This is caused by an increase in the conduction electrons scattering, which leads to the loss of the spin information they carry when going from one ferromagnetic layer to the other [259, 260]. Moreover, a large part of the current flows in the highly conductive spacer. The minimum spacer thickness is determined by the demand of decoupling of the two ferromagnetic layers. Too thin spacer results in high interlayer coupling, originating from either the orange-peel coupling (interface roughness) or the RKKY interaction (antiferromagnetic or ferromagnetic depending on the spacer thickness). Moreover, direct coupling through pinholes and other discontinuities may arise. In this case the maximum GMR is smaller and the magnetization of the layers does not switch independently.

The nature of the prevailing spin-dependent scattering influences the optimum thicknesses of magnetic layers. In case the bulk spin-dependent scattering is more important, the maximum GMR occurs for larger thicknesses [258]. However, if any of the magnetic layers is too thick, it will short-circuit the GMR system, i.e. the spin state of conduction electrons will not be confronted with that of the second magnetic layer. The decrease in GMR at low thicknesses is often due to an enhanced scattering on the outer surfaces (substrate, buffer or capping layer) [57].

3.3 Multilayer Configuration

3.3.1 Notation convention

For simplicity, we use a short notation SV 2-5-3-5-(2.8) instead of Cu 2 nm/NiFe 5 nm/Cu 3 nm/Co 5 nm/CoO_x 2.8 nm/Si. In case the thickness in parentheses is missing, the sample was prepared without the CoO underlayer. For the optimization process, all samples were deposited on Si (100), of a specific resistivity of 6-9 $\mu\Omega\cdot$ cm, with a native SiO_2 layer.

3.3.2 Optimization of Layer Thicknesses

Let us assume that the spin-valve multilayer system optimized for the highest GMR will likely feature the most effective spin tranfer torque acting on the DW in the NiFe layer. We performed the basic optimization which was focused on finding the best layer thickness configuration. The sequence of the deposited materials has been imposed by the XMCD-PEEM experiments: the NiFe has to be on top because the technique is surface sensitive. The deposition rates of materials used for the optimization can be found in Tab. 3.1.

Material	Deposition rate (Å/s)
Co	0.8
Cu	1.6
NiFe	0.9

Table 3.1: Deposition rates of selected materials for an ion current of 50 mA and a primary ion energy of 600 eV.

No external magnetic field was applied to the sample during the deposition. Due to the well defined angles of incidence of the sputtered atoms, the samples present a uniaxial anisotropy with the easy axis perpendicular to the plane of incidence (see Fig. 3.7).

All the GMR measurements were carried out in the CIP geometry with the magnetic field applied along the easy axis[3]. Fig. 3.5 shows the dependence of GMR loops on

[3]For angular dependence of GMR, see the papers by Dieny and Barnaś [57, 251, 264].

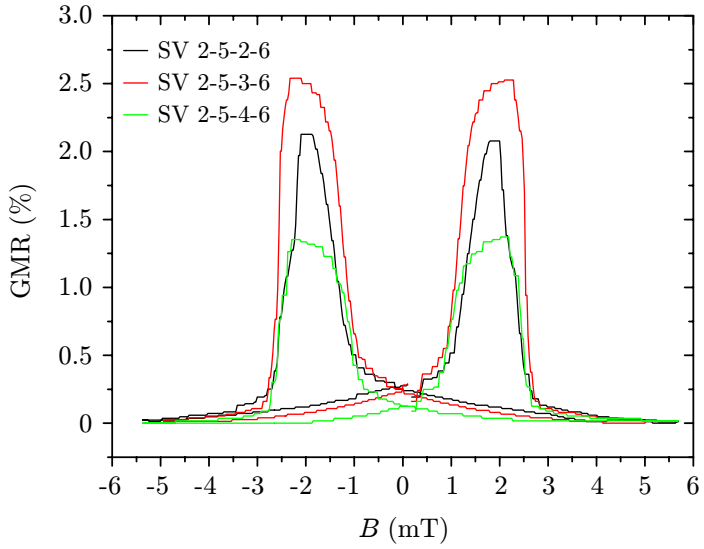

Fig. 3.5: Basic optimization of the Cu/NiFe/Cu/Co/Si spin valve. Cu spacer thickness is varied.

the Cu spacer thickness. The remaining layer thicknesses were fixed (SV 2-5-X-5). For a thin Cu spacer of 2 nm, the magnetic layers are ferromagnetically coupled and the antiparallel state is not entirely achievable. For 3 nm of Cu the GMR is maximum and exhibits a large plateau; for 4 nm of Cu the GMR decreases. For further steps the 3-nm Cu spacer was selected.

The GMR loops follow the general trends described in Section 3.2. Fig. 3.6 shows the GMR curves for some selected values of Co and NiFe thicknesses. Best results are

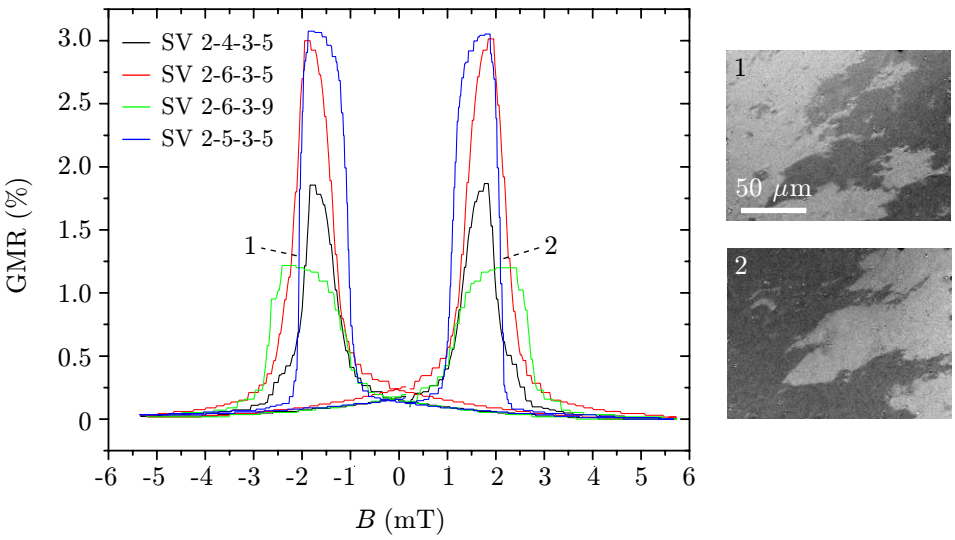

Fig. 3.6: Basic optimization of the Cu/NiFe/Cu/Co/Si spin valve. NiFe and Co thickness is varied. The Kerr microscopy images marked with 1 and 2 show the magnetic domain structure in Co for the points indicated on the blue curve in the graph.

obtained for 5 nm of Co and more than 5 nm of NiFe. The Kerr microscopy images of the SV 2-5-3-5 illustrate the magnetic domain structure in the Co layer during its reversal. The white and black colors stand for opposite directions of in-plane magnetization. The magnetic domains are rather small, with very rough boundaries. This seems to indicate that DW propagation is locally hindered by pinning at defect sites and that nucleation may also play a role in the reversal.

Fig. 3.7 shows the hysteresis loops measured by magneto-optical Kerr effect (MOKE) for the spin valve giving largest GMR, SV 2-5-3-5. Note that the Co coercivity is larger than in Fig. 3.6. This is simply due to the fact that in Kerr measurements the magnetic field was swept at a high frequency (approx. 200 Hz), whereas the GMR measurements were carried out in quasi-static conditions. For both the GMR and Kerr measurements the magnetic field was calibrated using a teslameter.

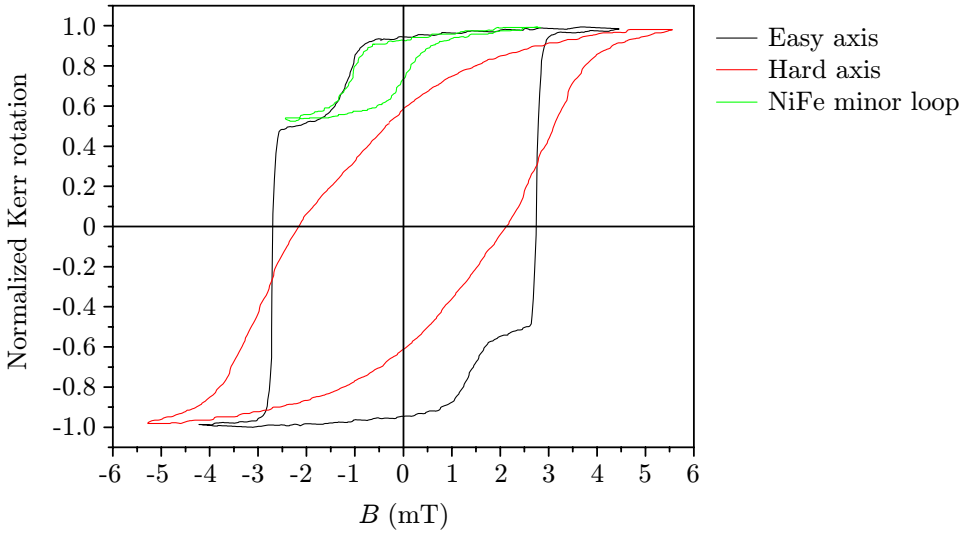

Fig. 3.7: MOKE curve of the best configuration, SV 2-5-3-5.

3.4 Buffer and Capping Layers

Buffer and capping layers represent boundaries of the GMR system where the electron scattering can largely influence the GMR. In case of a non-specular, spin-flip scattering, the GMR decreases. The capping layer serves to protect the spin valve from oxidation. However, it may also decrease the GMR as it shunts the current from the functional part of the trilayer system. Note also that in some works [265, 289] the GMR systems are not capped, resulting in a similar GMR amplitude to that presented in this work.

It was found that the GMR amplitude of the Cu/NiFe/Cu/Co multilayers was increasing over time. A GMR increase up to 20% at certain samples was observed (the absolute resistance increased by 6%). This effect was attributed to the passivation of the Cu capping layer. It has been recently shown that surface oxidation of a Cu capping layer causes enhanced spin diffusion and favors back-scattering into the FM

electrode of the NiFe/Cu bilayer [267]. This indicates that the scattering events were spin-conserving.

The importance of underlayers on the structure growth and its influence on GMR is well known. The difference between Ta and Cu buffer layers for growing NiFe/Cu/NiFe/Cu(Ta) sandwiches was shown by Tang et al. [266]. Parkin et al. [249] used Fe buffer layers to obtain Co/Cu structures with very flat Co and especially Cu layers which were very thin. However, the GMR and magnetic anisotropy can be modified directly by the topography of the Si substrate, for instance by using vicinal surfaces [265].

In our case, to increase the difference between the coercivities of NiFe and Co, different pinning possibilities were considered. One of them is represented by insertion of a CoO underlayer below the Co layer. Alternatively, different antiferromagnetic layers, such as NiO or FeMn[4] could have been used. In this case, exchange-bias would have been obtained at room temperature. Moreover, the Ni and Fe elements are already present in the functional NiFe/Cu/Co trilayer, so the chemical contrast (see Section 5) could be ambiguous. However, if different ferromagnetic layers were selected, NiO or FeMn might be considered in the future experiments.

Although the Néel temperature of bulk CoO reaches 290 K, a slight increase of the Co coercivity is expected because of the AF/FM interaction. Details on the resulting magnetic properties are shown in Section 3.4.2. The temperature dependence is described in Section 3.9. We have found that depositing the SV on a specifically prepared CoO underlayer changes substantially the quality of SV multilayers and consequently the GMR.

The different procedures of CoO preparation follow.

3.4.1 Preparation of CoO Layers

The CoO layers were prepared by oxidation of Co layers. Essentially, two different oxidation procedures were followed:

- in-situ oxidation by introducing oxygen after Co deposition,
- in-situ oxidation by introducing oxygen during Co deposition.

The quality of oxidation, in terms of homogeneity and the content of oxygen, was determined from depth profiles of the multilayers by using the Secondary Ion Mass Spectroscopy (SIMS). The technique basics are described in Section B.1. The method determines the number of ionized particles of a specific mass (atoms, molecules, clusters) per second, sputtered from the sample by an incident ion beam. The depth profiles described in the following section were obtained by an Ar ion beam of an energy of 1500 eV and a diameter of approx. 0.8 mm (FWHM). The signal of detected ions significantly increases in the presence of intrinsic oxygen. This is caused by the ability of electronegative oxygen to capture electrons and thus to ionize sample atoms (leading to an increase of the secondary ion yield). For illustration of the oxygen effect on the Co

[4]The selection is restricted by the availability of targets for our IBAD instrument.

signal see Fig. 3.8(b). The ratio of Co and O signals (orange curve) is approximately constant throughout the multilayer, indicating that the variance in the Co signal is caused by the presence of oxygen.

Generally speaking, the mass spectrometer is set to transmit the particles of a given ratio m/Q, where m is the mass and Q the charge of the particle. However, in reality the signal of e.g. Co_2^{2+} is four orders of magnitude lower than Co^+ of the same m/Q ratio. Hence, the selected mass largely corresponds to a simply ionized particle and the signal interference with heavier and multiply ionized particles can be conveniently neglected.

SIMS spectra analysis

Fig. 3.8 compares the depth profiles of five samples, each of which consists of four oxidized cobalt layers deposited on silicon substrates with a native oxide layer and prepared using different oxidation procedures. The signals of cobalt, oxygen and related compounds and clusters together with the silicon signal have been measured as a function of the sputter time. As different materials and compounds have different sputter yields, the sputtered depth cannot be directly assigned to the sputter time. For monitoring the Si content we chose the isotope ^{29}Si instead of ^{28}Si to avoid an interference with N_2 and CO.

During the sputtering process the layers are intermixed by incident primary ions. Moreover, polycrystalline layers show different sputtering efficiency for different crystallographic grain orientations and this effect results in increasing roughness of the sputtered area with the depth. Consequently, the resolution in the measured profile decreases, making the study of interfaces more difficult (the signal slopes decrease). This fact has to be taken into account during the data interpretation.

The top label of each graph schematically shows the material structure in the multilayer. In the labels the wide vertical lines serve to distinguish the different Co layers, each of which is prepared by a specific deposition procedure. The top oxide layer of the capping Co layer was created under the ambient atmosphere, while moving the sample from the deposition chamber to the analytical chamber.

- Co (3 nm) / 3×(Co (3 nm) oxidized *after* Co deposition for 30 min at 1000 Pa of O_2) / Si [Fig. 3.8(a)].
  Due to the effects of intermixing and roughening, the identical oxidation of three consecutive Co layers does not result in identical peaks in the Co signal in the corresponding regions of the depth profile. The maximum degree of oxidation in each layer, associated to the maximum content of oxygen, can be determined as the ratio between the signal value at the Co peak in the oxidized layer (indicated by the arrows 2) and the level of the Co signal in the unoxidized layer (indicated by the arrow 1). We obtained ratios of 35, 27 and 22 from the top to bottom layers respectively. Another way to quantify the degree of oxidation is to integrate the area under the peak (with a subtracted background value which is the unoxidized Co level) and to divide it by the maximum value (arrows 2) subtracted by the background value. As the time needed to sputter off the material of one layer

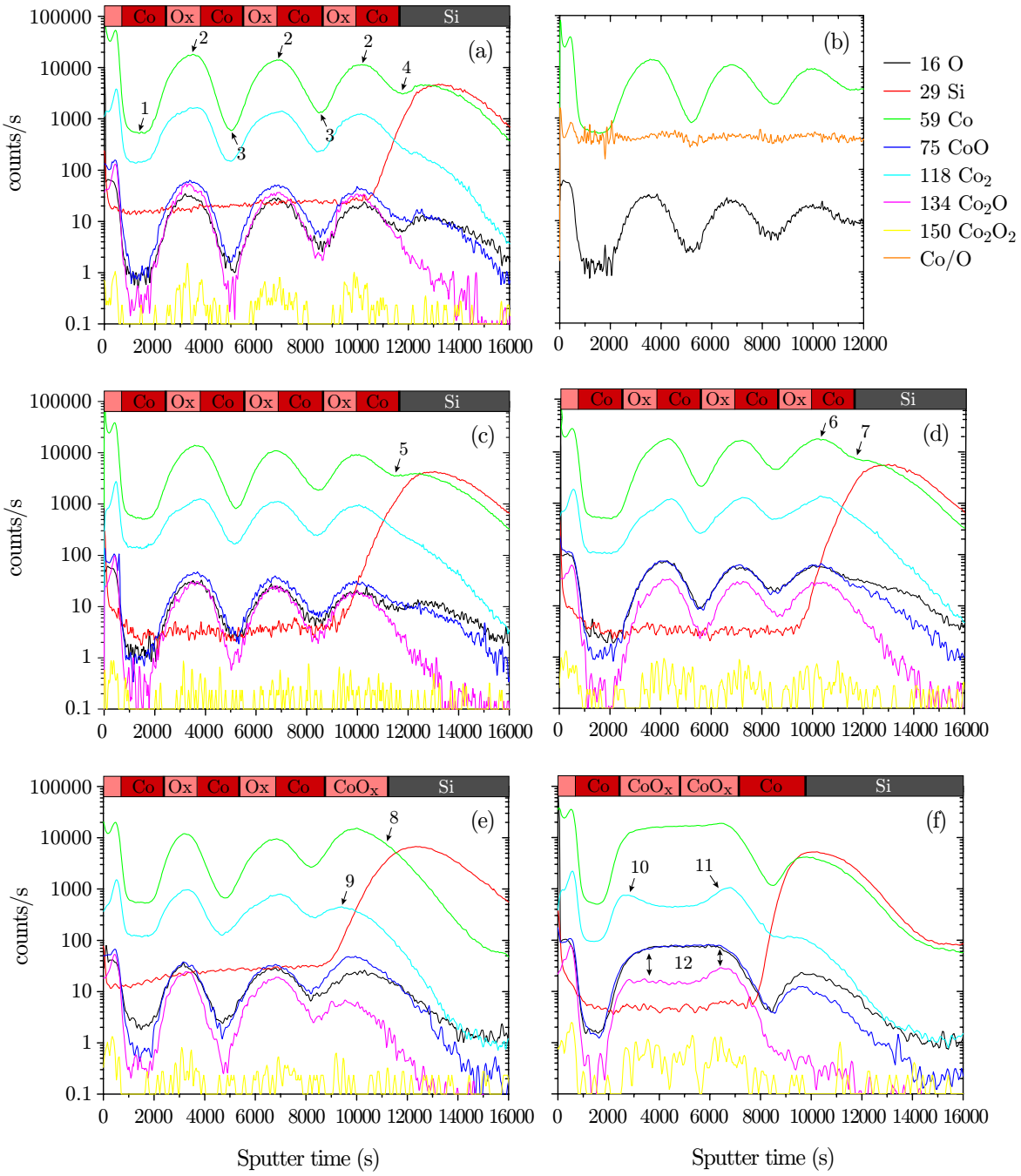

Fig. 3.8: SIMS depth profiles of selected Co multilayers with different oxidation of the individual layers. (a) – identical oxidation of the Co layers after deposition, $p = 1000\,\mathrm{Pa}$, $t = 30\,\mathrm{min}$, (b) – figure shows a linear proportionality of the Co signal to the O_2 content; the orange curve gives the ratio of Co and O signals. (c) – oxidation at different pressures after deposition, $t = 30\,\mathrm{min}$, (d) – oxidation for different times after deposition, $p = 1000\,\mathrm{Pa}$, (e) – oxidation by atmosphere, $t = 20\,\mathrm{min}$, after deposition; $1000\,\mathrm{Pa}$ of O_2 for 30 min, after deposition; $p = 1.1 \times 10^{-2}\,\mathrm{Pa}$, during deposition. (f) – two CoO_x layers oxidized during deposition, the bottom one with the assisting oxygen ions.

increases with the depth, we relate the average sputter time of the oxidized part to the total sputter time of one layer. The boundaries between the layers were determined from the dips indicated by the arrows 3. However, for this task it is more convenient to use the Co_2 signal, as the Co_2 clusters originate most probably from the Co layers and are thus not influenced by the presence of oxygen in the neighboring layers. The effect of oxygen is responsible for an additional peak in the Co signal when SiO_2 is reached. Finally, following this procedure we find that approx. 45% of each layer is oxidized. However, it is not possible to quantitatively determine the distribution of oxygen throughout the layer.

The partial oxidation of layers can be also deduced from the dip (arrow 4) in the Co signal at the interface of the Si and the bottom Co layer. The dip indicates that there is a significant decrease in the content of oxygen between the oxidized part of the Co layer (CoO_x) and the SiO_2 layer.

- Co (3 nm) / Co (3 nm) oxidized *after* deposition for 30 min at 100 Pa of O_2 / " at 1000 Pa / " at 20000 Pa / Si [Fig. 3.8(c)].
  The figure shows that oxygen pressure does not have a directly observable influence on the degree of cobalt oxidation, as the oxidation ratios (defined above) at the three peaks decrease similarly as for the identical oxidation in Fig. 3.8(a). However, by comparing the oxidation ratios of the 100-Pa peak with that of the corresponding first peak of 1000-Pa in Fig. 3.8(a), we find that it is approx. 1.3× lower (27 vs. 35).

  The dip indicated by the arrow 5 is less pronounced than that of the arrow 4 in Fig. 3.8(a), suggesting that the layer is oxidized deeper for 20 kPa than for 1 kPa of O_2. From the area of the peaks and the layer boundaries we can deduce that for the 100-Pa case 43% of the layer is oxidized, for the 1000-Pa case 45% and finally for 20 kPa 55%.

- Co (3 nm) / Co (3 nm) oxidized *after* deposition for 15 min at 1000 Pa of O_2 / " for 30 min / " for 45 min / Si [Fig. 3.8(d)].
  Here we compare the influence of the time of oxidation. The degree of oxidation is very similar to that presented in Fig. 3.8(a), the oxidation ratio of the first peak is 36. A remarkable exception is the last peak (arrow 6) where almost the same ratio – 35 – is found indicating higher degree of oxidation in this bottom layer. The depth of oxidation is again identical as in Fig. 3.8(a), except of the last peak of the longest oxidation – here approx. 60% of the layer is oxidized. The dip indicated by the arrow 7 is even less pronounced than in Fig. 3.8(c) (arrow 5).

Hence we can deduce that while increasing the oxygen pressure influences the degree of oxidation, increasing the oxidation time rather influences the depth of oxidation. Longer times of oxidation, more than 30 min, lead also to a higher oxidation degree.

- Co (3 nm) / Co (3 nm) oxidized *after* deposition by atmosphere for 20 min / Co (3 nm) oxidized *after* deposition for 30 min at 1000 Pa of O_2 / Co (3 nm) oxidized *during* deposition at 1.1×10^{-2} Pa of O_2 / Si [Fig. 3.8(e)]. We compare

the influence of oxidation in atmosphere and, from the processing point of view, oxidation after and during the deposition. The atmospheric oxidation leads to a lower degree of oxidation – 23 – than under the previous parameters. The depth of oxidation – 38% – was also rather low.

The dip in the Co signal in between the Co layer and the Si layer apparent in the case of the oxidation after deposition is not present anymore. Instead, there is a continuous transition of the Co signal into the SiO_2 layer indicating a continuous oxidation of this layer (arrow 8). As the continuous CoO_x layer contains proportionally less cobalt, the oxidation ratio cannot be directly compared to that of the oxidation-after-deposition peaks, even at the same depth. However, its value, 30, almost reaches that of the peak indicated by the arrow 6. Noteworthy, the signal of Co_2 at the same peak decreases, together with the Co_2O signal. This indicates preferential creation of CoO, as the corresponding peak is, on the contrary, higher. If there was a stable compound of Co_3O_4, the signal of its larger fractions would increase.

- Two CoO_x layers oxidized *during* deposition are compared in Fig. 3.8(f). The upper one was deposited at an oxygen partial pressure of 1.6×10^{-2} Pa, the bottom one was deposited at 5×10^{-3} Pa, but with the assistance of secondary ions (see Section 3.1.2) extracted from the oxygen plasma of the secondary ion source. Before exploring the assistance of oxygen ions, the influence of oxygen pressure during deposition on the degree of oxidation was verified. As expected, the degree of oxidation continuously increased with the oxygen pressure.

  In case of assisting oxygen ions, we observe a higher ratio of Co_2O/CoO clusters (arrows 12, right) than without the assistance (arrows 12, left). As the other parameters were kept constant, we can deduce that the impingement of oxygen ions probably causes a more significant creation of the Co_3O_4 phase. Also the presence of Co_2O_2 clusters indicates more complex oxides (= with a higher oxygen content) in the layer. As the Co_2O_2 signal is very low, in the deeper-placed layers the information is largely smeared out and does not allow a meaningful comparison of the Co_3O_4 content in the oxide layers.

  Two peaks [Fig. 3.8(f), arrows 10 and 11] in the Co_2 signal are probably due to the diffusion of O_2 at the interface with the Co layer, where detection of the Co_2 clusters is more probable than in the oxidized layer itself. The diluted oxygen then increases the Co_2 signal. This is consistent with the dip in the Co_2 signal in the middle of the oxidized layer, in between these two peaks.

Note that although the etching rate of CoO is expected to be lower than of pure Co [268], the sputter time of the CoO layers is shorter. This suggests that the CoO layers are thinner than the Co ones for the same deposition time. As confirmed by the quartz measurement of the CoO deposition rate, it is almost 3× lower than in case of Co. In addition, the thickness of CoO was determined from AFM measurements. A 3-minute deposition resulted in a CoO layer of a 5.5-nm thickness. Assuming that the deposition rate is linear with the layer thickness, this value is consistent with the data

provided by the quartz measurement during deposition, as a 90-s deposition resulted in 2.8 nm of CoO.

XPS spectra analysis

Prior to the XPS analysis of an oxide structure, the topmost capping layer was first sputtered off by 500-eV Ar ions[5]. The depth position was checked by simultaneous SIMS analysis [Fig. 3.9(a),(b)]. Then the sample was transferred to the XPS chamber (without breaking vacuum, see also Fig. B.1). After precise positioning the photoelectrons were collected from the central part of the crater made by the SIMS ion gun. We have taken two spectra – for pure Co [Fig. 3.9(a)] and for CoO_x oxidized after deposition [Fig. 3.9(b)].

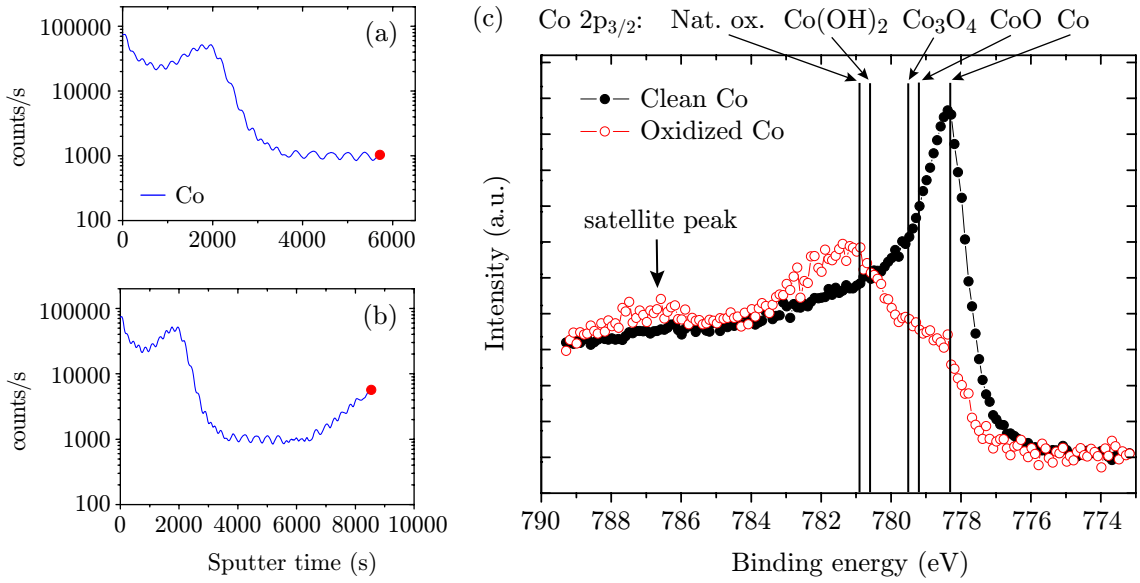

Fig. 3.9: (a, b) SIMS depth profiles indicating the sputtering stopping point for the XPS analysis of pure Co (a) and CoO_x oxidized after deposition. (c) XPS spectra of pure and oxidized Co.

Comparing the oxide peak positions [Fig. 3.9(c)] with the binding energy shifts found in literature, we realize that the oxidation after deposition results in an oxide structure similar to that found in native oxides formed in the air atmosphere (the peaks of the native oxide and the $Co(OH)_2$ peak which is formed at presence of H_2O). The oxide energy shifts were taken from [269].

The satellite peak indicated in the figure corresponds to the CoO phase, i.e. to the Co^{2+} state. The satellite peak structure is pronounced for 3*d* metals with unpaired electrons in the 3*d* shell. Co^{3+} is diamagnetic (it is usually found in the low-spin state induced by the crystal field) and therefore does not exhibit the satellite structure [270].

The same experiment investigating an oxide formed during the deposition was not carried out for temporal reasons and will be performed in the near future.

[5]The primary ion energy was reduced to minimize intermixing.

3.4.2 Magnetic properties of CoO/Co layers

The general purpose of adding an antiferromagnetic layer into the spin-valve system is to pin the hard magnetic layer via the exchange-bias interaction. As the room temperature is above the blocking and Néel temperatures (T_N=291 K) of CoO, we expect just an increase of the Co coercivity[6]. The magnetic characterization of the Co/CoO bilayer was first carried out by MOKE. Fig. 3.10 shows MOKE hysteresis loops of a 7-nm Co layer deposited on top of differently oxidized Co layers and capped by 5 nm of Cu to prevent oxidation from top. Note that in this figure we plot directly the Kerr rotation which is proportional to the total magnetic moment in the sensed volume.

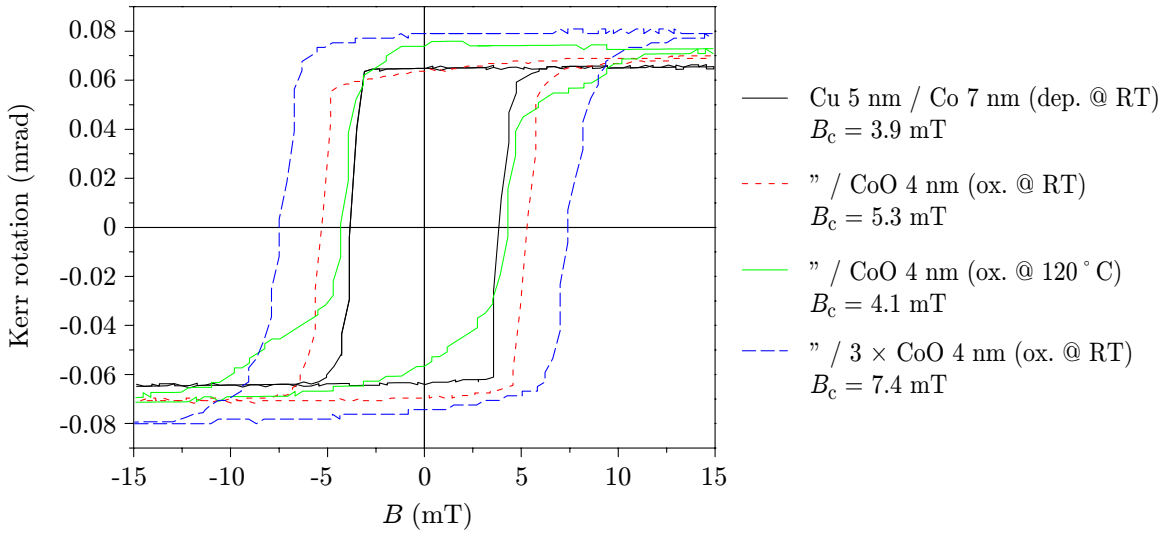

Fig. 3.10: MOKE hysteresis loops of the Cu/Co/CoO_x multilayers. CoO was created by oxidation of Co after the deposition. RT stands for room temperature.

At first glance we might deduce that the Co coercive field increases with the total thickness of CoO. The largest coercivity is obtained for the three Co layers which were successively oxidized.

Consistently with the SIMS depth profiles for the case of CoO_x oxidized after deposition, we expect that more than 50% of the Co layer remains unoxidized. In the figure we can see that increasing the number of CoO_x layers leads to both an increase in the Kerr rotation (proportional to the magnetization) and the Co coercivity (compare red and blue curves). Hence, it seems likely that the increase of the Co coercive field originates from the non-homogeneous oxidation throughout the system.

In one of the samples (green curve) the Co layer was oxidized at an elevated temperature of 120°C. From the SIMS depth profile (not shown) we deduce that higher temperature leads to a more homogeneous oxide layer (a less pronounced dip between

[6]Above the T_N the long-range antiferromagnetic order is disturbed. However, close to T_N the ordering fluctuations are not sufficient to cancel the local interaction of Co with antiferromagnetic domains in CoO.

the CoO and SiO_2 layers), but the oxidation degree at the contact with the pure Co layer is lower. However, it is likely that even the elevated temperature is not sufficient to oxidize the bottom Co layer completely, as the corresponding MOKE loop (the green curve) shows switching of two partially uncoupled magnetic layers.

Fig. 3.11 compares a typical MOKE hysteresis loop of a 5-nm Co layer deposited on a 2.8-nm CoO layer oxidized during deposition (black curve) with the loop obtained for a 7 nm thick Co layer directly deposited on the substrate. The loop measured for the Co/CoO bilayer presents very sharp transitions, indicating that magnetization reversal is governed by DW propagation with a well defined nucleation field; the reversal of the simple Co layer is less sharp, indicating that the reversal proceeds through DW nucleation at different defect sites, followed by DW propagation. This figure suggests that Co grows better on CoO oxidized during deposition, than directly on SiO_2 (red curve). However, no significant increase in the Co coercivity is found for the CoO underlayer.

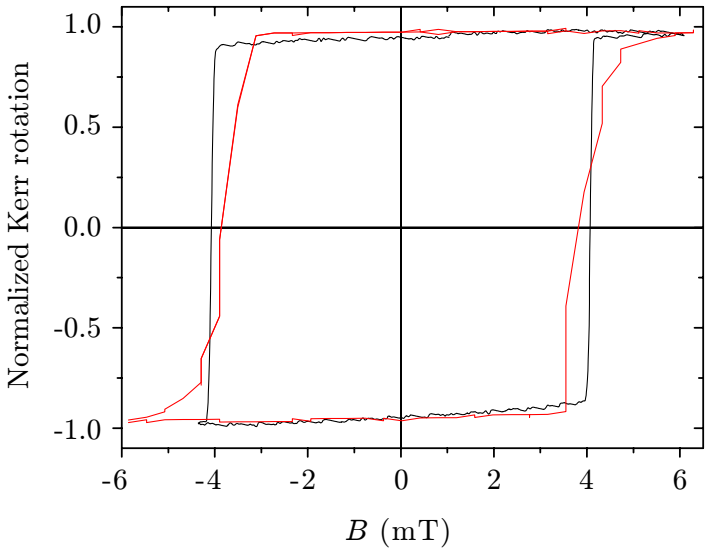

Fig. 3.11: MOKE hysteresis loops of a 7-nm Co layer deposited on SiO_2 (red curve) and a 5-nm Co layer deposited on a 2.8-nm CoO layer oxidized during deposition (black curve).

The difference in the growth quality might be used for an explanation of the differences in magnetic properties of spin-valve multilayers deposited on differently prepared CoO layers (oxidized after or during deposition). Fig. 3.12 represents the GMR loops of the optimized SV 2-5-3-5 multilayers deposited on various substrates. Note the significant increase of GMR as high as 50%, in the case of CoO oxidized during deposition compared to a spin-valve multilayer deposited directly on native SiO_2. This is probably caused by a strong spin-conserving electron specular reflection at the specific Co/CoO interface [271]. The Co coercivity is increased and well defined. Also the plateau at the antiparallel state is wider, indicating the presence of a weaker interlayer coupling between the two ferromagnetic layers.

By preparing the CoO during the Co deposition with the assisting oxygen ions (50 eV, 20 mA), we further increase the Co coercivity, but the GMR drops substantially.

It is likely that the oxygen ions increase the layer roughness, by inducing defects and dangling bonds on the surface, thus favoring nucleation of new islands and decrease smoothness. Moreover, as mentioned in Section 3.4.1, the assisting oxygen ions might induce preferably the Co_3O_4 phase.

In the case of the CoO layer oxidized during deposition, the Co coercivity increased when reaching the CoO thickness of 2.8 nm (Fig. 3.13). This behavior does not suggest a relevant dependence of the Co coercivity on the CoO thickness, but rather indicates a worse Co growth for very thin CoO layers. Note also that the GMR results in approximately the same value for all the CoO thicknesses (within the reproducibility tolerance).

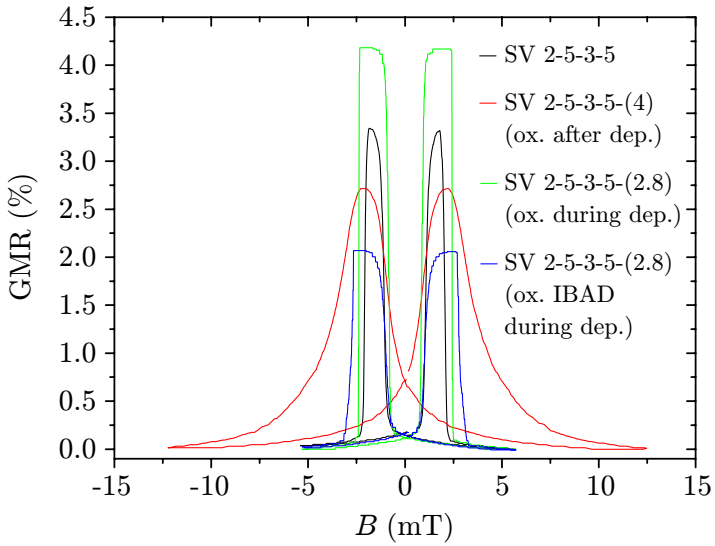

Fig. 3.12: GMR loops of a SV 2-5-3-5 deposited on SiO_2 (black curve), 4 nm of CoO oxidized after deposition (red curve), 2.8 nm of CoO oxidized during depositon (green curve) and 2.8 nm of CoO oxidized during depositon using assisted deposition of oxygen ions (blue curve).

3.5 Effect of Ion Beam Assisted Deposition

Although its influence is not fully understood yet [57], interfacial roughness depends on a particular material combination (FM/NM interface) and it plays a significant role in determining the spin-valve properties. In multilayers where the interfacial spin-dependent scattering is important, the interfacial roughness may increase the density of scattering centers at the interfaces and may therefore lead to larger GMR [57]. This is valid for Co/Cu and Fe/Cr [272] systems.

On the contrary, in NiFe/Cu systems where the bulk scattering is more important the interfacial roughness decreases the GMR [273]. We will further address this question in Section 3.6. Moreover, in case of very flat interfaces, the specular reflection of the conduction electrons at the interfaces may be increased, leading to a channeling of the electrons within each layer [57].

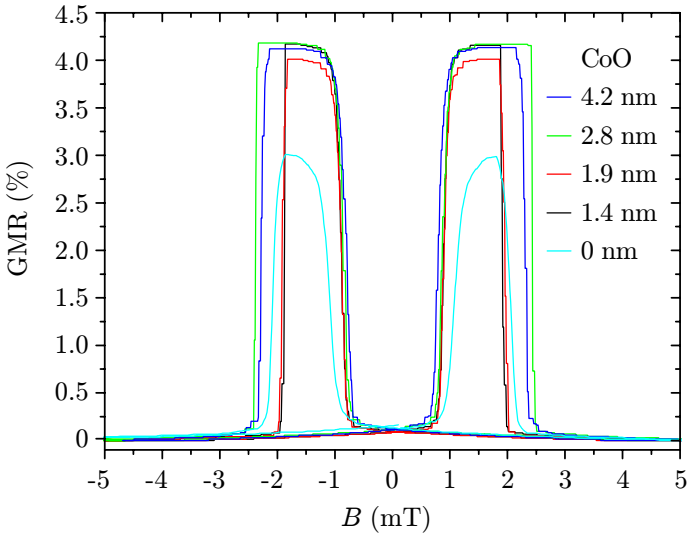

Fig. 3.13: GMR hysteresis loops of a SV 2-5-3-5 deposited on various thicknesses of CoO oxidized during deposition.

The structure of interfaces also influences the magnetostatic coupling between the layers and may even give rise to direct exchange coupling in case of pinholes. This might cause an insufficient antiparallel alignment of the ferromagnetic layers and prevent the multilayer from reaching the largest GMR.

Modifying the layer growth by IBAD offers another free parameter for optimization of the multilayer magnetic and structural properties. In Section 3.1.2 we showed that IBAD provides a good possibility to grow multilayers with smooth, low-roughness multilayers, when the ion energy is well set not to promote the bulk diffusion and material intermixing.

Fig. 3.14 shows the influence of assisting bombardment of 50-eV (a) and 100-eV (b) Ar ions. The primary ion current of the assisting beam was 20 mA. The spin-valve multilayers were deposited without the CoO underlayer in this case. For 50-eV bombardment we can see that the samples show lower NiFe coercivities and higher Co coercivities. This clearly indicates lower coupling between the two magnetic layers which is likely to be caused by improved smoothness of the interfaces (see also Section 1.2.1, paragraph Orange-peel coupling). In other words, the longer plateaus in the antiparallel state indicate an independent switching of the individual layers. For 50 eV the GMR is not yet diminished significantly.

For 100-eV bombardment the intermixing becomes more important and the GMR decreases. At this higher energy of the assisting ions the deposition rate decreased by 15% (for 50 eV by 8-10%) which indicates higher resputtering and in principle higher layer intermixing. The deposition rates were taken from a resonant quartz measurement.

In Section 3.4.2 we discussed the positive influence of CoO underlayers on the NiFe/Cu/Co multilayer growth. By using the CoO the multilayer magnetic properties become more reproducible and a more reliable comparison of the role of different depo-

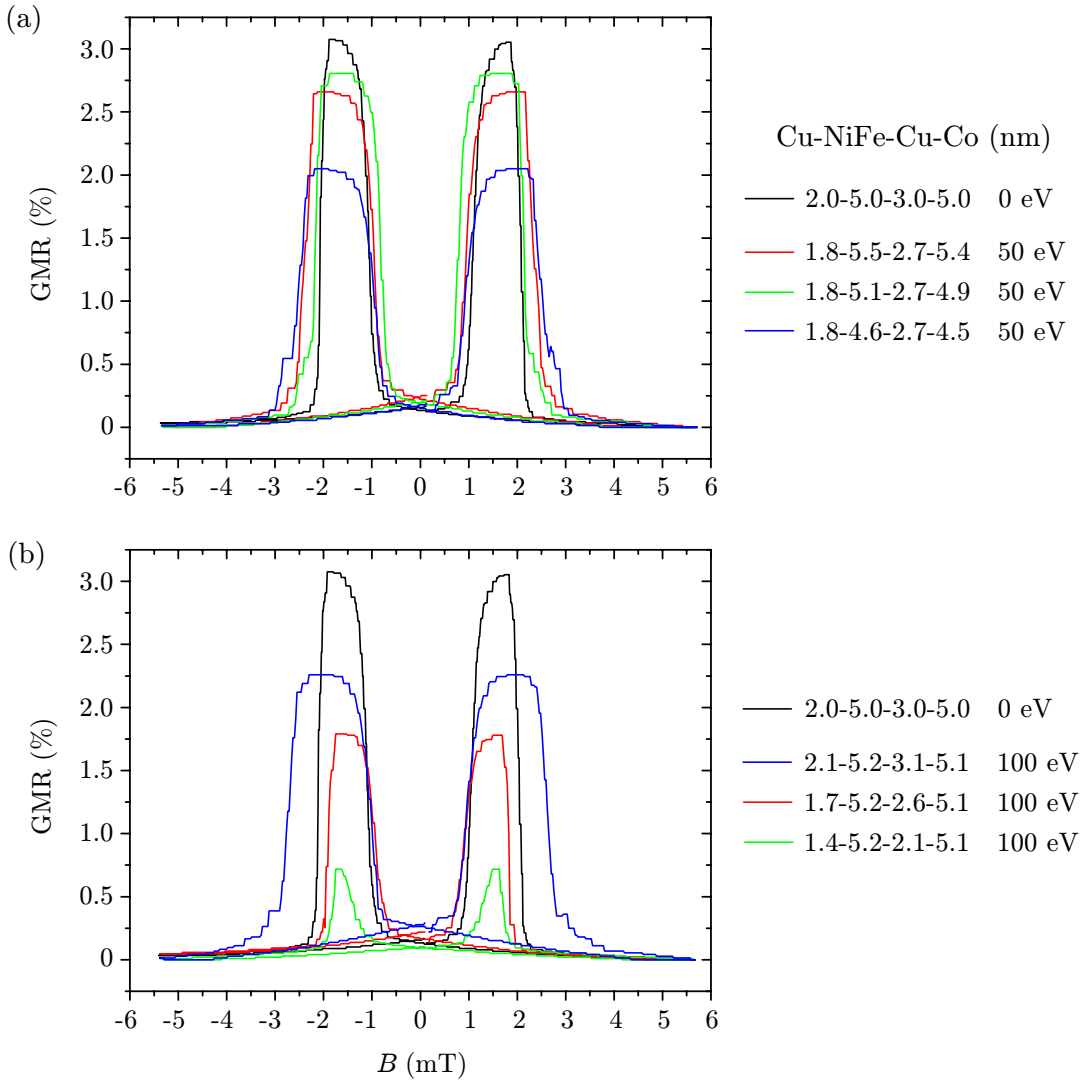

Fig. 3.14: Influence of the assisting bombardment on the GMR loops for different ion energies: (a) 50 eV, (b) 100 eV. The spin valves are prepared without the CoO underlayer.

sition parameters is possible. Fig. 3.15 shows the best configuration – SV 2-5-3-5-(2.8) – with (red curve) and without (black curve) the 50-eV assisting ions bombardment. Although the GMR decreased by almost 20% (but the GMR is still bigger than without CoO – Fig. 3.13), the NiFe became significantly softer – the coercivity decreased from 0.8 to 0.5 mT.

The coupling of the NiFe and Co layers can be quantified by measuring the NiFe minor loops, i.e. by recording the NiFe magnetization reversal loop without switching the Co magnetization.

- Fig. 3.16(a) shows a GMR full loop (black curve) and a NiFe minor loop (red curve) of a SV 2-5-3-5-(2.8) deposited *without assisting bombardment*. The minor loop is asymmetric and it is shifted by 0.45 mT with respect to zero field. This is due to the coupling bias from the Co layer.

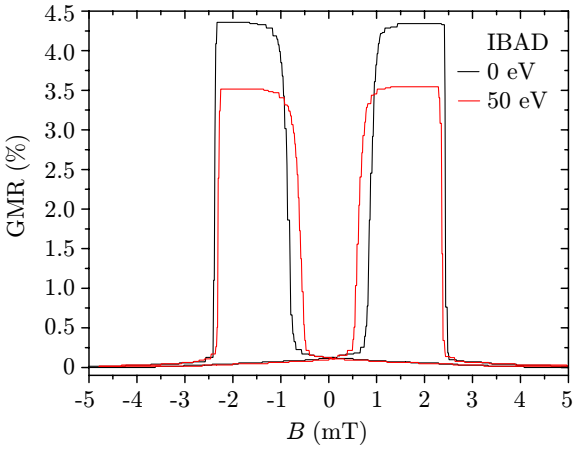

Fig. 3.15: Influence of a 50-eV assisting bombardment on the GMR loop of a SV 2-5-3-5-(2.8) sample.

Kerr images were taken for field values corresponding to the reversal of the NiFe layers. Images 1 and 2 show that the NiFe magnetization switching is governed by nucleation of small domains rather than by DW propagation. On the contrary, the Co magnetization switches by propagation of few nucleated domains. This is indicated both by the slope of the reversal in the GMR loop, and by the size of Co domains in Fig. 3.16(b), image 3. The difference in the magnetization reversal mechanism for Co and NiFe can be explained by different microstructure of the layers and different properties of the substrates (CoO vs. Cu).

The character of magnetization reversal in NiFe above the domains in Co is shown in Fig. 3.16(b). The field was increased until a domain structure in Co was created, then the field was swept in the other direction to avoid the saturation of Co. There are three distinguishable gray levels in the Kerr images. The lightest and the darkest ones correspond to parallel magnetization in the two layers, the intermediate to one of the antiparallel magnetization states. The NiFe reversal is clearly initiated above the black Co domain (image 4). After the area above the black Co domain is completely switched, reversed domains above the white Co domain appear (image 5). This is due to the coupling between the two layers. In the ideal uncoupled case the magnetization reversal in the NiFe layer should be homogeneous and take place at the same time in the whole layer with no regard on the Co state below.

- In the case of the multilayer deposited using *IBAD* (ion energy of 50 eV), the minor loop shift decreases to 0.09 mT only [Fig. 3.16(c)], indicating that the Co and NiFe layers are practically decoupled. This is a significant improvement with respect to multilayers prepared by IBS without assisting ion bombardment, to multilayers prepared by magnetron sputtering (Section 3.7) and even to the recently reported results on similar multilayers prepared by IBAD [296]. The corresponding NiFe domains indicated in the images 1 and 2 do not show any significant differences with respect to Fig. 3.16(a).

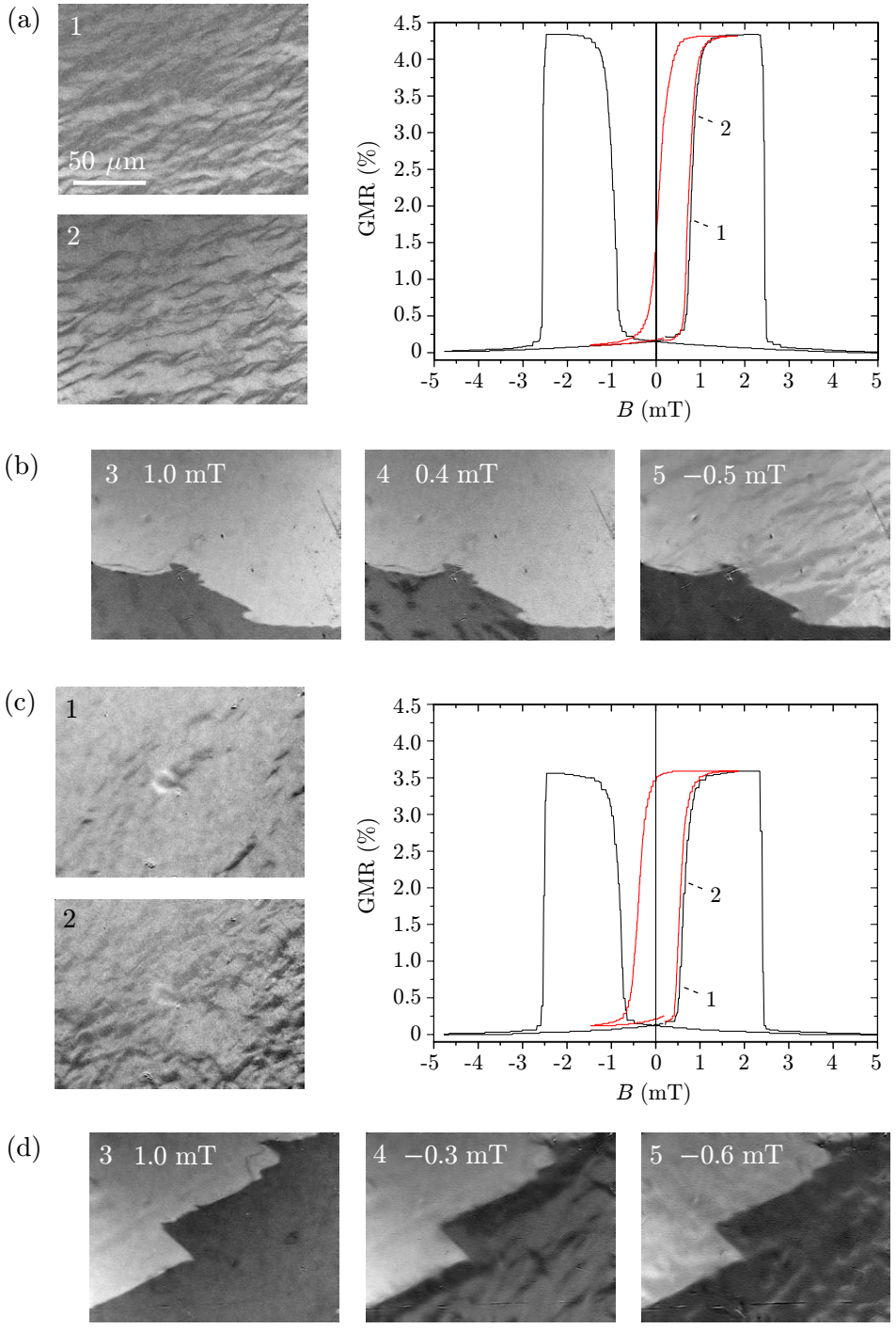

Fig. 3.16: GMR curves including minor loops and domain structures taken using Kerr microscopy for normal (a) and IBAD (c) SV 2-5-3-5-(2.8) multilayers. The Kerr microscopy images marked with 1 and 2 show the magnetic domain structure in NiFe for the points indicated in the graph. The magnetization reversal of NiFe above the large domains in Co is also compared for normal (b) and IBAD (d) cases. Images marked with 3 show the initial state, 4 the early stage of NiFe reversal, 5 the final stage. The small domains in NiFe are superimposed on the magnetic contrast of the Co domains.

The magnetization reversal above the Co domains [Fig. 3.16(d)] is again initiated above the black domain (image 4), but the reversal above the white Co domain takes place earlier than in the previous case and finally both parts saturate almost simultaneously (image 5).

It is likely that the decoupling of the NiFe and Co layers is caused by enhancing the spacer quality in terms of roughness. The interlayer coupling is almost suppressed for a spacer thickness of 3 nm, and for an assisting Ar ion-beam energy of 50 eV and ion current of 20 mA. A complete study of the dependence of magnetic coupling on the spacer thickness is planned as a next step. For comparison, note that using a standard magnetron-sputtering device (Section 3.7), a spacer of 8 nm or more was needed to assure the magnetic layers to be decoupled.

3.6 Annealing of NiFe/Cu/Co Multilayers

Sufficient thermal stability is one of the main demands on the spin-valve structure. Thermal reaction and annealing effects in NiFe/Cu thin films were studied in detail [274, 275, 276]. It was observed that magnetoresistance of NiFe/Cu based spin valves decreases above 200°C [274]. The reason for the GMR degradation was identified as an intermixing and alloying tendency of Ni and Cu [275].

The intermixed phases at the NiFe/Cu interfaces are paramagnetic [277] and thus induce significant spin-flip scattering of the incoming or outgoing conduction electrons. The spin-flip scattering leads to a loss of "spin-memory" of the electrons crossing the Cu spacer layer, and therefore reduces the MR amplitude [57].

On the contrary, it is known that the Co and Cu phases are immiscible at room temperature and annealing the samples above 200°C causes demixing of the as-deposited layers [278, 279]. The system consisting of Co/Cu keeps its GMR up to 400°C [275]. Hence, by inserting thin Co layers at the NiFe/Cu interfaces [257] one not only increases the GMR, but also improves the thermal stability of the system. However, such Co layers as thin as 1.5 nm are not enough thick to significantly attenuate the GMR decrease [280] and thicker Co layers may lead to an unwanted increase in the NiFe layers' coercivity.

For the evaluation of our multilayers we addressed the effect of annealing on the Cu/Co interface first. We prepared a Cu 2 nm/Co 2 nm/Cu 3 nm/Co 4 nm/CoO 2.8 nm/Si multilayer for magnetotransport measurements. The top Cu/Co bilayer was chosen for an additional measurement of the depth composition using Angle-Resolved X-ray Photoelectron Spectroscopy (AR-XPS, see below). Hence, the top Cu thickness is limited because of the surface sensitivity of this technique. To make the antiparallel alignment possible, different coercivities of the two Co layers were ensured by the difference in their thicknesses and by adding the CoO underlayer. Although these steps were not sufficient to switch the Co layers independently, the effect of annealing was anyway evident.

The as-deposited multilayer featured quite a low GMR, the easy axis was not well defined and the coercive fields were not sufficiently separated (see Fig. 3.17). After a

two-step annealing, first for 15 min at 80°C and second for 15 min at 170°C, the GMR increased more than 6×. The increase in the bottom Co layer coercivity could be attributed to the change of the Co/CoO interface and diffusion of oxygen into the Co layer.

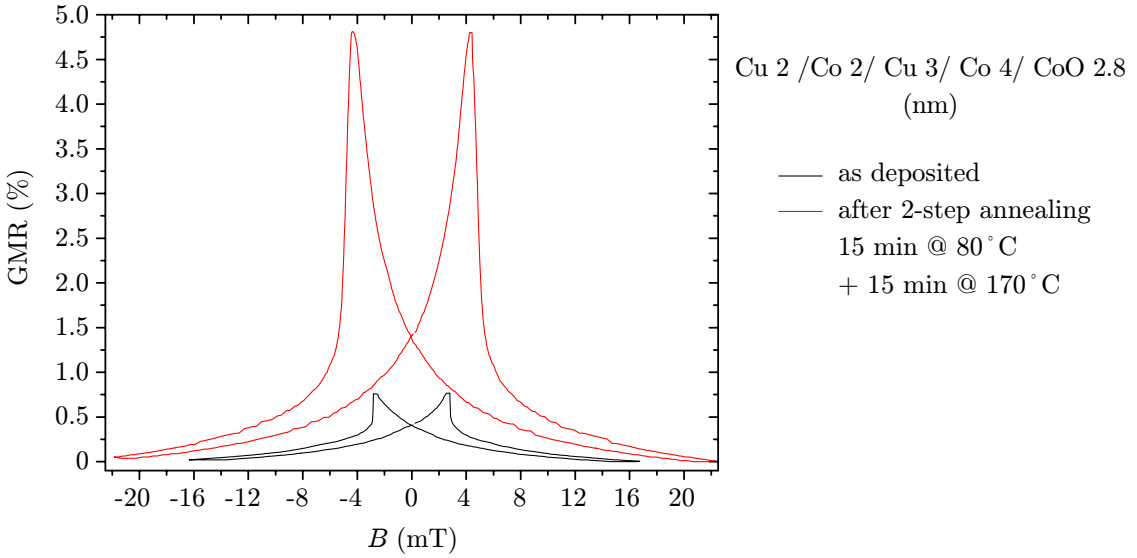

Fig. 3.17: Annealing of a Cu 2/Co 2/Cu 3/Co 4/CoO 2.8/Si multilayer. After the indicated two-step annealing the GMR increased more than by a factor 6.

The evolution of the interfaces during annealing was verified by AR-XPS (the method is described in more detail in Section B.2). This method allows us to determine the depth profile of the sample elemental composition. At each depth, the relative concentration of components is calculated (the sum equals to 1). Only one characteristic peak is selected for evaluation of each component. In case of compounds only one representative element is selected.

Fig. 3.18 describes the evolution of the depth profile of a sample Cu 2 nm/Co 2 nm/Si during annealing. In (a) the profile after annealing for 15 min at 80°C is shown. The interface between the Cu and Co layers is at 2-2.5 nm below the surface. It is obvious from the figure that the Co component is intermixed with the Cu one and vice versa. For a proper calculation of the depth profile from the measured AR-XPS spectra, the analytical method requires homogeneous layers with sharp interfaces. This condition was not yet fulfilled after annealing at 80°C. We also carried out the measurement for the as-deposited state, but the convergence became unstable so we could not provide an unambiguous depth profile for this situation. However, the intermixing was still apparent.

The top of the Cu capping layer got oxidized and the surface was covered by carbon during the transfer from the deposition equipment to the analytical one. Due to the surface sensitivity of the technique the Co was defined as the substrate layer as a boundary condition.

A clear change is found after second annealing for 15 min at 170°C [Fig. 3.18(b)].

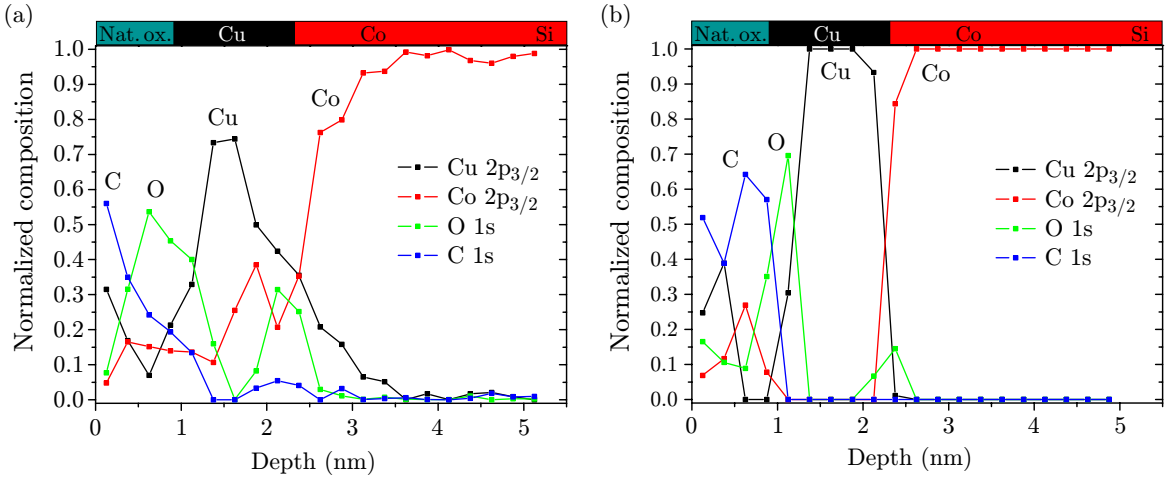

Fig. 3.18: Compositional depth profiles of a Cu 2 nm/Co 2 nm/Si structure obtained by analysis of AR-XPS spectra. The Cu and Co phases tend to separate with increasing the temperature. (a) profile after annealing for 15 min at 80°C, (b) profile after annealing for 15 min at 170°C.

The Cu/Co interface is better defined and much sharper. Note that Co segregated at both sides of the Cu layer. This confirms the situation in Fig. 3.18(a) where the Co is present at some part everywhere throughout the Cu layer.

From the binary Co-Cu diagram one can deduce that the maximum solubility of Cu in Co is 19.7% at 1367°C and decreases quickly with temperature [284]. Approx. at 400°C the Cu solubility reaches zero. If the Co and Cu phases are mixed at room temperature (a disequilibrium state), through thermally activated processes they tend to separate. This indicates that the annealing produces a well defined Cu/Co interface which is responsible for the significant GMR increase. As described in Section 3.5, in case of a Cu/Co system the interface is important for the spin-dependent scattering [257]. Hence, it seems that although increasing the interfacial roughness increases the GMR, the intermixing of the phases causes the opposite effect [281].

Concerning the NiFe/Cu interface a very similar binary diagram to the Co-Cu one is valid for Fe and Cu [283], i.e. the Cu and Fe phases do not mix at low temperatures below 600°C. On the contrary, Cu and Ni form a thermodynamically stable solid solution even at room temperature [282] and heating the sample only pronounces this effect.

Fig. 3.19 represents a SIMS profile of a SV 3-6-3-6 multilayer. The selected mass signals are all normalized to the highest count number, except of the Cu signal from the native CuO_x at the multilayer surface (much larger signal than in the rest of the multilayer). In this case the Cu signal was normalized to the maximum count value in the Cu spacer. The second exception are the Ni and Fe signals, for which the sum of the signals was normalized instead of the individual ones [285]. This reveals that the corresponding counts in the SIMS depth profile are proportional to the composition of NiFe – Ni (80%), Fe (20%).

It is apparent that the NiFe/Cu interface is not identical for both the Ni and Fe phases – Ni is diffused in the Cu layer more than Fe, as expected. Moreover, this effect

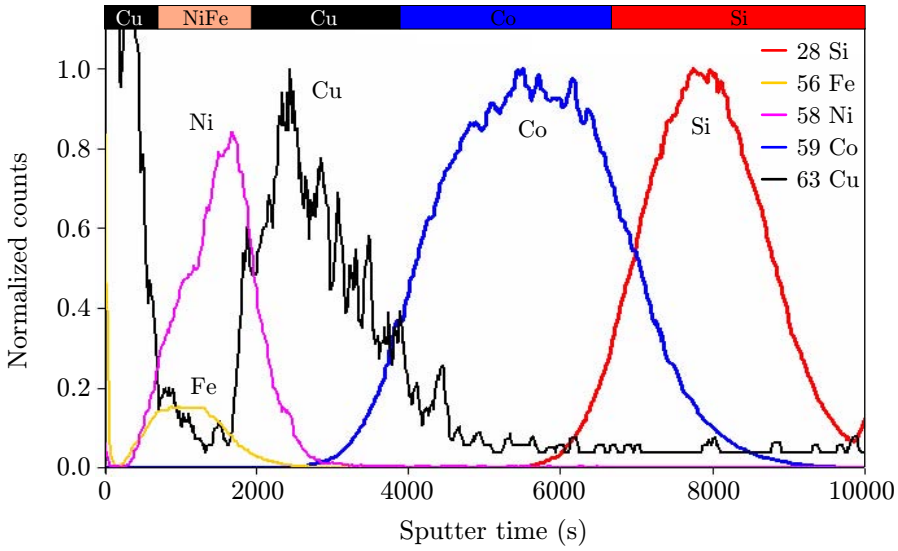

Fig. 3.19: SIMS depth profile of a SV 3-6-3-6. Adapted from [285].

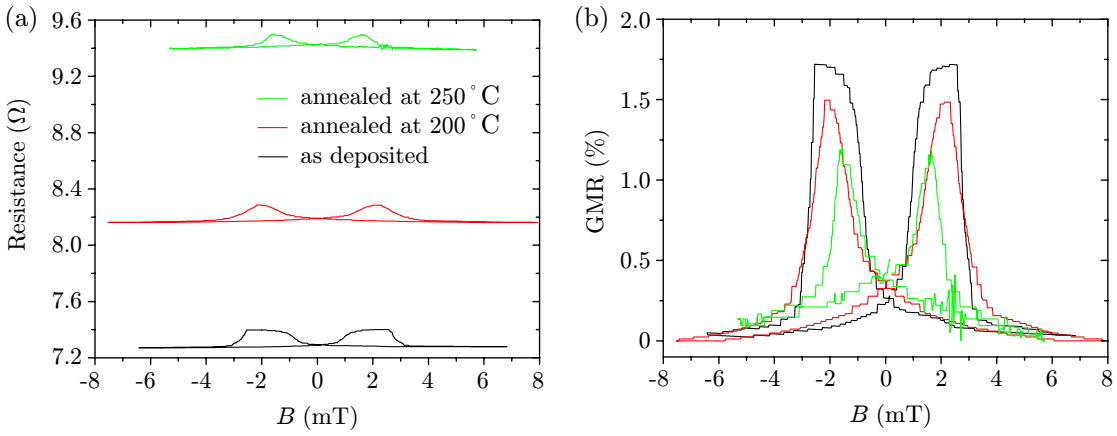

Fig. 3.20: Effect of annealing on the SV 2-5-4-5 resistance (a) and GMR ratio (b).

is observed close to the surface where the signal transitions at the interfaces are still sharp enough.

When annealing these structures the overall thermal stability of the IBS-prepared SV multilayers was checked. For temperatures below 100°C no changes in the magnetoresistance loops were observed. The degradation takes place gradually and significant changes appear close to 200°C. In Fig. 3.20 both the resistance (a) and the GMR ratio (b) evolution dependent on the annealing temperature are shown. The sample was annealed for 20 min at each temperature and for the magnetoresistance measurement it was cooled down to room temperature. This behavior during annealing indicates that the diffusion of Ni in Cu has a larger effect on the overall properties of the system than the segregation of Co and Cu. A commonly used solution, insertion of a thin Co layer in between the NiFe and the Cu spacer, is not applicable in our case, as we

need unique materials in each of the functional magnetic layers for our DW motion experiments (see introduction to this chapter).

3.7 Magnetron-Sputtered Multilayers

Magnetron sputtering is the most widely used technique for the deposition of spin-valve multilayers. Langer et al. [286] showed that dc magnetron sputtering produces more sensitive[7] spin-valves of the type Co/Cu/Co/FeMn than rf sputtering or rf diode method. This was caused by a reduced number of structural defects in the Co layer.

The optimization of the NiFe/Cu/Co system started by tuning the layer thicknesses [287] and by increasing the difference in the coercivity of the magnetic layers [288]. Paul et al. [289] modified the grain size by differing the Ar pressure and obtained one of the highest GMR reported for magnetron sputtering (4%). Dependence of GMR on the grain size in Co/Cu multilayers was studied by Modak et al. [290].

The multilayers presented in this section were prepared at the IN. Our measurements showed that the individual layer thicknesses optimized to obtain the largest GMR were very similar to those obtained by IBS optimization, with the exception of a 7-nm Co layer (instead of 5-nm in case of IBS). The largest GMR was obtained for a SV 4-5-4-7 where the capping layer was Au instead of Cu. The influence of the spacer thickness on GMR of a SV 4-5-X-7 is shown in Fig. 3.21(a). Fig. 3.21(b) represents the same comparison for the SV 4-5-X-7 deposited on a CoO underlayer of a thickness of 4 nm oxidized after deposition in 5×10^4 Pa of O_2 for 20 min. Here the spacer thickness which maximizes GMR is 3 nm. Without CoO, the shape of the curves without pronounced plateaus in the antiparallel state indicate that for a 3-nm spacer the NiFe and Co layers are still coupled. The coercivity of NiFe decreases for thicker spacers. This

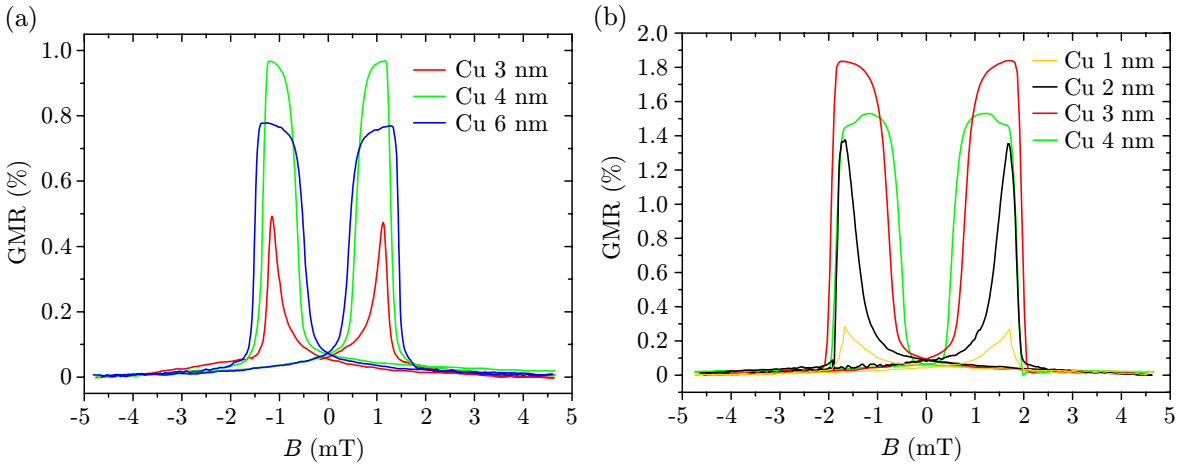

Fig. 3.21: GMR curves for magnetron-sputtered SV 4-5-X-7 multilayers. (a) without CoO, (b) with CoO of 4 nm oxidized after deposition.

[7]The maximum GMR divided by the minimum field necessary to switch between the low and high resistance configurations.

suggests a better growth of the multilayer on CoO. When compared to the IBS, the CoO oxidized after deposition shows better properties for magnetron-sputtered structures. This could be accounted for smaller grains of the Co layer (see Section 3.8) and consequently a higher amount of oxygen diffusing during oxidation. Note that the oxygen diffuses preferentially at the grain boundaries [291].

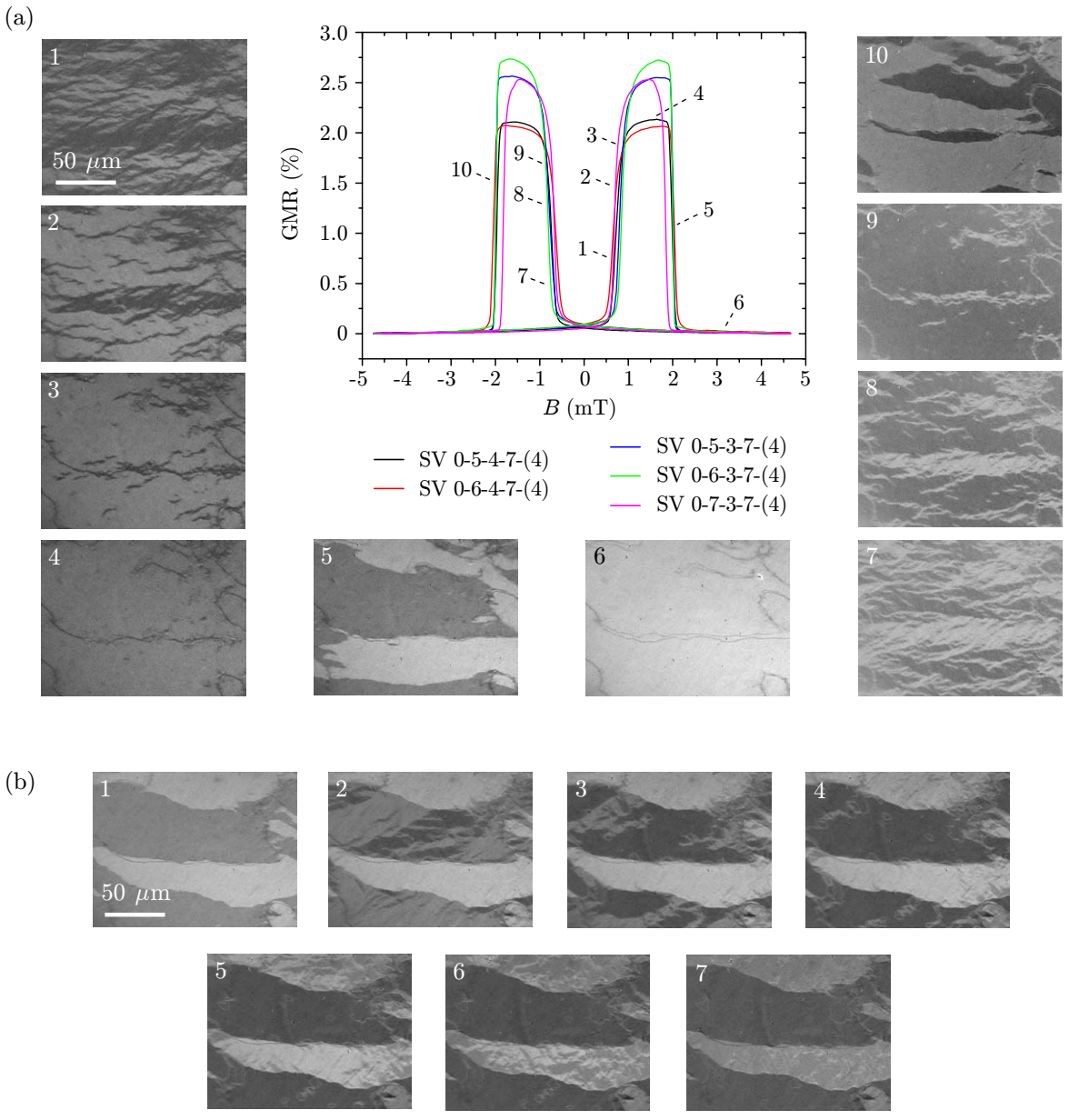

Fig. 3.22: (a) GMR loops and Kerr images of selected magnetization configurations in magnetron-sputtered SV multilayers. (b) magnetization reversal of NiFe above Co domains.

Generally the GMR values are substantially lower than those obtained in multilayers prepared by IBS. The GMR loops shown in Fig. 3.22(a) were deposited without the capping layer (we suppressed shunting of the current to the Au layer) and in this case

the GMR almost reached the values obtained for IBS multilayers, however just for those without CoO. Fig. 3.22(a) further shows a comparison of GMR loops corresponding to the multilayers where the layer thicknesses were slightly varied. Let us focus on the black curve representing the SV 0-5-4-7-(4). Kerr microscopy images (1-10) represent different phases of magnetization reversal in the SV 0-5-4-7-(4) multilayer, indicated by numbered arrows in the corresponding GMR loop. Images (1-4) illustrate the reversal of the NiFe layer up to reaching the antiparallel state with Co (4). Images (5-6) show switching of Co up to reaching the saturated state of both magnetic layers. Images (7-10) then represent the switching of NiFe and Co in the opposite branch.

Magnetization reversal of NiFe above Co domains oriented in opposite directions is demonstrated in Fig. 3.22(b). Similarly to the IBS-sputtered multilayers without the assisting bombardment, a complete switching takes place first above the black Co domain and then above the white domain, thus confirming the Co and NiFe interlayer coupling.

The quality of Kerr microscopy images is better than in Section 3.5 (less noise, higher contrast). This is most probably caused by the absence of a capping layer in this case. The samples deposited by IBAD were capped with a Cu layer which was oxidized on the top.

Note that during the deposition by magnetron sputtering an external field of approx. 125 mT was acting on the samples. The field imposed an uniaxial anisotropy in the system. This results in a dependence of the shape of domains on the angle between the applied field and the easy axis during the magnetization reversal. Fig. 3.23(a) shows the NiFe domains when the field is applied along the easy axis (dashed white line). The domains are elongated and merged in the direction of the field. In case of a misalignment of the applied field and the easy axis [Fig. 3.23(b)], the field elongates the domains which preferentially merge in the direction of the easy axis.

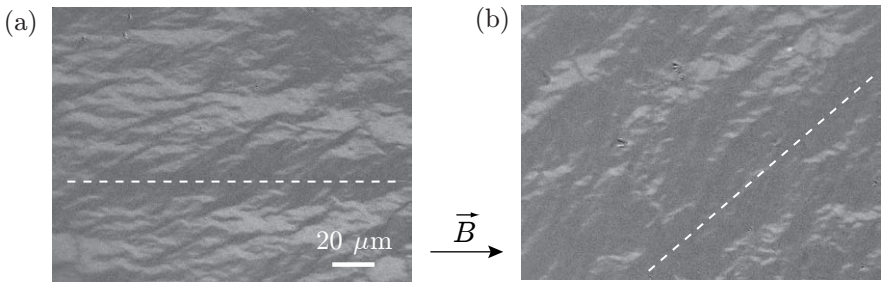

Fig. 3.23: Domain structure in NiFe when magnetic field is applied (a) along the easy axis, (b) at 40° with respect to the easy axis. At the initial stage of the NiFe reversal, the small domains tend to merge in the direction of the easy axis.

3.8 Transmission Electron Microscopy of Interfaces

The decrease of magnetic coupling in the multilayers prepared by IBAD together with the increase of GMR by incorporating the CoO underlayers lead us to the assump-

tion that the layer growth was substantially improved and the interfacial roughness decreased. For this purpose we employed transmission electron microscopy (TEM) to compare the multilayer-interface quality in the samples of:

- an IBAD-prepared multilayer with a configuration of Cu 2 nm/NiFe 5 nm/Cu 3 nm/Co 5 nm/CoO 2.8 nm/Si,
- a magnetron-sputtered multilayer with a configuration of Cu 3 nm/NiFe 5 nm/Cu 8 nm/Co 7 nm/CoO 4 nm/SiO_2 prepared in the collaborating laboratory of CNRS-Thales in Orsay.

Fig. 3.24 compares the cross-sections of the two systems visualized by TEM. One can clearly see the different substrates, thermic $Si0_x$ in case of the magnetron-sputtered sample and a native SiO_2 on top of Si (100) in case of the IBAD-prepared sample. The top layers are smeared out in the glue[8], therefore we cannot distinguish the capping layer and the top of the NiFe layer.

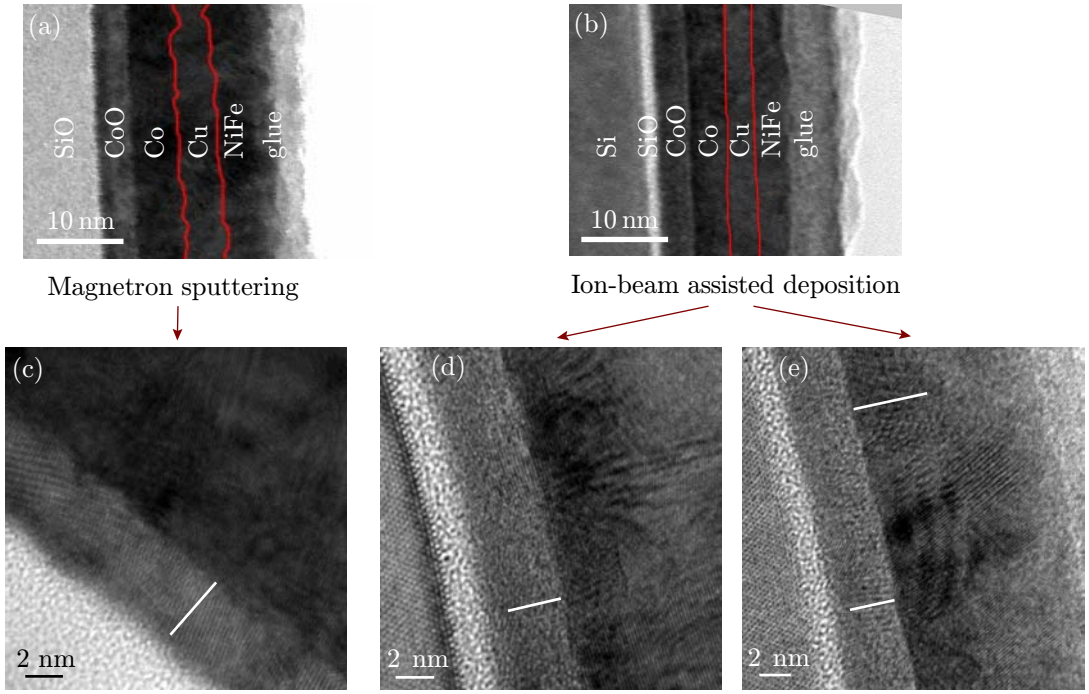

Fig. 3.24: TEM images of the multilayer cross-sections of a magnetron-sputtered sample (a) and IBAD-prepared sample (b). (c)-(e) show a detailed grain structure of the corresponding multilayers. White bars represent nominal thicknesses of selected layers: (c) 4 nm of CoO, (d) 2.8 nm of CoO, (e) 2.8 nm of CoO and 5 nm of Co.

The four elements present in the sample (Co, Cu, Ni and Fe) are of similar atomic masses and this makes the observation of layer boundaries difficult. To visualize the

[8]For the TEM observation of multilayer cross-sections the sample is cut in two pieces and these are glued at the multilayer face. Then the sample is thinned, polished and ion-milled. More details in Section B.5.

interfaces the image had to be slightly defocused. In the figures the interfaces are highlighted by red lines. From a visual comparison it is evident that the IBAD-prepared sample contains less rough and compact interfaces. The multilayer deposited by ion-beam sputtering without assisting bombardment featured a similar appearance of the interfaces (not shown) as that prepared with assisting bombardment. Hence, the difference in interface roughness could be only deduced from the magnetic coupling shifting the NiFe minor loops in GMR or MOKE measurements.

Details of the grain structure can be seen in Fig. 3.24(c)-(e). The oxide layer appears to be lighter than pure Si or Co. It is clear that only in the case of CoO oxidized during the deposition of Co [Fig. 3.24(d)-(e)] the layer is oxidized homogeneously. In the magnetron-sputtered sample [Fig. 3.24(c)], the CoO was prepared by oxygen plasma after the deposition of a 4-nm Co layer and there is a remainder of pure Co between the CoO and SiO_2 layers.

The grains in the unoxidized layers of the magnetron-sputtered sample are on average approx. 2× smaller than in the IBAD-prepared one (diameters of approx. 4 nm vs. 8 nm, respectively). To check the layer thickness the white bars in Fig. 3.24(c)-(e) represent the nominal thickness of corresponding layers – 4 nm of CoO in (c), 2.8 nm of CoO in (d), 2.8 nm of CoO and 5 nm of Co in (e). The CoO layer in (d)-(e) is thinner than the nominal value by almost 1 nm. However, the boundary between the SiO_2 and CoO is not well defined.

3.9 Low-Temperature Magnetotransport Experiments

3.9.1 Temperature Influence on Magnetoresistance

Another important parameter that influences the GMR amplitude is the temperature [261, 263]. The GMR ($\frac{\Delta R}{R}$) generally decreases with temperature at a rate depending on a particular system. This tendency can be explained by two main factors [57]:

- Intermixing of the spin-up and spin-down currents caused by magnon scattering in the bulk of the ferromagnetic layers or by paramagnetic fluctuations at the FM/NM interfaces. It was found that the higher the Curie temperature of a material, the weaker the thermal variation of the GMR is [261, 263]. ($\Delta R \downarrow$)

- Scattering on phonons in the nonmagnetic spacer decreases the spin-dependent scattering and prevents the transfer of conduction electrons from one ferromagnetic layer to the other one. ($R \uparrow$)

To investigate the evolution of GMR and magnetic layer coercivities while decreasing the temperature, we carried out measurements of magnetoresistance for temperatures between 300 K and 5 K. These measurements were carried out on ion-beam-sputtered multilayers.

The resistance per square was measured by a modified van der Pauw technique. The original method as proposed by its author [367] requires the probes to be at the

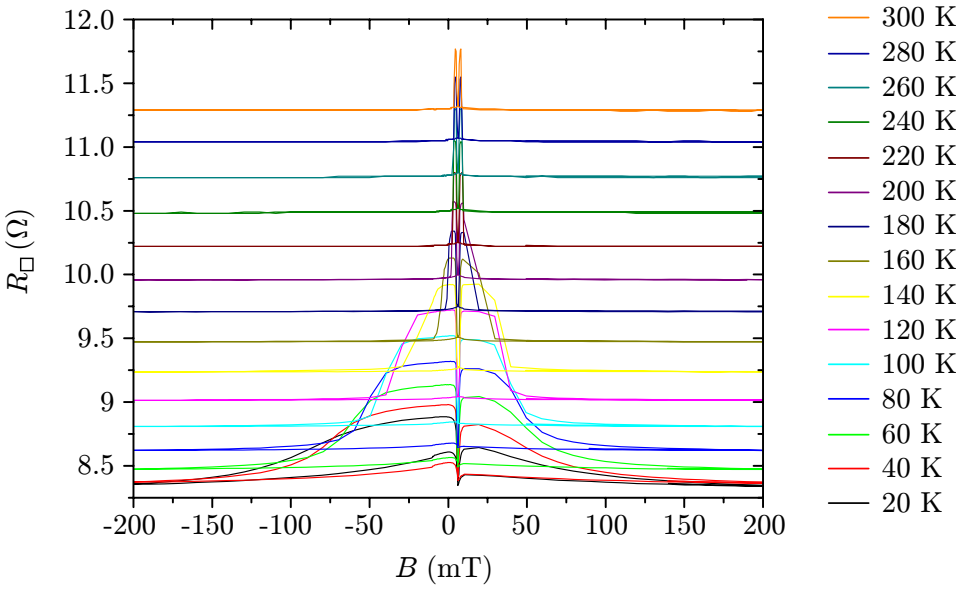

Fig. 3.25: GMR loops of a SV 2-5-3-5-(4.2) multilayer measured for different temperatures down to 20 K.

edges of the sample (see Section B.4). Errors of relative resistivity $\frac{\Delta\rho}{\rho_0}$ for different geometries can be calculated [367]. In our case the condition of the edge probes was not fulfilled, the probes were placed in the corners of a $4\times4\,\mathrm{mm}^2$ square while the size of samples was $10\times14\,\mathrm{mm}^2$. By using the finite-element method of calculating resistance[9] we estimated that such a geometry would require a correcting factor for the resistivity up to 35%. However, this does not have a substantial effect on the observed phenomena that we discuss in the following.

Fig. 3.25 shows GMR loops taken for temperatures ranging from 300 K to 20 K. The samples were cooled in a positive magnetic field[10] after each loop was completed, i.e. they were not brought to the room temperature each time. On one hand, this explains why at low temperatures the antiparallel state is better defined in the negative field (showing higher resistance). In the positive branch, the Co magnetization of some parts of the sample is already reversed with the help of the exchange bias field when the NiFe is being switched. On the other hand, the exchange bias direction is not so well defined as when cooling the system in field from temperatures well above the Néel temperature of the antiferomagnet. Moreover, the training effect (Section 1.2.1) might decrease the asymmetry of the Co coercive fields at low temperatures. The remanent field (trapped flux) in the superconducting coil causes a shift of the GMR loops of approximately +5 mT.

Further on we focus on the dependence of resistance on temperature. Generally, any fluctuations of the magnetic arrangement are suppressed when high-enough magnetic field is applied. However, any variation of R_P when increasing the field is not observable

[9] Comsol Multiphysics finite-element modeling software was used.
[10] The field polarity is consistent with the presented figures.

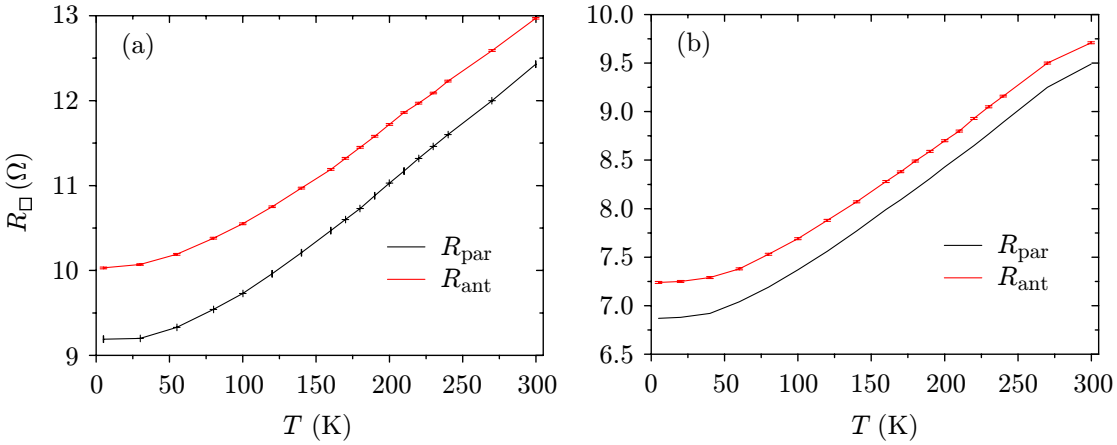

Fig. 3.26: Dependence of resistance R_{P} and R_{AP} on temperature of typical NiFe/Cu/Co spin-valve multilayers with a 1.4 nm thick CoO underlayer (a) and without CoO (b).

(see Fig. 3.25) and therefore indicates that scattering of electrons on magnons is not significant already at room temperature.

Fig. 3.26 shows typical R_{P} and R_{AP} curves when cooling down the spin-valve multilayers. Fig. 3.26(a) represents a SV 2-5-3-5-(1.4) multilayer. The GMR increases from 4.3% at room temperature to 9.4% at 5 K. The corresponding resistance decreases by approximately 25% and the same temperature dependence can be found for all the measured multilayers with different CoO thicknesses. This suggests that the principal contribution to the resistivity does not arise from scattering on phonons, but rather from the grain boundaries and interlayer interfaces, which define the residual resistance R_{P} at 5 K. There is also no difference when comparing SV 2-5-3-5-(2.8) multilayers deposited with and without assisting ion bombardment. Suzuki and Taga [281] found an approximate T^2 dependence of resistance in Co/Cu multilayers, similarly to our results, although the underlying scattering processes were not clarified.

Fig. 3.26(b) shows resistance per square of a SV 2-5-3-5 multilayer deposited without CoO. The multilayers deposited on CoO underlayers featured a similar R_{P} resistance within a 10% difference both at the room temperature and at 5 K. The R_{P} of the multilayer deposited directly on a native SiO_2 layer was significantly smaller – it dropped below 7 Ω at 5 K. This indicates that the Co/SiO_2 might be more specular than the Co/CoO interface. However, the smaller GMR (ΔR) in case of SiO_2 substrates implies less probable spin-conserving electron reflection at this interface.

Importantly, the antiparallel state might not be well defined, in case the NiFe and Co layers' easy axes are misaligned with the applied field or an interlayer coupling is present. These effects might prevent an entirely antiparallel state from being reached. In this case we might observe a plateau in the R_{AP} near the blocking temperature of the antiferromagnet [see Fig. 3.27(d)]. At T_{B}, indicated by the black arrow in the figure, the Co magnetization direction becomes stabilized along the applied field by AF/FM exchange field which prevails the local mismatch between the applied field and the crystallographic easy axes, thus better defining the Co/NiFe antiparallel state and increasing R_{AP}.

3.9.2 Blocking and Néel Temperatures of CoO_x Layers

By extracting the data from GMR loops of SV 2-5-3-5-(X) multilayers measured at temperatures from 300 K to 5 K (Fig. 3.25), we derived graphs of cobalt coercivity versus temperature, for different CoO thicknesses [Fig. 3.27(a)]. To emphasize the strong increase of Co coercive field below T_B, a difference of coercive fields in the positive (B_{C+}) and negative (B_{C-}) field branches was computed[11]. Two regimes can be clearly distinguished: a high-temperature one where the increase of Co coercivity with decreasing temperature is not important and a low-temperature one where the coercivities significantly increase and become asymmetric for positive and negative applied fields. Linear fits were applied in both regimes [Fig. 3.27(b)] and their intersect was defined as the blocking temperature. Indeed, the remanent field of the superconducting coil does not have an influence on the determination of T_B.

The dependence of T_B corresponds well to [26] for thin CoO layers of 1.4 and 2.8 nm (Fig. 1.5). For thicker layers, the dependence diverges and even drops for a 9.3 nm thick CoO layer. The reason remains unclear, but might be connected to formation of a Co_3O_4 phase instead of CoO. The two oxides are both antiferromagnets, but vary significantly in the value of bulk T_N:

- CoO — rock-salt structure, T_N=291 K [25],
- Co_3O_4 — spinel structure, T_N=40 K [30].

It was shown that the CoO_x phase can be selected by varying the partial oxygen pressure upon deposition by ion-beam sputtering [29] or dc magnetron sputtering [31]. In case of ion-beam sputtering, 8% of O_2 led to a single-oxide phase of CoO, 34% of O_2 led to pure Co_3O_4 [29].

In our case the oxygen partial pressure varied between 1.4×10^{-2} Pa and 1.7×10^{-2} Pa for different samples, corresponding to 56-60% of the total Ar+O_2 pressure. This suggests that there might be a substantial part of Co_3O_4 in our CoO_x layers. This would explain the dependence of T_B on CoO_x thickness – for thin layers the T_N of Co_3O_4 is enhanced by the Co layer, thus increasing also the T_B [32]. For thicker CoO_x layers the Co effect diminishes and T_B drops. As there can be a mixture of CoO_x phases and the exact composition could vary also with the layer thickness, a more elaborated study is needed to explain the presented behavior.

In summary, a substantial increase of Co layer coercivity due to the AF/FM interaction at room temperature cannot be indeed expected. Better growth of Co layers on CoO_x is likely behind the observed increase of Co layers' coercivity.

[11] By adding the two coercive fields one obtains the asymmetry parameter – the exchange-bias shift. However, this leads to a subtraction of close values resulting in introducing large errors and thus this characteristic is not suitable for determination of T_B.

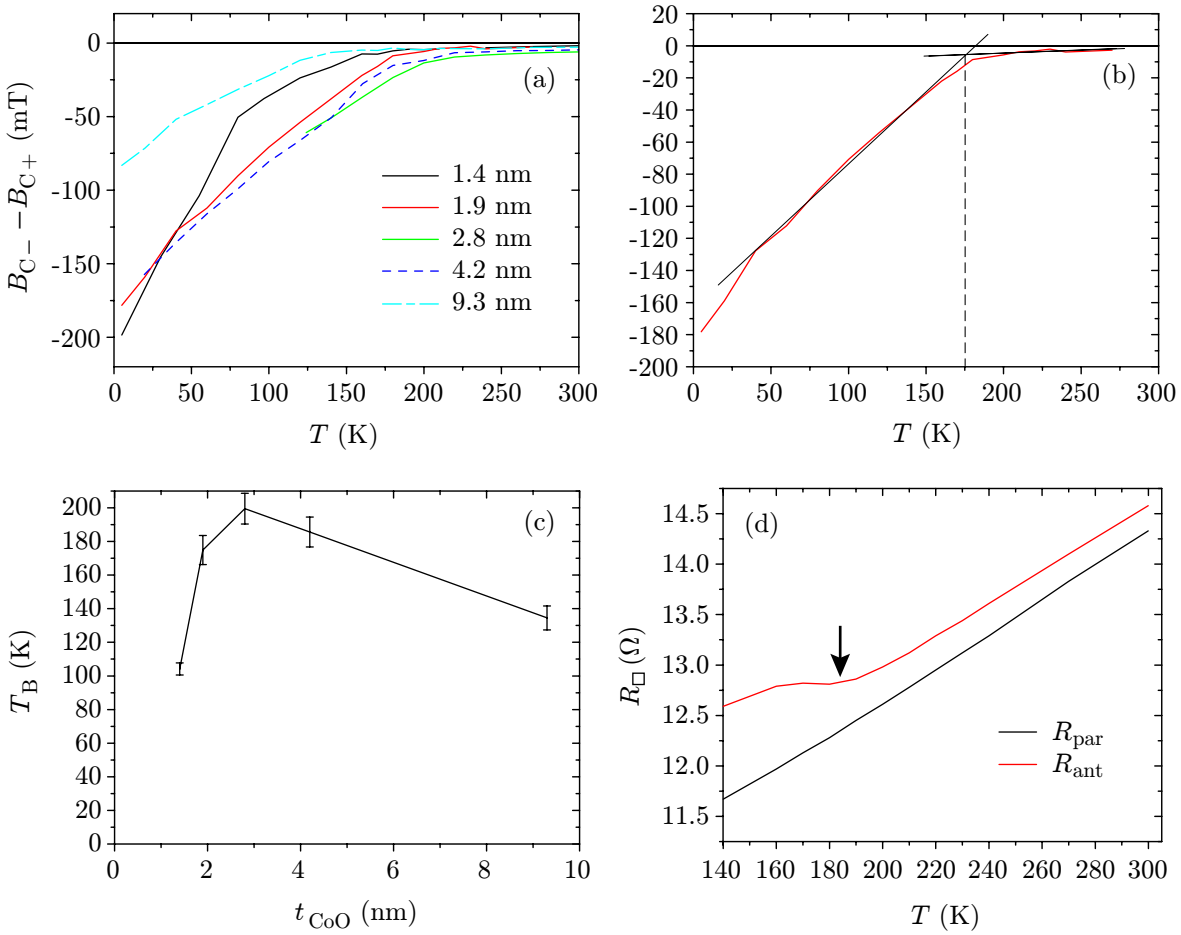

Fig. 3.27: (a) Temperature-dependent Co coercivities in SV 2-5-3-5-(X) multilayers. The CoO thicknesses are indicated in the graph. (b) Determination of T_B for a SV 2-5-3-5-(4.2) multilayer. (c) T_B plotted as a function of CoO thickness. (d) Dependence of resistance R_P and R_{AP} on temperature for a SV 2-5-3-5-(2.8) in case the applied field and the easy axis are misaligned by approx. 5%.

3.10 Analysis of Surface Roughness

3.10.1 As-deposited Multilayers

The roughness of the IBS-prepared spin-valve multilayers was determined by Atomic Force Microscopy (AFM). The multilayers prepared without assisting ion bombardment showed some defect-like peaks reaching a height of 4 nm [see Fig. 3.28(a)], but the surface roughness in the defectless regions (characterized by RMS – Root Mean Square) was comparable or slightly lower (RMS 0.15 nm versus 0.16 nm, respectively) than in the case of IBAD [assisting ion energy 50 eV, Fig. 3.28(b)]. This small difference comparable to the error bar might be induced by the impingement of assisting ions.

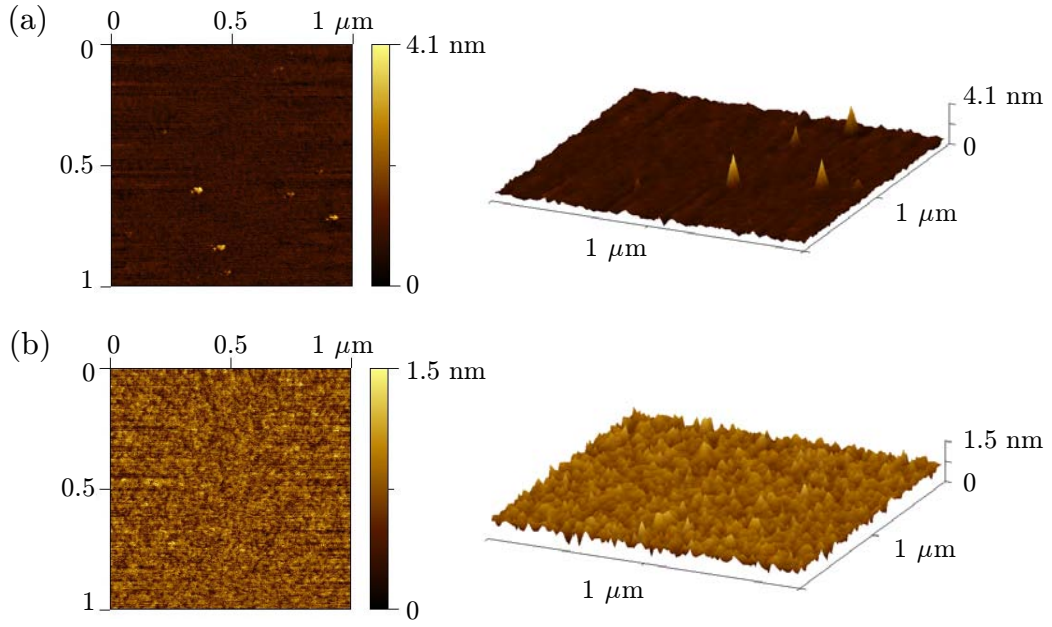

Fig. 3.28: Surface roughness of a SV 2-5-3-5-(2.8) multilayer without (a) and with (b) 50-eV assisting bombardment. The topography was obtained after deposition in the non-contact AFM mode.

3.10.2 Ageing of Single Layers

The temporal evolution of surfaces under different conditions was checked subsequently for the individual layers without capping, grown directly on silicon substrates with a native SiO_2. Initial investigation revealed that during ageing of Co single layers in the ambient atmosphere an important waviness and bulges (reaching a height of 10 nm or more) evolve on the surface after approximately one week. Basically two reasons might be considered:

- oxidation and continuous degradation of the surface (corrosion),
- gradual relaxation of a strain in the deposited layers.

Fig. 3.29(a)-(c) represent temporal evolution of the surface of a 10-nm Co layer after 15 days under different conditions – Fig. 3.29(a) shows the as-deposited state (RMS 0.1 nm), Fig. 3.29(b) the state after exposure to air for 15 days (RMS 1.8 nm). A bulge structure with the highest peaks of 13 nm is clearly formed on the surface. On the contrary, when kept in vacuum of 1×10^{-7} mbar for the same period of 15 days, the surface stays unperturbed similarly to the as-deposited state. This strongly indicates that the changes in surface topography are connected to the oxidation-induced degradation rather than to the strain relaxation of the Co layer.

The formation of bulges can be suppressed by capping the Co layer by a suitable material that is more resistant to corrosion, e.g. Al or Au. Fig. 3.29(d) shows the surface of a Al 2 nm/Co 10 nm bilayer after 45 days in the ambient atmosphere (RMS 0.4 nm).

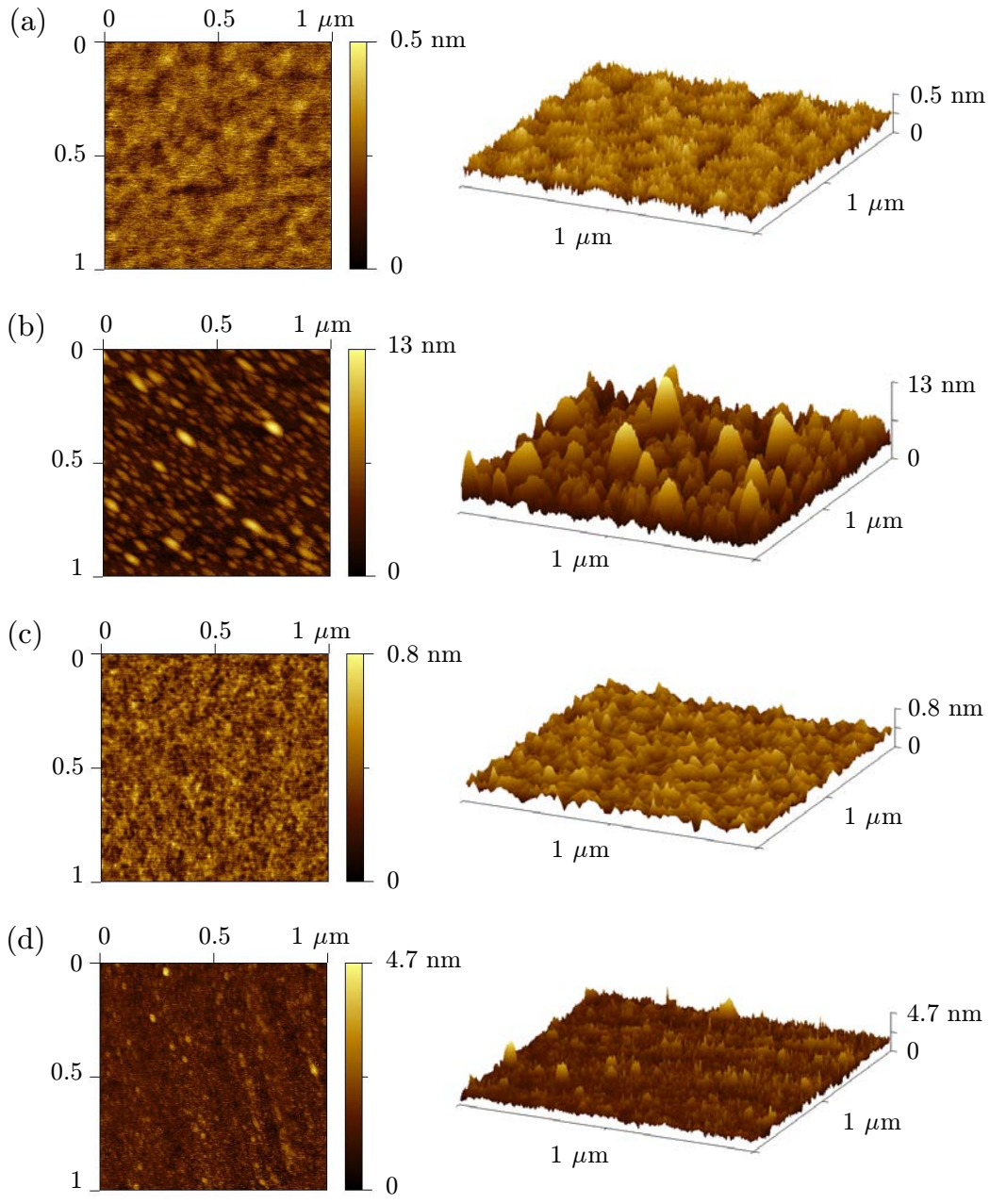

Fig. 3.29: Topography of a 10-nm Co layer measured by AFM in the non-contact mode: (a) – as deposited (RMS 0.1 nm), (b) – after 15 days in air (RMS 1.8 nm), (c) – after 15 days in 1×10^{-7} mbar vacuum (RMS 0.1 nm), (d) – after 46 days in air, capped by a 2-nm Al layer (RMS 0.4 nm).

The aluminium is more resistant to the atmospheric corrosion, as illustrated by Fig. 3.30. The topography of a 6-nm Al layer did not undergo any relevant surface changes. The RMS roughness almost did not change after 40 days of exposure to air (0.15 nm versus 0.12 nm) and after 10 months it reached 0.4 nm.

The interaction of the Co surface with oxygen and particularly air has been studied extensively [292, 293]. The early stage of the Co exposure to air results in the for-

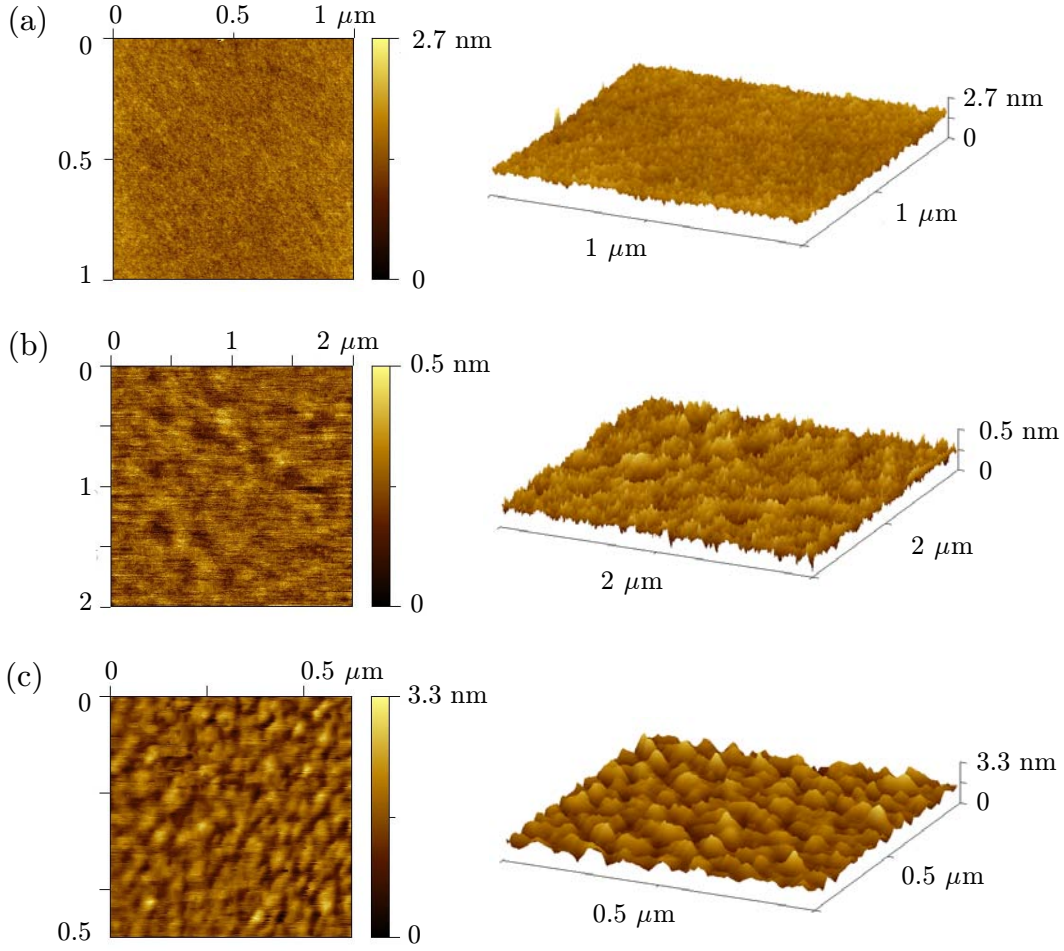

Fig. 3.30: Topography of a 6-nm Al layer measured by AFM in the non-contact mode: (a) – as deposited (RMS 0.12 nm), (b) – after 40 days in air (RMS 0.15 nm), (b) – after 10 months in air (RMS 0.4 nm).

mation of a very thin film (few monolayers) of a hydroxylated oxide ($Co(OH)_2$) and subsequently a CoO layer of several nanometers is formed [293].

In the following we compare the topography evolution of a Co layer oxidized by 1000 Pa of O_2 for 30 min after deposition (Fig. 3.31) to that of a pure Co layer (Fig. 3.29), both exposed to the air. Fig. 3.29(a) shows the oxidized layer after 6 days of exposure to the air, Fig. 3.29(b) after 9 days in the air. Keeping the sample in vacuum and subsequent exposure to the air confirmed that the corrosion needs a certain time of an initial phase to develop the bulge structure.

Although we do not possess the direct comparison after the same number of days[12], it is likely that the in-situ oxidized Co layer is less perturbed by the atmosphere than the pure Co layer. The difference might arise from the initial formation of $Co(OH)_2$ and generally a more pronounced water-vapor effect on the pure Co sample. The CoO_x

[12]The highest peaks of the bulges in case of the pure 10-nm Co layer reached more than 10 nm after 10 days.

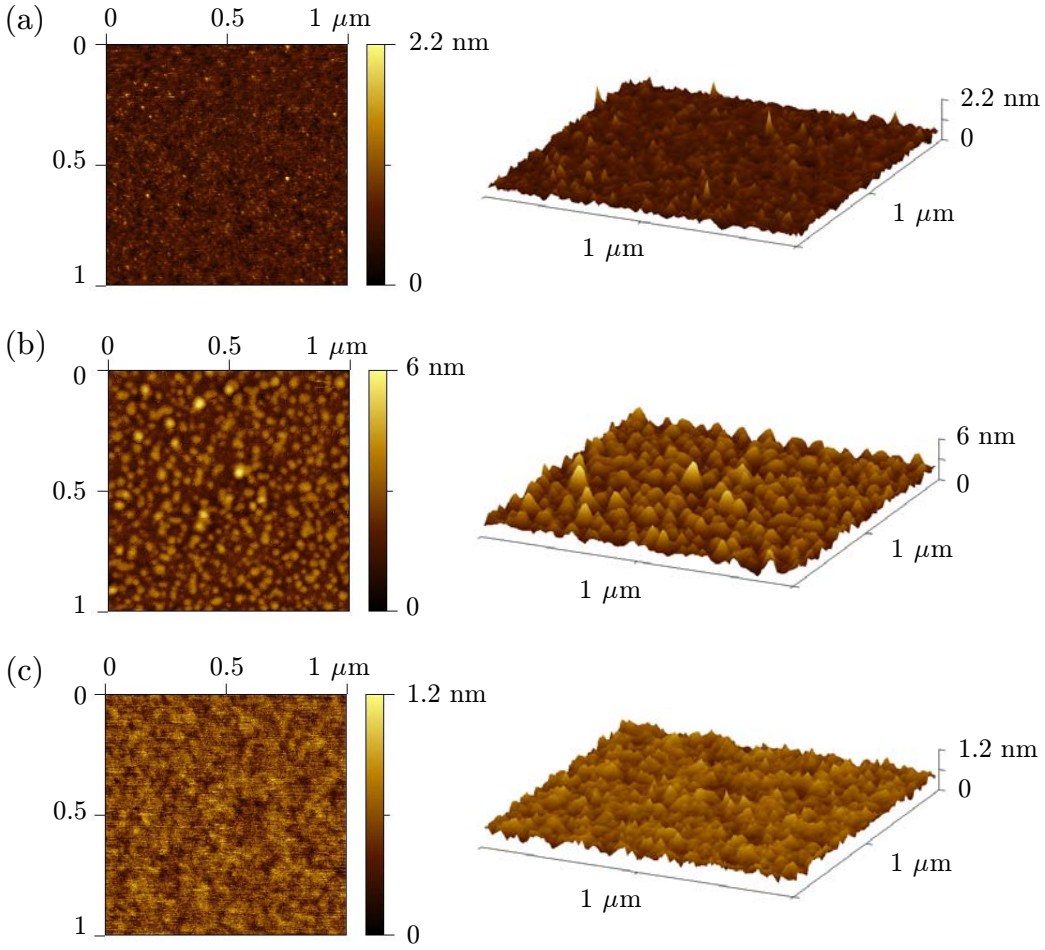

Fig. 3.31: Topography of a 10-nm in-situ oxidized Co layer measured by AFM in the non-contact mode: (a) – after 6 days in air (RMS 0.16 nm), (b) – after 9 days in air (RMS 0.92 nm), (b) – after 4 days in vacuum and 3 days in air (RMS 0.14 nm).

phase present on the in-situ oxidized sample probably slows down the corrosion of the layer in the ambient atmosphere. As the oxygen was introduced after pumping down the system to 5×10^{-7} mbar, the water-vapor content should be negligible with respect to the standard atmospheric conditions.

The nature of corrosion and especially the water-vapor effect stimulated an explicit test of the humidity influence. Indeed, the effect was particularly significant. Two samples, a 10-nm Co layer and a 10-nm Cu layer, were kept in a box with 100-% humidity. After 10 days the highest peaks[13] reached 40 nm [RMS 5.0 nm, Fig. 3.32(a)], substantially more than the sample oxidized in the air of approximately 40-% humidity (standard conditions).

Under the same conditions, the topography of the Cu layer is less affected [Fig. 3.32(b) – highest peaks 13 nm, RMS 0.8 nm], indicating a higher resistance of Cu layers to corrosion.

[13]Peak-valley distance.

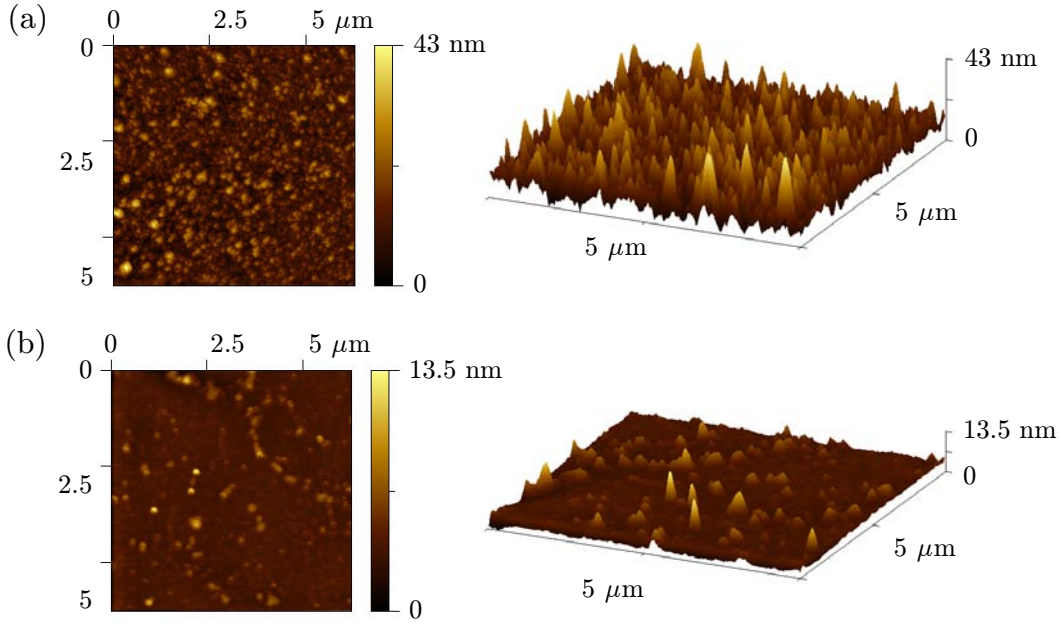

Fig. 3.32: Surface roughness of a 10-nm Co layer (a) and a 10-nm Cu layer (b) after the exposure to air with 100-% humidity for 10 days.

The corrosion processes were investigated basically in order to test the resistance of spin-valve structures to atmospheric conditions. It is known that for instance the UV light also accelerates the corrosion of thin films. We conclude that it is inevitable to protect the multilayer by noble metals like Au, but also Al or eventually Cu are utilizable. The choice depends on the purpose – in our study the material and thickness of the capping layer was adjusted to the magnetic imaging technique (Chapter 5). After lithography, patterned nanowires have to be kept under vacuum or covered with a resist layer to avoid degradation.

3.11 Discussion and Perspectives for Further Optimization

The general aim to maximize the GMR requires as thin Cu spacers as possible. However, in our structures, below 3 nm the magnetostatic interlayer coupling becomes significant and prevents the antiparallel alignment of the layers from being reached.

Without precise definition of the interfaces it is also difficult to control the RKKY interaction which is extremely sensitive to the spacer thickness. Egelhoff et al. [294] modified the layer growth by deposition at lower substrate temperature (150 K). Both the interdiffusion of the Cu and Co and the surface roughness were reduced and the interlayer coupling of the system FeMn/$Ni_{80}Fe_{20}$/Co/Cu/Co/$Ni_{80}Fe_{20}$/glass decreased to approx. 0.4 mT. This kind of system was also optimized by ion-beam sputtering [295] and compared to the dc magnetron-sputtered multilayers. The ion-beam-sputtered multilayers contained straight interfaces without waviness, although the GMR was

found lower than in the magnetron-sputtered ones.

High GMR in NiFe-Cu-Co systems, up to 20%, was achieved using multilayers [287] or up to 12% by adding a Co interlayer between the NiFe and Cu layers in double NiFe/Co/Cu/Co/NiFe sandwiches [257, 294, 295, 271]. GMR amplitudes similar to our work were found in magnetron-sputtered NiFe/Cu/Co sandwiches [289, 265], but these structures did not incorporate a capping layer. The only case reporting a higher GMR for a pure NiFe/Cu/Co sandwich at room temperature (6.5% [57]) incorporated an antiferromagnetic FeMn layer instead of a capping layer. This could play a role in specular back-scattering of the conduction electrons.

Low-energy ion-beam- assisted deposition has been already used to optimize Cu/FeMn/Co/Cu/Co/NiFe/Ta multilayers [296]. The ion energies of the simultaneous ion-beam bombardment of the substrate varied up to 20 eV. The highest GMR (7%) was obtained for a 33 Å thick Cu spacer. The assisting bombardment increased the GMR, yielding the maximum (9%) at an ion energy of 10 eV. At this energy the interlayer coupling was minimal, however reaching almost 20 Oe (2 mT).

In our case, using the IBAD technique we managed to decrease the interlayer coupling down to 0.1 mT for a Cu spacer of 3 nm and with an assisting ion energy of 50 eV. The nanowires patterned from these optimized continuous NiFe/Cu/Co sandwiches presented approximately 2-3× lower coercive fields in the direction transverse to the zigzags than the nanowires made from magnetron-sputtered films. They also featured a clear and sharp magnetization switching (see Appendix D). In the future, we will focus on reducing the magnetostatic coupling by ion-beam-assisted deposition while keeping the GMR at the original value or increasing it, and on determining the dependence of the interlayer coupling on the Cu spacer thickness.

It is worth noting that a part of the presented optimization was carried out before the quartz thickness-meter was installed in the IBAD chamber. This made the variations in deposition parameters difficult, because each time the deposition rate had to be recalibrated. At the moment the experimental options are much wider and depending on the final request (e.g. multilayers optimized for imaging by Photoemission Electron Microscopy, Chapter 5) one can further investigate:

1. Influence of the ion current, generated by the primary and secondary ion-beam sources.

2. Influence of the primary ion energy. This will change the energy distribution of the reflected Ar particles and the ion-to-atom arrival ratio.

3. Influence of the Ar implantation. Using a heavier sputtering gas, e.g. Xe. The flux of reflected Xe particles should be much smaller than of Ar ones and most of them will not encounter the substrate.

4. Grain size effect.

    - Parameter – ion current (constant pressure, variable discharge current).
    - Parameter – Ar pressure (constant ion current, variable discharge current).

5. Changing the order of the NiFe and Co layers.
6. Using FeMn or NiO antiferromagnetic layers.
7. Using magnetic field during the deposition to impose an easy axis, so that this direction will be better defined.

Chapter 4

PATTERNING OF MAGNETIC NANOWIRES

The experimental observation of current-induced DW motion requires current densities in the order of 1×10^{11} A/m^2. The first experimental studies by Berger and Freitas [120] and Gan et al. [179] used wires of a millimeter or micrometer widths[1], respectively, resulting in applied currents of 1-20 A. Although the current pulses lasted only 1-2 μs, the dissipated power was huge and often led to a local heating and electrical breakdowns of the wires. Moreover, the Oersted field at the wire edges, though antisymmetric with respect to the center of the wire, might increase enough to distort the DW and to modify its pinning potential. To avoid the heating effect and to isolate the spin-torque effect on the DW motion, the width of the wires has to be reduced to hundreds of nanometers. For this purpose we may employ various lithography techniques, including a combination of electron-beam and UV lithography or focused-ion-beam lithography.

4.1 UV and deep-UV Lithography

The optical lithography consists in the insolation of a photoresist by a UV lamp, through a mask partially transparent to the light. The resist is spread on a substrate by a spin-coating technique. The resist is a polymer sensitive to the UV light – it either increases (positive resist) or decreases (negative resist) the solvability of the exposed areas (see Fig. 4.1). After the exposure the areas having a larger solvability are removed by a developer. Some details concerning the recipes used for the fabrication of our patterns are described in Appendix E.

The quality of the pattern, the number of defects and the resolution depend on the type of the resist, the UV lamp power and the time of exposure, the material of the mask and the wavelength of the used UV light (200-400 nm). The lower bound is obtained with the so-called deep-UV (DUV) lithography which yields the best resolution of the optical lithography techniques. The smallest feature size achievable with the DUV lithography is approximately 500 nm using a chromium mask.

The optical lithography is thus not suitable for creating narrow nanowires of a width below 500 nm. In this work, it has been used to fabricate the alignment marks for electron-beam lithography, the Au/Ti electrical contacts for the magnetic nanowires, and for fast fabrication of micron-sized structures which are to be refined into nanowires using Focused-Ion-Beam etching (see Section 4.4).

[1]The thickness was in the order of tens of nanometers.

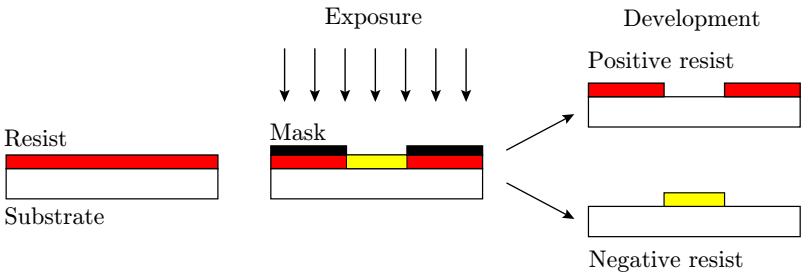

Fig. 4.1: Insolation of a resist using a mask. In case of a positive resist, the exposed areas are removed by a developer. The negative resist becomes harder upon exposure and remains on the surface after development.

4.2 Electron-Beam Lithography

This maskless technique consists in directly exposing a positive resist (generally PMMA – poly-methyl methacrylate) by an electron beam[2]. It is commonly used to fabricate features having lateral dimensions of the order of tens of nanometers. Its main drawback is that it is time-consuming due to the sequential scanning of the electron beam. It is thus suitable for the exposure of low-area features.

In the following two processing methods commonly used with both the UV and e-beam lithographies will be described.

4.2.1 Lift-off Technique

The basic lift-off technique is schematized in Fig. 4.2(a). The selected materials (in our case, the metallic multilayers) are deposited, either by evaporation or by sputtering techniques, on a developed resist pattern (PMMA for e-beam lithography). The resist is subsequently dissolved by a solvent whose composition depends on the resist type. The material deposited on top of the resist is removed and only the material deposited directly on the substrate will remain.

In this work, this technique has been regularly used for the fabrication of Au/Ti contacts and micrometric patterns for FIB, following the UV or DUV lithography. Our magnetic nanowires were initially prepared by lift-off techniques, both in the Laboratoire de Physique des Nanostructures in Marcoussis and at the Nanofab facilities in Grenoble.

In case the magnetic material is deposited by magnetron sputtering, which is a largely non-directional technique, it appeared that the edges of nanowires prepared by lift-off exhibited some remnants of the deposited material originating from the resist walls of the pattern. To avoid this, we tested the possibility to use a PMMA/MAA bilayer resist. Each resist features a different sensitivity to exposure and after development an undercut in the bilayer is formed [Fig. 4.2(b)]. Hence, the edges of the deposited pattern do not come into contact with the resist. Unfortunately, AFM measurements showed that in our case a homogeneous deposition over the nanowire

[2]The e-beam lithography might be an option of Scanning Electron Microscopes (SEM).

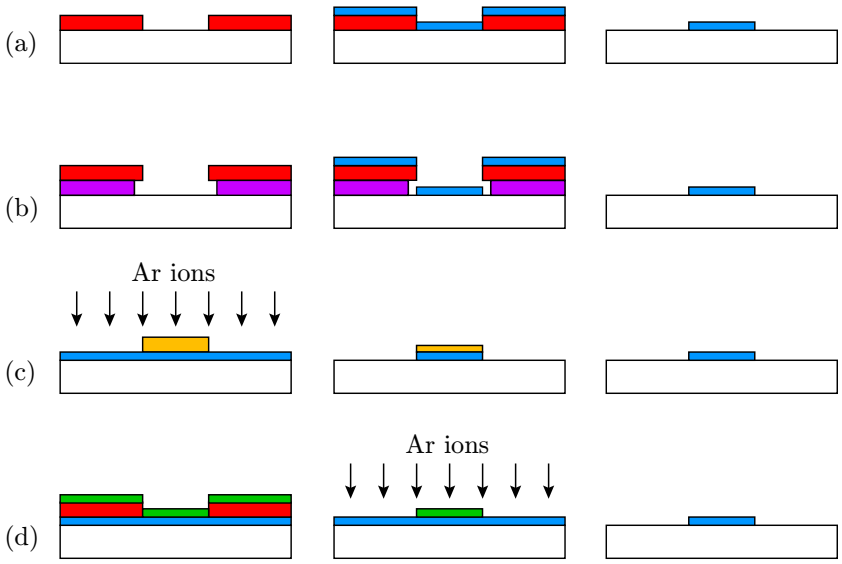

Fig. 4.2: (a) Standard lift-off technique. (b) Lift-off technique using a PMMA/MMA resist bilayer which forms an undercut after development. The edges of the pattern are not in contact with the resist. (c) Ion-Beam Etching technique using a resist mask. The resist remainder has to be removed by chemical solvents or oxygen plasma. (d) Ion-Beam Etching technique using a metallic mask which is prepared by a standard lift-off technique. Etching of the mask might be monitored by a SIMS signal of a reference layer.

width could not be achieved. For this reason the lift-off procedure was abandoned and nanowires were further patterned using Ion-Beam-Etching techniques.

4.2.2 Ion-Beam Etching Technique

The principles of Ion-Beam Etching (IBE) are shown in Fig. 4.2(c). The layer, in our case a magnetic spin-valve trilayer, is pre-deposited on the Si substrate. One option consists in creating a negative resist pattern on top of the magnetic layer by e-beam lithography. This resist pattern will act as a hard mask during the subsequent etching of the sample by a broad ion beam. The pattern is thus transferred to the magnetic layer. If the IBE system disposes of a SIMS detection, the atomic mass signal of the etched layer can be monitored and it serves to stop the etching as soon as the substrate is reached. The lateral roughness of the resulting structures is in general smaller than in the case of lift-off.

The main drawback that we found with this method is that the resist, hardened by the ion beam, is very difficult to remove from the top of the pattern. The remaining resist may be burned with an oxygen plasma but this method is not suitable for structures sensitive to oxidation as it is the case for our magnetic trilayers.

A different approach, which proved to be more reliable, consists in preparing a hard metallic mask (e.g. Ti or Al) on top of the magnetic layer, rather than a resist mask [Fig. 4.2(d)]. This mask is prepared by evaporation of the metallic layer on an e-beam patterned PMMA, followed by a standard lift-off process. Its thickness must be

calibrated so that its etching time is larger than the time needed to etch the magnetic trilayer. Two options are then possible for the etching process:

- The ion-beam etching is carried out while monitoring the mass signal of the magnetic layer. The process is stopped when the magnetic layer is fully etched away. The remainder of the mask (generally Al) can be chemically removed by developers (e.g. LDD-26W). In our case, the chemical treatment left many Al "flakes" in the surroundings of the structures and the procedure was abandoned as a solution could not be found.

- An alternative method to the chemical removal of the metallic mask after etching is to finely calibrate the thickness of the metallic mask, so that only a very thin (2-3 nm) layer is left on top of the pattern. A reference metallic layer (Ti in our case) whose thickness is calibrated so that its etching time is larger than that of the magnetic layer, is evaporated on a separate substrate. A metallic mask having a thickness 2-3 nm larger than that of the reference layer is deposited on the magnetic layer. The two wafers are then etched at the same time and the reference Ti mass signal is monitored. The process is stopped when the reference layer is fully etched. At this point, if the etching rate is homogeneous, when the etching is stopped only 2-3 nm of the metallic mask is left on the pattern. This method gave the best results, providing nanowires with lateral roughnesses of the order of 10 nm.

4.3 Sample Composition and Patterning

Composition The functional part of the multilayer stack is based on a NiFe/Cu/Co spin-valve structure where the DW motion is investigated in the NiFe layer. The multilayers were deposited either by magnetron sputtering (Cu 3 nm/NiFe 5 nm/Cu 8 nm/Co 7 nm/CoO 4 nm/Si 100, made in the laboratory of the CNRS-Thales group in Orsay) or ion-beam sputtering (Cu 3 nm/NiFe 5 nm/Cu 5 nm/Co 5 nm/CoO 3 nm/Si 100, made at the IPE in Brno). The layer configuration of choice will be indicated at each experiment (Chapter 6). The layers were deposited on highly resistive substrates (300 Ωcm) covered by a native oxide layer.

Patterning The layers were patterned into zigzag-shaped nanowires of widths 200, 300 and 400 nm using the techniques described in the previous section. Au 80 nm/Ti 20 nm electrical contacts were subsequently prepared by evaporation and lift-off. The lithography was carried out in the Laboratoire de Physique des Nanostructures in Marcoussis (in collaboration with G. Faini), at the Nanofab facility of the IN and at the PTA facility at the CEA in Grenoble.

The zigzag shape[3] [297, 298, 186] was initially chosen so that DWs could be created at the corners under the application of a strong-enough magnetic field perpendicular to the longitudinal axis of the zigzag [see Fig. 4.3(a),(b)].

[3]Although more simple geometries like L shapes are possible to achieve the same result [184], the

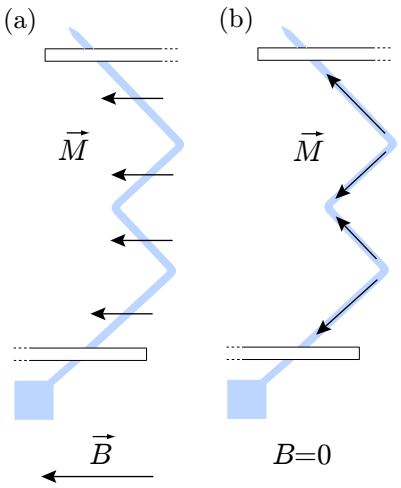

Fig. 4.3: (a) Sketch of a magnetic zigzag nanowire (blue) under applied magnetic field. (b) In zero field the magnetization relaxes along the sections of the nanowire because of the shape anisotropy.

This method should in principle allow a highly reproducible DW creation and thus should be suitable for pump-probe experiments. However, quite a high magnetic field is needed to overcome the shape anisotropy of the zigzag sections. For this purpose one end of the nanowire is connected to a square-shaped pad [Fig. 4.3(a)] which serves as a DW injector [299]. Due to its reduced shape anisotropy, a lower field is required for DW nucleation in the pad. The function of the square-shaped pad is only fullfiled when a magnetic field is applied along the longitudinal axis of the zigzag. The other end of the nanowire is terminated by a tip end which attracts the DWs to the narrower part and annihilates them [300].

We will see in the experimental part (Section 6.3.1) that because of the strong pinning of DWs by sample defects, the configuration with saturated magnetization along each zigzag section is not always obtained and a multidomain configuration is most often found.

The final layout of the contacts and the nanowires is presented in the SEM images of Fig. 4.4. One sample consists of six nanowires of different widths connected in parallel to a common ground.

4.4 Focused Ion Beam

Patterning of nanowires by focused ion beam (FIB) has been reported less often in literature although this technique offers a lot of advantages [301, 302]. The main advantage of this method compared to usual lithography techniques is a maskless one-step process based on direct ion-beam writing, i.e. transferring a pattern by impingement of the focused ion beam onto a sample. The FIB direct writing can combine a series of techniques such as milling, implantation, ion-induced deposition and ion-assisted

zigzag geometry allows to create more DWs.

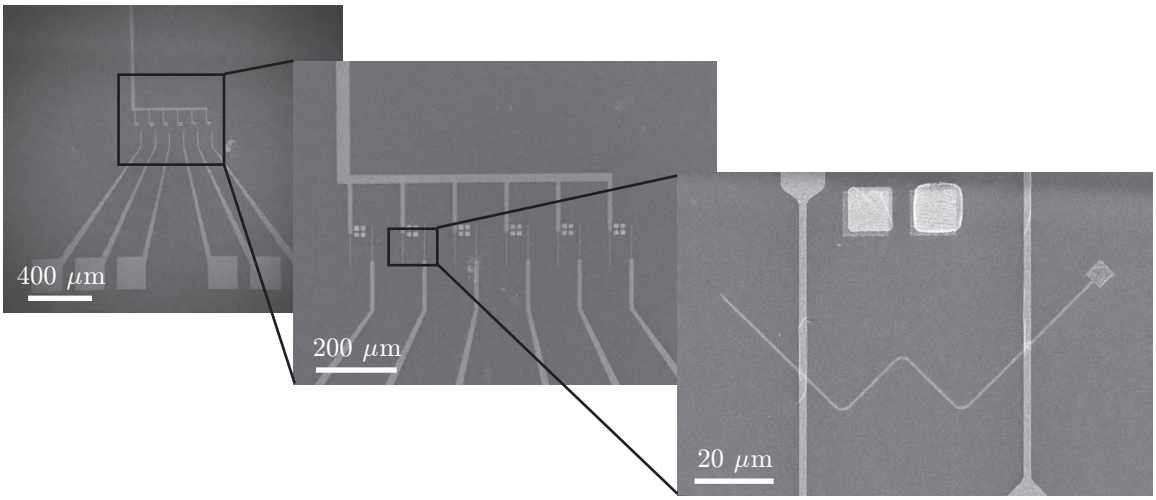

Fig. 4.4: SEM images of the layout of the contacts and the nanowires. Two squares in the down-right close-up represent alignment marks for DUV lithography.

etching. A schematic of a FIB instrument combined with a SEM ("dual-beam set-up") is shown in Fig. 4.5(e).

FIB-induced chemical vapour deposition (FIB-CVD) is a very convenient option for the fabrication of our nanowires, as it enables to make the electrical contacts just after the milling. Moreover, the place where the contact will be deposited can be locally etched to remove an oxide layer, if present. The deposition principle is based on a local decomposition of an organometallic precursor which is injected on the substrate by a heated nozzle [Fig. 4.5(f)]. The impinging ions decompose the adsorbed precursor to volatile compounds and to a metallic part which remains on the surface.

Ion milling or deposition of metals on larger areas (i.e. larger than approximately $30\times30\,\mu m^2$) is time-consuming and a drift of the sample deteriorating the pattern quality occurs very often. To surpass these limits, we proposed a pre-fabrication of a region to-be-etched and making macroscopic contacts by two-step UV lithography [Fig. 4.5(a)-(c)]. The structures shown in the images represent a first test of the procedure feasibility and a care for obtaining well-defined shapes was not taken. The arbitrary-shape structure in the center of Fig. 4.5(c) is a NiFe/Cu/Co trilayer which is subsequently milled to a nanowire of a 400-nm width and connected to Au macroscopic contacts by Pt bridges by FIB-CVD [Fig. 4.5(d)].

The resistance of these bridges is influenced by residual carbon and a heat treatment is necessary to increase the Pt conductivity. The structure shown in Fig. 4.5(d) presented a resistance of 1.6 kΩ, comparable to the resistances of the structures prepared by e-beam lithography. In future developments, a use of Au[4] bridges is planned.

[4]Au precursors were not commercially available at the time of the sample fabrication.

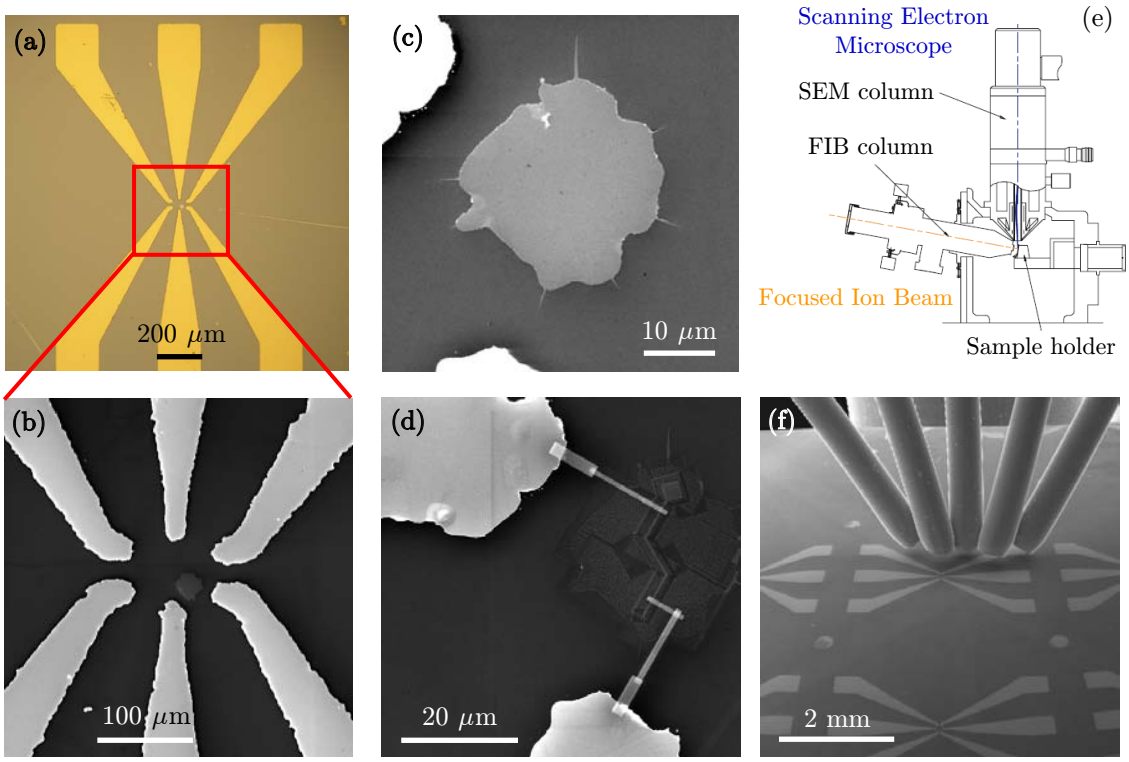

Fig. 4.5: (a) Optical image of the pre-fabricated NiFe/Cu/Co area (the small spot in the middle of the red square) and macroscopic Au contacts. (b),(c) SEM details of the pre-fabricated structures. (d) 400 nm wide nanowire milled by FIB connected by FIB-CVD-deposited Pt bridges to the Au contacts. (e) Schematic of the dual-beam FIB-SEM instrument. (f) Nozzles for introducing different precursor gases to the proximity of the surface.

4.4.1 Etching of Co Films

As shown in the previous section, FIB is very advantageous in research and rapid prototyping applications. However, a series of drawbacks needs to be overcome. For instance, residual roughness of a milled surface, which is also transferred into the edges of fabricated structures, can lead to DW pinning or implantation of Ga^+ ions from the tail of the Gaussian-shaped ion beam, causing a degradation of the functional properties of the structures [303, 304]. This section deals with such problems and suggests methods to reduce them. The results of this section were obtained in collaboration with M. Urbánek, who has carried out most of the experimental work.

When 30-keV Ga^+ ions hit the surface of a magnetic film, they penetrate into a depth of approximately 5–40 nm. On their way through the film, the ions lose their energy due to interactions with target atoms and form collision cascades [305]. If sufficient energy is provided to an atom through such collisions, it can overcome the surface binding energy and escape from the sample, i.e. it can be sputtered away. The ratio of atoms sputtered per one incident ion for given ion beam parameters is a statistical property of the material and is called the sputter yield (atoms/ion). Ideally, there should be a linear relationship between the ion dose and the sputtered volume.

However, in the sputtering process several additional parameters and effects take place and must be considered.

1. *Variance in the local angle of incidence.* The sputter yield increases with the incidence angle (measured from the surface normal) up to 80° and then rapidly drops. When milling inhomogeneous and rough surfaces, the varying local incidence angle causes an uneven milling rate over the sample surface. This results in further evolution of surface morphology and leads to surface rippling [306, 307].

2. *Channelling.* When milling polycrystalline thin films, the sputter rate depends on the crystallographic orientation of grains with respect to the incident ion beam. At certain orientations, ions easily channel deep into the material, thus making it less probable that the collision cascade bounces out atoms. This causes a relative decrease of the sputter yield in grains where the channelling can occur in comparison with those where channelling is less dominant [308, 309].

3. *Ion-induced grain growth (recrystallization).* Ion irradiation leads to a grain growth in polycrystalline thin films [30]. The grains oriented in favor of channelling can increase in size under 30-keV FIB bombardment [310].

4. *Redeposition.* As the sputtered atoms are not in their thermodynamic equilibrium state, they tend to condense back into the solid phase after their collision with any nearby surface. The redeposition can be affected by the scanning strategy (one pass versus multiple passes), scanning pattern (e.g. raster versus spiral), shape (aspect ratio) of the milled structures [311], dynamics of ejected atoms and the sticking coefficient of the target material.

In experiments, samples consisting of 5-30 nm thick Co thin films prepared by ion beam sputtering on Si(100) substrates covered by a ∼3 nm layer of native SiO_2 were used. Fabrication of nanostructures based on the complete removal of a magnetic layer was made by a FIB/SEM system (Tescan Lyra). An ion energy of 30 keV has been used for all experiments in order to obtain the highest possible lateral resolution together with the high sputter yield. The $20\times20\,\mu m^2$ field of view was chosen for milling of the structures. Ion beam parameters have been set to the following default values: incidence angle 0°, dwell time 0.8 μs, probe current 8.7 pA (spot size approximately 10 nm) and overlap 1 (Fig. 4.6). All parameters have been gradually varied (one at a time per each test structure) and consequently the roughness of the bottom of the milled areas was measured by AFM (NT-MDT Ntegra, contact mode).

Our metallic thin films prepared by ion beam sputtering deposition have polycrystalline structure with a grain size of approximately 8-10 nm (see Section 3.8). As can be seen in the FIB image [Fig. 4.7(a)], there is a big contrast between various groups of grains of the thin film, due to the channelling effect. The grains where the crystallographic orientation allows channelling are black and the grains where no channelling occurs are imaged as white. The channelling causes uneven sputtering over the sample surface, which results in the development of a rough surface. After application of an ion dose higher than $0.01\,nC/\mu m^2$ the grains become visible also in SEM images [Fig. 4.7(b)] due to the topographic contrast.

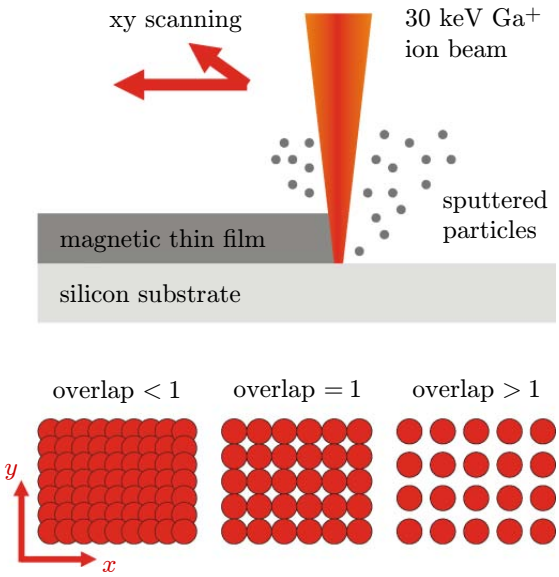

Fig. 4.6: Schematic of the FIB milling. A 30-keV Ga^+ ion beam is focused to a spot $\geq$7 nm and is scanned across the selected areas of the surface. The beam current, duration at each impact spot (dwell time), distance between the impact spots (overlap) and the angle of incidence of the ion beam can be independently controlled.

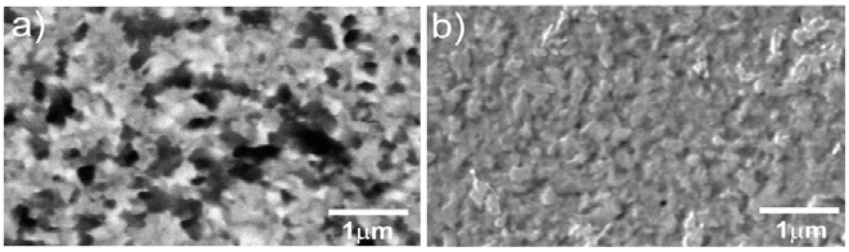

Fig. 4.7: (a) FIB image (secondary-electron detector) of a virgin 30-nm cobalt thin film showing a channelling contrast caused by different crystallographic orientations of grains. (b) SEM image of a Co thin film after irradiation by an ion dose of 0.024 nC/μm^2. The arrow points to the dark hole with round edges indicating reaching the Co/Si interface.

In Fig. 4.8, the time evolution of the milling process is shown. A 30-nm Co thin film on a Si substrate has been irradiated step-by-step with an increasing ion dose and the bottom of the milled surface has been subsequently measured by the AFM. In the first stages of milling, where only the cobalt thin film is affected, the sputter rate decreases at the grains where ions can channel deeper under the surface and the resulting milled depth is lower. The sputter yield at grains where no channelling occurs is approximately two times higher [Fig. 4.8(a) and (b)]. The difference in the sputter yield for various grain orientations causes the topography of the milled surface to partially replicate the grain structure of the thin film. The grain structure is also changing with an increasing ion dose (and the depth of milling) due to the ion-induced grain growth and topographical inhomogeneities leading to a variance in the local angle of incidence.

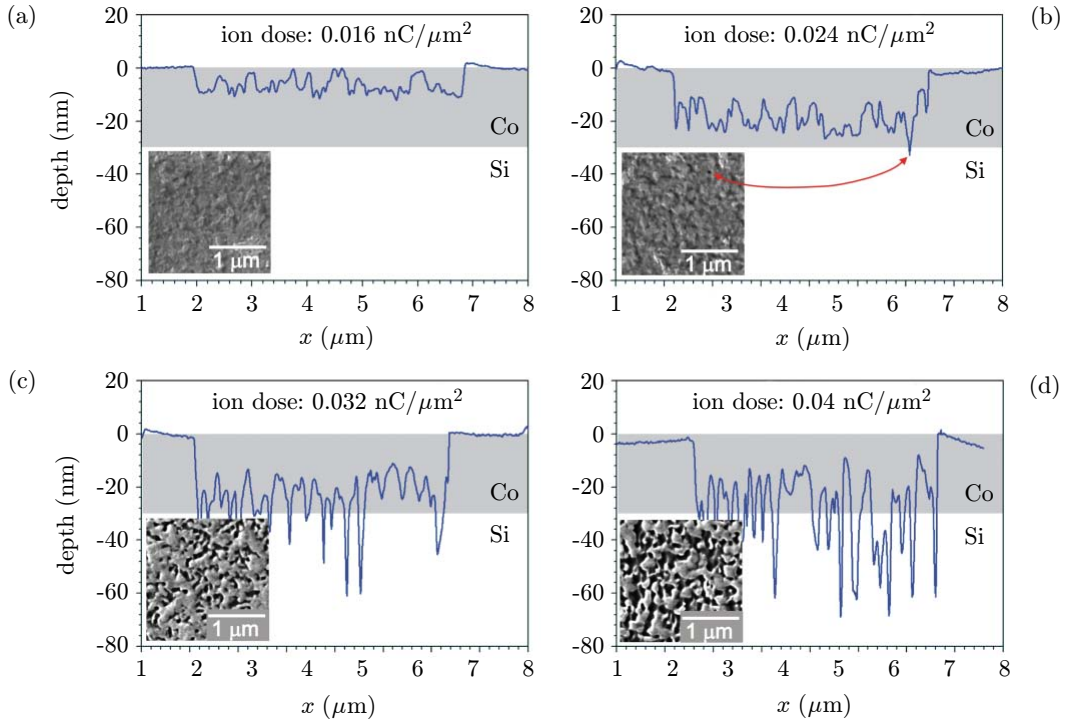

Fig. 4.8: Milling a 30-nm Co thin film by 30-keV Ga^+ ions, at the normal incidence angle. AFM profiles together with corresponding SEM images of the milled surface after ion irradiation with an increasing ion dose are shown. (a) Only the thin film is affected – the roughness profile follows the grain distribution in the thin film. (b) Co/Si interface is reached, the first evidence of the ripples is shown by the red arrows. (c), (d) Further evolution of the ripple structure.

A single-crystalline silicon substrate does not exhibit variable sputter yields caused by channelling through the grains. However, the topography of the sputtered cobalt layer significantly influences the milling of the silicon substrate. The milling is driven by the following effects: valleys and pits are milled faster due to the focusing effects of their sidewalls – most of the Ga^+ ions are reflected forward when they hit the almost vertical sidewalls, i.e. they are aiming towards the bottom of the milled structures. This creates deep narrow holes, as can be seen in Fig. 4.8(c) and (d). Another effect leading to a random ripple pattern is the angular dependence of the sputter yield. The sidewalls of the milled structures, which are not steep enough to reflect Ga^+ ions (for sidewall angles smaller than 80°), are milled faster than the elevated sites where ions hit the surface perpendicularly. The redeposition also takes place here, as the atoms sputtered from the trenches and pits can redeposit at the edges and further slow down the milling of the elevated areas. All these effects are also responsible for an increase of the roughness at the polycrystalline metal/single-crystal silicon interface.

The evolution of the milling process described for the 30-nm Co thin film on the silicon substrate was also observed in the milling of other metallic thin films (Co, Cu, Al, NiFe) and multilayer structures (NiFe/Cu/Co spin-valves) prepared by ion-beam sputtering and having thicknesses ranging from 5 to 50 nm and more.

Influence of FIB Parameters on Surface Roughness

The parameters of the ion beam have been varied in order to determine their influence on the milling process and to find the optimum values for suppression of the effects of surface roughening caused by the ion channelling. A detailed study can be found in a publication [312]. In the following the main results are summarized.

The selected *Ion-beam current* is in a direct link with the spot size and influences the milling speed. Both characteristics increase with increasing the current. For the fabrication of typical spintronic nanostructures (Co or NiFe thin films, milled area $20\times20\,\mu\mathrm{m}^2$, depth 20 nm) the milling time is a few minutes even for the lowest currents, so there is no need to use high currents (>100 pA) resulting in large spot sizes. Slightly higher currents with somewhat larger spot sizes (e.g. 36 pA, spot size ∼15 nm) do not result in an increase of roughness in depths smaller than the thickness of the thin film [312].

The biggest improvement in surface smoothness occurs when the *overlap* is approximately 0.7. At this overlap, the homogeneity of the ion dose areal distribution is 99% (assuming a Gaussian beam shape). These results correspond to studies made on silicon [311].

Another parameter influencing the milling process is the *dwell time* (the time defining how long the ion beam stops at each pixel). In our experiments, the dwell time ranged from 1 to 150 μs. We have not observed any dependence of roughness on the dwell time. However, we have observed an increase in the sputter yield for longer dwell times. For a given ion dose (pC/$\mu\mathrm{m}^2$), we have compared the sputter yield ($\mu\mathrm{m}^3$/nC) when the structures were milled at 10× shorter dwell times and the ion beam was scanned 10× over the milled structures (in order to keep the ion dose constant) to that of a single-scan milling. It turns out that the average value of the sputter yield for the longer dwell time was bigger by 30% than the integral one of the shorter dwell times, in the case of perpendicular ion-beam incidence. For an ion-beam angle of 55°, the difference was 10% [312].

The most influential parameter is the *angle of incidence* of the ion beam. The sputter yield increases with increasing angle. At an angle of 55° the sputter yield is 3.5× higher than at 0°. Such an increase of the sputter yield combined with an increase caused by longer dwell times can be used to minimize unwanted damage caused by collision cascades and Ga implantation.

Besides the increased sputter yield, the angle of incidence of the ion beam has a strong influence on the surface roughness. The effect of different sputter yields at different grains of the thin film, resulting in enhanced surface roughness, is suppressed due to shielding of the milled valleys and pits by surrounding protrusions. By milling the structures at a tilted angle it was possible to reach a substantial improvement in their quality [Fig. 4.9(a),(b)]. Dependence of the surface roughness on the angle of incidence can be found in [312]. Fig. 4.9(c) shows a NiFe/Cu/Co nanowire milled according to the optimum parameters together with FIB-CVD-deposited platinum contacts.

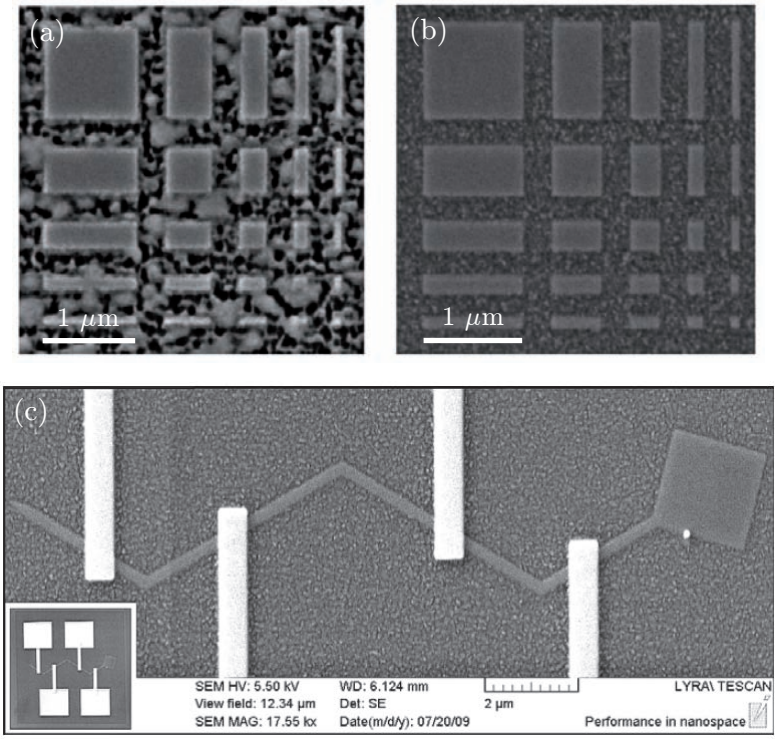

Fig. 4.9: SEM images of patterns milled into a 30-nm NiFe thin film by the 30-keV Ga^+ ion beam: (a) perpendicularly, (b) at an angle of 55° to the surface normal. Widening of the horizontal lines caused by tapering and undercutting of the edges due to the oblique ion beam incidence is noticeable. (c) NiFe/Cu/Co nanowire of a 200-nm width and 16-μm length with FIB-deposited Pt electric contacts.

Influence of Ga Implantation on Magnetic Properties of Nanostructures

The tail of the Gaussian beam extends to 100 nm in diameter even for the smallest spot sizes (<10 nm) [313] and can cause deterioration of magnetic properties at the borders of the milled structures. Typically, the ion doses needed to destroy the magnetic properties of, for instance, Co thin films are quite high, of the order of $10^{-12}\,\mathrm{C}/\mu\mathrm{m}^2$ [313, 314], which is above the dose introduced by the tail of the Gaussian beam during the removal of a 30-nm thin film. However, magnetic multilayers can be generally more sensitive due to the interlayer mixing caused by collision cascades [313, 303, 315].

Ga ion irradiation might have several consequences on the magnetic properties of nanowires – e.g. the magnetization on the edges could be suppressed. It might have also positive results – the pinning of DWs would be lower due to a disorder introduced by the impinging Ga ions [316].

From the high-resolution PEEM magnetic imaging (a surface-sensitive technique described in Chapter 5) we have deduced that the irradiation does not destroy the spontaneous magnetization in the sample as a strong magnetic domain contrast was still present in the images (not shown). However, the exact influence of ion irradiation has to be investigated before carrying out a quantitative analysis of DW motion in FIB-prepared nanowires.

Part III

CURRENT-INDUCED MAGNETIZATION REVERSAL

Chapter 5

MAGNETIC IMAGING BY XMCD-PEEM

X-ray Magnetic Circular Dichroism combined with Photoemission Electron Microscopy (XMCD-PEEM), together with other x-ray microscopy techniques, has shown itself to be an extremely powerful technique to visualize the magnetic configuration of thin films [317] and nanostructures [318, 319, 320, 186]. The time structure of the synchrotron radiation brings a possibility to perform dynamic experiments, i.e. to resolve the magnetization dynamics in the time domain [319, 320, 321, 353].

It also offers high sensitivity, $10^{-5}\,\mu_{\mathrm{B}}$ [322], i.e. thin films down to 1 monolayer (ML) can be probed. Moreover, its elemental specificity enables different materials to be imaged selectively [317]. Spatial resolution below 20 nm (for high-resolution PEEM, corrected for aberrations) and temporal resolution shorter than 50 ps (depending on the synchrotron radiation source) can be reached.

Our study aims to direct imaging of DWs and their displacement by this technique and brings substantial information in addition to transport experiments carried out for spin-valve nanowires.

5.1 X-ray Magnetic Circular Dichroism

The most simple model of x-ray absorption is based on a photon-dipole interaction within the single-electron model. In the dipolar approximation the effective interaction cross-section is given by the Fermi golden rule which reads

$$W_{\mathrm{abs}} \propto \sum_{\mathrm{q}} \left|\langle \Phi_{\mathrm{f}} \left| \vec{e_{\mathrm{q}}} \cdot \vec{r} \right| \Phi_{\mathrm{i}} \rangle\right|^2 \delta\left(E_{\mathrm{f}} - E_{\mathrm{i}} - \hbar\omega\right). \tag{5.1}$$

The first term on the right is a square modulus of the matrix element of the interaction operator of the electromagnetic field with the electron of the absorbing atom. $\vec{e_{\mathrm{q}}} \cdot \vec{r}$ is the dipolar operator, $\vec{e_{\mathrm{q}}}$ is a unit polarization vector (with q=0, ± 1); Φ_{f} and Φ_{i} are respectively the final and initial state of the absorbing atom. The function δ describes the energy conservation.

During the interaction of a circularly polarized wave with the bound electron, the total angular momentum is conserved and the selection rules imply that transitions are possible only between the states for which the angular momentum differs by 1: $\Delta m_l = \pm 1$ and $\Delta m_s = 0$. Moreover, x-ray wavelengths provide element specificity, arising from the characteristic binding energies of the atomic core electrons [323], i.e.

different materials can be probed by tuning the x-ray photon energy to the desired element-specific absorption edge.

The most used absorption edges in magnetism probe the final states responsible for magnetic properties: the $L_{2,3}$ edges of $3d$ transition metals ($2p \rightarrow 3d$ transitions) and the edges $M_{4,5}$ of rare-earth metals ($3d \rightarrow 4f$ transitions).

As presented in Section 1.1.3, the density of states of a magnetized metal exhibits splitting of the valence energy bands, leading to different populations of spin-up and spin-down electrons at the Fermi level. This difference, which is proportional to the magnetic moment, can be probed by the X-ray Magnetic Circular Dichroism (XMCD). The dichroism is generally defined as the difference in absorption of right- (RCP) and left-circularly polarized (LCP) light. In the case of x-ray dichroism it results from the fact that:

- the number of excited core-level electrons with a given spin which depends on the light polarization and the sign of spin-orbit interaction at the initial level,
- the absorption of an electron in spin-split magnetic bands is spin-dependent.

5.1.1 XMCD at the $L_{2,3}$ Absorption Edges of $3d$ Transition Metals

L_2 and L_3 absorption edges of $3d$ transition metals have different energies due to the fine structure of $2p$ levels originating from the L-S coupling [the spin-orbit interaction, see also Fig. 5.1(a)]. The angular momentum associated to the circularly polarized wave interacts with the spin of the excited electron also through the spin-orbit interaction. It can be shown that at the L_3 edge LCP x-ray photons excite 62.5% spin-up electrons and 37.5% spin-down electrons. At the L_2 edge the situation reverses, LCP photons excite 25% spin-up electrons and 75% spin-down electrons [324]. RCP photons induce inverse proportions of excited spins at the two edges. As the dichroism is defined as the difference between the absorption of the RCP (angular momentum $-\hbar$) and LCP ($+\hbar$) light, it is thus opposite for the L_3 and L_2 edges [Fig. 5.1(b)].

The excited electrons are promoted to the magnetically split $3d$ band. In the simpler case of Ni or Co, the majority (spin down) band is completely occupied and only spin-up electrons can realize the transition (since spin flips are forbidden in X-ray absorption). It means that at the L_3 absorption edge the RCP photons will be much less absorbed than the LCP photons, as they excite more spin-down electrons for which there are no free states in the $3d$ band. The opposite occurs at the L_2 edge.

The quantization axis of the magnetic band is given by the magnetization direction. The size of the dichroism effect scales as $\cos\Phi$, where Φ is the angle between the direction of photon propagation (defining the photon angular momentum) and the magnetization direction. The maximum dichroism (absorption difference) is observed for their parallel and antiparallel orientations [Fig. 5.1(b)], whereas for the perpendicular directions the difference is zero for both magnetization orientations. In absorption spectroscopy it is equivalent whether the photon polarization is changed and the magnetization direction is kept fixed or whether the magnetization direction is changed

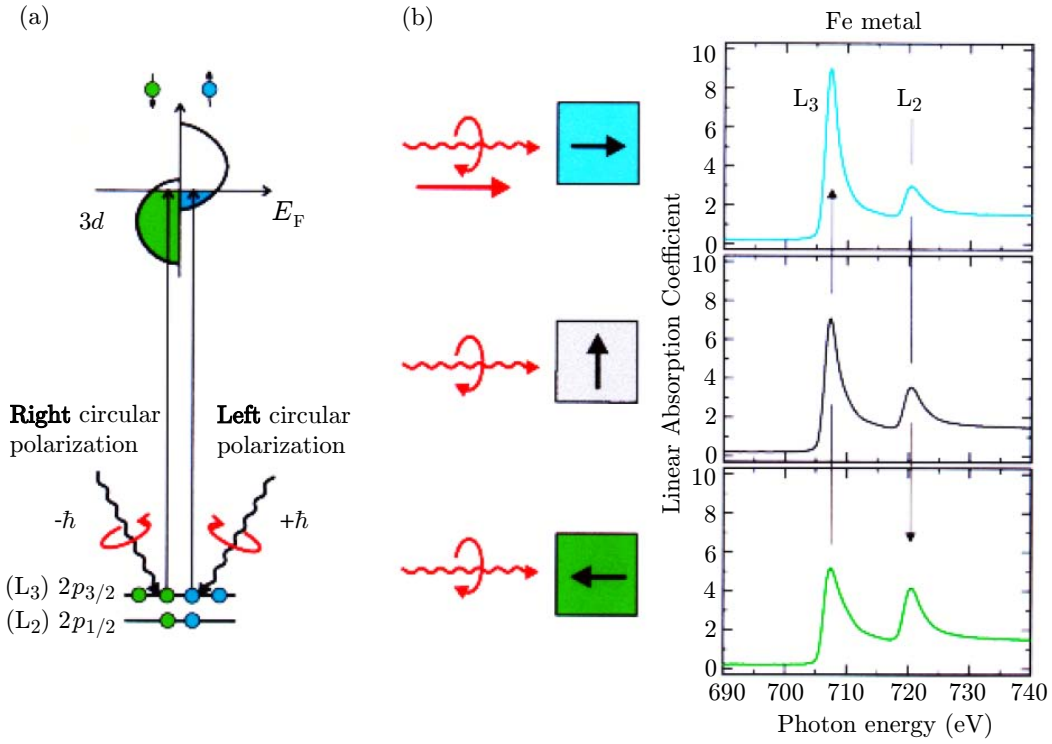

Fig. 5.1: (a) Absorption of circularly polarized X-rays in a $3d$ transition metal at the L_3 edge. (b) X-ray absorption for a fixed X-ray polarization (RCP) and different relative orientations of the magnetization and the propagation direction of the photon (center). An example for Fe metal is shown (right). The figure is taken from [323].

and the photon helicity is fixed [323]. This means that the XMCD signals obtained for magnetic domains of opposite magnetizations will be opposite.

Note that two sum rules have been developed to relate the amplitude of the XMCD signal to the spin and orbital momenta of the $3d$ states. The sum of the XMCD values at the L_3 and L_2 edges is related to the orbital momentum [325] while the difference is related to the spin momentum [326].

5.1.2 Sources of Circularly-Polarized Photons

As explained above, XMCD experiments require polarized x-ray photons which can be obtained at the synchrotron radiation sources where electrons circulating around the storage ring emit electromagnetic radiation. Initially the polarized x-rays were produced in bending magnet devices, where linearly polarized radiation is emitted in the plane of the electron circulation and circular polarization below and above this plane [1, 322, 323]. However, the beam intensity out of the circulation plane decreases significantly.

The main characteristics of the third generation synchrotron radiation sources is the use of insertion devices in the straight sections of the storage rings [327]. These devices typically consist of permanent magnet arrangements which cause oscillations of the electrons. “Wigglers” use high magnetic fields and large oscillations amplitudes.

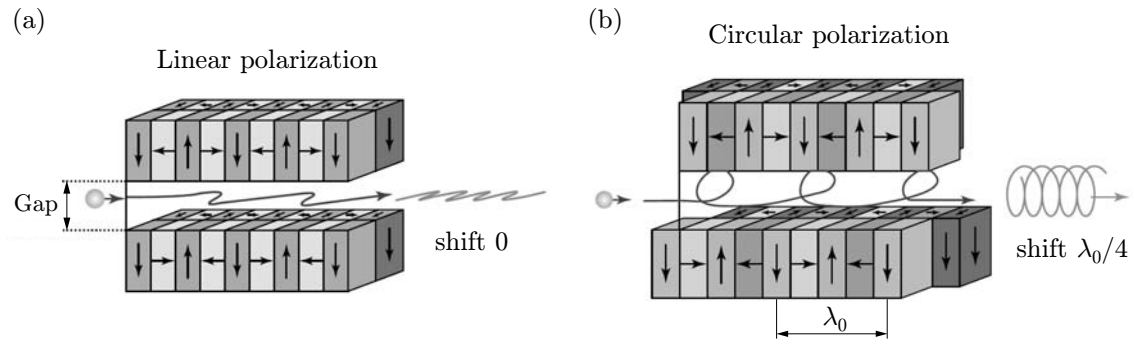

Fig. 5.2: Helical undulator configuration. The x-ray polarization is directly connected to the radiating electron trajectories, defined by the arrangements of permanent magnets. Arrangements to form linear (a) and circular (b) polarizations are shown. Reproduced from [322, 327].

The radiation interferes incoherently and it is unpolarized. It is used in cases where high flux is needed. "Undulators", which we used in our experiments, modulate the electron motion in a well defined way so that both a linear [Fig. 5.2(a)] or a circular [Fig. 5.2(b)] polarization can be obtained by adjusting the horizontal shift of the magnet arrangements. The vertical gap (Fig. 5.2) that defines the magnitude of the magnetic field has to be adapted according to the desired x-ray photon energy.

5.2 XMCD-PEEM Imaging

In thin films, x-ray absorption is in general not obtained directly by measuring the transmitted x-ray intensity, but indirectly by measuring the total electron yield. The x-ray absorption results in empty core-level electronic states [Fig. 5.3(a)] which are filled by electrons relaxing from higher energy levels [Fig. 5.3(b)]. The relaxed energy is provided to Auger electrons which are emitted out of the atom and subsequently cause a secondary-electron cascade which is proportional to the x-ray absorption.

The total number of secondary electrons emitted from the material for a fixed circular polarization enables us to obtain a map of the magnetization in the sample. See for instance Fig. 5.4(b): in a square element with a close-flux domain structure, the domains with a magnetization parallel to incoming X-rays will absorb more photons and therefore emit more secondary electrons (bright signal) than in the antiparallel case (dark signal). The intermediate intensity will be found for domains with a magnetization perpendicular to the incoming X-rays.

The device used for such magnetic imaging is called a Photoemission Electron Microscope [see Fig. 5.4(a)]. The secondary electrons are extracted by the objective lens kept at a high potential (4 – 12 kV in our Focus IS-PEEM[1]), focused and expanded by a set of projection electrostatic lenses. The image is formed on a fluorescent screen combined with a microchannelplate and captured on a CCD[2] camera. A spatial resolution below 100 nm could be achieved, being limited in particular by the extraction

[1]Manufactured by Focus, supplied by Omicron NanoTechnology GmbH.
[2]Charge-Coupled Device.

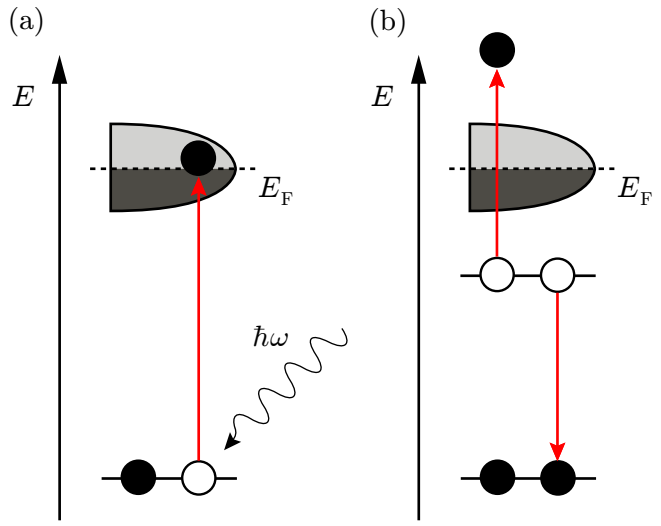

Fig. 5.3: (a) Excitation of an electron by an x-ray photon with the energy tuned to the desired electronic transition. (b) Relaxation of the excited state and emission of an Auger electron. Reproduced from [328].

voltage and the aberrations:

- *Spherical aberrations*, caused by the imperfections of the lenses. These could be corrected to some extent by inserting a contrast aperture in the electron optical path, thus reducing the number of off-axis electrons in the focal point. At present special set-ups with correction mirrors and filters allowing resolution increase below 10 nm are under development [330, 331].

- *Chromatic aberrations*, caused by the wide range of secondary electron energies (Fig. 5.5). When using a mercury UV lamp, the photon energy is just enough to provide the work function and to emit the electrons out of the material. However, X-rays can excite core electrons and the energy of secondary electrons is therefore wide-spread. In the case of X-ray illumination, the distribution of secondary electrons in Fig. 5.5 was approximated by Tonner and Dunham [329]: $n_e = \frac{E_K}{(E_K+\phi_w)^4}$, where ϕ_w denotes the work function of the material and E_K kinetic energy of the secondary electrons. In some PEEMs, energy filtering can be used to reduce the chromatic aberrations [332].

Photoemission electron microscopy is a surface-sensitive technique. Absorption length[3] of X-rays in Fe, Co and Ni depends on the exact photon energy. It is approx. 500 nm before the edge, 20 nm at the L_3 edge and 80 nm above the edge [1]. However, the main reason for the surface sensitivity is a low extraction depth of secondary electrons. 1/e electron yield depth is approx. 2-3 nm for Fe, Co and Ni [333], meaning that 63% of the electrons come from the region down to this depth.

The fact that PEEM exploits electrons for imaging may cause a shift in the image when applying magnetic field to the sample during the measurement. In our experi-

[3]Distance in a material at which the intensity drops to 1/e of the original value.

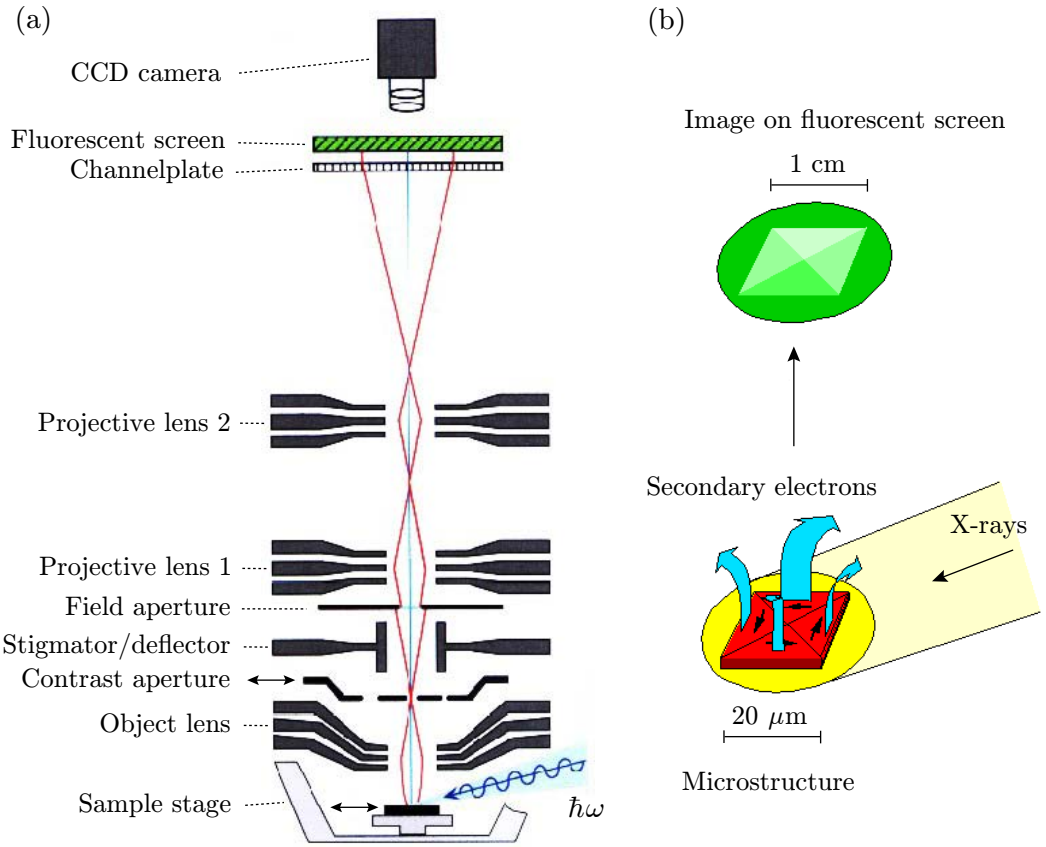

Fig. 5.4: Schematic view of the internal configuration of the PEEM microscope (a). The incident X-ray beam excites secondary electrons which form a magnified XMCD absorption image on the fluorescent screen and CCD camera (b). The original figures were designed by W. Kuch.

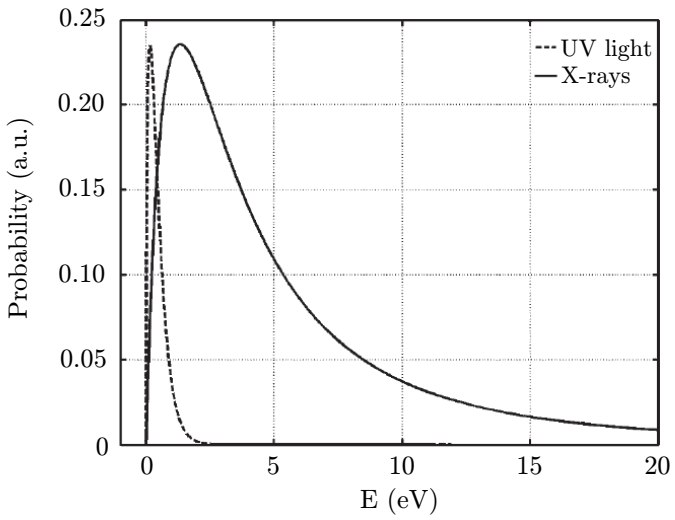

Fig. 5.5: Comparison of distributions of kinetic energies of secondary electrons emitted by UV light and X-rays. Reproduced from [328].

ments we usually apply magnetic field pulses in a static mode, before the image acquisition, so the magnetic field does not coincide with the electron bunches. Note that other techniques, such as X-ray transmission or fluorescent microscopies[4], are better suited for studies in the presence of a magnetic field, but the contrast is much lower than by using the XMCD-PEEM [1, 323].

Finally, let us summarize the contrast mechanisms we can exploit with PEEM microscopy:

1. elemental contrast with UV light, arising from specific work functions of materials,

2. elemental contrast with x-rays, arising from specific binding energies of core electrons (see Fig. 5.6),

3. magnetic contrast associated to the XMCD, arising from a spin-split valence band of magnetic materials and core-level spin-orbit coupling.

For illustration of the elemental selectivity of the combined XMCD-PEEM technique, Fig. 5.6 shows an X-ray absorption spectrum around the Co L_3 edge, accompanied by corresponding PEEM images of a structure consisting of a Au contact (visible in all the images) and a Co wire with a square end. The Co pattern is visible only when the X-ray photon energy is tuned to the Co L_3 edge (image 5). Au is visible for all shown photon energies because it is a heavy metal with a multitude of electronic levels with binding energies lower than the used photon energy. The absorption spectrum was obtained by measuring the intensity in the square of the Co structure while sweeping the photon energy.

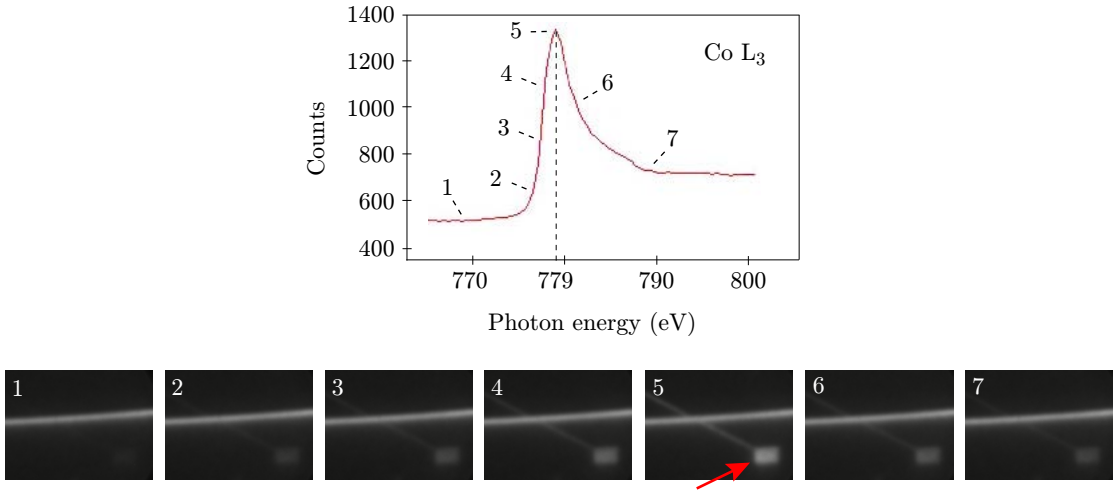

Fig. 5.6: X-ray absorption at the Co L_3 edge. The numbered images corresponding to the absorption curve illustrate the selection of an element (Co in this case) by tuning the photon energy to the desired specific absorption edge. The white horizontal bar is a gold contact.

[4]These techniques measure photon intensities.

5.2.1 Time-Resolved Imaging Mode

By exploiting the time structure of the synchrotron radiation, one can perform stroboscopic[5], time-resolved imaging of reproducible events. The filling of the storage ring by electrons is not continuous. A given set of electron bunches orbit at a frequency specific for each synchrotron – 357 kHz at the ESRF[6]. The lowest bunch mode at the ESRF is a four-bunch mode, in which the X-ray bunches pass the front-end at a repetition rate of 1428 kHz. By synchronizing the current or magnetic field pulses with the x-ray photon bunches, we obtain an instantaneous image of the magnetization configuration for a particular delay, before, during or after the applied pulse [355, 354, 321]. The acquisition time of one image was set to 30 s, therefore the image is an average of $10^7 - 10^8$ photon pulses, depending on the integration frequency. This implies that only reproducible events might be recorded in the averaged signal. The temporal resolution is limited by the photon bunch length specific for each synchrotron[7] and operation mode. As the power supply used to generate the current pulses in the microcoil would have excessive requirements in terms of maximum power and cooling (see Section 5.2.2), we exploit only 1 out of 2 bunches. For this reason, a negative voltage pulse (-80 V)[8], synchronized with the X-ray bunches, is applied on a grid in front of the microchannelplate to prevent the odd bunches of secondary electrons to form an image on the screen [see Fig. 5.7(c)]. This is equivalent to integrating the absorption images at a repetition rate of 714 kHz.

5.2.2 PEEM Instrumentation

In order to study current-induced DW motion with our Focus IS-PEEM, several construction changes had to be performed. A new sample stage was developed, integrating current terminals and a folded copper stripline ("microcoil",[9] see Fig. 5.8 – top-right) so that both current and magnetic pulses could be applied to the sample. At the same time the PEEM UHV chamber was modified to lead out the current cables. Though this intervention does not allow us to use a standard loadlock of the PEEM and substantially prolongs the time necessary to change the sample, the versatility and possibility to study magnetization dynamics induced by current or magnetic field pulses is unique.

Current pulses The current terminals are connected to the copper strips (Fig. 5.8 – bottom-right), to which the sample is contacted using wire microbonding. Current pulses were injected using two different pulse generators: the first one provides short voltage pulses of a 0.3-ns risetime and tunable length up to 12 ns, the second one

[5]Also called a "pump-probe" experiment. We excite magnetization with an external stimulus (pump) and record (probe) the response of the system.

[6]European Synchrotron Radiation Facility, Grenoble, France.

[7]Typically 80 ps at the ESRF.

[8]By measuring the brightness decrease while increasing the blanking voltage, we estimate that 80% of the extracted electrons have energies below 80 eV.

[9]The name "microcoil" was chosen for historical reasons – the actual size would rather suggest a name "minicoil".

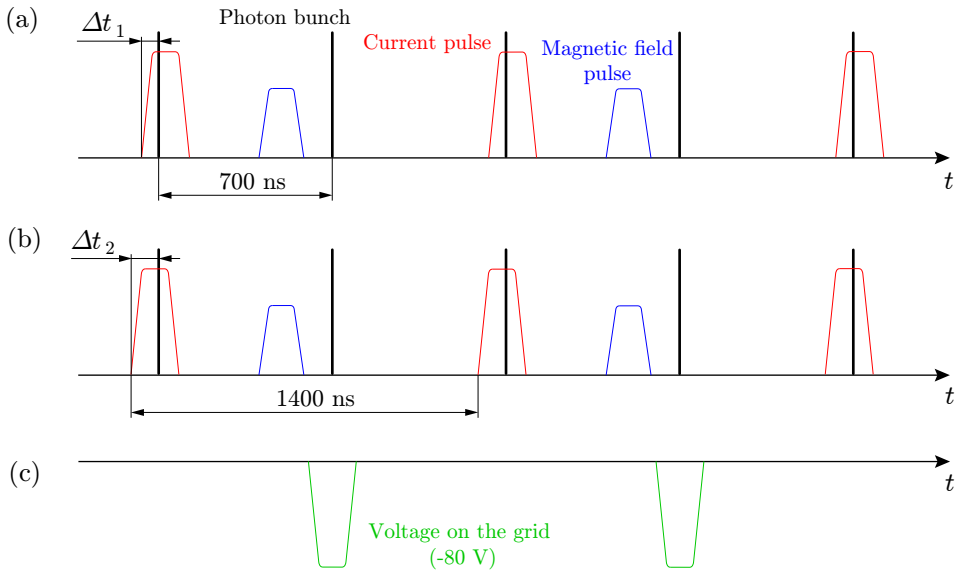

Fig. 5.7: Timing of various pulses in the time-resolved XMCD-PEEM experiment. (a) Photon bunches are synchronized with field and current pulses with a given temporal delay. (b) Different delay of the current pulse. The period of current pulses is a double of the photon bunches period. (c) Corresponding blanking pulses prevent the secondary electrons induced by odd photon bunches to reach the microchannelplate.

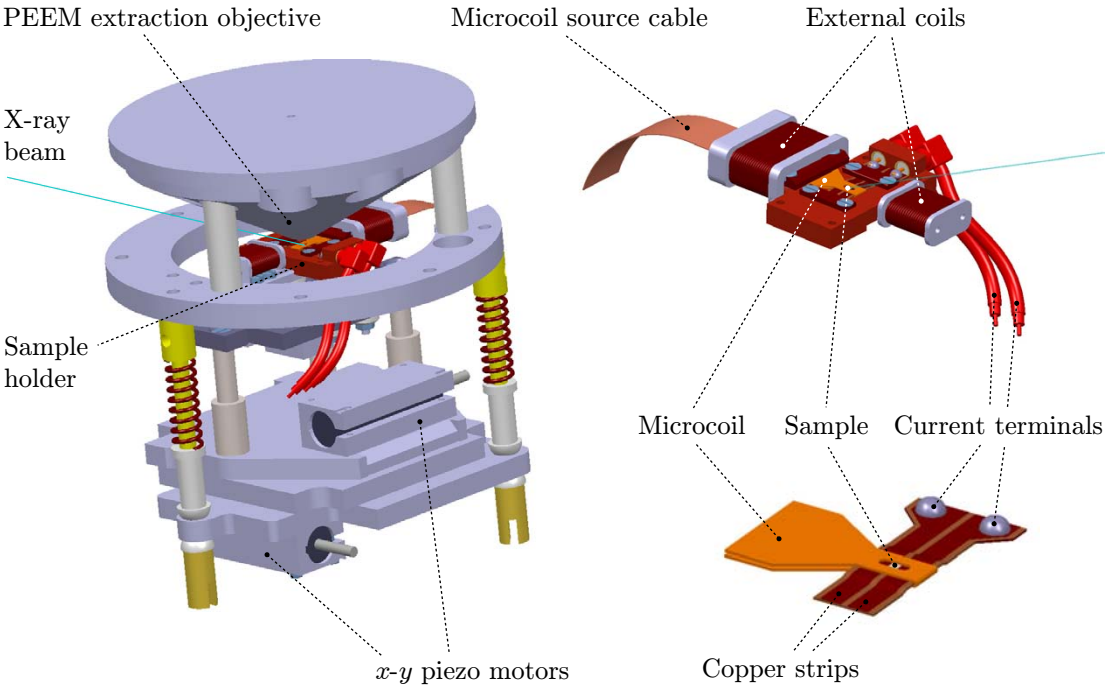

Fig. 5.8: View of the PEEM details. Top-left: sample stage position with respect to the PEEM extraction lens. Top-right: sample stage integrating current terminals, a double stripline (microcoil) and additional coils. Bottom-right: microcoil serves for applying magnetic pulses in the plane of the sample. 3D design by P. Perrier.

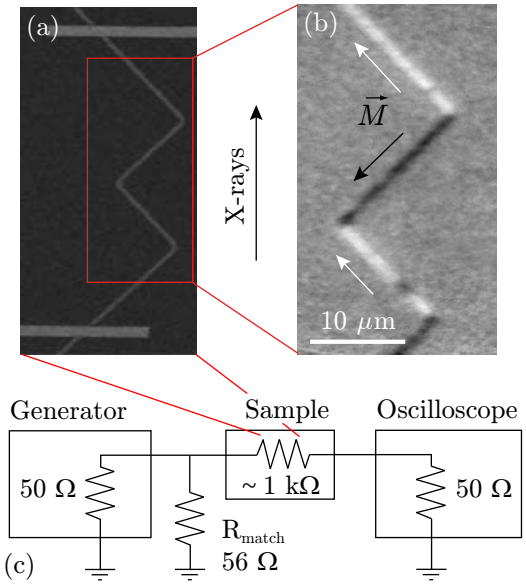

Fig. 5.9: (a) SEM topographic image of the zigzag nanowire of a width of 200 nm and an angle 90°. The horizontal lines correspond to the Ti/Au contacts. (b) XMCD-PEEM image of the magnetic domain structure in the NiFe layer after application of a field perpendicular to the longitudinal axis of the zigzag. (c) Schema of the electronic circuit.

provides longer pulses. The sample resistance was of the order of 1 kΩ. To assure impedance matching, a resistance of 56 Ω was added in parallel to the samples. The current flowing through the nanowires was deduced from the voltage measured over the 50-Ω entrance of a 6-GHz oscilloscope connected in series with the nanowires. The electronic schema is shown in Fig. 5.9(e).

Magnetic field pulses To produce field pulses, we used a combination of double stripline-like microcoils and a home-made pulsed current supply. The maximum current we can apply to the microcoil is 100 A in pulses which give a magnetic field of 23 mT[10] in the sample plane (for a calibration of the microcoil magnetic field see Table 5.1). Hence assuming 50-ns pulses at a repetition rate of 714 kHz and a maximum field amplitude, we obtain a dissipated power of 570 W! This is the reason why when using magnetic field pulses in the time-resolved mode, the current supply has to be water-cooled and the full four-bunch mode (1428 kHz) of the ESRF cannot be exploited.

Imaging The XMCD-PEEM experiments have been carried out at the European Synchrotron Radiation Facility (beamline ID08) and at the Synchrotron SOLEIL (beamline TEMPO). In order to avoid discharges from the objective lens of our Focus IS-PEEM, which is at a distance of 2 mm from the grounded sample (see Fig. 5.8), the

[10]The magnetic field values were calculated for a double-strip loop using the Biot-Savart law under the assumption that at high frequencies (>100 MHz) the current flows mainly at the surface of the conductor [334].

HT voltage (V)	TTL read (V)	Microcoil current (A)	Magn. flux density (mT)
30	1.08	27.0	6.2
60	1.91	47.8	11.0
90	2.78	69.5	16.0
100	2.94	73.5	16.9
110	3.16	79.0	18.2
120	3.34	83.5	19.2
130	3.50	87.5	20.1
140	3.66	91.5	21.1
150	3.81	95.3	21.9
160	3.94	98.5	22.7

Table 5.1: Calibration of the microcoil magnetic field. "HT voltage" – voltage applied to the current source; "TTL read" – a read-out voltage value on the oscilloscope corresponding to the current flowing in the microcoil. The magnetic flux density corresponds to the center of the microcoil where the nanowires are situated.

voltage on the objective lens was kept much lower than the nominal 12 kV at which the highest resolution can be obtained.

The resolution was determined from intensity profiles at the structure edges which represent a step function convoluted with a resolution function. Fig. 5.10 shows such a profile for the extraction voltage of 5.4 kV. In order to obtain the resolution function, a derivative of this profile was calculated. Subsequently the derivative was fitted by a gaussian function (Fig. 5.10). Generally the resolution is defined by the separation of two resolution functions for which the intensity in between falls to 80%. Following this routine we obtain a resolution of (510±10) nm for the extraction voltage of 7 kV, (570±10) nm for 5.4 kV and (600±10) nm for 4 kV.

Even though the DW shape was convoluted with the resolution gaussian, the relative change of the DW position could be detected with a much higher accuracy (approximately 50 nm). In order to image the domain structure in the NiFe layer, the X-ray energy was tuned to the Ni L_3 absorption edge (852.8 eV). To optimize the magnetic contrast, the difference between two consecutive images obtained with 100-% left- and right-circularly polarized X-rays was computed. The presence of a rather thick Cu spacer (8 nm) layer, combined with the limited escape depth of the secondary electrons, prevented images of the Co domain structure in our regular samples to be taken (for details on sample composition see Section 4.3). The Co magnetization state was checked by a high-resolution PEEM of the Nanospectroscopy beamline at the synchrotron ELETTRA. In order to image the magnetic configuration of Co directly, we sputtered off a portion of the NiFe layer. We also used samples with a thinner Cu spacer (3 nm) to perform this check with our standard PEEM. In these cases the X-ray energy was set to the Co L_3 edge (779 eV).

To obtain a good statistics and to suppress the additive noise in the images, the acquisition time was set in the order of tens of seconds for each polarization. During this time the image drift can be several tens of nanometers or more. Therefore a series of images (30-200 pieces) was taken, each image for a short temporal interval (0.5-

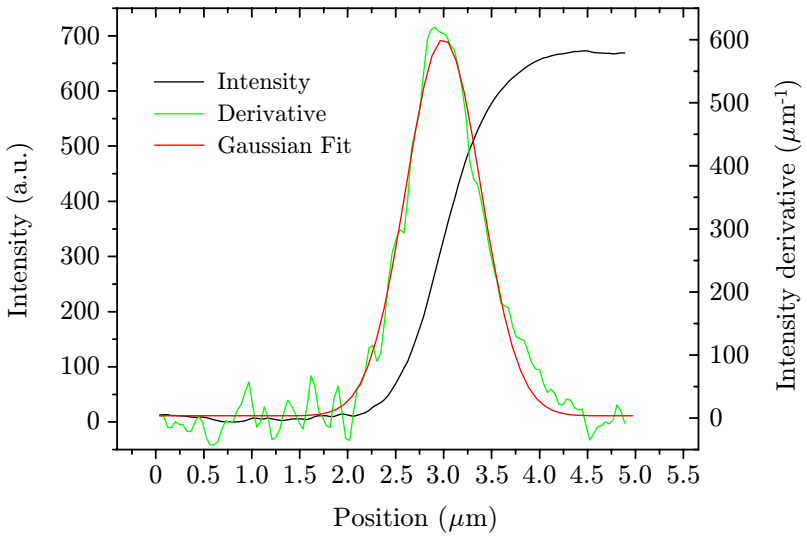

Fig. 5.10: Intensity profile at the edge of an imaged structure for the extraction voltage of 5.4 kV (black curve). The green curve represents the resolution function obtained by differentiating the intensity profile. A gaussian fit of the derivative is represented by the red curve.

2 s). Subsequently, the individual images were added after realignment. The alignment procedure was extremely important for the quality and sharpness of the final XMCD image. For this purpose a new programme with a specialized aligning algorithm[11] has been developed.

5.3 Historical Note

The first beamtime allocated for the time-resolved observation of current-induced DW motion took place in May 2006, a few months before the beginning of this thesis. On one hand, the complicated timing scheme required for the pump-probe measurements was successfully tested. On the other hand, technical problems associated with the samples' extreme sensitivity to electrical discharges did not allow the team to acquire any XMCD-PEEM image of the samples' domain structure. The high tension important to obtain high-resolution PEEM images, in combination with the small distance of the sample from the objective lens, led systematically to a destruction of the sample [see Fig. 5.11(a)-(c)]. Several important experimental details were learned which were subsequently taken into account in the following beamtimes:

- The sample and its surrounding area should be as flat as possible in order to avoid field emission and discharge effects.

[11] The programme for image alignment was carried out in collaboration with J. Novotný from the Institute of Mathematical Engineering, Brno University of Technology, who developed the method and wrote the code. The differential algorithm enables subpixel registration of individual images. As it is not based on the cross-correlation of images, the sensitivity of the alignment to impulse noise is minimized.

- The architecture of the sample pattern has to be such that the macroscopic contacts are far away from the sample, ideally covered by the microcoil.
- The lithography processing has to be carefully optimized, as any remainder of residual resist leads to important charging of the sample.

Initially, the multilayers were deposited (by magnetron sputtering) in the laboratory of Unité Mixte de CNRS-Thales in Orsay (in collaboration with Vincent Cros, Sana Laribi, Julie Grollier and Abdelmadjid Anane) and the patterning was carried out at Laboratoire de Physique des Nanostructures in Marcoussis (in collaboration with Giancarlo Faini, until May 2008). We decided for a parallel patterning optimization in the "Nanofab" and "Plateforme Technologique Amont" facilities of Institut Néel. In the beamtime of May 2007, we successfully used the samples from Nanofab for the first time[12]. These new samples were less sensitive to electrical discharges, as a lot of care was taken not to leave any residual resist at or near the structures. The Al wires bonded to the contacts were placed far away from the magnetic pattern (actually they were hidden under the microcoil double stripline) and therefore from the objective lens. These improvements allowed us to increase the extractor lens potential up to 6-7 kV without destroying the sample.

However, for most of the observations only 4-5 kV was used to stay below the critical voltage values. This is essential as the sample exchange and the pumping procedure takes approximately 16 hours of the precious time at the beamline.

During the first beamtime, we learned that an insufficient vacuum in the PEEM chamber, above 10^{-8} mbar, most probably leads to a strong contrast deterioration after approximately 12 hours of exposition of the patterns to the x-ray beam [see Fig. 5.11(d),(e)]. This is due to the fact that the high photon flux at the ESRF leads to a fast deposition of carbon on the sample surface. In the following beamtimes all the optimization phases were carried out using a mercury lamp rather than x-rays. This increased substantially the lifetime of the patterns.

Moreover, as the vibrations blurr the images of nanowires [Fig. 5.11(f),(g)], the vibration sources close to the PEEM chamber, like the rotary pump or the ventilator of the turbomolecular pump, have to be switched off during the image acquisition.

All the mentioned aspects have made the observation particularly difficult and have attracted a lot of effort to avoid the known and anticipated complications and to remove the weak points of the experimental set-up which could be often revealed only at the synchrotron facilities.

The results of the XMCD-PEEM experiments are summarized in the following chapter. The quasi-static imaging for DW motion statistics was carried out during the beamtimes at the synchrotrons ESRF in May 2008 and Soleil in December 2008, the time-resolved experiments during the beamtimes at the ESRF in May 2009 and Soleil in July 2009.

[12] In the following beamtimes we used samples from both sources.

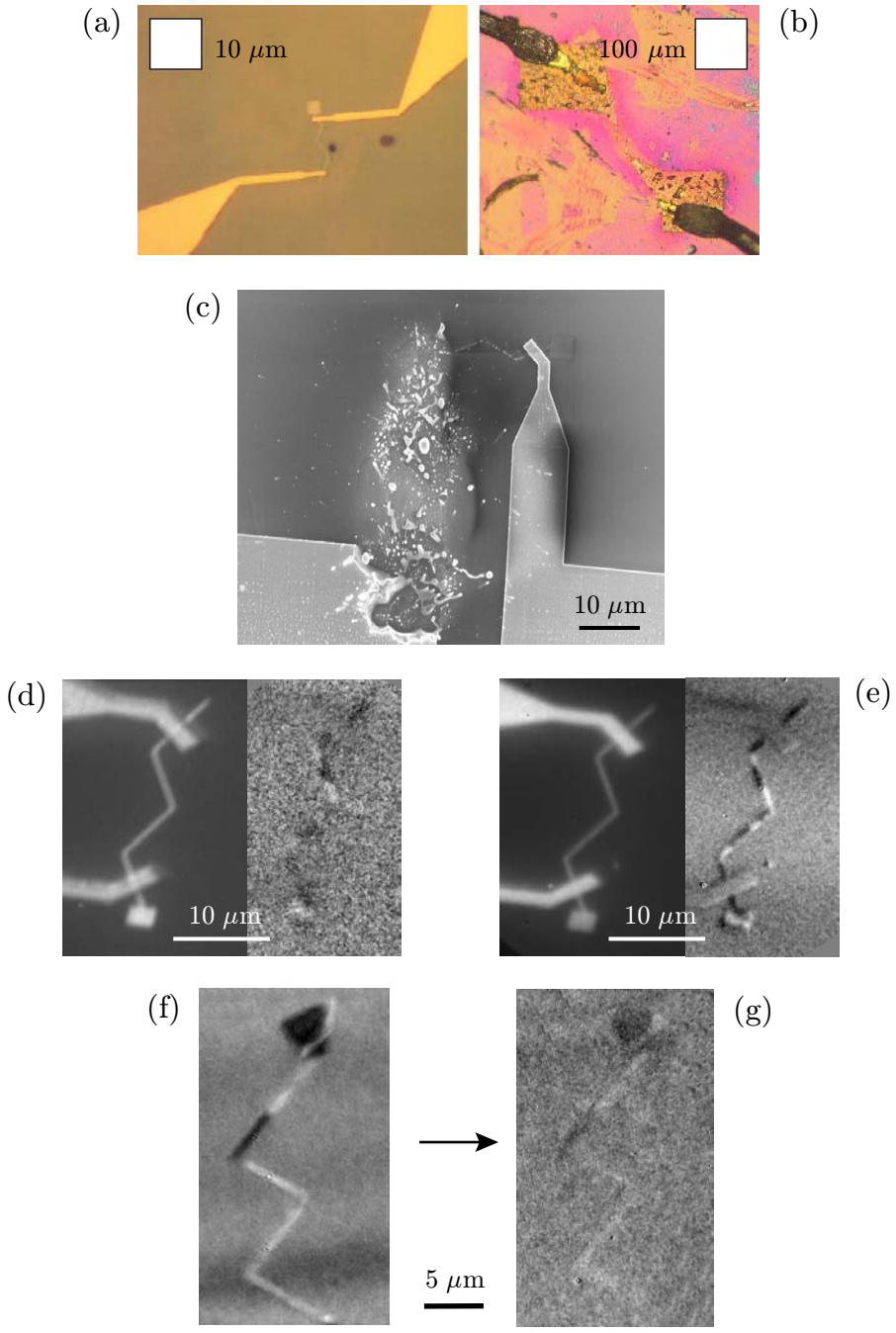

Fig. 5.11: (a) Optical microscope image of the magnetic zigzag nanowire and the gold contacts. (b) The sample after discharges between the PEEM objective lens and sample contacts. (c) SEM image of another sample after a discharge. (d) Any vibrations substantially decrease the image quality, (e) shows the situation with the ventilator off. (f),(g) Long exposition to the X-ray beam deteriorates the contrast by deposition of carbon on the top of the sample.

Chapter 6

CURRENT-INDUCED DOMAIN-WALL MOTION IN SPIN-VALVE NANOWIRES

6.1 Effects of Current in Multilayer Nanowires

The electric transport in magnetic multilayers is naturally a more complex issue with respect to single magnetic layers where the current-induced DW motion is often studied. One needs to take into account an inhomogeneous and asymmetric current distribution due to different resistivities of the materials, even more complicated due to the spin-dependent scattering at the interfaces of magnetic layers. This inhomogeneous current flow results in uncompensated Oersted fields in each layer. Moreover, the magnetic layers may be coupled by interlayer dipolar interactions or, in case of thin metallic spacers, RKKY interaction.

Joule heating during long and high-amplitude current pulses, which leads to thermal nucleation of domains or even reaching the Curie temperature, is also a well known general aspect that will be discussed in the following.

6.1.1 Calculation of Inhomogeneous Current Distribution

The current densities reported in Section 6.2 refer to the NiFe layer and are calculated assuming an inhomogeneous current distribution in the trilayer. Calculations based on the Fuchs-Sondheimer model [335, 202] have been carried out by André Thiaville (Laboratoire de Physique des Solides, Orsay). This model takes into account not only the layer resistivities, but also spin-dependent scattering at the interfaces. It solves the Boltzmann equation of conduction for the current densities of two spin channels in the individual layers.

The parameters necessary for the calculation are the following:

- resistivities ρ of the thin layers;
- mean free paths ℓ of the electrons, which are connected to the corresponding resistivities by the product $\rho\ell$, a material-specific constant proportional to the Fermi velocity;
- spin asymmetry parameters $\zeta = \rho_\uparrow/\rho_\downarrow$, where $\downarrow$ denotes majority and $\uparrow$ minority electrons, allowing the resistivity and mean free path of each spin channel to be expressed;

- layer thicknesses t';
- transmission spin asymmetry coefficients N_{a};
- specular reflection parameters p.

At the interfaces we define a probability P_{T} that an electron will be transmitted specularly (without a change in its velocity) and a probability $P_{\mathrm{D}} = 1 - P_{\mathrm{T}}$ of a diffusive transmission, i.e. the electron loses its movement history. Transmission spin asymmetry coefficient N_{a} reads

$$N_{\mathrm{a}} = \frac{1 - P_{\mathrm{T}\uparrow}}{1 - P_{\mathrm{T}\downarrow}}. \tag{6.1}$$

Specular reflection parameter p, defined at the outer borders of the multilayer, determines the ratio of specularly reflected (p) and diffusively reflected ($1-p$) electrons. More details can be found in [202] and [336].

The resistivities of the layers used in the calculation are the following: $\rho_{\mathrm{Co}} = 30\,\mu\Omega\cdot\mathrm{cm}$, $\rho_{\mathrm{Cu}} = 3 - 6\,\mu\Omega\cdot\mathrm{cm}$ and $\rho_{\mathrm{NiFe}} = 35\,\mu\Omega\cdot\mathrm{cm}$. These values were provided by our partner laboratory – CNRS-Thales. By varying the Cu resistivity (3-10 $\mu\Omega\cdot$cm) and the interface-related parameters in a meaningful range, we found that the sum current of the two spin channels flowing in the NiFe layer is

- (10±1)% of the total current in the multilayer for the Cu 3 nm/NiFe 5 nm/Cu 8 nm/Co 7 nm/CoO 4 nm/Si configuration;
- (15±1)% for the Cu 3 nm/NiFe 5 nm/Cu 5 nm/Co 5 nm/CoO 3 nm/Si configuration.

For the configuration with a 8-nm spacer, these results suggest that current density values in NiFe are approximately 2× lower than those obtained supposing a homogeneous current distribution. A more precise estimation of the current distribution could be obtained if we experimentally measured the resistivities of the individual layers and bilayers, to determine the interface-related variables.

6.1.2 Oersted Field

Apart from STT effects, an electrical current flowing through a nanowire also generates a magnetic Oersted field (H_{Oe}) transverse to the wire section. It has been shown that Oersted fields have an important influence on STT induced reversal in trilayered pillars for current flowing perpendicular to the plane of the layers [351, 352]. For in-plane systems, H_{Oe} has been invoked to explain the resonant behavior of constricted DWs [227] and the reversal behavior in notched mesoscopic bars of NiFe/Cu/Co/Au [347].

H_{Oe} is transverse to the current direction and should not favor motion of DWs in one direction or the other of a magnetic nanowire if the magnetization direction is along the wire, as in the case of soft magnetic materials such as NiFe. However, it has been shown that a transverse magnetic field can modify the DW shape and

velocity for magnetic field induced DW motion in nanowires [92, 88, 91]. In general, DW velocities [184, 84] and DW transformations [186] are deduced from quasistatic measurements, where the DW position and shape is studied before and after a current pulse. However, the influence of H_{Oe} can only be investigated in detail by direct observations of the magnetic configuration *during* current pulses. The results of the time-resolved experiments will be given in Section 6.5.2.

We will show that the effect of the Oersted field in the NiFe layer can be largely underestimated if it is based on crude approximations like uniform magnetization in the nanowire, absence of edge roughness and/or neglect of the stray field of the cobalt layer. For what concerns the current-induced DW motion in multilayer systems, the effect of the Oersted field has not been explicitly taken into account in simulations up to now.

6.1.3 Joule Heating of Nanowires

Current densities required for CIDWM[1] are large and often lead to significant heating of the nanowires, especially for μs-long current pulses. The thermally induced effects often reported in the literature may arise even for ns-long pulses, in case the substrate is a bad thermal conductor and the investigated system has an overall large resistance.

Thomas et al. [346] applied 9-ns current pulses of a current density of $5 \times 10^{11}\,\mathrm{A/m^2}$ to spin-valve nanowires deposited on SiO_2-coated Si wafers and showed that the Néel temperature of the antiferromagnetic IrMn ($\sim 700\,\mathrm{K}$) was reached. The DW position was determined by a change of GMR in a spin-valve system and the pinning of a reference magnetic layer to the antiferromagnet was thus essential.

Togawa et al. [345] observed thermally activated domain nucleation in NiFe nanowires of a significantly high resistance[2] by Lorentz microscopy. This technique, based on TEM observation, required deposition of the nanowires on a 30 nm thick Si_3N_4 membrane, which did not allow proper heat dissipation. Although T_{C} was not reached, the energy barrier for domain nucleation was decreased by the increase of temperature and the decrease of magnetic moment, which is also temperature-dependent.

Change of resistance due to Joule heating has a large impact on the determination of the critical current density. If it is calculated from the applied voltage assuming a nanowire resistance at room temperature [184], large errors are introduced. The current density needed for the DW motion can thus be overestimated and moreover a thermally activated nucleation may arise [185]. The critical current densities corrected and not corrected for Joule heating effects differed by a factor 2 in the studies [185] and [184], respectively.

This suggests that to ensure a good heat dissipation, the choice of the substrate is essential. For this reason we have selected a high-resistivity silicon substrate with a native SiO_2 layer. A balance has to be found between the requirements of a highly resistive substrate for prevention of a current short-circuit and of a thermally conducting substrate.

[1] Generally $\approx 10^{12}\,\mathrm{A/m^2}$ for single NiFe nanowires.

[2] $1.3\,\mathrm{k\Omega}$ for a NiFe nanowire 30 nm thick, 500 nm wide and approximately $30\,\mu$m long.

In order to check the effect of heating on the nanowire resistance induced by current, we recorded the shape of current pulses on an oscilloscope (Fig. 6.1). Fig. 6.1(a) shows a 100-ns voltage pulse applied to nanowires of a high resistance (6 in parallel which yield a 1.6 kΩ total resistance) and the corresponding current response. Due to heating, the current drops by 30% at the end of the pulse. The inset of Fig. 6.1(a) shows a detail of the current curve for the first 20 ns of the pulse.

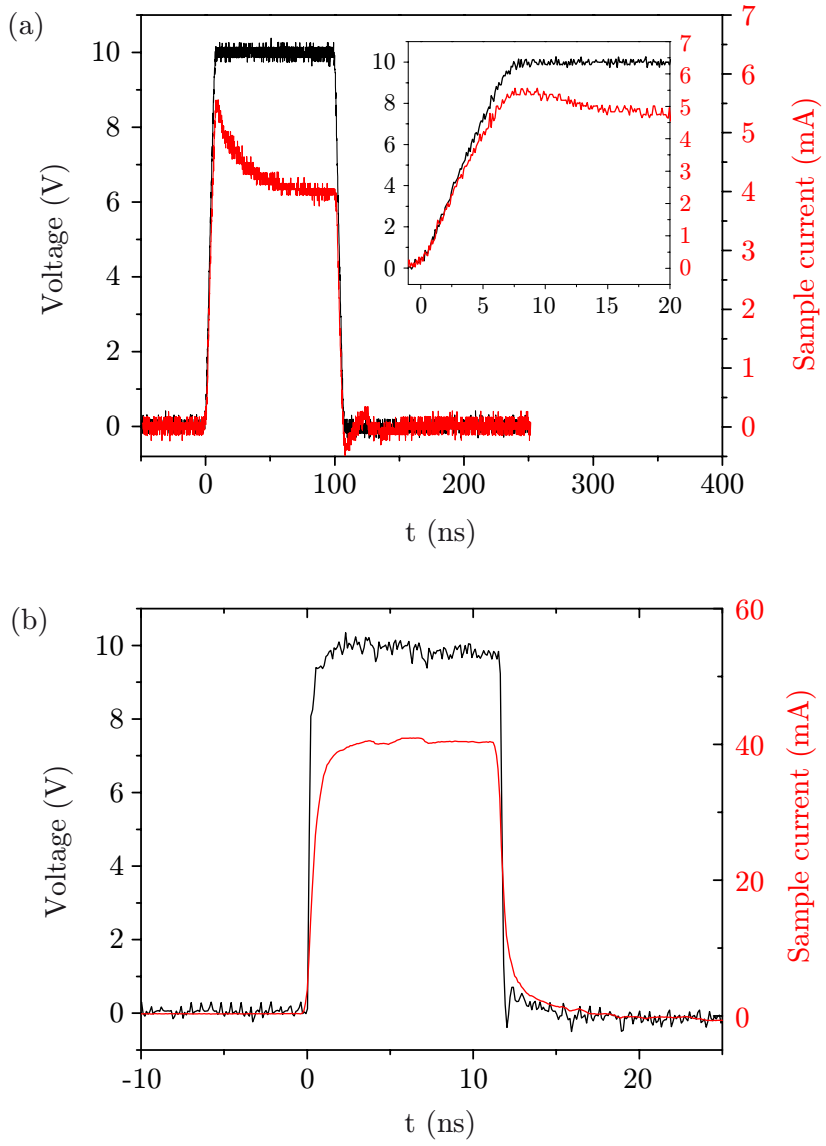

Fig. 6.1: Effect of heating on the nanowire resistance during a current pulse. Black trace represents the voltage pulse of the generator, the red one its current response in the nanowires. (a) Current amplitude in nanowires of a high resistance (1.6-kΩ resistance of 6 nanowires in parallel) presents a substantial drop at the end of a 100-ns pulse. The inset shows a detail of the first 20 ns of the pulse. (b) Current amplitude in nanowires of a standard resistance (0.25-kΩ resistance of 6 nanowires in parallel) lacks any such decrease. Maximum applied current amplitude is shown in (b).

Fig. 6.1(b) shows a 12-ns voltage pulse applied to nanowires of a standard resistance (6 in parallel which yield a 0.25 kΩ total resistance) which were used in experiments described in this chapter. The current amplitude corresponds to the highest current density used in Section 6.2.2, 4.2×10^{11} A/m^2 in the NiFe layer (9.5×10^{11} A/m^2 assuming a homogeneous current distribution). No decrease of the current amplitude due to heating during a current pulse as short as 12 ns can be observed. The current value indicated in the figure corresponds to a sum of six zigzag structures connected in parallel. Longer current pulses used in Section 6.2.1 featured 2-4× lower amplitude and the absence of heating effects was verified for current pulses as long as 100 ns.

A related phenomenon, the effect of heating on interdiffusion of Ni and Cu at the interface during the current pulses, should be very small – the diffusion requires a certain time, longer than nanoseconds, to considerably modify the interface. Moreover, it was shown that the temperature of nanowires does not significantly increase even upon the maximum applied current pulses.

6.2 Quasi-static measurements of DW motion

Manifestation of electric current effects on DW depinning and displacement is discussed in this section. The nanowires described in this section consist of Cu 3 nm/$Ni_{80}Fe_{20}$ 5 nm/Cu 8 nm/Co 7 nm/CoO 4 nm magnetron-sputtered layers. Images are obtained in a quasi-static mode, after application of one current or magnetic field pulse. In all the images presented here, the contrast is given by the projection of the magnetization on the beam direction, i.e. white (black) domains have their magnetization pointing downwards (upwards), along the nanowires.

6.2.1 Current-Induced DW Motion in Spin-Valve Nanowires

Fig. 6.2(a) presents a typical NiFe magnetic configuration showing a multidomain structure in a 200 nm wide nanowire obtained after the application of a transverse magnetic field pulse of an amplitude not sufficient to saturate the magnetization of each zigzag section. Most DWs move upon application of a current pulse of 10-ns length and 4.2×10^{11}-A/m^2 current density. As expected for spin-torque driven motion, the direction of DW motion is determined by the sense of the electron flow, as no magnetic field is applied during the current pulses. The DWs can be moved forth [Fig. 6.2(b)] and back [Fig. 6.2(c)] with opposite current polarities, unless the pinning potential is stronger in the final than in the initial position. Our measurements show that DW motion is often not symmetric for opposite polarities. In many cases, as we will see later, the DW motion is stopped by defects and the probability of DW depinning is not equal for opposite current directions. The average velocity of a DW can be calculated by dividing the distance traveled by a DW by the corresponding pulse duration. The average velocity of the moving DWs in Fig. 6.2 ranged from 130 to 240 m/s.

An apparent DW motion against the electron flow has sometimes been observed. Every time we found such a behaviour, a region with an intermediate XMCD intensity (gray shade, for discussion refer to Section 6.3.2) was observed at the arrival point of

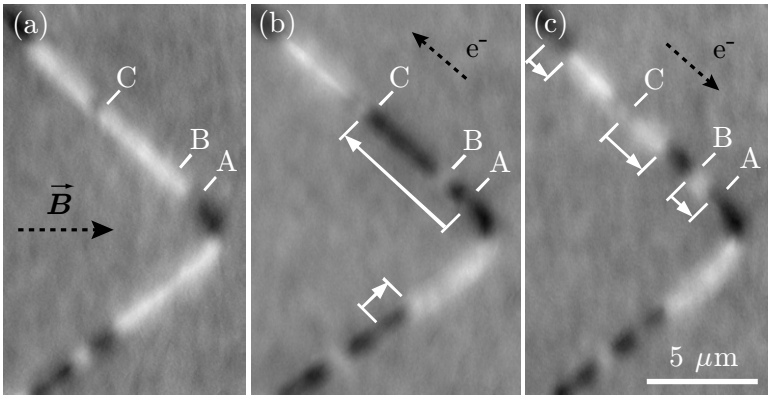

Fig. 6.2: Initial-state domain structure obtained for a 200 nm wide nanowire by applying a magnetic field pulse of 11 mT (a). DW structure obtained after the application of 10 ns long current pulses with an amplitude of 4.2×10^{11} A/m^2 with positive (b) and negative (c) polarities. The DW motion follows the direction of the electron flow. (c) Application of a negative pulse, leading to the displacement B-A, shows DW nucleation at site B.

such a displacement. These regions are possible sources of DW nucleation [Fig. 6.2(c), position B], suggesting that the apparent "opposite" sense of the DW motion corresponds in fact to nucleation of a DW at this location followed by a movement in the correct direction. The "nucleation" can be explained by a one-directional expansion of a 360° DW, smaller than our resolution, trapped in the nanowire [Section 6.3.4, Fig. 6.17(c),(d)]. Assuming the possibility of such a nucleation of a domain at position B [Fig. 6.2(c)], we realize that the displacement A-C [Fig. 6.2(b)] could actually consist of two displacements, A-B and B-C. Such displacements are not highly probable and have not been considered in the statistical analysis of Section 6.2.2.

To prove that the DW motion is governed by spin torque and not by a residual magnetic field, Fig. 6.3 shows head-to-head and tail-to-tail DWs moving together. Magnetic field would move these DWs in opposite directions.

An example of a long-range back and forth DW displacement, in this case for a 400 nm wide nanowire, is shown in Fig. 6.4. Fig. 6.4a shows the initial domain struc-

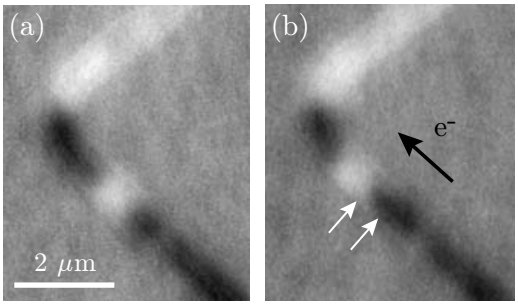

Fig. 6.3: (a) Initial domain structure obtained with magnetic field pulses before applying current pulses. (b) Head-to-head and tail-to-tail DWs move together upon application of a current pulse (2.5 ns, 3.3×10^{11} A/m^2). White arrows indicate the initial position of the DWs.

ture. After the application of one 50 ns long current pulse of an amplitude of +4.2 mA [Fig. 6.4(b)] a DW moves from the position A to B, while the other DW is pinned. After a subsequent 50 ns long pulse of an opposite polarity [−4.2 mA, Fig. 6.4(c)] the DW moves back to the position C. Upon applying an identical positive (d) and negative pulse (e) again, the DW moves forth to D and back to E, respectively. The DW motion denoted by F occurs only in (e). Back and forth movement induced by current pulses of opposite polarity is unique for CIDWM induced by spin transfer torque and cannot be due to Joule heating or the presence of an external field.

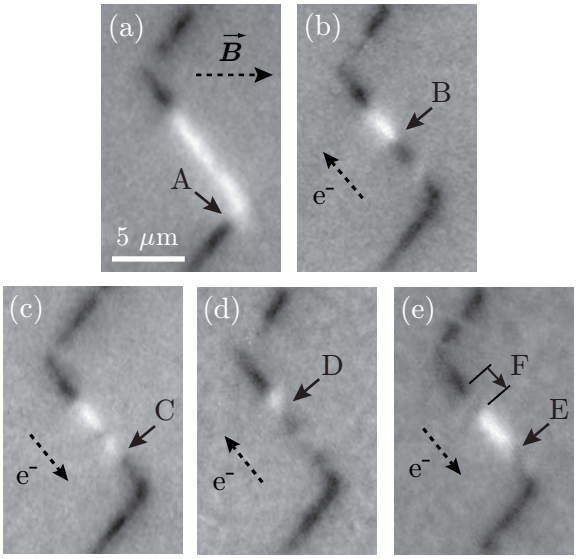

Fig. 6.4: XMCD-PEEM image of a NiFe layer of a 400 nm wide spin-valve like nanowire with a 120° zigzag angle (a) after applying a static magnetic field perpendicular to the longitudinal axis of the zigzag nanowire; (b) after application of a 50-ns, +4.2-mA current pulse; (c) after application of a subsequent 50-ns, −4.2-mA current pulse. (d) Repetition of the positive and (e) negative current pulse.

In Fig. 6.5, we show current-induced DW motion in a 400 nm wide nanowire with zigzag angles of 120°. The domain structure in Fig. 6.5(a) could be obtained reproducibly by applying 50 ns long magnetic field pulses with an amplitude of 17 mT. Starting from this initial state, we applied current pulses with different amplitudes and lengths, in order to determine the DW velocity and the threshold current in this section. Figure Fig. 6.5(b) shows the domain structure obtained after applying one 100 ns long current pulse with an amplitude of +2 mA, a value below which no DW motion was detected for these relatively short pulses. This threshold current pulse causes a displacement of the domain wall from position A to position B in the images. A consecutive pulse with the same amplitude and length induces a further movement of the same domain wall in the same direction, from B to C [Fig. 6.5(c)]. Note that in these images only one DW moves for the applied amplitude of the current, showing that the pinning strengths can strongly differ at different positions in the nanowire. The free motion of the NiFe DW over section A–C in Fig. 6.5 indicates that pinning in this section is relatively small.

The first pulse causes a CIDWM of $(1.75 \pm 0.20)\,\mu$m, the second pulse $(1.92 \pm 0.20)\,\mu$m, resulting in a DW velocity of about (18 ± 2) m/s. The current density in the NiFe layer corresponding to the +2mA pulse is 2.3×10^{11} A/m^2 if we consider a uniform current distribution through the trilayer stack and 1×10^{11} A/m^2 if we suppose that the current density is proportional to the conductivity in each layer. The value of 2.3×10^{11} A/m^2 gives thus an upper bound for the current density in the NiFe layer. In Figs. 6.5(d) and 6.5(e), we show results of measurements using current pulses with the maximum available amplitude of 5 mA (corresponding to a current density of 5.7×10^{11} A/m^2, or 2.5×10^{11} A/m^2 in the NiFe layer for non-uniform current distribution) and lengths of 15 and 20 ns, in both cases starting from the initial state shown in Fig. 6.5(a). The CIDWM for the 15 and 20 ns pulses are (2.7 ± 0.2) and $(3.4 \pm 0.2)\,\mu$m, showing that in this section of the nanowire the displacement is about proportional to the pulse length. The resulting DW velocities are (180 ± 10) and (170 ± 10) m/s, respectively.

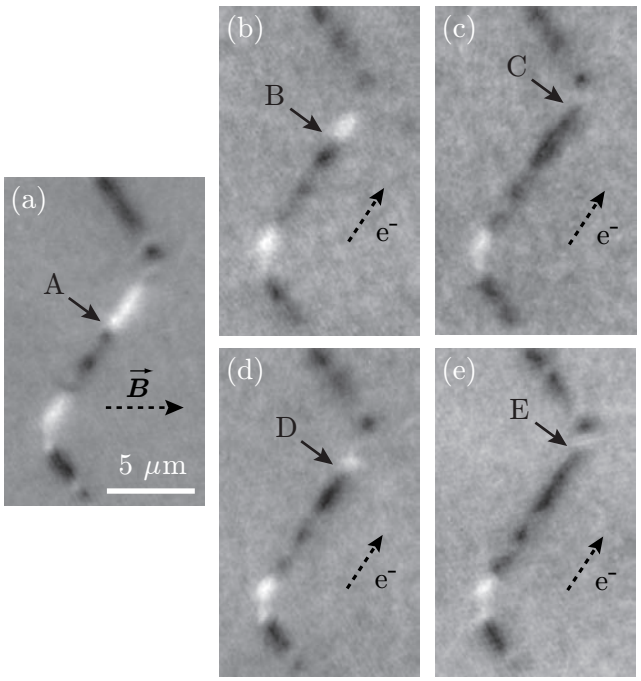

Fig. 6.5: XMCD–PEEM images of the NiFe layer of a 400 nm wide spin-valve nanowire with a zigzag angle of 120°. (a) gives the initial domain state, obtained after applying an in-plane 50 mT magnetic field pulse perpendicular to the long direction of the stripe. (b) and (c) show the images after application of one, resp. two 100 ns long current pulses of +2 mA starting from the domain state of (a). The indicated DW moves from position A to position B upon the first pulse, and from B to C with the second pulse. (d) and (e) show images obtained after application of one 15-ns pulse of +5 mA and one 20-ns pulse of +5 mA, respectively, in both cases starting from the initial state of (a). The 15-ns pulse makes the DW move from position A to D, the 20-ns pulse causes a motion from A to E.

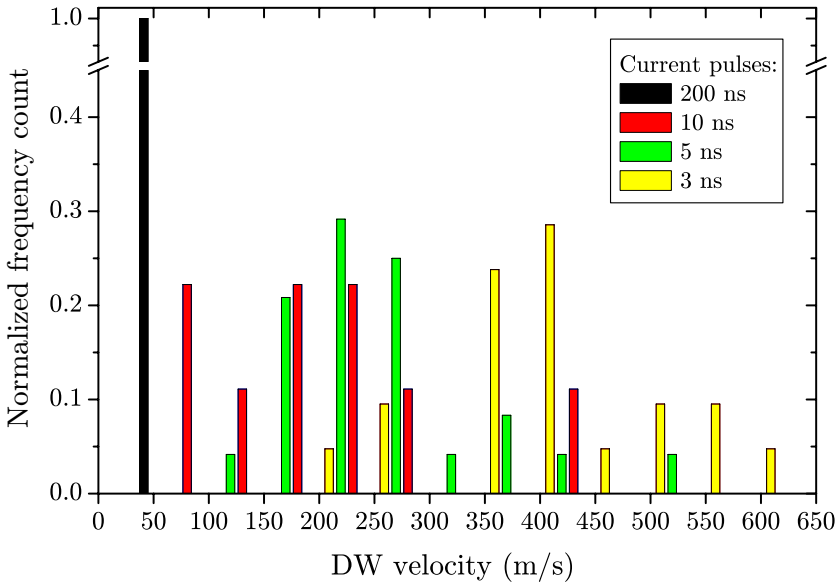

Fig. 6.6: DW velocity distributions obtained for a 200 nm wide nanowire using a current density of 3.3×10^{11} A/m^2 and pulse durations ranging from 3 ns to 200 ns. The computed velocities for 200-ns pulses all lie in the region below 50 m/s. The columns represent a relative number of events of a given pulse duration in the marked interval (0 – 50 m/s, 50 – 100 m/s, etc.)

6.2.2 Statistics of the Current-Induced DW Motion

As seen in the previous section, the XMCD-PEEM images taken after application of a single current pulse to an initial multidomain structure show that in general some DWs move, but also many DWs are pinned and do not move for the range of current densities used during the experiment ($1.0 \times 10^{11} - 4.2 \times 10^{11}$ A/m^2 in the NiFe layer). Taking into account only the DWs which were mobile for the applied current densities, we have deduced, starting from many different initial configurations, DW displacement and velocity distributions for different pulse lengths and current densities (see Fig. 6.6-6.8).

Note that these statistical distributions do not correspond to a description of repeated displacements of the same DWs, but to the displacement of a multitude of DWs in different parts of the nanowire. This gives a good description of the average behavior of the system, i.e. such a comparison of DW displacements is not burdened by a specific pinning potential of a particular DW. Also, DW displacements which occurred between the same pinning sites multiple times, thus influencing the statistics, were removed from the statistical file.

Fig. 6.6 shows DW velocity distributions for a 200 nm wide nanowire using a current density of 3.3×10^{11} A/m^2 and different pulse lengths. For each pulse length, approximately 50 events were analyzed. A very large distribution of velocities is obtained, ranging from below 50 m/s to more than 600 m/s. The highest velocities could be achieved only using 3 ns long pulses. On the contrary, for very long current pulses (200 ns) only very low velocities are observed. A direct comparison of the displacements obtained with these very different pulse durations shows that they do not scale

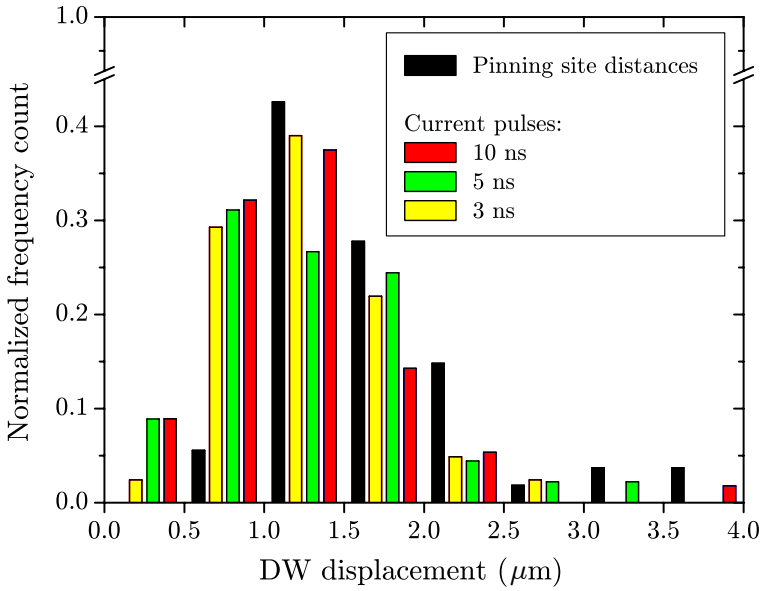

Fig. 6.7: Distributions of DW displacements compared to the distribution of nearest neighbor pinning site distances in a 200 nm wide nanowire, obtained for current densities in the range $2 \times 10^{11} - 4.2 \times 10^{11}$ A/m^2. For each pulse length, approx. 50 events were analyzed. The count of displacements is integrated for each marked interval. Note that the spatial resolution of our experiment did not allow determining pinning site distances smaller than 500 nm, though a relative DW displacement can be determined with a higher precision.

with the pulse length and that their values are very close in general. This strongly suggests that the motion is actually limited by the positions of the pinning sites. This also explains why only by using short pulses we can provide a reliable estimate of the absolute value of the DW velocity.

To further support the assumption of DW motion limited by pinning, we have compared the integral distributions of current-induced displacements for pulse durations of 3, 5 and 10 ns in a 200 nm wide nanowire — including all current density values — with the distribution of the apparent pinning site distances (see Fig. 6.7). The pinning site positions were identified as zones with an intermediate XMCD intensity (see Section 6.3.2). The distances between them were determined from an image of the saturated state, like in Fig. 6.12(a), where the pinning site positions are indicated by white arrows.

It appears that a clear correlation exists between the current-induced displacement distributions and the distances between pinning sites. For current pulses ranging from 3 to 10 ns most of the displacements are constrained between 0.5 and 2 μm. This is again an indication of the role of pinning sites in the DW motion. As a matter of fact, a distribution of displacement scaling with the pulse duration would result in a diagram where the highest number of events (the distribution modus) should be found in increasing displacement ranges for increasing pulse durations.

Comparing the frequency count of the DW displacements and pinning site distances in detail, it appears that the number of DW displacements in the 0.5 - 1 μm range is significantly higher than the number of nearest neighbor pinning site distances in the

same interval. This could mean that the pinning potential is considerably higher for pinning sites separated by 0.5 - 1 μm, which is unlikely, or that these DW displacements correspond to events where the DW has stopped in between two pinning sites more distant than 1 μm.

Because of the large pinning probability, DW displacements scaling with the pulse duration were only observed in a few cases and for current pulses shorter than 12 ns (shorter than 20 ns for 400 nm wide nanowires in Section 6.2.1). Given the values of the DW velocities and the most probable pinning site distances, it is clear that these events are unlikely: a DW propagating freely at a velocity of 400 m/s moves by 4 μm in 10 ns; as seen in Fig 6.7, there are indeed very few regions of the nanowire where pinning sites are so distant. We emphasize however that the occurrence of displacements scaling with the pulse durations is an important proof that the DW moves during the current pulse and not only during the leading and falling edge of the current pulse [343].

Since the pinning causes a strong dependence of determined DW velocities on the pulse length, the DW velocity values are often underestimated. A DW moving at 600 m/s for 3 ns travels a distance of 1.8 μm, i.e. even 3-ns pulses might be too long for observation of the ultimate DW velocity in this spin-valve system.

Hence, in the following we will rather focus on the dependence of the DW displacement on applied current density (Fig. 6.8). Though the minimum current density for which we observed DW motion was 2×10^{11} A/m^2, for better orientation in the graph we limit the number of distributions and in particular those obtained for higher current

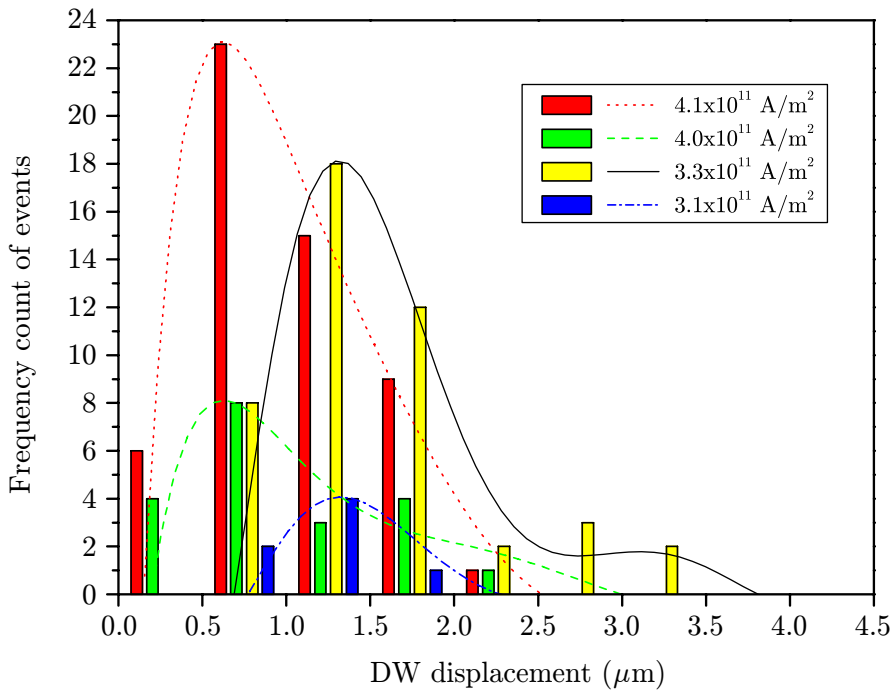

Fig. 6.8: DW displacement distribution in the NiFe layer, induced by current pulses of variable density. The lines are polynomial fits of the displacement distribution for a given current density and represent guides to the eye.

densities are shown. The average value of the DW displacement first shifts towards higher values as the current increases, but for the highest current values the average displacement decreases.

One can notice that the displacements shorter than the minimum measurable pinning site spacing (i.e. less than 500 nm, see Fig. 6.8) are exclusively induced by current densities higher than 4×10^{11} A/m^2. These displacements were obtained for pulse durations from 3 to 10 ns as indicated in Fig. 6.7. Given the influence of pinning on the DW displacement, especially for long pulses, we verified that the shift of displacement distributions induced by high current densities was reproduced also when only short pulses of 5 ns were taken into account.

In Fig. 6.9 we display the dependence of the average DW velocity on the injected current density. The DW velocity value was obtained by dividing the average DW displacement by the length of the corresponding current pulse, either 3 or 5 ns. For the shortest pulses, 3 ns long, we indeed obtained the highest DW velocities (see also Fig. 6.6).

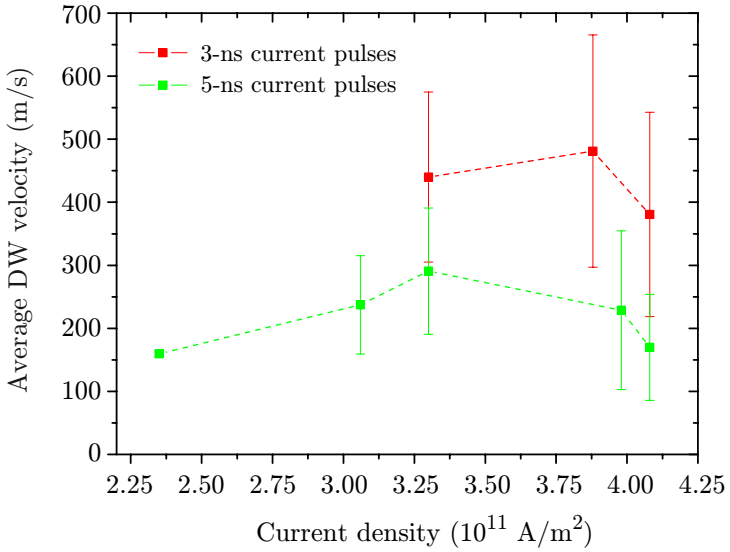

Fig. 6.9: DW velocity in 200 nm wide nanowires as a function of current density for short pulses of 3 and 5 ns.

The average DW velocity increases linearly with current density up to 4×10^{11} A/m^2. Above 4×10^{11} A/m^2, a substantial drop in the average velocity occurs. This phenomenon is apparent for both indicated pulse durations. The large error bars are mainly due to the influence of pinning which widens the displacement distributions.

The current-induced DW motion was also studied in 300 and 400 nm wide nanowires. Unfortunately, we do not possess enough data for a wide range of current densities and short current pulses as in the case of 200 nm wide nanowires. Fig. 6.10 shows a velocity versus current density diagram for a 400 wide nanowire where the velocity values were obtained for 15 and 25 ns long current pulses. We observe a linear increase of DW velocity without any decrease throughout the inspected current density range. The behavior at higher current densities has to be verified in future experiments.

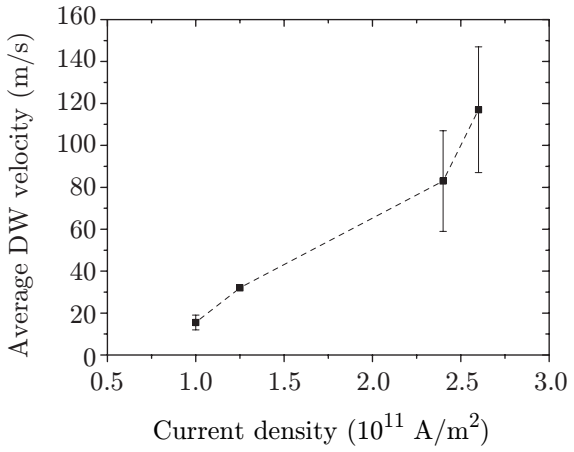

Fig. 6.10: DW velocity as a function of current density for a 400 nm wide nanowire.

6.3 Pinning

6.3.1 Determination of Pinning Strength

In Sections 6.2.1 and 6.2.2 we already showed that the DWs move at large velocities for relatively low current densities, but the DW motion is strongly hampered by pinning at local defect positions. This has been confirmed systematically in the present experimental series. Fig. 6.11 shows the NiFe domain structure obtained after application of one 40 ns long magnetic pulse of increasing amplitude. While some domains are unpinned by successive field pulses, a complete saturation of magnetization in the individual zigzag sections cannot be reached for the maximum field we used. This indicates that the pinning strength at specific positions of the nanowire is larger than 12 mT, i.e. the maximum field used here (17 mT) projected on the direction of the zigzag section.

These measurements prove that the DWs are pinned in both cases, when magnetic field and spin-torque are the driving forces for displacement. In our experiment, even if the domain structure cannot be saturated, we often use the magnetic pulses to reinitialize the multidomain configuration, in particular when the DWs get so strongly pinned that they cannot be moved with current anymore.

6.3.2 Possible Origin of Pinning

DW pinning may be induced by structural, topographic or magnetic defects. In Section 6.2.1 we showed that the DWs usually stop and often get blocked for subsequent current pulses in regions of the nanowires with intermediate XMCD intensities [further called “gray zones”, shown as an example in Fig. 6.12(a)]. The modified contrast in these regions could be induced by features lowering the total x-ray absorption, like defects introduced due to the lithography process or manipulation of the sample. However, this origin can be discarded, because the corresponding features are generally

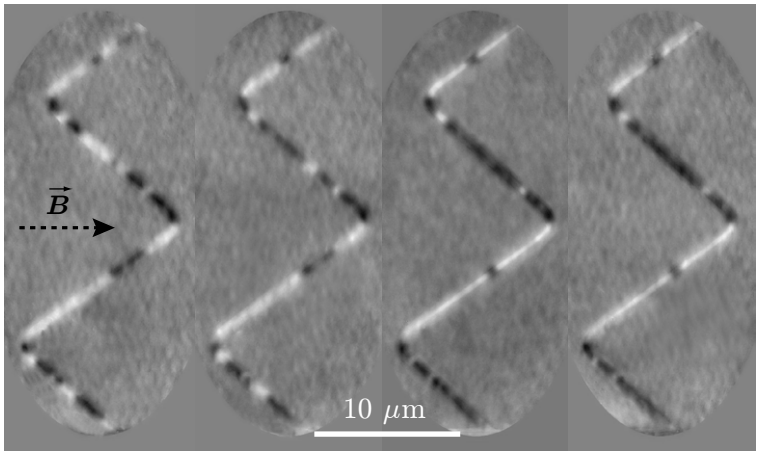

Fig. 6.11: Measurement of the pinning strength of DWs in a 200 nm wide nanowire. The NiFe domain structure is imaged after application of one 40 ns long magnetic pulse of increasing amplitude, going from 7 mT to 17 mT. The remaining small domains indicate the sites with the largest pinning potentials.

absent in the sum of the images obtained for right- and left-circular polarizations. By consequence, we conclude that the reduced XMCD intensity is of magnetic origin. Since the XMCD contrast is proportional to the projection of the local magnetic moment on the incoming photon direction [vertical in Fig. 6.12(a)], a modified XMCD intensity can be caused by a tilt of the local magnetization away from the easy axis, by a reduction of the local magnetic moment or by domains (360° DWs) smaller than our spatial resolution. In the following, we discuss the different origins of the defects that can give rise to DW pinning and their possible relation to the observed regions of an intermediate XMCD intensity – the gray zones.

6.3.3 Structural and Topographic Defects

The structural defects associated with DW pinning in the NiFe layer of our spin-valve nanowires could be of intrinsic character, corresponding to grain boundaries or a distribution of anisotropy directions among individual grains. However, it is unlikely that these defects act as pinning sites, as the magnetocrystalline anisotropy of NiFe is small and the grain size deduced from Transmission Electron Microscopy images (see Section B.5) is between 5 and 10 nm, which is much smaller than the minimum measurable DW displacement. Moreover, similar features were observed for samples where the soft magnetic layer was ultrasoft amorphous CoFeB, for which the effect of grain boundaries and magnetic anisotropy should be negligible.

DWs may also be pinned by geometrical constrictions in the nanowire [214] or by lateral roughness arising from the lithography process. This mechanism is also unlikely, as the Scanning Electron Microscopy images [Fig. 6.12(b)] of the nanowires described in Sections 6.2 and 6.3 do not reveal any substantial lateral roughness (larger than units

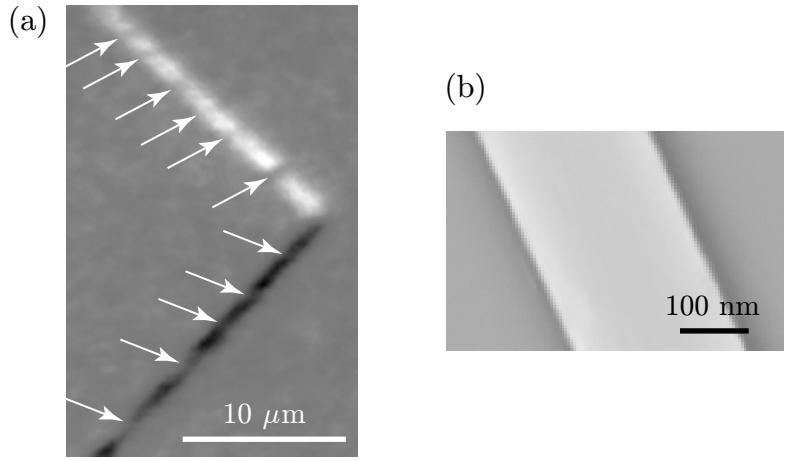

Fig. 6.12: (a) XMCD image of a 200 nm wide nanowire with magnetization saturated by a transverse field, showing regions of intermediate XMCD intensity associated with DW pinning sites (indicated by white arrows). (b) SEM image of the nanowire showing no considerable lateral roughness. In (a) the contrast was expanded in order to better visualize the gray zones.

of nm) that could influence the magnetization behavior. The gray zones associated with DW pinning are on average approximately 200-300 nm wide, suggesting that the edge roughness is not the main origin of the DW pinning.

When heating adjacent NiFe and Cu layers above 150°C, Ni and Cu intermix (see Section 3.6) and can form clusters of NiCu which would decrease locally the NiFe magnetization. To avoid this effect, the temperature during the lithography and deposition processes was always kept below 90 °C. At this low temperature, interface intermixing that could give rise to gray zones is not expected.

6.3.4 Interlayer Dipolar Interactions

In spin-valve nanowires, magnetic coupling between NiFe and Co due to the orange-peel interaction associated with rough interfaces might represent a possible source of DW pinning [12]. For this reason specific spin-valve samples with optimized interface quality were prepared using ion-beam-assisted deposition (see Section 3.5). We managed to strongly decrease the roughness of the NiFe/Cu/Co interfaces and the magnetic interlayer coupling was almost suppressed. Although the coercive field of NiFe in the zigzag structures was decreased substantially, the zones of modified contrast were still present in the XMCD images. These results rule out the possibility that the strong pinning is caused by interfacial roughness.

Stray fields associated with the presence of DWs in the Co layer are expected to have a strong influence on the local magnetization of the NiFe layer [116]. XMCD-PEEM measurements at the Co L_3 edge (779 eV) carried out for a NiFe/Cu/Co spin valve with a 3-nm Cu spacer [see Fig. 6.13(a)], allowed us to prove that for the same magnetic field values inducing a domain structure in the NiFe layer, the DWs in the Co layer are always and exclusively located at the zigzag corners and therefore are not

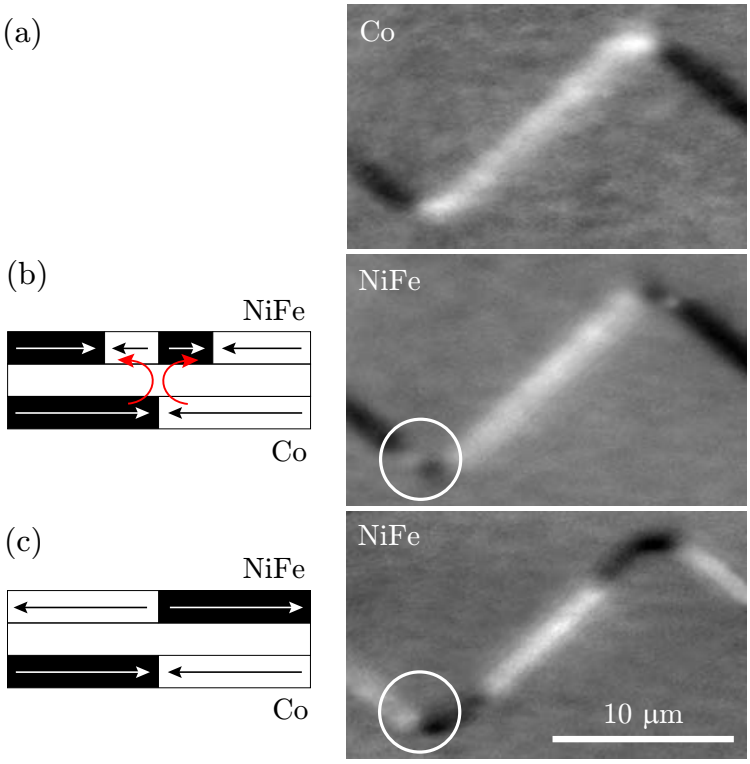

Fig. 6.13: XMCD-PEEM images of the NiFe and Co layers of a NiFe/Cu(3nm)/Co trilayer structure, obtained after application of a strong field in the transverse direction. (a) The image taken at the Co L_3 edge shows that the DWs in the Co layer are located exclusively at the zigzag corners; in the NiFe, two kinds of domain structures can be found close to the corners, depending on whether the NiFe and Co magnetizations are parallel (b) or antiparallel (c).

responsible for the modified contrast in the NiFe layer along the straight sections.

As already seen for spin-valve continuous layers [337], the stray field associated with the Co DWs strongly influences the domain configuration in the NiFe layer above. The character of the domain structure in the NiFe layer observed near the corners of the zigzag, is a signature of the mutual orientation of the two ferromagnetic layers. If the Co and NiFe magnetizations are parallel, the stray field of the Co DW locally reverses the magnetization in the NiFe layer, giving rise to the three DWs shown in the white circle in Fig. 6.13(b). If the Co and NiFe magnetizations are antiparallel, the magnetic flux closes naturally and a single DW is formed [Fig. 6.13(c)]. This strong coupling prevents current-induced DW motion across the local stray fields[3] of the Co DWs. This source of DW pinning can be avoided by creating a single domain in the Co layer along the nanowire.

Having excluded all the discussed defects as sources of DW pinning along the straight zigzag sections, we suggest that the localized gray zones could be induced by a local tilt of the magnetization in the Co layer (caused for instance by anisotropy

[3]The stray field of a Co DW in a NiFe layer of a 200 nm wide nanowire is approximately 40 mT in the transverse direction (calculated using the OOMMF code [338]).

defects) and the consequent tilt in the NiFe layer caused by the dipolar interaction.

In order to verify this, we have carried out micromagnetic simulations by OOMMF [338]. The following parameters were used: spontaneous magnetization $M_S^{NiFe} = 800\,kA/m$, $M_S^{Co} = 1400\,kA/m$, exchange constant $A_{ex}^{NiFe} = 1 \times 10^{-11}\,J/m$, $A_{ex}^{Co} = 3 \times 10^{-11}\,J/m$, magnetocrystalline anisotropy $K_1^{NiFe} = 0\,kJ/m^3$ and a cell size $4\times4\times5\,nm^3$.

For cobalt the bulk anisotropy constant $K_1^{Co} = 520\,kJ/m^3$ valid for the HCP structure was used. Assuming that the crystallographic easy axis (c-axis for HCP) points in the out-of-plane direction, the in-plane magnetization directions are energetically equivalent in the case of a continuous film. As the magnetization is forced to lie in the plane of a 5-nm Co layer due to the shape anisotropy, this situation is equivalent to setting the effective in-plane anisotropy constant K_{eff} to 0.

Another situation is found when the crystallographic easy axes of grains are oriented in-plane. Indeed, the effective in-plane anisotropy constant K_{eff} of cobalt then depends on the grain size. In the simulations we use K_{eff} of 50 kJ/m^3 with an easy axis oriented along the nanowire. Such a K_{eff} value might be realized by decreasing the grain size[4] to approximately $8\times8\,nm^2$, while keeping the K_1 of each grain at the bulk value and by assuming a random orientation of the easy axis in each grain. It was verified that a tilt of magnetization induced by a magnetic field transverse to the nanowire reaches the same value in cases of the described multi-grain nanowire and of a uniform nanowire with K_{eff} of 50 kJ/m^3. However, it should be pointed out that the value of K_{eff} does not influence the result of the following discussion.

In the actual simulation of the localized defects we considered a 200 nm wide NiFe/Cu/Co nanowire. K_{eff} of 50 kJ/m^3 is imposed to exist everywhere in the Co layer, except at the defect positions. Fig. 6.14(a) shows a defect of a size[5] of $100 \times 100\,nm^2$ and K_1 of $520\,kJ/m^3$ with an in-plane anisotropy axis tilted at 45° with respect to the nanowire. The shape anisotropy is not strong enough to balance the Co magnetocrystalline anisotropy and to align the magnetization of such a defect along the nanowire. It can be seen that the stray field associated with such a defect tilts the magnetization in the NiFe layer above by about 35°. Such a tilt of the NiFe magnetization is expected to result in a modified XMCD intensity with respect to the case when the magnetization is along the line [Fig. 6.14(a)]. The opposite change in XMCD intensity in the Co and NiFe layers is a clear indication of this effect. Fig. 6.14(b) shows high-resolution XMCD-PEEM images[6] of a NiFe/Cu 8 nm/Co trilayer. XMCD intensity variations corresponding to the opposite tilts of local magnetization are found at the same positions in the NiFe and Co layers.

Obviously, the tilt angle of the NiFe magnetization should depend on the value of the magnetocrystalline anisotropy in the Co layer and on the defect volume. However, we found that for a $100 \times 100\,nm^2$ defect the magnetization tilt in both layers was not modified upon reducing the magnetocrystalline anisotropy in the Co layer by 1 order

[4]The grain size was deduced from TEM observation of the Co layer cross-section.

[5]We suppose that the defect is a group of grains with a similar crystallographic orientation which causes a homogeneous magnetization tilt in the defect. These groups of grains were confirmed by FIB milling of Co films (see Section 4.4.1).

[6]The experiment was carried out at the synchrotron Elettra in Trieste, Italy. To visualize the XMCD contrast in the Co layer, the NiFe layer was partially sputtered off in-situ.

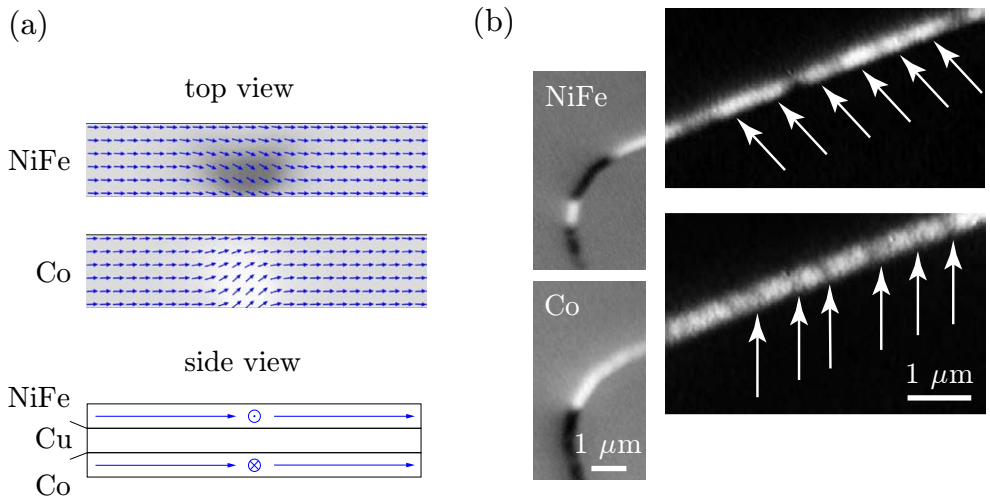

Fig. 6.14: (a) Micromagnetic simulations showing that a local defect associated with a variation of the Co anisotropy direction induces a local tilt of the NiFe magnetization that modifies the XMCD intensity. (b) High resolution PEEM images taken for the NiFe and Co layers – the white arrows indicate the positions of selected gray zones in the Co layer and corresponding magnetization tilts in the NiFe layer. In the right part of (b) the contrast was expanded in order to better visualize the gray zones.

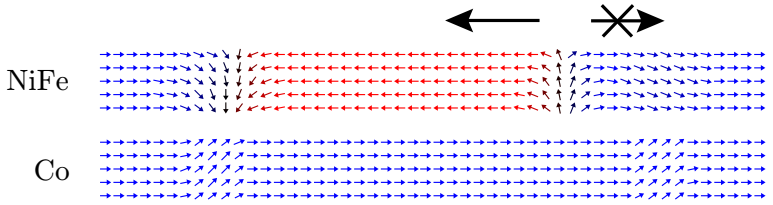

Fig. 6.15: Micromagnetic simulations showing the effect of an anisotropy defect in the Co layer on the magnetization and DW propagation in the NiFe layer. Each sketch represents a top view of the magnetization distribution in individual layers: The magnetization of the NiFe DW on the left is in the same direction as the stray field induced by the Co anisotropic defect just underneath; this DW is pinned. The DW on the right, situated beside the stray field region, has opposite chirality with respect to the Co stray field direction; this DW can be only moved away from the defect by current.

of magnitude.

The stray field generated by the Co anisotropy defects represents a considerable obstacle for the DW motion in the NiFe layer, as shown by the results of simulations presented in Fig. 6.15. Depending on the mutual orientation of the Co stray field and the transverse NiFe DW chirality, the DW is pinned (left panel) or is free to move away from the pinning site (right panel). Simulations show that whatever its chirality, a DW can cross the region where the Co stray field is present only when applying a strong-enough magnetic field dependent on the size and tilt of the anisotropy defect.

Moreover, the magnetic field needed to displace a DW pinned above a Co defect in opposite directions is not symmetric. The difference might be a few mT and depends on the mutual orientation of the magnetization in the Co layer and the applied field.

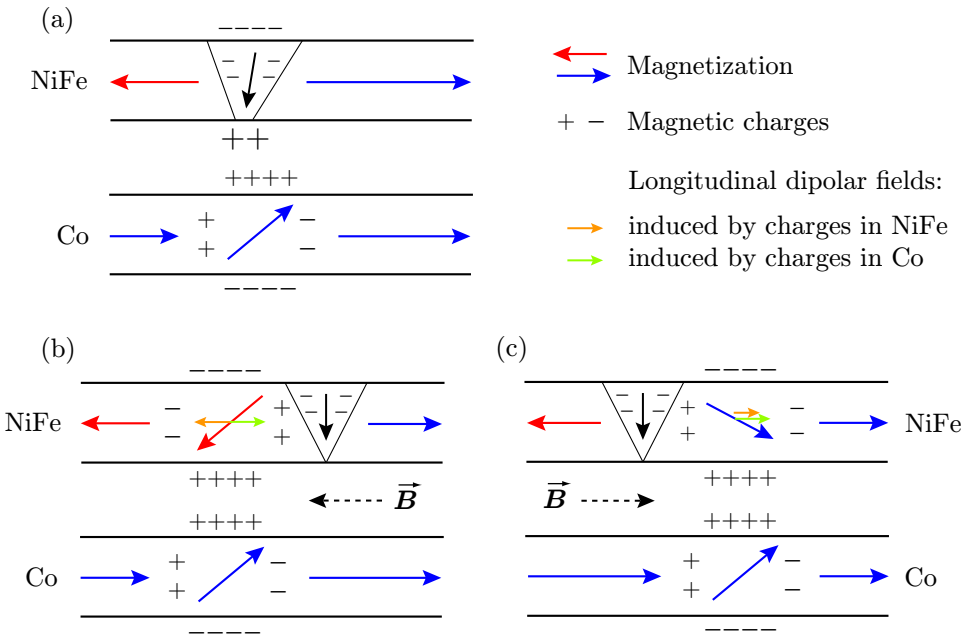

Fig. 6.16: Asymmetric pinning of a DW in the NiFe layer above a Co anisotropy defect: (a) Initial situation for a tail-to-tail DW. A different distribution of volume charges appears in the NiFe layer when the DW is displaced to the right (b) or left (c) of the defect. The DW is more pinned in (c), because it is attracted to the uncompensated volume charges in the NiFe and Co layers.

An explanation is schematically shown in Fig. 6.16. Fig. 6.16(a) represents the initial situation of the pinned tail-to-tail DW. Surface and volume magnetic charges are schematically indicated. When applying a magnetic field pointing to the left, the DW moves to the right and the NiFe magnetization above the Co defect tilts because of the stray field as indicated in Fig. 6.16(b). The longitudinal stray field arising from the tilt of NiFe magnetization compensates that one arising from the tilt in Co. Fig. 6.16(c) shows a situation when the applied field points to the right and the DW is displaced to the left. Now both the longitudinal stray fields point in the same direction and attract the DW back to the defect. The same is valid for a head-to-head DW. To reverse the prefered direction of the applied field for DW depinning, the Co magnetization has to be reversed.

Further we used an OOMMF spin-torque extension, developed by A. Vanhaverbeke et al. [341], to study the current-induced DW motion in the NiFe layer. Since it is not possible to set different spin-torque parameters for different layers in this code, we applied the same current density to the whole NiFe/Cu/Co system, supposing there are no spin-torque effects in the quasi-uniform[7] Co layer. Hence, the Co layer acts just as a source of local stray fields influencing DW motion in the NiFe layer. The spin-torque parameters α and β were set to 0.02 and 0.04, respectively, values for which the experimental observations of CIDWM were well reproduced [86, 46].

When applying current pulses to the nanowires, an interaction takes place between

[7]Except of the anisotropy defects.

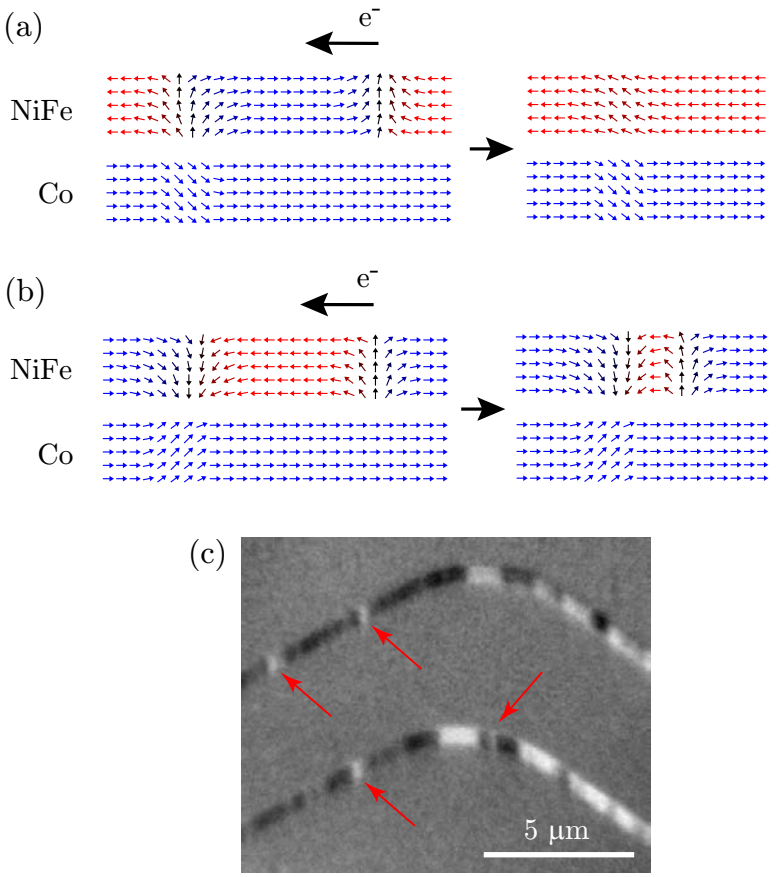

Fig. 6.17: (a) Effect of current when approaching two DWs of the same chirality in NiFe (left panel) is to annihilate them (right panel). (b) Current pushes the DW on the right (left panel) towards a DW of an opposite chirality and a 360° DW is formed (right panel). (c) High-resolution PEEM images of a 200 nm wide NiFe/Cu/Co nanowire. White arrows indicate the positions of possible 360° DWs in the NiFe layer.

a DW pinned above a Co defect and a free DW displaced by current. If two DWs of the same chirality approach, they annihilate [only a gray zone remains – at the place where one of the DWs was pinned, see Fig. 6.17(a)]. If two DWs of opposite chirality approach, they form a 360° DW [Fig. 6.17(b)]. A more detailed study of DW collisions dependent on their chirality has been published recently [339, 340]. Experimentally, the presence of possible 360° DWs can be seen in the high-resolution PEEM images [indicated by red arrows in Fig. 6.17(c)]. Because of the limited resolution of our IS-PEEM used for the DW dynamics, we cannot distinguish between a simple magnetization tilt and such a 360° DW. However, nucleation-like effects at the gray zones can be due to an expansion of this kind of a DW (see also Section 6.5.3).

6.4 Discussion

Pinning

Most DWs in our spin-valve nanowires were depinned within the range of current densities we applied. However, some DWs at particular positions in the nanowire were impossible to move. As mentioned above, these positions of strong pinning sites were always associated with zones of intermediate XMCD intensity. The conclusion of the above discussion on the possible origins of DW pinning is that the dipolar interaction between the magnetization of the NiFe layer and the anisotropic defects in the Co layer are likely to play the most important role.

Our results clearly indicate that the issue of DW pinning is the main drawback for the use of spin-valve-like systems in DW memory applications. Several ways may lead to decrease the role of the pinning.

The CoO underlayer could be one cause of the distribution of anisotropy axes in the Co grains, so although the CoO improves the Co growth, it might induce relevant pinning sites for the whole system. However, when examining spin-valve nanowires without CoO we realized that the effect of "gray zones" was still evident.

Switching to epitaxial systems might be the solution for obtaining trilayers with less defects. It can be foreseen that once pinning will be better understood and controlled, and reproducible DW motion will be obtained, spin-valve devices could become a very valuable system for applications. A proof of the fact that such reproducible back and forth motion between pinning sites can be obtained in our trilayer systems is shown in Fig. 6.18. The DW could be moved many times between the two positions, using 2.5-ns current pulses of opposite polarity and a relatively low current density (3.5×10^{11} A/m^2).

Pinning-limited DW motion may explain ambiguous results reported in the literature for both NiFe and NiFe/Cu/Co systems; when very long pulses are used [343] the DWs are likely to move only during the first part of the pulse before being pinned,

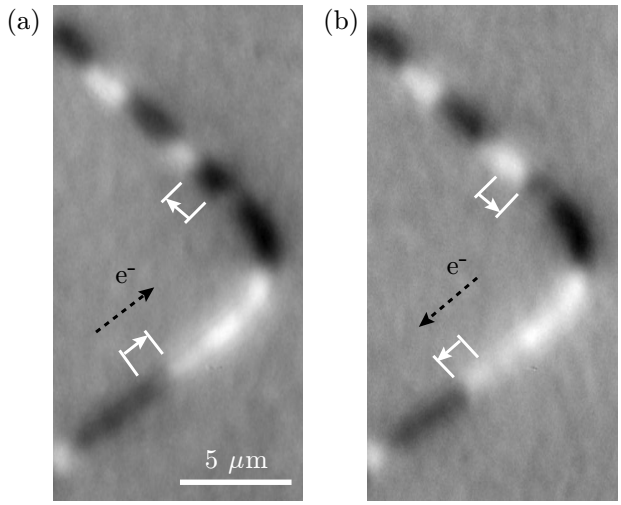

Fig. 6.18: Reproducible back and forth motion between pinning sites of two DWs using 2.5-ns current pulses of opposite polarity and a current density of 3.5×10^{11} A/m^2.

leading to DW displacements not related to the pulse length and underestimated DW velocities. Our study confirms that DW pinning during the pulse has to be thoroughly taken into account before discussing the DW dynamics.

Nucleation of Domains and DW Depinning

One of the obstacles we found for determining the velocity of the DW is the fact that, particularly at high current densities, nucleation and annihilation of domains may take place, thus increasing or decreasing the apparent DW velocity.

It was theoretically shown that large spin currents applied to a uniform ferromagnet lead to a spin-wave instability resulting in nucleation of magnetic domains [344]. Current-induced domain nucleation was also observed experimentally, by measurements of GMR in spin-valve nanowires [215] and by Lorentz microscopy and electron holography [345]. The latter study shows nucleation induced by thermal excitation (see Section 6.1.3).

Using time-resolved XMCD-PEEM (see Section 6.5.2) we have demonstrated that the Oersted field generated by the current flowing in the Cu and Co layers of a spin-valve nanowire has an important effect on the NiFe magnetization.

The effect of the Oersted field on the magnetization reversal was also observed by Morecroft et al. [347] in notched Au/Co/Cu/NiFe nanowires. In this study the Cu resistivity was surprisingly found bigger than in the other layers. The current flowing in the Au/Co/Cu sandwich induced a transverse field in NiFe which was however not sufficiently high to induce a magnetization reversal without application of a longitudinal bias field.

Besides its implication on the static magnetic configuration in SV nanowires, we also find that the Oersted field torque clearly affects the magnetization dynamics, by inducing a precession of the magnetization around the effective transverse field (see Section 6.5.2). This phenomenon might be responsible for domain nucleation above a threshold current density. This nucleation is most probable to happen at locations where a magnetization tilt in the transverse direction is already present before the current pulse, like at position B in Fig. 6.2(c). This effect is similar to the reversal of magnetization in magnetic nanostructures [362] by the application of perpendicular magnetic field pulses.

In Ref. [213], a non-explained reversal of the direction of the DW motion was observed above a certain current threshold value, in spin-valve nanowires of identical composition as ours. Our results suggest that this effect could possibly be explained by a nucleation of a domain followed by DW motion in the direction of the electron flow, as proposed in Section 6.2.1. It is clear that a direct observation of the domain structure and DW motion using magnetic imaging can greatly help understanding results obtained using magnetoresistance measurements.

In addition, the nucleation of several DWs moving at the same time could result in occasionally observed large DW displacements, even longer than $10\,\mu$m [213]. Particularly for short nanosecond current pulses, this can lead to large overestimation of the DW velocity. Another aspect which should be borne in mind, reported in literature, is the assumption that a DW can move after the end of the magnetic field or current

pulse [62, 137]. In our time-resolved experiments, when the photon bunches were synchronized with the end of the current pulse, the DW was found at its final position, the same where it was observed after the pulse. Hence, no evidence of an inertial DW motion was found, but this effect could be hindered by pinning.

Thomas et al. reported that the character of DW depinning from a notch is very sensitive to the pulse length [222]. This behaviour is related to the current-induced precession of the DW trapped in a pinning potential. It was shown that, depending on the pulse duration with respect to the instantaneous phase of the DW precession when the pulse finishes, the DW can be depinned and displaced in or against the direction of the electron flow. This could explain the occasional opposite-to-current DW motion. However, as this effect takes place at the end of the pulse, it should not be a cause for long-range displacements in the opposite direction to the current.

Critical Current Density

The lowest current density for which the DW motion was observed in our samples was $2\times10^{11}\,\mathrm{A/m^2}$ for both the 200 nm and 300 nm wide nanowires and $1\times10^{11}\,\mathrm{A/m^2}$ for the 400 nm wide nanowires. This value is slightly larger than for CoFeB/Cu/Co nanowires [230], but is 3-4× lower than those published for single NiFe nanowires for similar thicknesses and widths of the NiFe layer [182]. For thicker and wider NiFe layers, a decreasing trend of critical current density is found [349]. The actual depinning current value is determined by the strength of the individual pinning sites. In our experiments, once depinned, the DWs move at high velocities, showing we work well above the intrinsic critical density. Because of the short pulse length and limited spatial resolution in our experiment, DW motion at very low velocities could not be detected. This seems to indicate that dc current injection [181, 230] is better suited for finding the critical current density. However, it was also shown that the depinning probability decreases with the rise time of the current pulses [188].

The Oersted field might also modify the DW shape resulting in either DW widening or narrowing. If the DW widens, depinning becomes easier and this might explain the lower critical current densities found for spin-valve nanowires [181, 213, 230] with respect to single NiFe nanowires [141, 349].

High Domain-Wall Velocities

In contrast to previous publications where very low values of DW velocities were reported for single NiFe nanowires [343], Hayashi et al. [141] presented a maximum DW velocity of 110 m/s (for $j = 1.5\times10^{12}\,\mathrm{A/m^2}$) at zero applied field in 300 nm wide NiFe nanowires. The DW velocity was obtained for optimized nanowires in terms of DW pinning [350] and the value was determined using a time-resolved magnetoresistance measurement, by dividing the DW displacement by the time the DW takes to move between these points. The mentioned velocity value is larger than the spin angular momentum transfer rate u for any $P < 1$ (for $P = 0.7$, u is about 75 m/s and $\frac{\beta}{\alpha} \approx 1.5$). Using the same parameters, our current density $j \approx 5\times10^{11}\,\mathrm{A/m^2}$ would lead to an expected spin transfer rate u of about 25 m/s. An experimentally associated velocity of 600 m/s would then correspond to a very large $\frac{\beta}{\alpha}$ of about 24. Such a large

nonadiabaticity seems unlikely and new spin transfer mechanisms must be considered to explain our high DW velocities. In this study, the highest DW velocity found for 200 nm wide nanowires was (700 ± 20) m/s induced by a 3-ns pulse of a current density of 3.9×10^{11} A/m^2. Nevertheless high velocities appeared more frequently in the range of 600 – 650 m/s.

We believe that the presence of the Oersted field may strongly influence the DW dynamics. Transverse DWs with a magnetization parallel to the Oersted field should be stabilized. The stabilization of one type of transverse DWs during the CIDWM should inhibit DW transformations during propagation (beyond the Walker breakdown), which are known to significantly slow down the DW motion [128, 75]. This mechanism probably leads to a shift or a suppression of the Walker breakdown and therefore allow high velocities to be reached. This effect is equivalent to that observed for field induced DW motion, where Glathe et al. [88] have shown that application of a transverse magnetic field can considerably increase the longitudinal field for which the Walker breakdown takes place. This has also been modeled recently [92]. However, micromagnetic simulations of CIDWM including the Oersted field are necessary to confirm and extend this hypothesis.

The very large DW velocities observed in NiFe/Cu/Co systems force us to question the actual mechanisms related to the current-driven DW motion in such devices. Besides the amplification of the effect by the Oersted field, another specificity of the SV nanowires is the existence of a spin accumulation inside the Cu spacer layer in the region of the DW, giving rise to a spin current injected vertically in the DW. The better efficiency of spin torque in this situation has been theoretically demonstrated by studying DW motion in long and narrow SV nanowires with a perfect vertical injection of the current [231]. In the case of a planar polarizer (as in our case), micromagnetic simulations predict a linear dependence of the DW velocity with the injected current density, with velocities above 200 m/s for a current density of 2×10^{11} A/m^2. Even if the comparison with our experiments is not straighforward as we inject the current in the film plane, such additional spin transfer torque due to local spin accumulation can be can contribute to the very large DW velocities.

Recently, Boone et al. [232] have indirectly measured DW velocities up to 800 m/s in the NiFe layer of a spin-valve nanowire from the resonant excitation of a DW in a local pinning potential by a vertical current injection (current density of $j_{\mathrm{ac}} = 9 \times 10^{10}$ A/m^2). This velocity value, obtained with the current flowing entirely in the direction perpendicular to the multilayer plane, is very close to our observations.

Finally, we discuss the decrease of the average DW velocity observed for current densities above 4×10^{11} A/m^2. A first reason of this decrease could be related to the increase of the total number of DWs that are depinned for high current densities, as we have observed in our images. Very large current densities may lead to an increased depinning probability (see also Section 6.5.1) of some strongly pinned DWs, giving rise to short DW displacements. Note that this hypothesis is weakened by our observation that some very mobile DWs moved over a substantially shorter distance for a current density of 4×10^{11} A/m^2 than for a lower current density of 3.1×10^{11} A/m^2, as shown in Fig. 6.19. This observation suggests that the observed decrease in the DW velocity

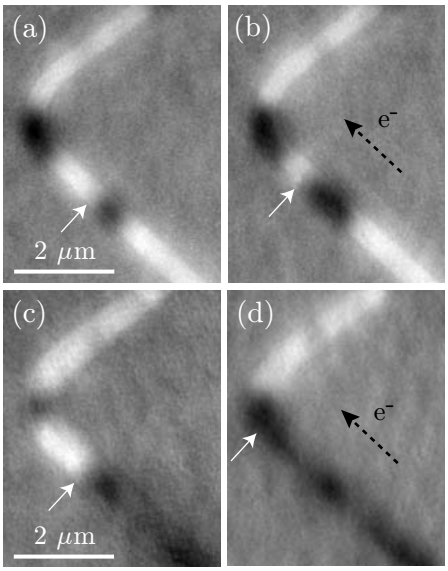

Fig. 6.19: Domain structures obtained: (a) before and (b) after the application of a 10-ns pulse of a current density of $4.1 \times 10^{11}\,\mathrm{A/m^2}$; (c) before and (d) after the application of a 5-ns pulse of current density $3.1 \times 10^{11}\,\mathrm{A/m^2}$. The displacement induced by the first stronger and wider pulse is shorter than that induced by the subsequent shorter pulse of lower current density. Positions of the DWs are indicated by white arrows.

above a certain current density is real and not an artefact due to the measurement procedure or to pinning restrictions.

We conclude that the Oersted field (for details see Section 6.5.2) is probably also at the origin of the drop in the DW velocity observed above a certain threshold current density. On one hand, the Oersted field can stabilize the transverse walls, but on the other hand, it induces precession of the magnetization of a DW during its motion which might be a cause for the velocity drop above $4 \times 10^{11}\,\mathrm{A/m^2}$. Another consequence of the Oersted field parallel to the magnetization of a DW is the DW widening which could result in a lower efficiency of the nonadiabatic component of the spin torque and therefore lead to lower DW velocities. Note however that it was shown for field-induced DW motion that canting of magnetization in the nanowires caused by a transverse field increases the DW velocity if the field and the DW magnetization are parallel and decreases for the antiparallel alignment [92]. This behavior was observed for magnetic fields below the Walker breakdown.

6.5 Dynamic Imaging

The time-resolved imaging technique was described in Section 5.2.1. In the present study the stroboscopic set-up is exploited to investigate different aspects of the magnetization dynamics in trilayered nanowires.

6.5.1 DW Depinning

As explained above, when working in the stroboscopic mode with the current pulses synchronized with the x-ray bunches, each image is an average of several millions of DW configurations. When the current density is above the critical value for depinning, the contrast of the image acquired with the x-ray bunches set after the current pulse gives information on the depinning probability.

The data were obtained for a 300 nm wide CoFeB/Cu/Co nanowire with identical layer thicknesses as the NiFe/Cu/Co nanowires described in Section 6.2. A lower pinning and lower critical current densities are expected for CoFeB, respectively because of the amorphous nature of the magnetic layer and because of its lower damping [230].

This experiment was carried out at the ESRF in the four-bunch mode, exploiting one out of two bunches, i.e. at a frequency of 714 kHz. Before inserting the sample in the PEEM, the magnetizations of both the CoFeB and Co layers was saturated along the longitudinal axis of the zigzag, in order to avoid the presence of a Co DW in the corners of the nanowire. We have seen (Section 6.3.4) that the magnetostatic effects associated with such Co DWs prevent the movement of the DW in the soft layer across the zigzag corners. A 40 ns long magnetic field pulse was applied before each current pulse, in order to set the CoFeB DW in the same position in one of the corners of the zigzag nanowire. This initial state is visualized in the stroboscopic mode by setting the x-ray photon bunch after the magnetic pulse and before the current pulse [Fig. 6.20(a)].

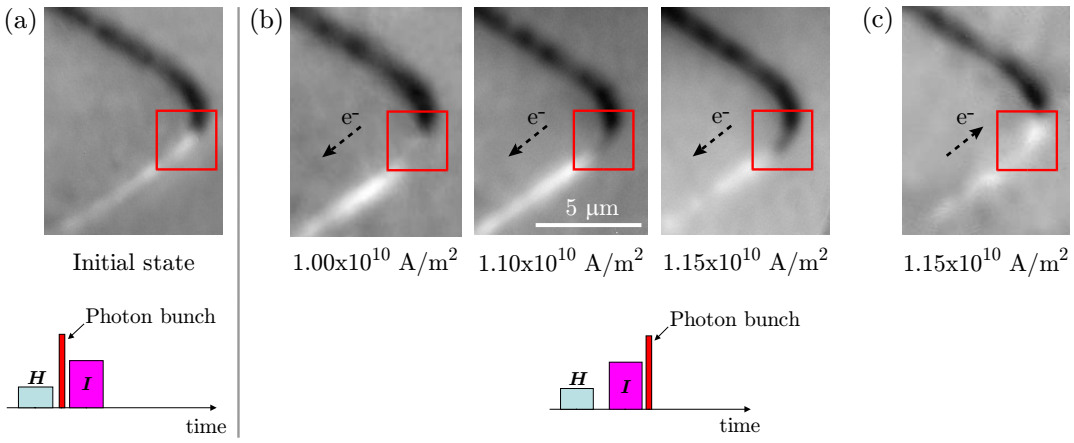

Fig. 6.20: Domain wall structure in the CoFeB layer of a 300 nm wide nanowire, obtained using pump-probe experiments. The images integrate approx. 2.1×10^7 events. The magnetic pulse is used to reinitialize the magnetic configuration. (a) the x-ray photon bunch arrives after the magnetic pulse and before the current pulse, thus recording the initial state. (b-c) the photon bunch arrives after the current pulse, for three current density values. In (c) the polarity of the current was reversed.

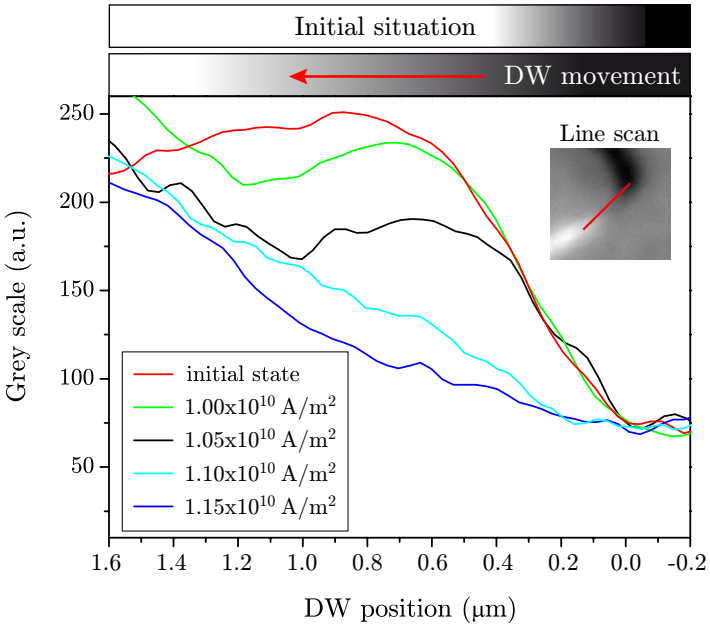

Fig. 6.21: Line scans of the XMCD intensity shown in Fig. 6.20, across the DW position in the initial state (red curve) and for four current densities. The DW moves from the right to the left as indicated by the red arrow.

Fig. 6.20(b) shows the average DW position obtained after the application of a current pulse of three different density values. 20 ns long current pulses were applied for $1.1 \times 10^{10}\,\mathrm{A/m^2}$ and $1.15 \times 10^{10}\,\mathrm{A/m^2}$, while a 50 ns current pulse was applied for the lowest current density, $1.0 \times 10^{10}\,\mathrm{A/m^2}$. The images were obtained by setting the x-ray photon bunch after the current pulse.

Fig. 6.20(c) shows that the DW can be also moved in the opposite direction, upon application of a current pulse with an opposite polarity.

We focus on the red-square areas in the XMCD-PEEM images of Fig. 6.20, showing differences in the XMCD contrast associated to the differences in DW motion obtained with the three current density values. The linescans shown in the inset of Fig. 6.21 contain information about the probability distribution of the DW depinning and the associated displacement[8]. The sharp XMCD intensity change across the DW, drawn as a red curve in Fig 6.21 shows that the initial position of the DW is well defined (reproducible) after the application of the transverse magnetic field pulse.

For the lower current densities, $1.0 - 1.05 \times 10^{10}\,\mathrm{A/m^2}$ (green and black curves in Fig. 6.21), a variation in the XMCD-PEEM intensity at the initial DW position indicates that the DW is not depinned by each current pulse. The XMCD-PEEM intensity deviates from the curve of the initial DW position by an amount proportional to the DW depinning probability. The DW is depinned with a 15% probability at $1.0 \times 10^{10}\,\mathrm{A/m^2}$ and 33% probability at $1.05 \times 10^{10}\,\mathrm{A/m^2}$.

[8]From the principle of the time-resolved experiment, each image averages millions of DW displacements and the probability of a displacement corresponds directly to the brightness level (XMCD intensity). The same gray level as the nonmagnetic background indicates 50% probability.

When the DW is depinned, the XMCD intensity associated to the average displacement continuously decreases, indicating a large distribution of displacements, as expected for current densities close to the depinning value (creep regime — [83]). Note that the fact of using longer current pulses in the case of 1.0×10^{10} A/m^2 did not result in an increase of the DW depinning probability with respect to 1.05×10^{10} A/m^2.

For higher current densities ($1.1 - 1.15 \times 10^{10}$ A/m^2) the DW is depinned each time and for the highest current density of 1.15×10^{10} A/m^2 the final DW position is better defined, as shown by the dark blue curve in Fig. 6.21. This is expected for current densities well beyond critical values for depinning (flow regime — [83]).

This measurement confirms that the probability of DW depinning and of reaching the final position (on a short-range scale) increases with the applied current density. In the time-resolved mode we are able to record even lower current densities to move the DW from a specific potential than by applying single pulses.

6.5.2 Magnetization Dynamics during an Electric Current Pulse

Up to this section, even in the time-resolved mode, we investigated the final state of the DW induced by the application of a magnetic field or current pulse (see Fig. 6.20). By setting the delay so that the photon bunches arrive during the current pulses, we observe the instantaneous magnetization state and might obtain the DW dynamics.

In this one and the following sections we will present results obtained for spin-valve nanowires with widths of 300 nm and 400 nm patterned in zigzag shapes, with angles of 90° and 17 μm long straight sections, prepared by combining electron beam lithography and ion-beam etching techniques. The actual stack composition was Cu 2 nm/$Ni_{80}Fe_{20}$ 5 nm/Cu 5 nm/Co 5 nm/CoO 3 nm prepared using optimized IBAD deposition on highly resistive Si(100) (ρ = 300 Ω.cm). In this section we used 400 nm wide nanowires.

The measurements were performed at the TEMPO beamline at the synchrotron SOLEIL, using the 8-bunch mode, where photon bunches impinge on the sample surface at a repetition rate of 6.77 MHz. By using solely unipolar or dipolar current pulses, the measurements were not limited by the maximum power of the magnetic field generator and the repetition rate of the x-ray source could be used. This brought a positive impact on the quality of the images – the signal to noise ratio for a given acquisition time was improved substantially with respect to the single-bunch mode required for using the magnetic pulses (see Sections 5.2.2 and 5.2.1).

Prior to the measurements, the sample surface was cleaned using in-situ Ar-bombardment, removing part of the 2-nm Cu protective layer. The voltage between the sample and the object lens of the PEEM was increased to 5.4 keV (with respect to the quasi-static experiments in Section 6.2), limiting the spatial resolution to about 0.6 μm.

Unipolar current pulses with variable lengths (2-12 ns) and amplitudes (0-10 mA) were applied to the nanowires at the repetition rate of 6.77 MHz. The acquisition time selected for one XMCD image was about 2×30 s (for each polarization), meaning that

two sequences of about 2×10^8 current and photon pulses were averaged.

While performing the experiment we found that different sections of the nanowire could not be focused at the same time and the difference in the voltage set at the focal lens required for focusing at the opposite ends of the nanowire corresponded approximately to the potential drop induced by the applied current pulse. For this reason an intermediate focus had to be set for the whole structure and the image quality was not optimal.

The effect of relatively long, 10-ns current pulses on the NiFe magnetization of a 300 nm wide nanowire is shown in Fig. 6.22. XMCD-PEEM images of the nanowire were taken before (a) and during the application of current pulses with amplitudes of +4 mA (b) and -4 mA (c). The corresponding current density equals to 8.9×10^{11} A/m^2 assuming a homogeneous current distribution in the stack. The electron flow direction along the nanowire is indicated in the Figure.

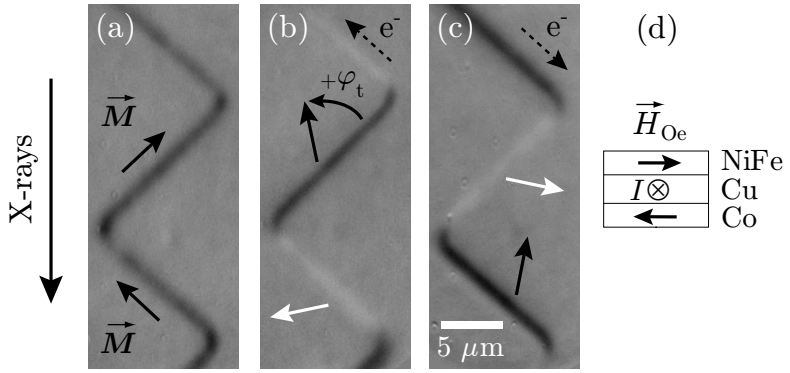

Fig. 6.22: Time-resolved XMCD-PEEM images of the NiFe layer of a 300 nm wide nanowire before **(a)** and during +4 mA **(b)** and -4 mA current pulses **(c)**. The arrows give the approximate magnetization direction in the nanowire, while their color gives the sign of the projection of the magnetization on the incoming x-ray direction, positive (black) or negative (white). The tilt angle φ_t, the angle between the magnetization direction and the nanowire axis, is indicated in **(b)**. The directions of H_{Oe} acting on the NiFe and Co magnetization for one current direction are schematically shown in **(d)**.

Before and after the current pulses, the magnetization is aligned along the nanowire and no DWs are present, leading to an almost homogeneous XMCD intensity for the NiFe layer [Fig. 6.22(a)]. The contrast is slightly larger in the bends, where the magnetization is parallel to the incoming x-ray direction, than in the straight sections where the angle between magnetization direction and incoming x-rays is 45°. Surprisingly, during the current pulses, the XMCD intensity in alternate nanowire sections reverses [Fig. 6.22(b)]. Importantly, after the end of the pulse, the magnetization configuration returns back to the state before the pulse. When applying pulses of opposite polarity, the XMCD intensity reverses in the sections that stayed black before. We interpreted this effect as a tilt of the NiFe magnetization away from the nanowire axis, with a tilt angle denoted φ_t. This tilt is anti-clockwise for a positive [Fig. 6.22(b)] and clockwise [Fig. 6.22(c)] for a negative current direction. The projection of magnetization on the x-ray incidence direction changes sign for one orientation of the sections if the tilt angle exceeds 45°, as can be inferred from the magnetic contrast in the differently oriented

sections of the nanowire. This is expected for a magnetization tilt induced by the Oersted field of the current in Cu and Co layers which acts on NiFe in opposite directions transverse to the nanowire for opposite current directions.

As expected, this effect takes place only in the nanowire sections where the current flows. Fig. 6.23 shows that during the application of a current density of $8.9\times10^{11}\,\mathrm{A/m^2}$ the magnetization tilts only in the region in between the current contacts, while the contrast in the section below the contact, where no current flows, remains the same.

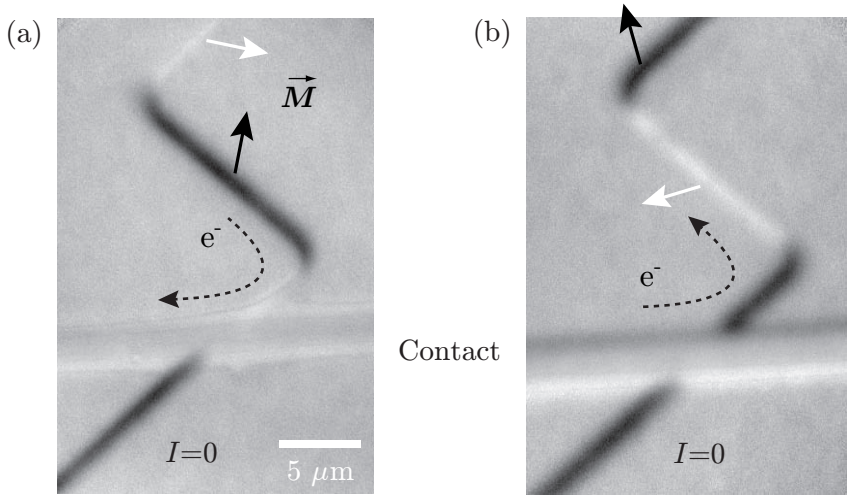

Fig. 6.23: XMCD-PEEM images of the NiFe layer of a 300 nm wide nanowire during the application of a current pulse of $8.9 \times 10^{11}\,\mathrm{A/m^2}$. The magnetization tilts solely in between the current contacts, the bottom part stays unaffected.

To quantify the effect of the Oersted field on the NiFe magnetization, we acquired, for a 400 nm wide nanowire, a series of XMCD-PEEM images during the application of *bipolar* current pulses (Fig. 6.24). The positive/negative part of the pulse is about 2 ns/1 ns long, with a maximum amplitude of +7 mA/−9 mA. The latter value corresponds to a current density of $1.5 \times 10^{12}\,\mathrm{A/m^2}$ assuming a homogeneous current distribution in the stack.

Fig. 6.24 shows a selected series of images of the temporal evolution of magnetization, for both current directions, which confirm the opposite behavior for the perpendicularly oriented nanowire sections, as in Fig. 6.22. The magnetization is initially saturated in the long direction of the nanowire (homogeneous white contrast). With positive current pulses, the XMCD contrast changes sign in the sections at 45°, while in the section at −45° the XMCD intensity slightly increases. With negative current pulses the opposite behavious occurs.

The tilt angle φ_t between the nanowire direction and the magnetization can be extracted from the XMCD intensity in the bends of the nanowire, where the magnetization is parallel to the x-ray beam direction before the current pulse. The XMCD intensity is proportional to the projection of the magnetization on the incoming beam direction, $\cos\Phi$, given by

$$\cos\Phi = \cos\varphi_\mathrm{t} \cdot \cos(\xi - \phi) \tag{6.2}$$

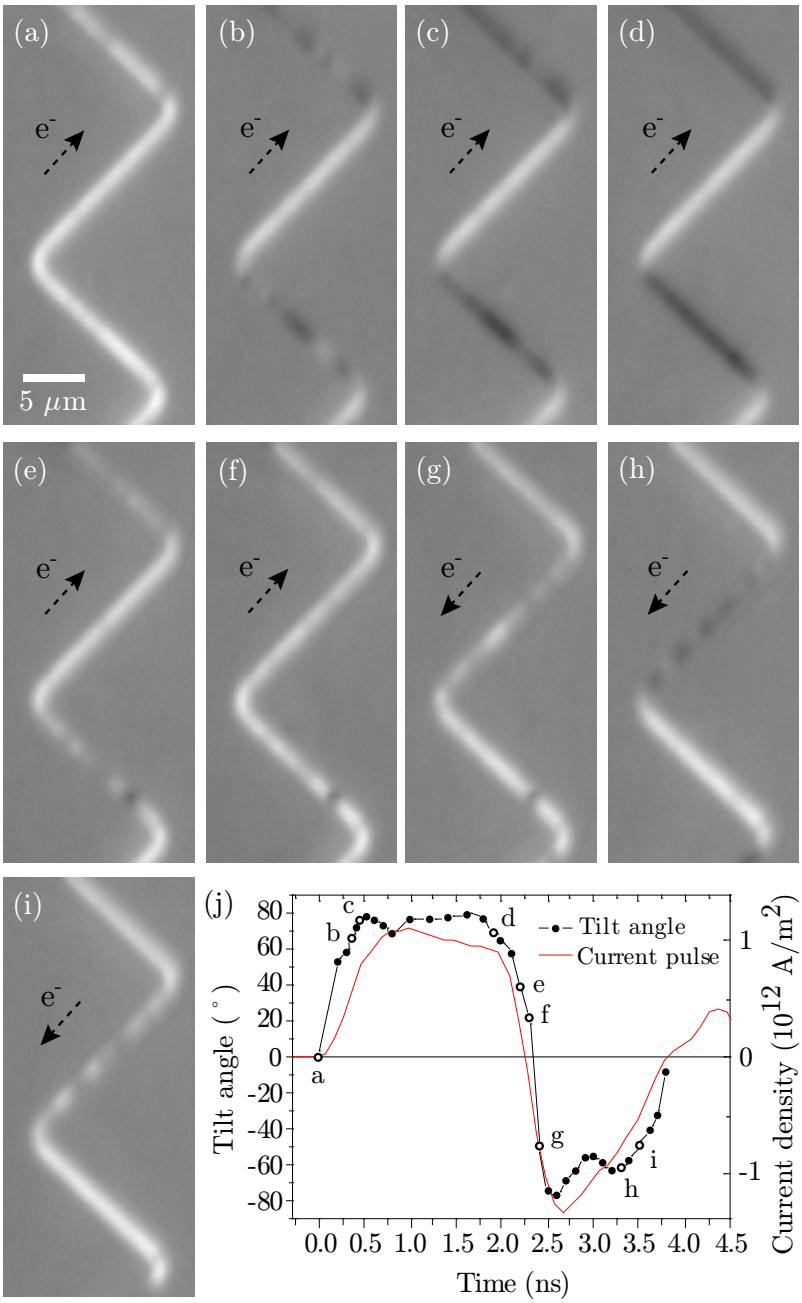

Fig. 6.24: Time-resolved XMCD-PEEM images of the NiFe layer of a 400 nm wide nanowire at time delays of (a) 0 ns, (b) 0.35 ns, (c) 0.45 ns, (d) 1.9 ns, (e) 2.2 ns, (f) 2.3 ns, (g) 2.4 ns, (h) 3.3 and (i) 3.6 ns with respect to the beginning of the positive part of the bipolar current pulse. These delays are indicated on the magnetization tilt angle φ_t curve plotted in (j), together with the bipolar current pulse. The oscillations in φ_t at the beginning of the positive and negative parts of the pulse indicate magnetization precession about H_{Oe}.

where ξ is the angle between the plane of the sample and the x-ray incidence direction and ϕ is the out-of-plane angle of magnetization. We assume a magnetization vector lying in the sample plane (static regime) or inclined by a *small* out-of-plane angle

(dynamic regime), so that the formula (6.2) reduces to $\cos\Phi = \cos\varphi_t \cdot \cos\xi$, where $\cos\xi$ is a constant. Hence $\cos\varphi_t$ is directly proportional to the XMCD intensity. The tilt angle calculated with this method is indicated in Fig. 6.24(j). The angle φ_t reaches almost 80° at the beginning of the positive part of the pulse, before stabilizing around 75°.

The observed effect of the transverse Oersted field on the NiFe magnetization is surprisingly large. For a soft magnetic material such as NiFe the magnetization direction in a nanowire is mainly determined by magnetostatic effects, which favor magnetization along the nanowire axis. For a 5 nm thick, 400 nm wide nanowire the transverse demagnetization factor N_y is about 0.023 [356], meaning that to obtain $\varphi_t = 75°$ a transverse (Oersted) field of $0.023 \times \mu_0 M_S \times \sin 75° = 22\,\mathrm{mT}$ would be required (with $\mu_0 M_S = 1\,\mathrm{T}$ for permalloy).

Using the programme COMSOL Multiphysics® we calculated the H_{Oe} generated by the current flowing homogeneously in the NiFe/Cu/Co nanowire. Subsequently, the OOMMF code was used for determining the corresponding magnetization tilt angle and the transverse demagnetizing factor of the nanowires. Fig. 6.25 shows cross-sections of 200 nm wide nanowires and the magnetic flux density of the Oersted field calculated assuming a homogeneous[9] current distribution of $5 \times 10^{11}\,\mathrm{A/m^2}$ in both a 15 nm thick NiFe/Cu/Co trilayer nanowire (a) and a 5 nm thick NiFe nanowire (b). Inside the nanowire, the magnetic field increases linearly with the distance from the center, reaching 4.5 mT at the top surface for the 15 nm thick nanowire. Further on, above the nanowire, the Oersted field decreases very slowly, by approx. 5% over 10 nm. The Oersted field above the nanowire (resp. inside the NiFe layer) is independent of the nanowire width except of the area close to the horizontal edges of the nanowire.

Indeed, the Oersted field increases linearly with the applied current density. For a current of +7 mA in the 400-nm nanowire, the average current density is $1.2 \times 10^{12}\,\mathrm{A/m^2}$. As described above, we suppose a homogeneous current distribution over the NiFe/Cu/Co trilayer. For this current density the expected $\mu_0 H_{Oe}$ is 11 mT at the surface of the NiFe layer and 3.7 mT at the NiFe/Cu interface, giving an average of 7.4 mT acting on the NiFe magnetization. Such a transverse field would result only in a $\varphi_t = 10°$ tilt which is much smaller than the experimental values. A maximum $\mu_0 H_{Oe}$ of 11 mT would be obtained if the current was flowing entirely through the Cu

[9]Note that when using short nanosecond pulses, the skin effect may play an important role in the distribution of the electric current in the nanowire cross-section. At high frequencies, the current tends to flow near the surface and its magnitude is determined by

$$I = I_S\, e^{-\frac{d}{\delta_s}} \tag{6.3}$$

where I_S is the current at the surface and d distance from the surface. The skin depth δ_s, at which the current decreases e-times with respect to the surface value, is expressed as

$$\delta_s = \sqrt{\frac{\rho}{\pi f \mu}}. \tag{6.4}$$

ρ denotes the resistivity, μ the total permeability and f the given frequency of current variations. At a frequency of 1 GHz, the values of skin depths of the used materials are the following: $\delta_s^{NiFe} = 0.1\,\mu\mathrm{m}$, $\delta_s^{Co} = 0.6\,\mu\mathrm{m}$ and $\delta_s^{Cu} = 2.8\,\mu\mathrm{m}$, which are much above the typical thickness of our layers.

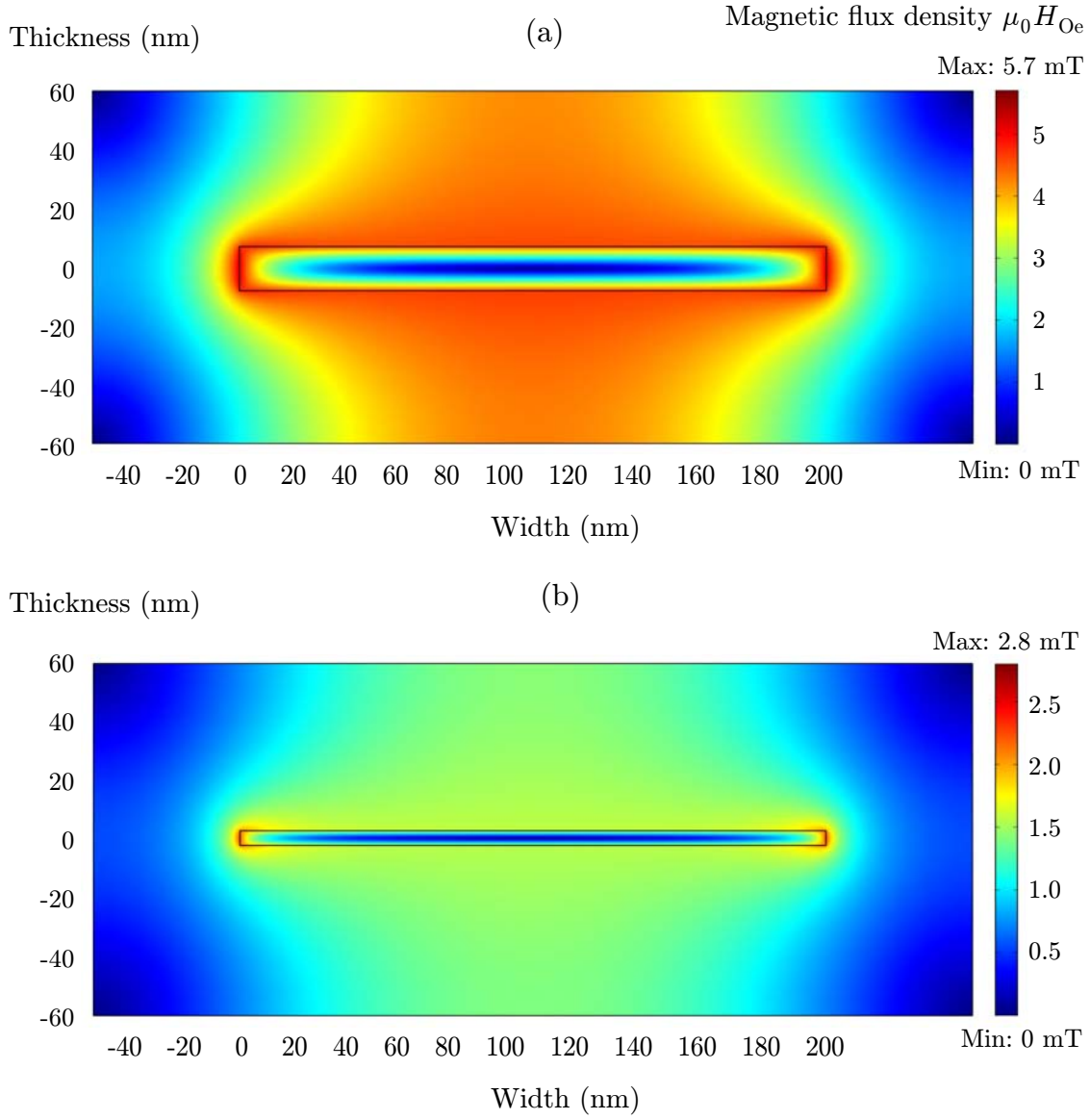

Fig. 6.25: Magnetic flux density induced by a homogeneous current density of 5×10^{11} A/m^2 flowing in the cross-sections of 200 nm wide nanowires. (a) corresponds to a 15 nm thick NiFe/Cu/Co trilayer, (b) to a 5 nm thick NiFe layer.

and Co layers, because of the higher resistivity of NiFe. Even the value of 11 mT is still low with respect to the 22 mT required to obtain the observed tilt experimentally .

An overestimation of the demagnetizing effect is most likely at the origin of the discrepancy between the observed and expected tilt angles.

1. A larger tilt of the magnetization in the center of the nanowire than at its edges is expected if one takes into account the exchange interaction and the real, non-homogeneous profile of the demagnetizing field, which results from highly non-homogeneous dipolar fields in thin flat nanowires. The analytical factor $N_y =$

0.023 corresponds to the volume-averaged demagnetizing energy. Fig. 6.26(b) shows that in the center of a 400 nm wide nanowire the demagnetizing factor N_y is 0.009, resulting in larger tilts in the central area. Fig. 6.26 shows the calculated magnetization tilt angles of NiFe (black curve) as a function of the transverse position in 300 nm and 400 nm wide nanowires. Representative values of Oersted field, 5.6 mT and 7.4 mT respectively, were calculated for the current densities of 8.9×10^{11} A/m^2 and 1.2×10^{12} A/m^2 applied in case of Fig. 6.22 and Fig. 6.24. The average tilt values are given in the figure.

The observed contrast in our XMCD-PEEM images corresponds to the convolution of the magnetization profile with the experimental resolution function over the width of the nanowire, causing a larger contribution of the center of the nanowire to the image contrast. We calculated the convolution of a resolution function (see Fig. 5.10) with the distribution of $\cos\varphi_t$ under the action of an Oersted field of 7.4 mT, obtained for a 400 nm wide nanowire as described above, and with the distribution of $\cos\varphi_t$ in the steady state, i.e. when the magnetization is parallel to the x-ray incidence direction ($\varphi_t = 0$). By dividing the peak values of the two convolutions we obtain $\cos\varphi_t$ that we measure experimentally. The resulting φ_t was by approximately 3% larger than a simple average of the tilt angles presented in Fig. 6.26.

2. Transverse demagnetizing factor can also be smaller, by several tens of percent, than the nominal value of 0.023 because of edge roughness effects [357], or an effective decrease of thickness due to surface oxidation or intermixing at the NiFe/Cu interface. However, the latter reason, a decrease of the effective thickness and/or magnetization of the NiFe layer, was found to increase the tilt only by few percent at maximum, according to the simulations.

   By introducing roughness of a square-function type – squares of 8×8 nm^2 with a 16 nm period on the edges – the tilt increase was tested by micromagnetic simulations. The tilt rose from 26.6° to 30.9° under application of a 7.4 mT magnetic field to a single NiFe 400 nm wide nanowire. The effect is even larger for a NiFe 5 nm/Cu 5 nm/Co 5 nm trilayer. Under the same parameters (7.4-mT field, 400-nm width), the average tilt increased from 69.1° to 83.8°. The discussion of this effect follows.

3. Larger tilt is expected from the magnetostatic interaction between the NiFe and Co layers. Micromagnetic simulations have shown that in these trilayers part of the magnetic charges on the edges of the NiFe layer is compensated by mirroring effects on the edges of the Co layer, which significantly decrease the transverse demagnetizing effects [38]. Moreover, if the current is centered in the Cu layer, the Co magnetization tilt induced by H_{Oe} will be opposite to that one induced in the NiFe layer, further increasing the compensating effect of the Co magnetic charges.

   The Co magnetization tilt also depends on the character of magnetocrystalline anisotropy in the Co layer (discussion on the choice of the K anisotropy constants

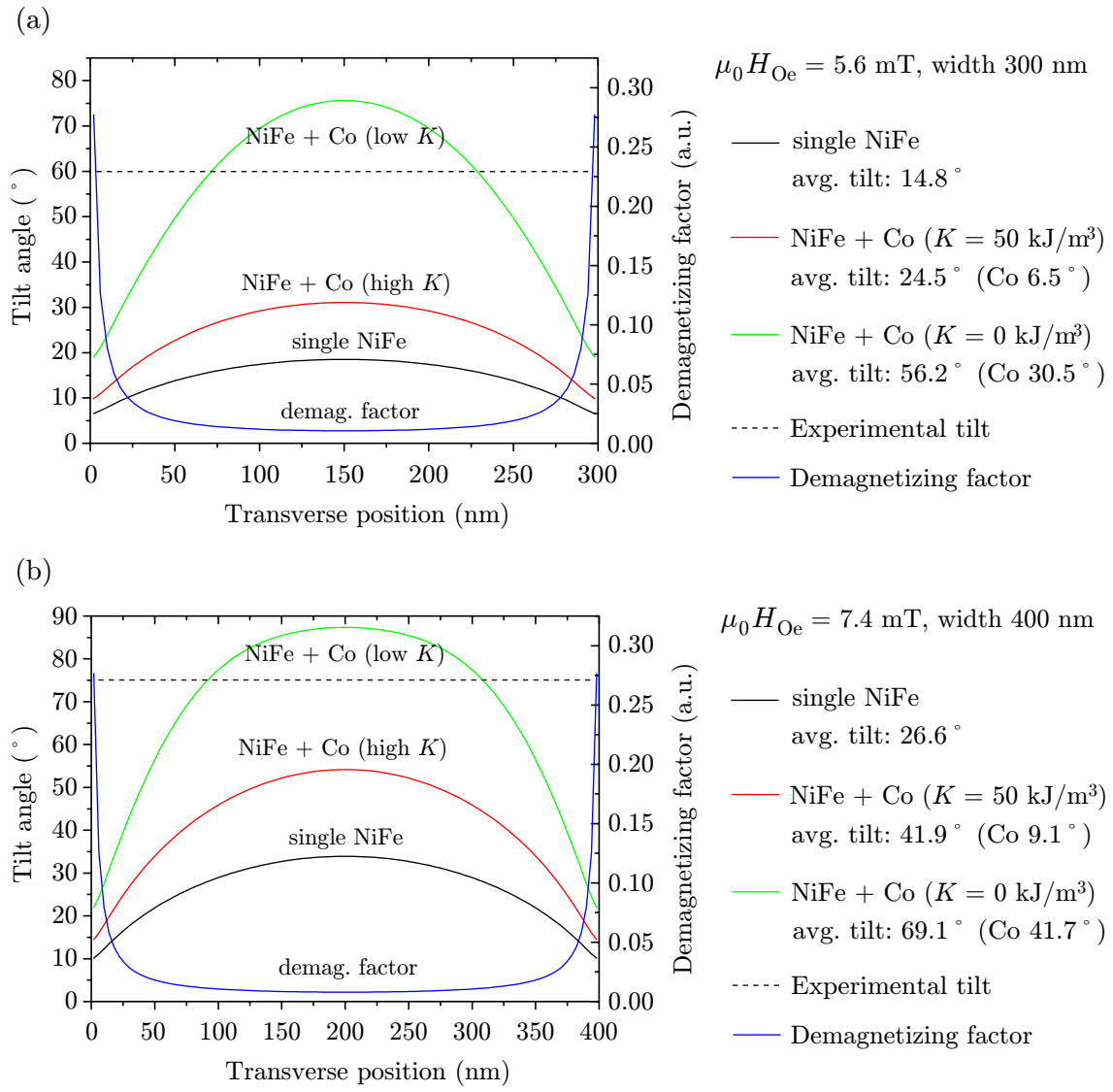

Fig. 6.26: Magnetization tilts and demagnetizing factors for (a) 300 nm and (b) 400 nm wide nanowires calculated using the OOMMF code. The experimental tilt angle is indicated by a dashed line. The average angle of the magnetization tilt for each simulated case is shown in the legend. The Oersted field denoted by $B_{\mathrm{Oe}}=\mu_0 H_{\mathrm{Oe}}$ acts on both the Co and NiFe layers and the corresponding magnetization tilt in the NiFe layer is indicated by the red and green curves. The lateral roughness at the edges is not taken into account. The demagnetizing factor is calculated for a magnetization completely transverse to the nanowire.

used in Fig. 6.26 can be found in Section 6.3.4). The largest effect on the NiFe magnetization tilt is found for vanishing in-plane Co anisotropy (the same effect as for purely out-of-plane anisotropy K). However, the average NiFe tilt is still smaller than the experimental value deduced from the XMCD-PEEM image.

The element selectivity of our technique was used to verify the tilt direction of the Co magnetization during the current pulses. Unfortunately, as the Co layer is buried below the Cu and NiFe layers, the weak magnetic signal obtained for

the Co L_3-edge images did not allow quantitative determination of the magnetization tilt in the Co layer during the current pulse. Micromagnetic simulations clearly showed that even a small transverse tilt of the Co magnetization can help considerably to tilt the NiFe magnetization (Fig. 6.26).

It is likely that only the combined effect of non-uniform magnetization in the nanowire, edge roughness and dipolar interactions between NiFe and Co layers may explain the large observed magnetization tilt induced by H_{Oe}.

Fig. 6.27 shows the dependence of the magnetization tilt angle on the current amplitude, determined experimentally from XMCD-PEEM images for 300 nm and 400 nm wide nanowires. Although we did not acquire enough experimental data to construct the error bars, from the tilt curves it can be deduced that the difference in the tilts associated with the 300 nm and 400 nm wide nanowires varies between 5 and 10%. This is in line with the results of the simulations: for a 7.4-mT applied field and $K = 0$ the calculated tilt values are 62.0° (300 nm) versus 69.1° (400 nm). As expected, the calculated tilt angles are larger for the wider nanowires where the demagnetizing effects are weaker.

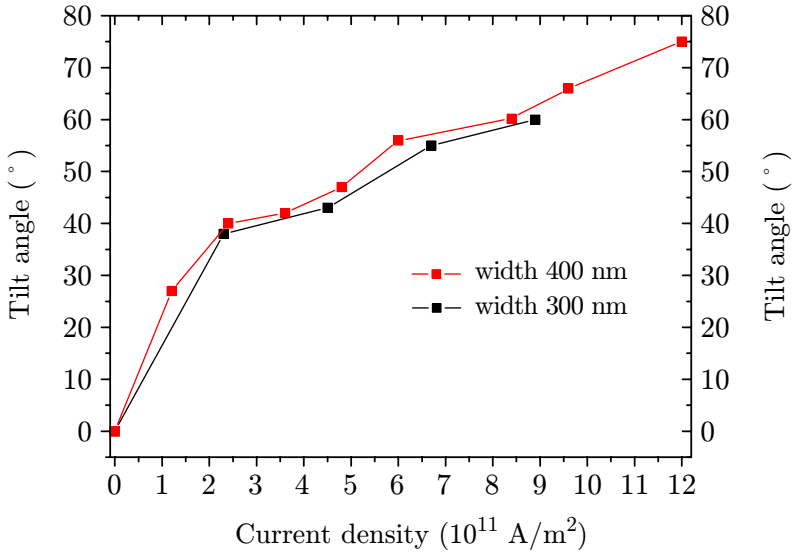

Fig. 6.27: Magnetization tilt angles in the NiFe layer extracted from the XMCD-PEEM images for 300 nm and 400 nm wide nanowires and different applied current densities.

Up to now, we have seen that the main effect of the Oersted field is to tilt the NiFe magnetization in the direction transverse to the nanowire. Fig. 6.24 and Fig. 6.28 show that the XMCD contrast (i.e. the tilt angle) undergoes oscillations at the beginning of the pulse. These oscillations are associated with the precession of the magnetization about the effective field direction.

Fig. 6.28 shows contrast-enhanced XMCD-PEEM images of the bottom section of the nanowire in Fig. 6.24, taken with delay steps of 100 ps at the beginning of the positive part of the current pulse. Since the images are averaged over 10^8 current

pulses, the large contrast reveals that the phase of the excited oscillations with respect to the current pulses is well defined and reproducible. The spatio-temporal variations in the magnetic contrast along the nanowire may be due to local inhomogeneities in the magnetization of the NiFe layer itself or to anisotropy fluctuations in the Co layer that can be transmitted to the NiFe layer through magnetostatic interactions. Nevertheless, these spatio-temporal variations of the tilt angle strongly resemble spin-waves. The excitation of spin-waves by the Oersted field in spin-valve trilayers was predicted by Kim et al. [358] and spin-wave-like features were observed using Lorentz microscopy on 30 nm thick NiFe nanowires upon current injection [359].

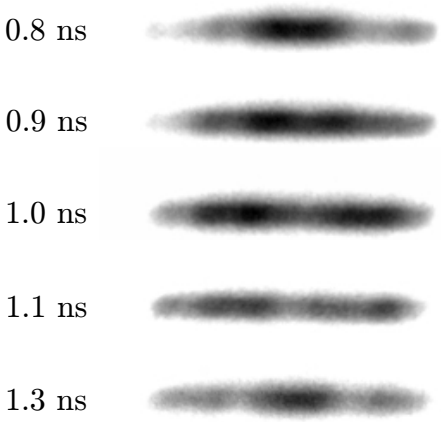

Fig. 6.28: Time-resolved XMCD-PEEM images of the lower section of the 400 nm wide nanowire, taken at the indicated delays after the beginning of the positive part of the current pulse. The oscillation frequency of the spatio-temporal variations of the XMCD contrast, resembling spin-waves, is about 2 GHz.

The period of the observed oscillations is about 500 ps, corresponding to a frequency of 2 GHz. According to Kittel's formula [360], the resonance frequency ω_0 is given by

$$\omega_0^2 = \gamma_0^2 \left[B_0 + (N_x - N_y)\,\mu_0 M_\mathrm{S}\right] \left[B_0 + (N_z - N_y)\,\mu_0 M_\mathrm{S}\right], \tag{6.5}$$

where γ_0 is the gyromagnetic ratio, B_0 is the field applied in the transverse direction, N_x, N_y, N_z are the demagnetizing factors in the directions parallel, transverse and perpendicular to the nanowire, and $\mu_0 M_\mathrm{S}$ is the spontaneous magnetic polarization corresponding to approximately 1 T for NiFe. For our nanowire, 400 nm wide and 5 nm thick, with demagnetizing factors $N_x = 0$, $N_y = 0.023$ and $N_z = 0.977$, a transverse field of 28 mT is needed to induce a 2-GHz precession frequency. So, as in the case of the measured tilt angle of the magnetization, the experimentally observed effect corresponds to a larger Oersted field than the analytical value expected for a perfect wire.

Note that the Kittel's formula reads for homogeneous magnetization precession. In the case of inhomogeneous precession, like in our nanowires (Fig. 6.28), the NiFe exchange interaction reduces the field needed to obtain precession at the observed frequency [361]. Also a reduction of the transverse demagnetizing factor, as discussed

for the NiFe magnetization tilt, will significantly reduce the necessary transverse field.

In conclusion, our results provide the first microscopic evidence of the importance of Oersted fields during the application of current pulses. We have shown that the Oersted-field induced magnetization tilt in non-centrosymmetric systems such as NiFe/Cu/Co nanowires can be very large for relatively modest current densities. The amplitude of H_{Oe} will depend on the amount of current passing in the metallic layers in the vicinity of the layer in which CIDWM is observed. It is thus particularly strong for the NiFe layer in our trilayer systems, due to the metallic underlayers with a total thickness of 10 nm. NiFe/Cu/Co systems studied before [213, 181], with a Cu spacer of 10 nm, and a CoFeB/Cu/Co system [230] with a 8-nm spacer, would feature even a higher Oersted field acting on the soft magnetic layer, which results in widening of the DWs with a parallel magnetization and lower critical current densities needed for their depinning.

In many cases reported in the literature, the DW motion is studied in single NiFe nanowires, where metallic buffer layers or protecting layers are present. Our measurements clearly indicate that also in these cases the quasi-static and precessional effects of the Oersted field should be carefully considered.

The inhomogeneous current flow due to the different conductivities in multilayer systems may be behind some surprising results recently shown by Vanhaverbeke et al. [342]. They observed a random switching of DW chirality upon injection of a current pulse in single NiFe nanowires. In the case of bilayered nanowires of NiFe/Fe this effect became predictable. It is not clear what the exact role of the current shunting through different layers was, but the results presented in this paper are also consistent with the effect of the Oersted field, even though the authors exclude it (on the basis of layer resistivities measured for continuous films). As expected, the effect depended on the chirality of a particular DW and the polarity of the injected current.

6.5.3 Effect of the Oersted Field on DW Depinning and Propagation

The results of time-resolved XMCD-PEEM experiments have shown that the Oersted field generated by the current flowing in the Cu and Co layers has an important effect on the NiFe magnetization, i.e. during the application of a current pulse the magnetization tilts in the direction transverse to the nanowires. In order to study the effect of the Oersted field on current-induced depinning of a TW, we carried out micromagnetic simulations using the OOMMF code. Fig. 6.29 shows the response of NiFe magnetization in a 200 nm wide NiFe 5 nm/Cu 5 nm/Co 5 nm nanowire presenting a transverse DW (TW) to an external field of 10 mT, acting in opposite directions in the two magnetic layers and thus mimicking the Oersted field. A TW with magnetization parallel to the magnetic field gets wider, while a TW with magnetization antiparallel gets narrower [92].

In the following we will provide some qualitative estimates of the DW depinning and propagation parameters using the OOMMF CIDWM extension. To speed up the calculation, narrower nanowires of a width of 100 nm instead of 200 nm were used.

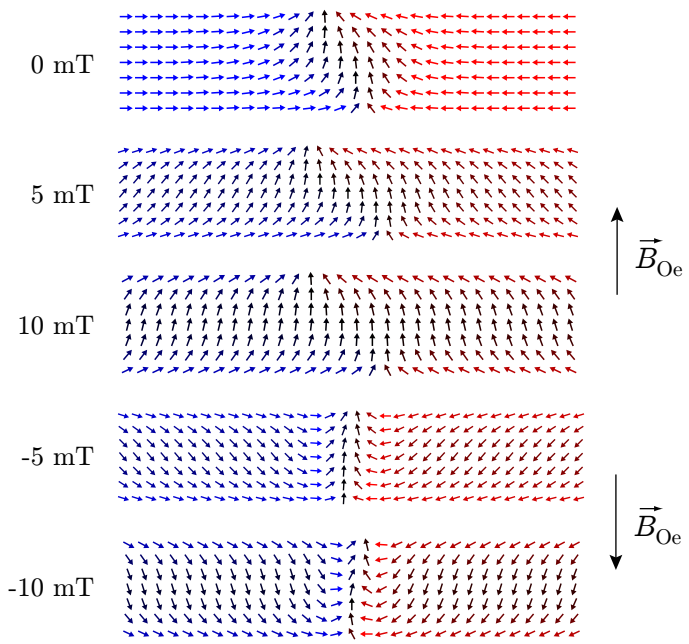

Fig. 6.29: OOMMF micromagnetic simulations showing the effect of an Oersted field on the NiFe magnetization in 200 nm wide NiFe/Cu/Co nanowires presenting a TW. A field applied in/against the direction of the DW magnetization widens/shrinks the DW width.

It should be emphasized that the results are preliminary and are mainly meant as a perspective work in view of a detailed study. The initial configuration is a tranverse DW pinned above an anisotropy defect in the Co layer (see Section 6.3.4). The Co defect size was $50\times50\,\mathrm{nm}^2$ with the anisotropy axis oriented at 45°.

The result of the simulation is that even when very large current densities ($10^{13}\,\mathrm{A/m}^2$) and transverse fields (10 mT acting in opposite directions on Co and NiFe) were applied for both polarities of current and field, the DW positioned above a Co defect could not be depinned.

Further a case of a 360° DW was studied. As described in Section 6.3.4, this DW type is formed when two DWs of antiparallel magnetizations approach. Let us suppose that one of these two DWs is pinned by the stray field of a Co defect [DW on the left in Fig. 6.30(a)]. In zero applied field, the 360° DW can be depinned and subsequently moved as a whole using a relatively high current density ($10^{13}\,\mathrm{A/m}^2$). This might be explained by the fact that with respect to a single pinned 180° TW, the 360° DW consists of two TWs oriented antiparallel, thus decreasing the magnetic charges and making the 360° DW a stable magnetic object that is difficult to decompose. The interaction with the stray field of the Co defect becomes also less significant.

Fig. 6.30(b) shows that a transverse field acting together with a current might play a significant role in the expansion of a 360° DW[10]. The 360° DW is driven by a current density of $4\times10^{12}\,\mathrm{A/m}^2$ under the action of an Oersted field of 10 mT and the corresponding transverse Co stray field that are both oriented parallel to the pinned

[10]This mechanism has been invoked to explain nucleation of domains in Section 6.3.4

TW magnetization. The transverse field makes the pinned TW wider and pushes the second TW out of the potential well. For a certain separation of the two TWs, the current is able to unpin the TW on the right completely.

If an Oersted field of 10 mT acts in the direction opposite to the pinned TW magnetization, the second TW cannot be depinned even with a current density of $7.4 \times 10^{12}\,\mathrm{A/m^2}$ [(Fig. 6.30(c)]. After reaching a density of $10^{13}\,\mathrm{A/m^2}$, the 360° DW moves as a whole similarly to the case without the transverse field. For wider nanowires a lower transverse field is necessary to induce comparable magnetization tilts needed for inducing similar effects.

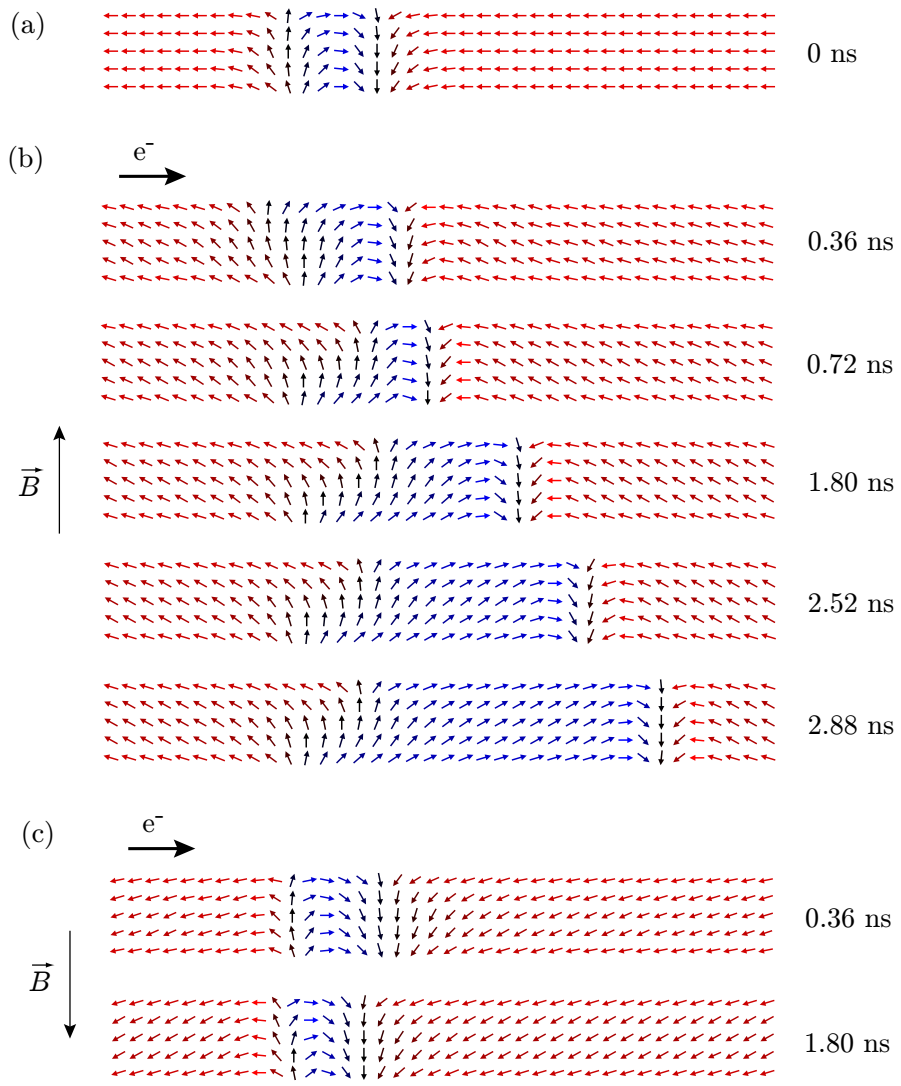

Fig. 6.30: Expansion and splitting of a 360° DW by both an electric current and a transverse magnetic field. (a) Initial state. The DW on the left is pinned by a Co defect stray field. (b) Upon application of a current density of $4.6 \times 10^{12}\,\mathrm{A/m^2}$ and an Oersted field of 10 mT oriented parallel to the pinned DW magnetization, the 360° DW expands and two separate TWs are created. (c) Under an Oersted field of 10 mT oriented antiparallel to the DW magnetization, a current density of $7.4 \times 10^{12}\,\mathrm{A/m^2}$ does not succeed to move nor expand the 360° DW.

6.6 Perspectives

6.6.1 Ultrafast Long-Range Displacements

For future devices based on the DW motion, a fast and reliable displacement of all the DWs in the nanowire is required. In the following we will show some premises of the NiFe/Cu/Co system to fulfil these requirements.

The experiment was carried out at the SOLEIL synchrotron in the eight-bunch mode, exploiting 1 of 8 bunches, i.e. at a frequency of 846 kHz, with a photon bunch length of approximately 50-60 ps. 40 ns long magnetic field pulses of 14 mT were applied to reset the DWs to the initial positions at the corners of the zigzag nanowire [see Fig. 6.31(a)].

The temporal delay was initially set so that the photon bunches arrived after the current pulses [12-ns length and current density of 1.2×10^{12} A/m^2 – Fig. 6.31(b)]. It was found that all three DWs moved by a substantial distance from the corners, reminding us the DW behavior in the "racetrack" concept [236]. However, the domain structure surrounding the middle corner and containing black and gray domains indicates that the displacements were not uniform and did not happen at each current pulse.

We performed a check in the quasi-static mode, by applying the pulses one by one [Fig. 6.31(c)-(f)]. (c) shows an initial domain configuration after applying one magnetic field pulse, (d)-(f) show results after application of one current pulse with identical parameters as in the time-resolved mode, each starting from the initial state (c). Only (d) shows a result similar to the domain structure in (b), (e) and (f) represent situations where either the DWs did not reach their final positions or it seems that some new DWs have nucleated. These results confirm the observation in the time-resolved mode, suggesting that the image (b) is a superposition of different domain configurations occuring with different probabilities.

The displacement from the position 0 to A in Fig. 6.31(a)-(b) is worth describing in detail. The associated displacement of 5 μm occured during a current pulse of 12-ns length. It should be noted that due to the large number of events averaged in the time-resolved mode this is unlikely an artifact of multiple DWs moving at the same time. The same displacement could be induced also when applying shorter pulses, although the current density had to be increased at the same time. Fig. 6.31(g) shows the situation after a pulse of 0.5 ns and 1.7×10^{12} A/m^2 (the corresponding DW velocity is 10000 m/s!); (h) 1 ns and 1.4×10^{12} A/m^2; (i) 12 ns and 9.7×10^{11} A/m^2. The minimum current density for which we managed to move this DW with 12-ns pulses was 5.6×10^{11} A/m^2, but the DW did not reach the final position A (j).

While increasing the current pulse length, although decreasing the applied current density, the probability of other DW movements and magnetization switching increased [Fig. 6.31(h)-(i)]. This is illustrated by the fact that in (g) there is no evidence for formation of gray domains above the position A, as in the images (h) and (i).

We conclude that the DW movement is on average highly stochastic and the pinning potentials influencing it depend strongly on the position along the zigzag. However, strikingly high DW velocities can be found in certain regions of the nanowire.

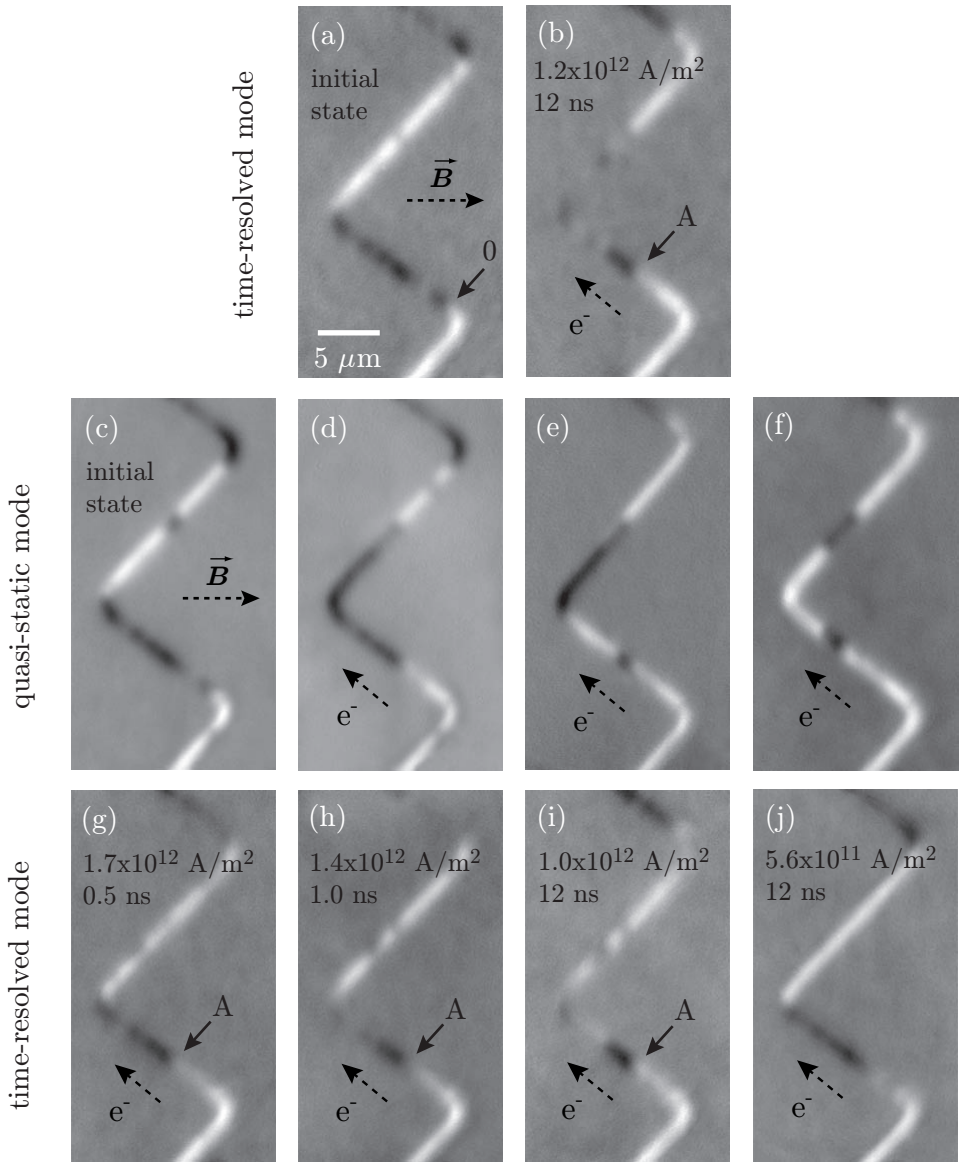

Fig. 6.31: (a)-(b) XMCD-PEEM images of the NiFe layer of a 400 nm wide spin-valve nanowire in the time-resolved mode: (a) – situation after application of a magnetic field pulse of 14 mT, (b) – average situation after the application of a current pulse. (c)-(f) – quasi-static images of the structure obtained after application of one magnetic field pulse (c) and one current pulse (d)-(f) of the same current density and pulse duration as in (b). (g)-(j) show the results of the time-resolved mode again. Photon bunches arrive after application of current pulses with a varying pulse amplitude and duration.

6.6.2 Observation of DW Motion during a Current Pulse

Observation of a DW motion during a current pulse is difficult, as the PEEM focus is inhomogeneous due to the potential drop at the nanowire and the magnetization tilt caused by the Oersted field prevents us from determining the exact DW positions. However, for low current densities such an observation is feasible. Unfortunately, due to the generally low reproducibility of back and forth DW motion and a lack of synchrotron

beam-time we were not able to repeat this experiment before finalizing this manuscript.

The following experiment was carried out at the ESRF at a 714-kHz repetition rate. We used positive magnetic field pulses of 6-mT amplitude and 50-ns length to reinitialize the magnetic configuration.

Fig. 6.32 shows magnetization dynamics in a 300 nm wide nanowire during a 1-ns current pulse of an amplitude of $1.4 \times 10^{11}\,\mathrm{A/m^2}$ (in the NiFe layer). We first observe a DW motion in image (b) where the DW denoted by A moves at a current density reaching approximately $2.5 \times 10^{10}\,\mathrm{A/m^2}$. The displacements indicated as A-B, B-C, C-D in the Figure occurred during a temporal interval of 100 ps. In image (d) the fine magnetization structure is already blurred by the Oersted field, so that the position D had to be determined from the final DW position indicated in (i). Note that the final position is visible already in (g). The values of DW displacements A-B ($0.6\,\mu$m), B-C ($0.95\,\mu$m) and C-D ($0.95\,\mu$m), give very high DW velocities, exceeding 5000 m/s and linearly increasing with the current density (see Fig. 6.33). Although we do not possess enough experimental data to reveal the whole curve of the DW mobility vs. current density, this result is very intriguing, as these velocities exceed all the values reported in recent literature. It should be noted that the velocity values are consistent with those presented in Section 6.6.1.

Although it is very dangerous to draw any conclusions from the dependence shown in Fig. 6.33, this result would suggest that there is not an intrinsic critical current density as expected for a DW motion driven by the nonadiabatic spin-torque term. However, low current densities induce short nanometric displacements when using pulse durations in the order of nanoseconds. Such displacements cannot be detected by our technique, as we discussed in Section 6.4.

As the current amplitude decreases and the magnetization tilt disappears, the images (f)-(i) reveal that actually two displacements occured during the pulse, A-D and E-F, indicated in image (i). The displacement E-F is $2\,\mu$m long. If we consider the total DW displacement during the whole current pulse, we calculate the average velocity during the current pulse. We still obtain very high velocities, (1250 ± 70) m/s for the A-D displacement and (1000 ± 80) m/s for the E-F one. However, we cannot reliably examine the formation of a small domain confined between the points E and F, as the observation of the reversal mechanism was hindered by the magnetization tilt.

For what concerns the bottom section, the initial configuration was not recovered after the end of the current pulse. As the domains seemed to switch coherently with the Oersted field, we cannot deduce the character of magnetization reversal in this region.

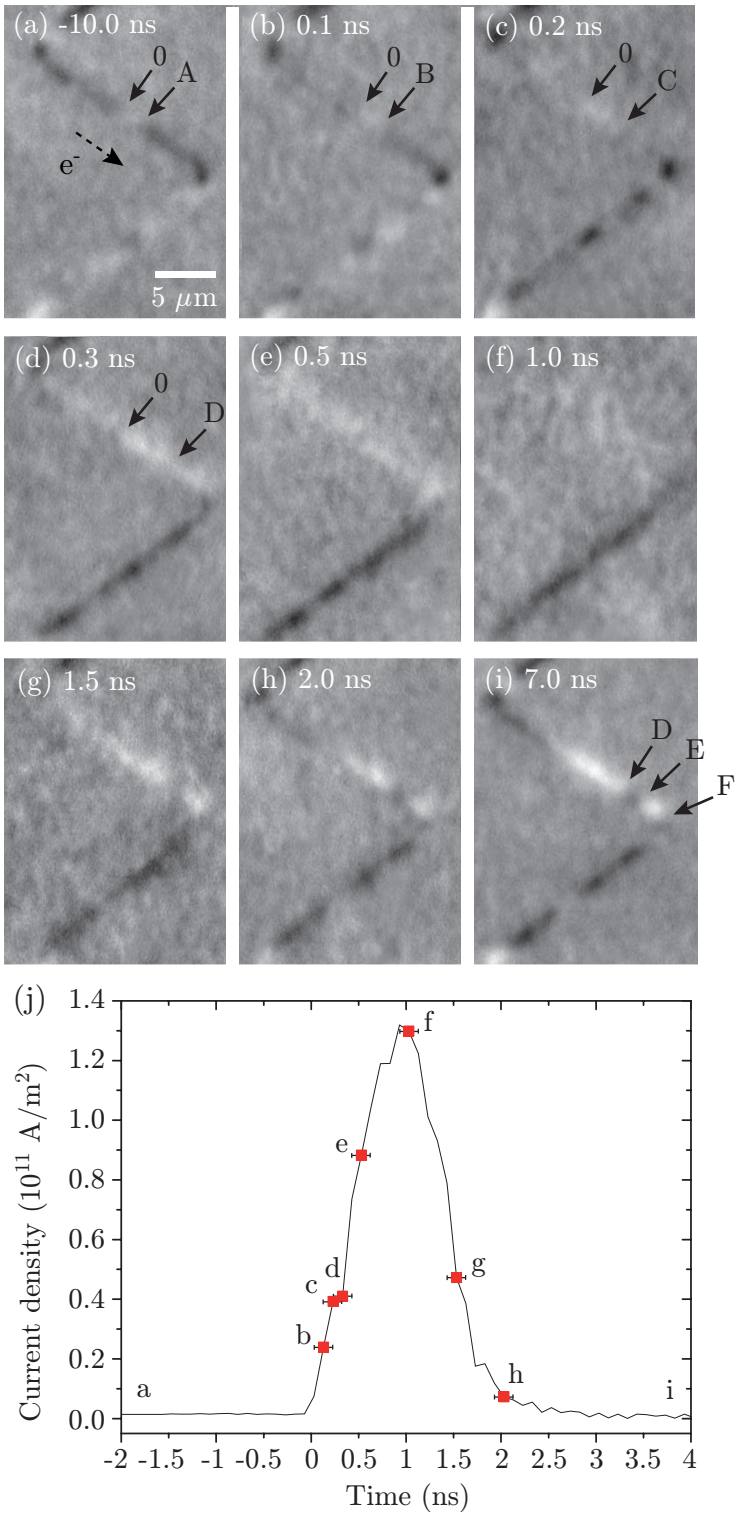

Fig. 6.32: Time-resolved XMCD-PEEM images of magnetization dynamics during a current pulse. Instantaneous positions of the moving DW (A-B-C-D) are indicated in (a)-(d). Position 0 represents a reference point. A new domain between the positions E and F is revealed after the magnetization tilts back to its initial position (i). The horizontal error bars arise from uncertainty of matching the photon bunches with the current pulse (±100 ps).

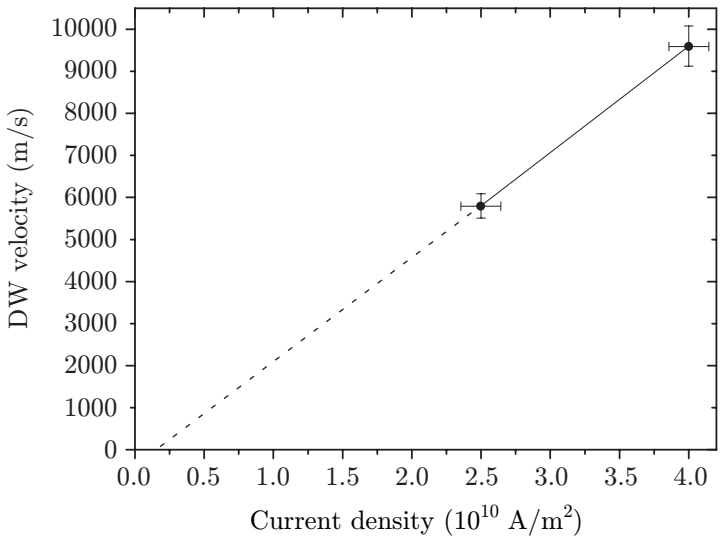

Fig. 6.33: Dependence of DW velocity on the instantaneous current density in a 300 nm wide nanowire. The experimental points were taken from the time-resolved DW motion shown in Fig. 6.32. The dashed line is a guide to the eye. The vertical error bars arise from multiple measurement of the DW displacement.

GENERAL CONCLUSION

The presented work addressed current-induced domain wall motion in spin-valve-like NiFe/Cu/Co nanowires, using both quasi-static and time-resolved magnetic microscopy measurements. The experimental tool is the x-ray photoemission electron microscopy (PEEM) using x-ray magnetic circular dichroism (XMCD) as a source of magnetic contrast. This synchrotron-based technique combines element selectivity with a high spatial and temporal resolution.

In the quasi-static mode, domain wall displacements are obtained by the observation of the domain configuration before and after the application of one current pulse. The quasi-static measurements revealed several points. First, very high velocities for current-induced DW propagation in NiFe/Cu/Co trilayered nanowires can be found, with maximum velocities exceeding 600 m/s. The current density needed for such a rapid DW motion is of the order of $4 \times 10^{11}\,\mathrm{A/m^2}$. The minimum current density for which the CIDWM was observed scales down to $1 \times 10^{11}\,\mathrm{A/m^2}$ for current pulses applied to 400 nm wide nanowires and $2 \times 10^{11}\,\mathrm{A/m^2}$ for both the 200 nm and 300 nm wide nanowires. The highest velocities largely exceed those found for single layer NiFe nanowires, for much larger current densities. These results show that the spin transfer torque effect is very efficient in the trilayer systems.

In quasi-static measurements, the DW velocities are deduced by the ratio of the displacement and the pulse length. The displacements do not in general scale with the pulse length. The highest presented DW velocities can be found quite rarely, as the DW motion is often stopped by pinning before the end of the current pulse. The pinning has been addressed in detail and different possible sources were carefully considered. Topography defects of whatever origin have been excluded due to the size of the pinning sites which were clearly visible as a modulation of the XMCD contrast in the images.

As no DWs in Co were present below these regions, we attributed the DW pinning to the dipolar interaction with nonuniform magnetization in the Co layer, which may be induced for instance by the crystallographic structure of Co. Micromagnetic simulations have supported this possible scenario.

The need to reduce and control pinning has speeded up the optimization of the NiFe/Cu/Co growth. We have employed Ion-Beam Assisted Deposition to modify the deposition process of this multilayer system. It was found that by assisting Ar ion bombardment of a specific energy of 50 eV, it is possible to strongly decrease the interlayer coupling so that with a 3-nm Cu spacer the NiFe and Co layers are practically decoupled. It was also observed that the use of CoO underlayers did not result in an increase of the Co coercivity, but the CoO layer prepared by oxidation during the Co deposition improved the transport properties of the system. The GMR increased up to 4.5% and the magnetization reversals became more sharp with a well defined switching field. The optimization was carried out in parallel with the XMCD-PEEM

measurements during my stays in Brno, therefore the final structures could not be used before the third year of the PhD thesis.

Besides the standard e-beam lithography technique, carried out in Grenoble, the preparation of the structures by FIB has been proposed and demonstrated with the instrumentation available in Brno. The FIB-CVD technique enables one to carry out both the etching of magnetic nanowires and deposition of contacts at the same processing step. A prototype of a FIB-made structure has been made. However, FIB etching of Co layers revealed one interesting feature – although the grain size in thin Co layers is of the order of 8 nm, larger regions of grains with close crystallographic orientations, with a size comparable to the pinning sites in the XMCD-PEEM images, are present in the layers.

The second set of measurements, XMCD-PEEM in the time-resolved mode, allowed us to observe the magnetic configuration changes during the application of current pulses. The changes in the magnetic contrast are consistent with a tilt of the NiFe magnetization in the direction transverse to the nanowire direction. The Oersted field generated by the current flowing in the Cu and Co layers has been identified as the origin of the NiFe magnetization tilt.

The large tilts could not be simply explained on the basis of the analytical model for the demagnetizing fields, which predict angle about four times smaller. This discrepancy is probably due to an overestimation of the the transverse demagnetizing factor. A first origin of the decrease of the demagnetizing factor can be attributed to its inhomogeneity along the cross-section.

The effect of the Oersted field is particularly important in spin-valve systems, where the center of the current flow is expected to be situated in the highly conductive Cu spacer. The partial compensation of magnetic charges at the edges of the NiFe lines by mirroring effects in the Co layer yields larger tilts than in the single NiFe layers. This effect is further enhanced by the fact that the Oersted field acts in opposite directions on the NiFe and Co layers.

The lateral roughness of the nanowires might also substantially modify the effective demagnetizing factor by the compensation of magnetic charges at the nanowire edges.

In addition to the tilt of the NiFe magnetization, the time-resolved measurements reveal that the magnetization undergoes fast oscillations after the onset of the current pulse. These oscillations are due to the precession of the magnetization about the effective field. The presence of a random distribution of dipolar pinning sites results in an inhomogeneous magnetic contrast in the sections of the spin-valve nanowire. It turned out that the initial phase for the precessional motion is different for each of the individual oscillators. The exchange interaction between each oscillator is however such that the spatio-temporal variation of the magnetic contrast resembles that expected for spin waves.

Let us return to the high efficiency of the spin transfer in SV nanowires. There are two likely explanations for this effect. First, vertical spin currents resulting from a local spin accumulation near the DW in the Cu spacer can provide an additional channel for the spin transfer resulting in large DW velocities, as it was theoretically predicted.

Second, the presence of a surprisingly large effect of the Oersted field on the nanowire magnetization could strongly influence domain wall dynamics in NiFe. It has been shown in the literature that transverse fields stabilize one chirality of TWs during field-driven DW motion. The spin-valve system is a bit more complex, as the flux closure between a TW in the NiFe layer and a quasi-wall in the Co layer should also contribute to preventing an easy switching of the structure by the Oersted field. In any case, we expect that the DW transformations responsible for the slow and chaotic DW motion beyond the Walker breakdown should be inhibited. This has not yet been confirmed by micromagnetic simulations.

In summary, we have shown that spin-valve nanowires are a very interesting research subject for fundamental understanding of spin torque effects in complex systems and moreover, are highly promising systems for applications to spintronic devices. The DW velocities in NiFe are 4 to 5 times larger than the maximum value reported for other in-plane anisotropy systems, where velocities in the order of 100 m/s have been published. Given the role of pinning in the NiFe/Cu/Co system and the way the velocities have been measured, we believe that the ultimate DW velocities in this kind of systems could even exceed 600 m/s. The idea is supported by intriguing preliminary results of the time-resolved DW motion where in two different measurement scenarios the DW velocity largely exceeded 1000 m/s.

High DW velocities achievable at relatively low current densities make spin-valve systems promising for spintronic devices based on DW displacement. Such trilayers are naturally much more complex than the generally used NiFe systems. We have identified the main pinning sources, among which the dipolar interaction of the NiFe layer with Co anisotropy inhomogeneities is the most probable and should be controlled in order to be able to discover the full capabilities of the system and to employ it in the future DW devices.

Appendix A

GENERAL CONSIDERATIONS CONCERNING MICROMAGNETIC SIMULATIONS

Influence of Mesh The mesh size plays an essential role, as an incorrect selection might cause misleading results. It is often compared to the exchange length $\Lambda = \sqrt{\frac{2A}{\mu_0 M_S^2}}$ of a given structure and material which represents the scale over which the magnetization may deviate in the presence of exchange and dipolar interactions. In NiFe it is of the order of 5 nm. Hence, the mesh size has to be smaller to reproduce the variations of the local magnetization direction. However, if the material features a strong magnetocrystalline anisotropy, the mesh size should be compared to the lowest of the exchange length or the Bloch length $\Lambda_B = \sqrt{\frac{A}{K}}$.

We have calculated the total magnetic energies of a transverse DW in a 200 nm wide NiFe nanowire for different mesh sizes. We found out that a compromise between the computation time[1] and the calculation accuracy can be found for a cell size of approximately 4 nm (Fig. A.1), which is below the exchange length. The accuracy was

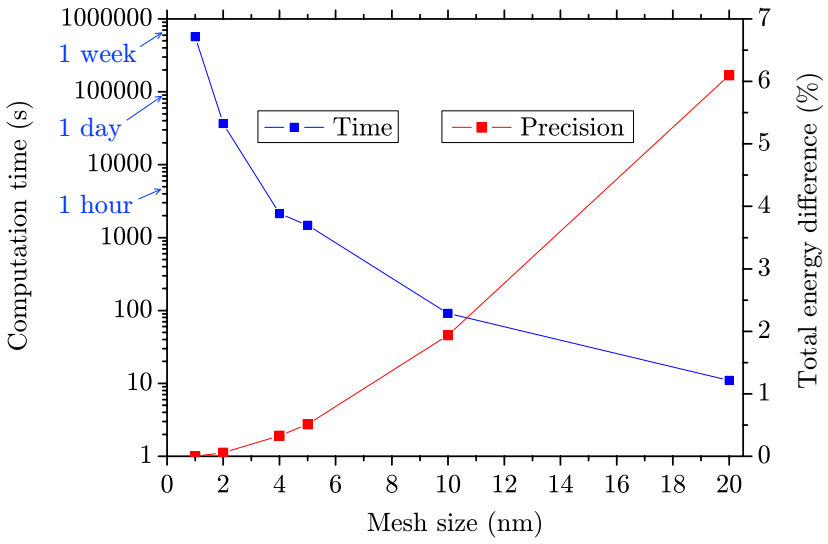

Fig. A.1: Computation accuracy vs. computation time as a function of the mesh size. Simulation was done for a TW in a NiFe 6000×200×5 nm^3 nanowire.

[1] All computational requirements were compared using a laptop with a dual-core processor running at a frequency of 1.83 GHz and possessing 3 GB of physical RAM.

determined as a relative error in the final energy with respect to that calculated with the smallest cell size – 1 nm.

Since there is almost no magnetization variation along the z direction, we can minimize the number of mesh cells in this direction. This was proved by simulation – the final total energy was almost identical for one cell and two cells along the z axis. However, one has to be careful with wires of a low aspect ratio (thickness-to-width of more than 1 to 10) – in this case the difference rose to 4.5%. For aspect ratios 1 to 20 and less the difference was less than 0.2%. Moreover, doubling the mesh count in the z direction caused computational time increase by a factor 3 to 10, depending on the wall type and wire geometry. Therefore, we usually use a mesh size of $4\times4\times z\,\mathrm{nm}^3$.

Influence of the alpha parameter For static experiments the value of α has zero effect (the final energy is constant). Low values, however close to the real ones, only increase the computation time [Figure A.2]. Therefore, in all simulations the alpha damping parameter was set to 0.5. The stopping condition was dm/dt reaching 0.1 deg/ns.

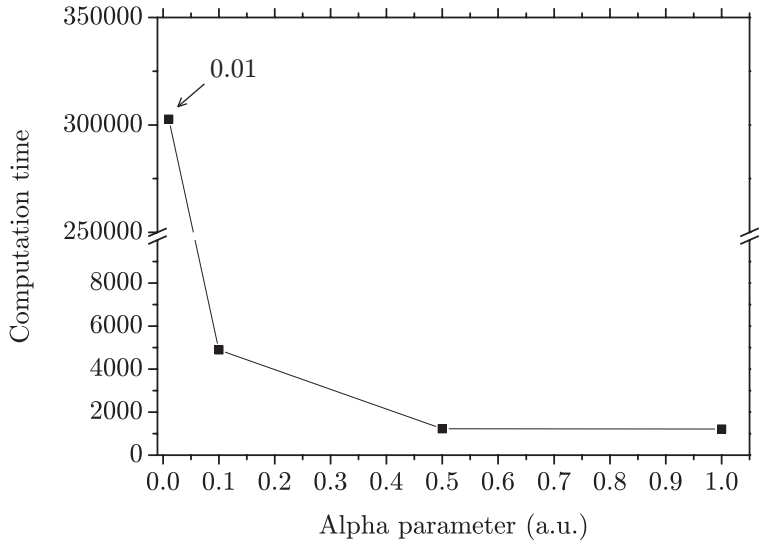

Fig. A.2: Influence of the alpha parameter value on computation time. Simulation done for a transverse wall in a NiFe $6000\times160\times5\,\mathrm{nm}^3$ nanowire.

A.1 Parameters of Used Materials

- Co
  $M_\mathrm{S} = 1400$ kA/m ($J_\mathrm{m} = \mu_0 M_\mathrm{S} = 1.7\,\mathrm{T}$)
  $A = 3 \times 10^{-11}$ J/m
  $K = 520\,\mathrm{kJ/m^3}$

- NiFe
  $M_\mathrm{S} = 800$ kA/m ($J_\mathrm{m} = \mu_0 M_\mathrm{S} = 1\,\mathrm{T}$)
  $A = 1 \times 10^{-11}$ J/m
  $K = 0.5\,\mathrm{kJ/m^3}$

Appendix B

PANEL OF INVOLVED ANALYTICAL TECHNIQUES

In this section a basic description of the experimental techniques used for the analysis and optimization of the magnetic multilayers will be described. The SIMS and XPS techniques are located in the complex multichamber ultrahigh-vacuum system (Fig. B.1) in a cleanroom of the Institute of Physical Engineering at Brno University of Technology. The experimental devices used in this work are marked in red.

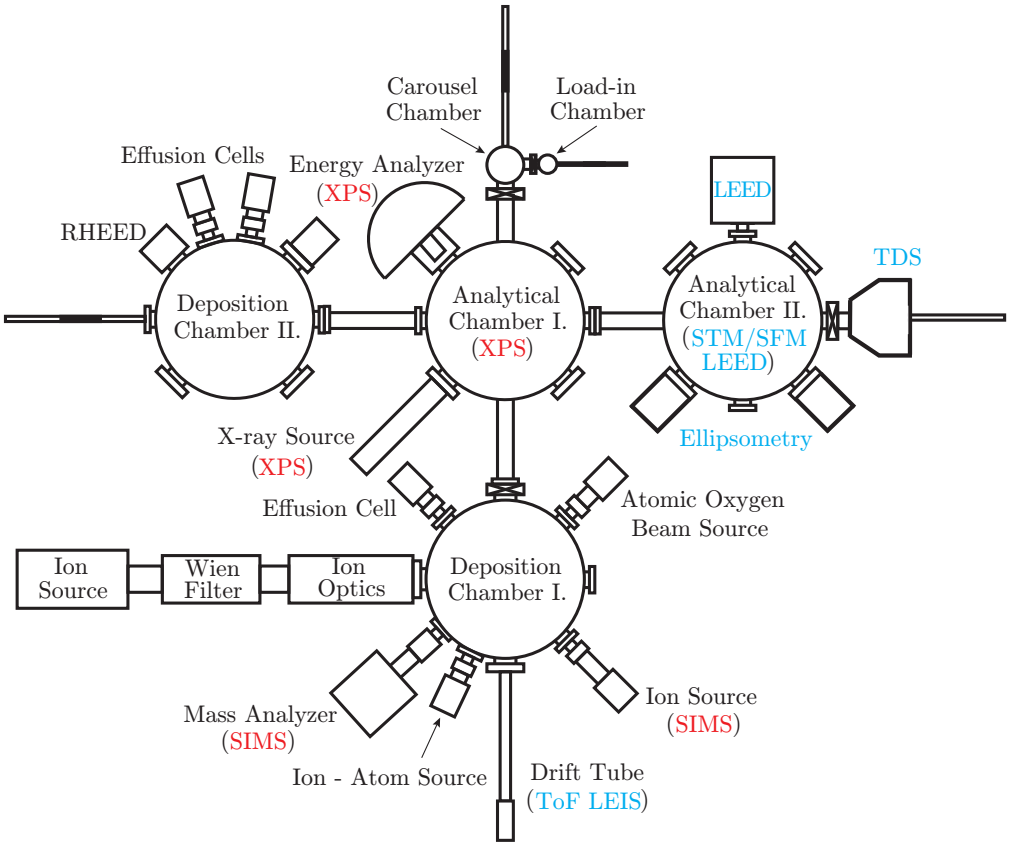

Fig. B.1: Multichamber vacuum system at the Institute of Physical Engineering.

B.1 Secondary Ion Mass Spectroscopy

Secondary ion mass spectroscopy (SIMS) is a mass spectrometry of secondary ions emitted under bombardment of a sample surface with a primary ion beam. The measured mass spectrum yields information about the elemental composition of the surface. Typical energies of the primary ion beam are between 0.5 and 5 keV [240]. The sputtered particles are both atoms and clusters of the sample material. They are electrically negative, positive or neutral and have kinetic energies ranging from zero to hundreds of eV [241]. The elemental analysis by SIMS relies on the fact that only the atoms which are present in the near-surface region[1] will be emitted. Moreover, the clusters are emitted only from the surface sites.

The mass spectra are obtained using a Quadrupole Mass Spectrometer. It consists of four quadrupole rods where a superposition of DC voltage and an AC component is applied. From the dynamic equation for the ion motion through the spectrometer [240] it follows that only species of a particular m/Q ratio can pass the spectrometer and arrive to a detector.

In principle, a quantitative analysis by SIMS would be possible. However, the most critical parameter in SIMS quantitative analysis, the *secondary ion yield*, depends primarily on the elemental composition of the surface, sample matrix and type of the primary ions [241]. An example of the matrix effect is a big increase in the metal ion yield upon replacing the pure metal by its oxide. The variations can range up to four orders of magnitude. Therefore, the practical quantitative SIMS analysis is usually carried out after experimental determination of the secondary ion yield from reference samples or standards and often by using relative sensitivity factors.

There are two principal modes of operation in SIMS:

- Static SIMS
  In this mode very low primary ion current densities of 10^{-10}-10^{-9} A/cm^2 are used and the sputtering rate is thus extremely low and the destruction of the surface is minor. The method is used to study surface composition with a detection limit as low as 10^{-8} ML [241].

- Dynamic SIMS
  The primary ion current densities are 10^{-5}-10^{-4} A/cm^2 and the sputtering rate is high (several ML per second) [241]. This mode is often used for depth profiling, i.e. the determination of the concentration versus depth for one or more elements present in the sample. The detection limit is typically between 10^{12}-10^{16} atoms/cm^2. The depth resolution is mainly limited by the sputtering process – atomic mixing, selective sputtering, roughening of the crater bottom which becomes more important with increasing the depth, and the crater edge effect. However, the edge effect can be eliminated by the so-called gating technique. It ensures that the signal is only recorded when the ion beam is passing through a defined area in the middle of the crater, thus eliminating the signal from the crater sides.

[1] The majority comes from the two topmost layers. 95% originates from the surface layer.

B.2 X-ray Photoelectron Spectroscopy

X-ray photoelectron spectroscopy (XPS) is a method for investigation of chemical composition of surfaces and thin films. The analyzed thickness is limited by the escape depth of secondary electrons. This characteristic length is of the order of few nanometers and is element-dependent.

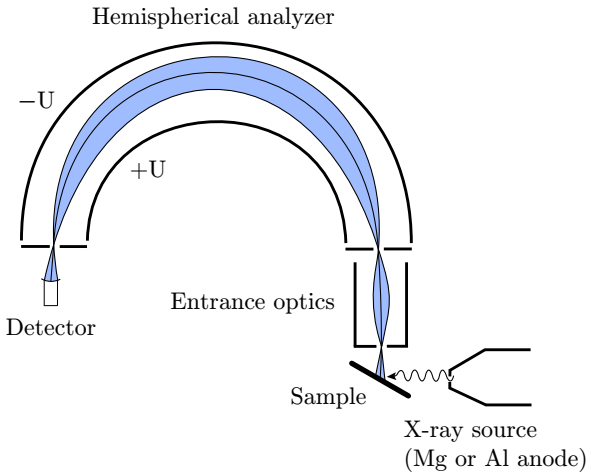

Fig. B.2: XPS scheme. X-rays excite photoelectrons and those with a specific kinetic energy pass the hemispherical analyzator.

The experimental set-up is shown in Fig. B.2. A magnesium or aluminium anode is used is an x-ray source. Electrons with an energy of 15 keV impinge on the cooled anode and excite an electron from the core level. The system then relaxes by filling the vacancy with an electron from a higher energetic level, followed by an emission of a characteristic x-ray photon. One obtains photons of an energy of 1253.6 eV (Mg anode) or 1486.6 eV (Al anode) which interact with the core electrons of the investigated material. The emitted electrons escaping into vacuum possess a kinetic energy of

$$E_{\mathrm{K}} = \hbar\omega - E_{\mathrm{B}} - \phi_{\mathrm{w}} \tag{2.1}$$

where $\hbar\omega$ is the energy of incoming x-rays, E_{B} the binding energy related to the Fermi level and ϕ_{w} the work function. The kinetic energy is measured by a hemispherical analyzer combined with a channel multiplier. The potential settings of $U+$ and $U-$ on the hemispherical analyzer (Fig. B.2) let only electrons with a specific kinetic energy pass. The binding energy E_{B} can be determined according to the formula 2.1. As a result, we obtain a photoelectron emission spectra for different binding energies which are element-specific and can be found in literature. Moreover, from the shifts of the studied peaks specific chemical bonds can be identified. The detection limit of XPS can go down to 1000 ppm. More details about the method and the interpretation of the XPS spectra can be found in [364].

B.2.1 Angle-Resolved X-ray Photoelectron Spectroscopy

AR-XPS is a special method of XPS. It is based on the fact that the depth of analysis is dependent on the electron angle of emission θ (see Fig. B.3). At normal electron emission ($\theta = 0°$) the analysis depth is at the limiting value of $\sim 3\lambda$ [364] where λ is the $1/e$ electron yield depth – the number of electrons emitted from an increasing depth decreases exponentially. At high values of θ, the analysis becomes even more surface-sensitive. The sampling depth is described as $3\lambda \cos\theta$.

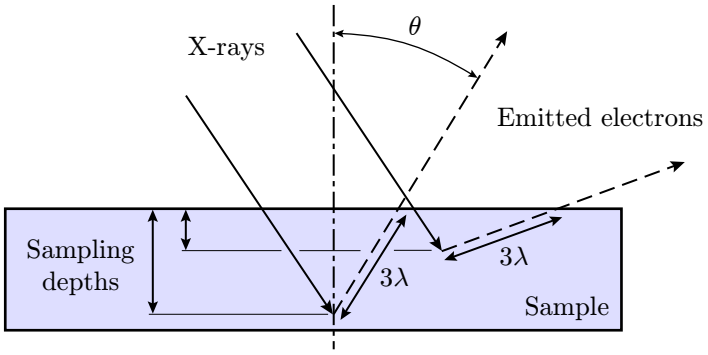

Fig. B.3: Angle-dependent electron emission. The sampling depth is described as $3\lambda \cos\theta$.

By measuring the electron emission spectra for different angles θ it is possible to reconstruct the compositional depth profile of the near-surface region [364]. There are many approaches to model such profiles. However, no unique transformation from angle-dependent intensities to depth-dependent concentration exists[2]. This implies that a least squares fit of trial profiles to experimental data is not sufficient to determine accurate concentration profiles.

There are different approaches for defining the trial profiles. A good choice of the initial profile is essential for the analytical method which determines the concentrations by solving the optimization task in the whole space of real numbers [365]. Another method applies the genetic algorithms to define the trial profiles as few discrete solutions. The fitting method comprises a special testing criterion – a standard least square method combined with the criterion of unsmoothness (maximalization of entropy) [366] – which compares the angle-dependent intensities calculated from the trial profiles to the experimental ones. Importantly, the method also assumes that the individual layers are continuous and have sharp interfaces.

B.3 Atomic Force Microscopy

Atomic Force Microscopy (AFM) is a method for a detailed imaging of solid-state surfaces. It is based on the interaction of a very sharp tip with the surface atoms.

[2]The opposite, calculating the theoretical angle-dependent intensities from a given compositional depth profile, is possible.

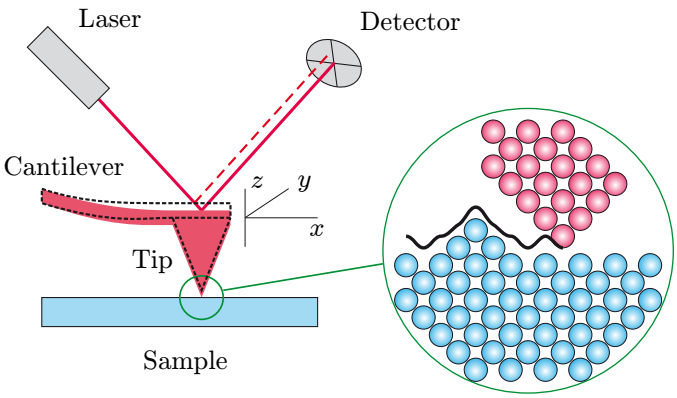

Fig. B.4: AFM scheme. Original image by R. Kalousek.

The sample is placed on a piezoceramic scanner which moves the sample in the plane parallel to the sample. The tip is placed on an elastic cantilever located above the sample (see Fig. B.4). The cantilever is being deflected due to the attractive or repulsive forces between the tip and the surface atoms. A laser beam focused at the end of the cantilever is reflected into a detector consisting of four photosensitive segments. The deflection of the cantilever is then quantified by the change of the differential signal on the detector. By recording the deflection during scanning of the sample we obtain a map of the sample morphology. The resolution is limited vertically by the piezo-scanner parameters (in the order of 1 Å) and laterally particularly by the tip sharpness (typically in the units of nanometers).

The interaction between the tip and the surface atoms is described by the Lennard-Jones potential [363]:

$$U(r) = 4\varepsilon \left[\left(\frac{\sigma}{r}\right)^{12} - \left(\frac{\sigma}{r}\right)^{6} \right]. \tag{2.2}$$

ε and σ are material-specific constants and r is the distance between two atoms. The potential is plotted in Fig. B.5.

Depending on the distance between the tip and the surface, we distinguish two measurement modes:

- Non-contact mode
  The tip is located above the surface and the cantilever oscillates at its resonant frequency. When approaching the tip to the surface, the attractive interaction shifts the oscillation frequency. From the shift we can determine the distance from the surface and form the morphology map.

- Contact mode
  The tip is in a close contact with the surface and the repulsive forces take place here. The cantilever is deflected proportionally to the repulsive force and the shift of the laser spot is recorded by the detector. Here we further distinguish the modes of:

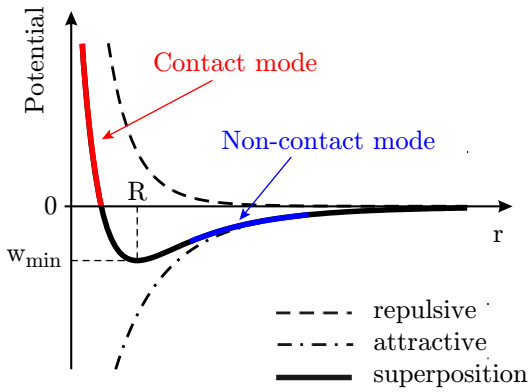

Fig. B.5: The force between the tip and the surface atoms is described by the Lennard-Jones potential plotted in the figure. The operating zones for the two basic AFM modes, the contact mode (red curve) and non-contact mode (blue curve), are indicated.

– Constant force
  We set a constant force acting on the tip. The feedback loop ensures a constant distance between the tip and the surface.

– Constant height
  This mode results in a faster scanning because of the absence of the feedback loop, but the tip or the surface can be easily damaged.

B.4 Resistance Measurement by van der Pauw Technique

When measuring small resistances, i.e. if the resistance of the contacts and cables is not negligible with respect to the measured resistance, we have to use a four-probe technique, i.e. to use two contacts for supplying a constant current through the sample and two more for measuring the corresponding potential drop on the sample itself. This technique is of a wide use, but might not be precise enough if there is a need for comparing the resistances of different samples of different shapes or for measuring the specific resistivity ρ/t' where t' is the sample thickness[3]. To avoid this setback, a solution was suggested by L. J. van der Pauw in 1958 [367].

His method is based upon a theorem which holds for a flat sample of an arbitrary shape, if the contacts are sufficiently small and located at the circumference of the sample. Furthermore, it cannot contain any holes (a simply connected structure) and the sample should be homogeneous in thickness. Then for measuring the specific resistivity ρ/t' of a flat sample it suffices to make four small contacts along its circumference and to measure the resistances $R_{\mathrm{AB,CD}}$, $R_{\mathrm{BC,DA}}$ (see Fig. B.6):

[3]This specific resistivity can be denoted as $\rho/t' \equiv \rho_{\square}$, i.e. as a resistance per square.

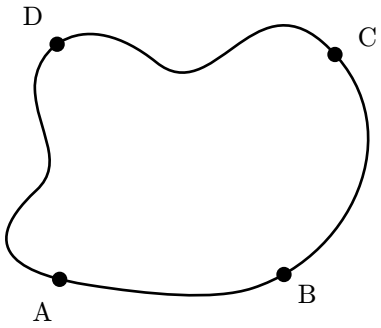

$$R_{\mathrm{AB,CD}} = \frac{V_{\mathrm{D}} - V_{\mathrm{C}}}{I_{\mathrm{A}\to\mathrm{B}}}$$

$$R_{\mathrm{BC,DA}} = \frac{V_{\mathrm{A}} - V_{\mathrm{D}}}{I_{\mathrm{B}\to\mathrm{C}}}$$

Fig. B.6: Configuration for measuring the specific resistivity using the van der Pauw technique.

$$1 = \exp\left(-\frac{\pi R_{\mathrm{AB,CD}}\, t'}{\rho}\right) + \exp\left(-\frac{\pi R_{\mathrm{BC,DA}}\, t'}{\rho}\right). \tag{2.3}$$

The formula was proved by van der Pauw for a semi-infinite plane and consequently he showed that it holds for a sample of an arbitrary shape with the restrictions defined above. The equation (2.3) can be solved numerically, or it can be shown [367] that ρ takes the form of

$$\rho = \frac{\pi t'}{\ln 2}\,\frac{R_{\mathrm{AB,CD}} + R_{\mathrm{BC,DA}}}{2}\, f\left(\frac{R_{\mathrm{AB,CD}}}{R_{\mathrm{BC,DA}}}\right). \tag{2.4}$$

f is a function of the ratio of the resistances and satisfies the equation

$$\frac{R_{\mathrm{AB,CD}} - R_{\mathrm{BC,DA}}}{R_{\mathrm{AB,CD}} + R_{\mathrm{BC,DA}}} = f\,\operatorname{arccosh}\left[\frac{\exp\left(\ln\frac{2}{f}\right)}{2}\right]. \tag{2.5}$$

If $R_{\mathrm{AB,CD}}/R_{\mathrm{BC,DA}}$ is close to 1, then

$$f \approx 1 - \left(\frac{R_{\mathrm{AB,CD}} - R_{\mathrm{BC,DA}}}{R_{\mathrm{AB,CD}} + R_{\mathrm{BC,DA}}}\right)^2 \frac{\ln 2}{2} - \left(\frac{R_{\mathrm{AB,CD}} - R_{\mathrm{BC,DA}}}{R_{\mathrm{AB,CD}} + R_{\mathrm{BC,DA}}}\right)^4 \left[\frac{(\ln 2)^2}{4} - \frac{(\ln 2)^3}{12}\right]. \tag{2.6}$$

Note also that in his original work van der Pauw gave an estimation of the errors $\frac{\Delta\rho}{\rho}$ in case the restrictions defined above are not fulfilled, i.e. if one of the contacts has a length l on the periphery of the sample, has a length l perpendicular to the periphery and/or although a point, it is situated at a distance d from the periphery. It could be shown that these errors for each contact and for all the contacts together are to a first approximation additive [367].

The errors can be largely avoided by choosing a convenient sample shape, e.g. a square-shaped sample connected to the four contacts by small "necks" at each of the corners. For this square-shaped sample, i.e. in case the length l and width w of the sample are equal, one directly obtains

$$R = \rho\frac{l}{tw} = \rho_{\square} \tag{2.7}$$

and the equation (2.4) reduces to

$$\rho_{\square} = \frac{\pi}{\ln 2}\frac{\Delta U}{I} \tag{2.8}$$

where ΔU is the potential difference between two points defined in Fig B.6.

B.5 Transmission Electron Microscopy

In transmission electron microscopy (TEM), the image is formed by electrons passing through the sample. The principle of operation is similar to that of an optical microscope, except of using electrons instead of photons and magnetic lenses instead of glass lenses [241]. The beam of electrons is focused by a condenser lens into a small spot (2-3 μm) on the sample and after passing through the sample is focused by the objective lens on the screen where a magnified image is formed. An essential element determining the image contrast and resolution limit of the microscope is the aperture located at the back focal plane of the objective lens [241]. Due to the limited penetration depth of electrons in solids, the samples should be very thin: the acceptable thickness is 100-1000 Å for conventional microscopes with accelerating voltages of 50-200 keV [241]. The required sample thickness depends on the sample material – the larger the atomic number the thinner the sample should be.

The TEM resolution is determined by the diffraction limit[4] and the imperfections of the lens system. In recent TEMs with a hardware correction of the spherical aberration a resolution below 1 Å is reached [368]. Using a high-resolution TEM, images revealing the atomic structure can be obtained.

TEM observations are widely used for studying interfaces in cross-sections of multilayered samples. Prior to the observation, the sample is cut to thin slices and is further made thinner by mechanical grinding or chemical etching and finally by ion milling.

[4]The electron wavelength is 0.037 Å for a voltage of 100 keV. It can be obtained from the de Broglie formula and the kinetic energy of electrons eU taking into account relativistic effects, as the velocity of electrons in TEM approaches the speed of light c:

$$\lambda_{\mathrm{e}} = \frac{h}{\sqrt{m_{\mathrm{e}}eU\left(2 + \frac{eU}{m_{\mathrm{e}}c^2}\right)}}. \tag{2.9}$$

m_{e} is the electron rest mass.

B.6 Focused Magneto-Optical Kerr Effect and Kerr Microscopy

These techniques are based on magneto-optical (MO) effects, i.e. on the interaction of polarized light with the internal magnetic field of a magnetized specimen. Generally, a linear light polarization is rotated upon transmission through an optically transparent sample (Faraday effect) or reflection from a nontransparent sample (Kerr effect, MOKE) [369, 33].

Depending on the geometry of the plane of the light incidence and the magnetization in the sample we distinguish three configurations for measuring MOKE (Fig. B.7). In the polar Kerr effect (a), magnetization is normal to the sample surface. In the longitudinal Kerr effect (b), the magnetization is parallel to the sample surface and to the plane of incidence. In the transverse Kerr effect (c), the magnetization is parallel to the sample surface and perpendicular to the plane of incidence.

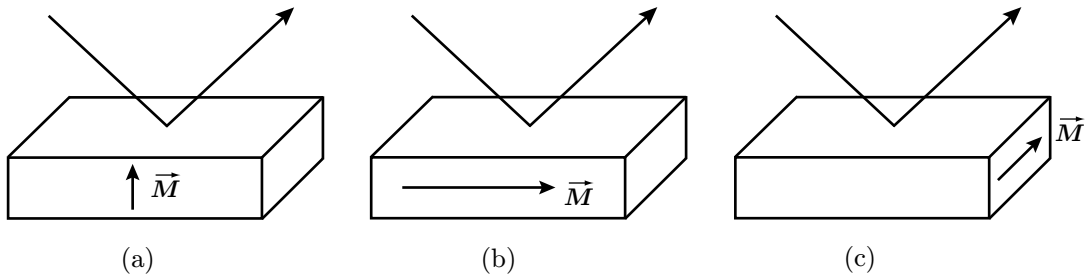

Fig. B.7: MOKE geometries: (a) Polar Kerr effect, (b) longitudinal Kerr effect, (c) transverse Kerr effect.

In this work the MOKE is exploited in two techniques:

- Focused MOKE – a linearly polarized laser beam is focused into a small spot (0.5 μm-1 μm) on a magnetized specimen and the rotation of light polarization is recorded upon sweeping a magnetic field. As the Kerr rotation ϕ_{K} is proportional to the magnetization in the laser spot, a hysteresis loop of normalized magnetization versus applied magnetic field can be obtained.

- Wide-field Kerr microscopy – this method is suitable for observation of magnetic domains in a sample. Kerr microscopes are standard reflected-light microscopes equipped with a polarizer and analyzer, an adjustable aperture diaphragm and strain-free optics to allow for polarization microscopy [369]. A layout of the microscope components is shown in Fig. B.8(a) and (b). The light emitted from a lamp arc is focused onto the aperture diaphragm by the collector lens. The desired MOKE geometry can be selected by defining the aperture diaphragm shape as shown in Fig. B.8(c). The aperture slits define the plane of light incidence with respect to the magnetization direction. As only in-plane-magnetization systems were studied in this work, we exclusively used the longitudinal geometry.

However, if the rectangular slit is extended over the central part of the cross[5], there can be a significant contribution of the polar MOKE to the signal, in particular if there is an out-of-plane magnetization component in the sample. As the polar Kerr rotation is in the same sense and the longitudinal Kerr rotation in the opposite sense for rectangular slits symmetric with respect to the optical axis of the microscope, the polar contribution can be avoided by subtracting the Kerr signals of these symmetric rectangular slits, taken one by one.

In this work, a commercial Zeiss optical microscope adapted for magneto-optical detection by Evico Magnetics[6] has been used.

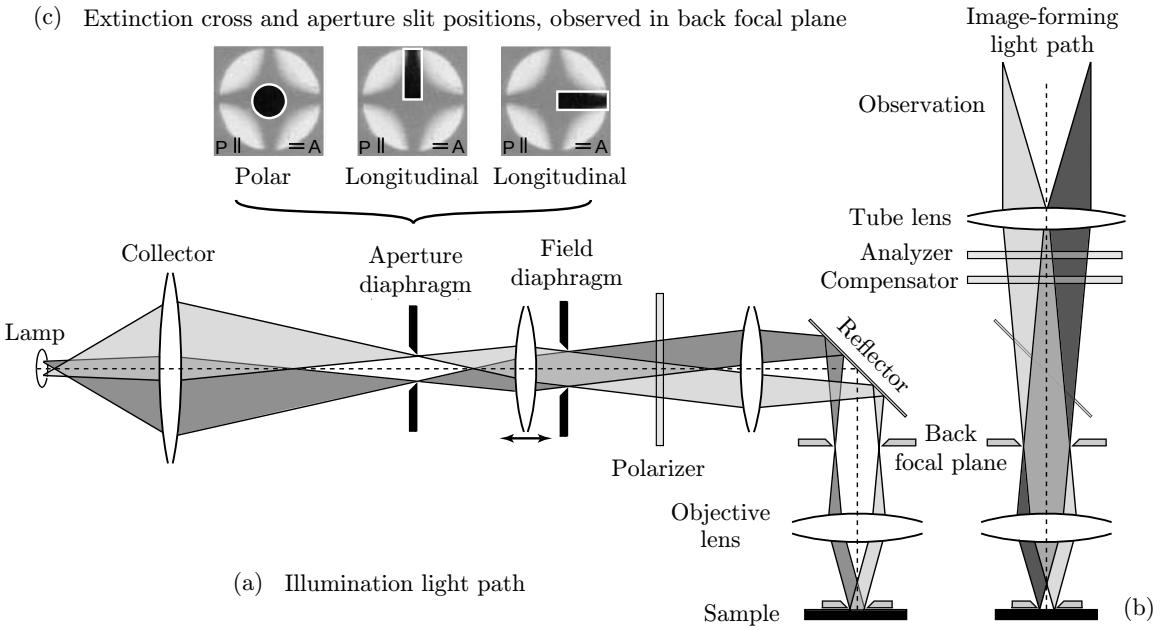

Fig. B.8: Layout of the Kerr microscope components: (a) illumination path, (b) image-forming light path. (c) The aperture diaphragm shape can be modified according to the desired MOKE geometry. The extinction cross orientation depends on the polarizer (denoted by P) and analyzer (denoted by A) setting. Reproduced from [369].

B.6.1 Contrast Formation and Microscope Adjustment

Generally, the polarization plane reflected from a magnetic material is elliptically polarized with the main axis rotated by ϕ_K with respect to the incident polarization. A compensator (a quarter-wave plate) is added to the optical path to eliminate the ellipticity and improve the magnetic contrast.

Before the observation the polarizer and analyzer are crossed to obtain extinction of the light intensity. Due to the oblique light incidence on the lenses, the extinction

[5]The orientation of light polarization is best defined here.

[6]Drs. J. McCord and R. Schäfer from the Institut für Festkörper- und Werkstoffforschung (IFW), Dresden, Germany.

is achieved only in a cross-like region which can be observed in the back focal plane together with the aperture diaphragm [Fig. B.8(c)]. The linear polarization of the incident light is defined by the polarizer (Fig. B.9, E_{P}). Upon reflection it is rotated by the angle ϕ_{K} in opposite directions for oppositely magnetized domains. To maximize the domain contrast, the difference of the absolute values of the projections of intensities E_{K} and $-E_{\mathrm{K}}$ on the analyzer direction has to be maximized. This is achieved by turning the analyzer by ϕ_{K} (Fig. B.9) ensuring the highest contrast. However, wider opening of the analyzer leads to a higher signal-to-noise ratio. The best settings for the analyzer and the compensator have to be adjusted each time according to the studied material.

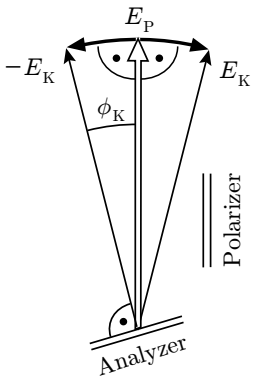

Fig. B.9: Setting the analyzer to maximize the MOKE contrast.

Procedure of the microscope adjustment:

1. Focus on the sample. In focus the field diaphragm[7] has to be sharp.
2. Image the light source in the back focal plane together with the aperture diaphragm. The back focal plane can be visualized by inserting the Bertrand lens.
3. Cross the polarizer and analyzer to obtain an extinction cross.
4. Set the aperture slits according to the desired magneto-optical effect.
5. Move the collector lens in order to see the arc. Move the arc well behind the selected aperture diaphragm (slit). Remove the Bertrand lens. Expand the image of the arc by moving the collector.
6. Apply oscillating magnetic field on the sample. Optimize the domain contrast by adjusting the compensator and analyzer positions.

[7]The aperture limiting the field of view.

Appendix C

KERR MICROSCOPY IMAGING OF MAGNETIC TRILAYERS

The Kerr microscope has been used to partially characterize the magnetic trilayers either in the form of continuous films or nanowires, prior to the XMCD-PEEM measurements. The optimization of the detection procedure has proved difficult for the nanowires with in-plane magnetic anisotropy, because of three reasons: i) the width of the nanowires is similar to the light wavelength, introducing diffraction effects; ii) depolarizing effects occur at the edges of the nanowires; iii) the insufficient mechanical stability of the set-up. For these reasons the magneto-optical characterization has been only exploratory. Some of the results and the problems that were encountered are described below. Note that the microscope has revealed an extremely useful tool for nanowires with perpendicular anisotropy, where the Kerr signal is larger and edge effects play a minor role. The perpendicular light incidence in this case also substantially reduces optical aberrations.

Fig. C.1(d) shows a typical image of a 500 nm wide NiFe nanowire after a standard optimization described in B.6.1. A magnetic field of 40 mT was applied in the plane of the sample, transverse to the longitudinal direction of the zigzag structures as indicated in the figure.

The aperture slit is set in the vertical direction [like in the central panel of Fig. B.8(c)] so that the measurement is sensitive to the magnetization in the same direction. The magnetic contrast (black or white for different zigzag sections) therefore corresponds to a magnetization pointing up or down in the plane of the film. In order to enhance the contrast, each magnetic image is the difference between two images taken with opposite directions of the magnetic field.

During the microscope commissioning time, we realized that the reflected light intensity from the nanowires was strongly dependent on the detection geometry. Typically in the longitudinal mode, the light reflected by adjacent sections of the zigzag structures can be very different [Fig. C.1(a)], completely hiding the magnetic contrast. After a thorough investigation, it was found that this feature might come from:

1. Directionality of light incidence and "shadowing effects". Better images are obtained when the aperture slit is aligned along the sections of the zigzag. Moreover, large optical aberrations are induced for non-paraxial rays. Obviously, the effect is negligible for a polar configuration [Fig C.1(b)].

2. High depolarization of light for a slit placed far from the optical axis [see the

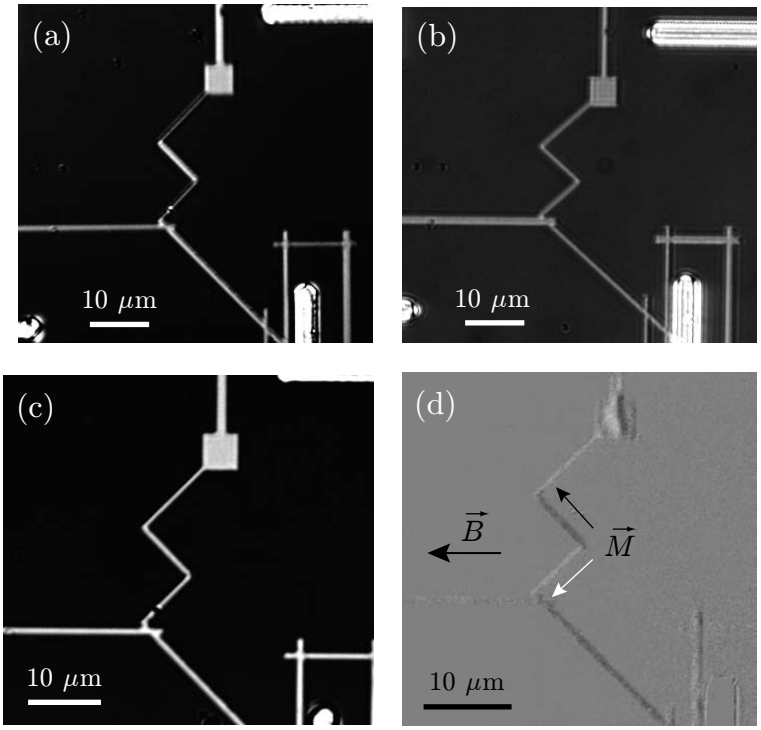

Fig. C.1: Images of a NiFe nanowire patterned to a zigzag shape of a 500-nm width, obtained with a Kerr microscope. (a) Kerr image in the longitudinal geometry with a low compensator correction, (b) in the polar geometry, (c) in the longitudinal geometry with a high compensator correction and a corresponding image (d) where a background image was subtracted to enhance the magnetic contrast. The magnetic contrast is indicated by the black and white colors representing magnetization pointing up or down in the plane of the sample (the longitudinal slit is vertical).

extinction cross shown in Fig. B.8(c)]. Making the slit narrower increases the fraction of polarized light, but this leads to a decreased spatial resolution (the numerical aperture is smaller).

3. High ellipticity of light reflected at high angles of incidence.

Another parameter contributing to the observation difficulties is the fact that the narrow width of the nanowires is comparable to the light wavelength. This fact is responsible for the diffraction patterns that sometimes appear at the structures edges.

Various tests showed that it is very important to optimize the slit dimension and the analyser/compensator angles, so that the light reflected by the different sections of the nanowires is homogeneous. A typical optimized image is shown in Fig C.1(c). The compensation of the ellipticity seems to be one of the important parameters of the optimization procedure. The magnetic contrast in image Fig C.1(d) is obtained by subtracting two images similar to Fig C.1(c) with opposite directions of the applied field.

The previous data were obtained using a 50× objective with a numerical aperture of 0.83. Better data with improved resolution were obtained with a non-magnetic 100×

objective with a 0.9 numerical aperture. Note the very high quality of the magnetic image which typically allows us to see that the magnetization within the various zigzag sections is not homogeneous.

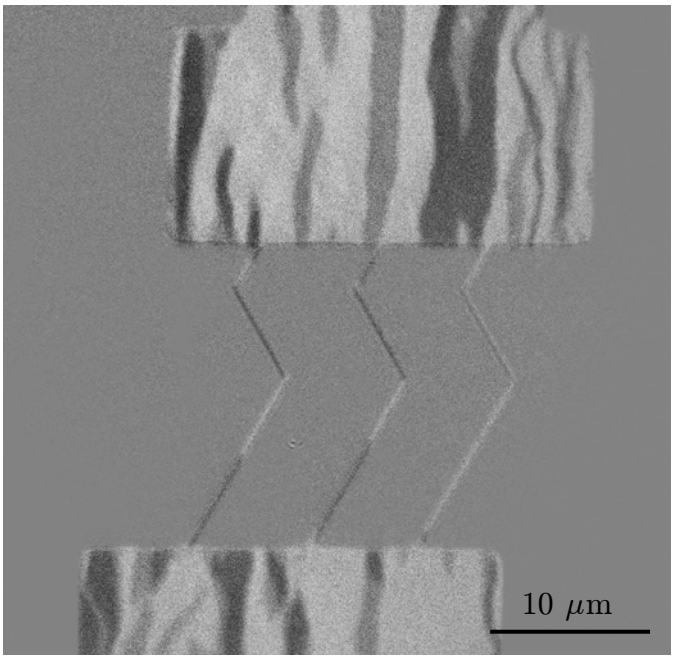

Fig. C.2: Kerr image of 500-nm NiFe/Cu/Co nanowires imaged with a 100× objective. There are three gray levels in the pads. The lightest and the darkest one stand for the parallel magnetization in the layers, the intermediate for one of the antiparallel magnetization states.

A series of tests was carried out to characterize the samples: i) the magnetic field values required for creating a DW in the zigzag corner were found; ii) the reproducibility of this process had to be verified; iii) the samples were electrically contacted and some preliminary tests on DW displacements as a function of current-pulse length were carried out. These tests contributed to show that DW displacements are not highly reproducible, since rare events of current-induced movement were observed. The results did not add anything significant to the findings presented in the Chapter 6.

Nevertheless, these tests prove that quasi-static measurements of DW movements induced by field or current are potentially feasible by magneto-optical measurements, even with 500 nm wide nanowires with in-plane magnetization.

Appendix D

GMR CHARACTERIZATION OF SPIN-VALVE NANOWIRES

The magnetization reversal properties of NiFe/Cu/Co nanowires were tested by GMR measurements. The system allows for determining the position of a DW displaced by a magnetic field [237] or electric current [181] by monitoring the resistance value of nanowires. Assuming that the magnetization points along the nanowires, completely parallel magnetizations in the NiFe and Co result in a low resistance R_{P} and completely antiparallel magnetizations in a high resistance R_{AP}. If there is one DW in the NiFe layer and Co is completely saturated, then a DW displacement by Δl evokes a change of resistance

$$\Delta R_{\mathrm{DW}} = \frac{\Delta l}{l} \left(R_{\mathrm{AP}} - R_{\mathrm{P}} \right) \tag{4.1}$$

or equivalently

$$\Delta R_{\mathrm{DW}} = \frac{\Delta l}{S_{\mathrm{c}}} \left(\rho_{\mathrm{AP}} - \rho_{\mathrm{P}} \right) \tag{4.2}$$

where l is the total length of the nanowire and S its cross-section. The GMR loops were measured by a constant current of $100\,\mu$A while applying a magnetic field along the longitudinal axis of a single bent nanowire with an opening angle of 120° [black full loops in Fig. D.1(a),(b)]. The sandwich structure was Cu 2 nm/$Ni_{80}Fe_{20}$ 5 nm/Cu 5 nm/Co 5 nm/CoO 3 nm deposited using optimized IBAD deposition. The sample exhibits a GMR of 1.7% and clean magnetization switching without an important pinning. The NiFe and Co coercive fields are 5 mT and 12 mT, respectively, projected on the direction of the zigzag section. Interlayer coupling can be excluded as the minor loops did not show any bias shift (not shown).

By applying a magnetic field perpendicular to the longitudinal axis of nanowires, switching of the individual sections can be recorded. The blue curve in Fig. D.1(a) shows switching of the longer section of the nanowire, the red one in Fig. D.1(b) shows switching of the shorter one. Corresponding schematic sketches are shown in Fig. D.1(c) and (d). The initial state is indicated in the figure.

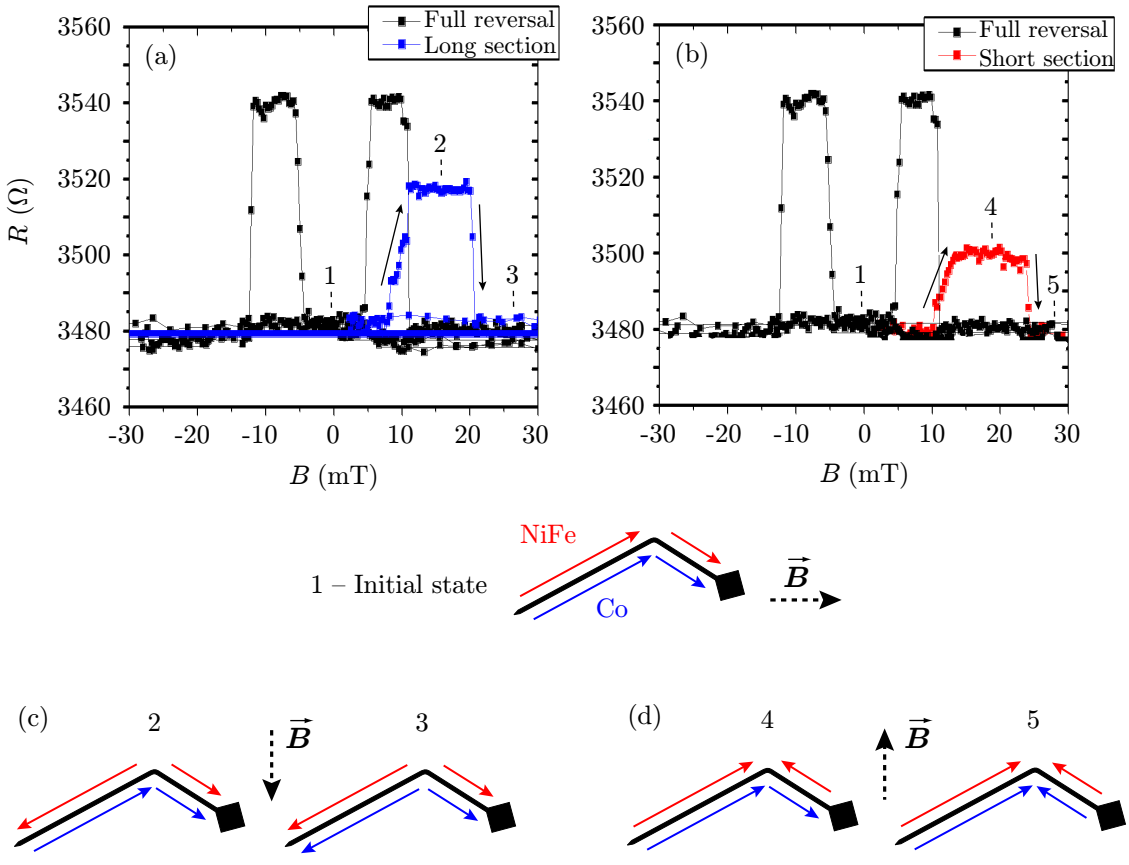

Fig. D.1: GMR loops of a 300 nm wide bent NiFe/Cu/Co nanowire with a 120° opening angle. The blue and red curves represent switching of the longer (a) and shorter (b) nanowire sections by a field perpendicular to the longitudinal axis. (c) and (d) show schematically this effect. The measurement and interpretation was carried out by P. Metaxas from the CNRS/Thales group in Orsay.

Appendix E

SOME DETAILS OF SAMPLE PATTERNING PROCESSES

Here we describe the procedures and recipes used for the lithography steps described in Section 4.

E.1 Substrate Preparation

For the lithography of nanowires we used p-doped (B) silicon (100) substrates of a resistivity of 300 Ωcm covered with a native SiO_2 layer (approx. 3 nm thick) on the surface. The substrates were cleaned in acetone, ethanol and baked on a hot-plate to get rid of the adsorbed vapors. Finally, the substrates were placed in an oxygen plasma in order to burn any remaining organic particles by the reactive ion etching technique.

Reactive Ion Etching – RIE

The substrate is placed in a vacuum chamber which is pumped and filled with a reactive gas. The plasma is created by an RF source. For burning organic materials and cleaning the developed features in the lithography process the oxygen is used. For removing SiO_2 layers, SF_6 is used. The process can be stopped at any time according to required treatment. In order not to oxidize the nanowires, RIE is not used after the exposition and development of contacts.

E.2 Resist Preparation, Exposition and Development

The layer of resist is spread using the classic spin-coating technique. When using the negative[1] SU8 UV-resist, it is recommended to place an Omnicoat underlayer in order to achieve the best lifting properties. After spin-coating the resist is hot-baked to harden it and expel bubbles present in the layer.

The masks for UV lithography are usually printed on a foil with a resolution of 9000 dpi. These can be cut to square pieces and fixed on a glass plate. However, higher resolution is obtained using chromium masks made by e-beam lithography.

[1] What is exposed is not removed by development.

The resists for e-beam lithography are prepared identically. The recipes follow.

Recipes

The following recipes are standard protocols developed at the Nanofab platform of the Néel institute.

UV Lithography

Negative resist SU8:

- Substrate cleaning (optional) in a mixture of H_2SO_4 & H_2O_2 (50:50) for 10 min
- Spreading of OMNICOAT (better lift-off, really necessary!)
  - Speed 3000 rpm, acceleration 100 rpm/s, 30 s (thickness approx. 3.5 μm).
  - Soft bake on a hot-plate at 200 °C for 180 s.
- Spreading of SU8
  - Speed 1000 rpm, acceleration 100 rpm/s, 30 s (thickness approx. 3.5 μm) speed 2000 rpm, acceleration 100 rpm/s, 30 s (thickness approx. 2 μm).
  - Soft bake on a hot-plate at 90 °C for 180 s.
- Insolation
  - For a dose of 60-80 mJ/cm^2 use exposure time 8-10 s.
  - Post-exposure bake at 90 °C for 90 s.
- Development
  - SU8 developer for 1 min (shake the glass), deionized water cleaning.
  - MF319 for OMNICOAT, 45 s with shaking (eventually longer according to the current state), deionized water cleaning.
  - If there are residues of resist, use RIE: SU8 – programme SUAYFE4 for 30 s, OMNICOAT – programme Omnic for 30-60 s.
- Lift-off: Remover PG at 80 °C for 15-30 min.

E-beam Lithography

Positive resist PMMA:

- Spin coating
  The resist thicknesses depending on the spin-coating parameters are in Table E.1. PMMA concetration of 2% or 4% was used according to the thickness of prepared nanostructures.

PMMA	Speed (rpm)	Acceleration (rpm/s)	Time (s)	Thickness (Å)
2%	1500	2000	60	956
2%	2000	2000	30	868
3%	2000	2000	30	1940
3%	3000	3000	30	1550
4%	2000	2000	30	3873
4%	4000	4000	30	2694

Table E.1: Different thicknesses of resist depending on the spin-coating parameters. Reproduced from the standard guideline of the Nanofab facility at the IN.

- Bake at 80(180) °C with pumping for 12(5) min, respectively. The use of a reduced temperature with respect to the nominal baking temperature (180 °C) reduces the interdiffusion of Cu and NiFe in the spin-valve trilayers.
- Insolation: Dose 150 μC/cm^2.
- Development:
  - MIBK/Isopropanol 1:3 for 30 s.
  - Isopropanol two baths: first for 15 s, second for 45 s.
  - N_2 drying.
- Lift-off: N- methyl-2 pyrrolidone (NMP) at 80 °C for 1 hour or acetone at room temperature; ultrasound if necessary (with care).

REFERENCES

Chapter 1 – Concepts of Thin Film Magnetism and Spintronics

[1] J. Stöhr, *Magnetism*, Springer-Verlag Berlin Heidelberg (2006).

[2] W. Heisenberg, *Zur Theorie des Ferromagnetismus*, Z. Phys. **49**, 619 (1928).

[3] S. J. Blundell, *Magnetism in condensed matter*, Oxford University Press, New York (2001).

[4] L. Landau and E. Lifshits, *On the theory of the dispersion of magnetic permeability in ferromagnetic bodies*, Phys. Z. Sowjet. **8**, 153 (1935).

[5] T. L. Gilbert, *A Phenomenological Theory of Damping in Ferromagnetic Materials*, IEEE Trans. Magn. **40**, 3443 (2004).

[6] J. P. Nibarger, R. Lopusnik, Z. Celinski and T. J. Silva, *Variation of magnetization and the Landé g factor with thickness in Ni-Fe films*, Appl. Phys. Lett. **83**, 93 (2003).

[7] J. P. Nibarger, R. Lopusnik and T. J. Silva, *Damping as a function of pulsed field amplitude and bias field in thin film Permalloy*, Appl. Phys. Lett. **82**, 2112 (2003).

[8] G. Nahrwold, J. M. Scholtyssek, S. Motl-Ziegler, O. Albrecht, U. Merkt and G. Meier, *Structural, magnetic, and transport properties of Permalloy for spintronic experiments*, J. Appl. Phys. **108**, 013907 (2010).

[9] D. C. Ralph, M. D. Stiles, *Spin transfer torques*, J. Magn. Magn. Mat. **320**, 1190 (2008).

[10] E. C. Stoner, *Collective Electron Specific Heat and Spin Paramagnetism in Metals*, Proc. Roy. Soc. (London) A **154**, 656 (1936).

[11] E. C. Stoner, *Collective electron ferromagnetism*, Proc. Roy. Soc. (London) A **165**, 372 (1938).

[12] L. Néel, *On a new mode of coupling between the magnetizations of two thin ferromagnetic layers*, Comptes Rendus Acad. Sci. Paris **255**, 1676 (1962).

[13] B. D. Schrag, A. Anguelouch, S. Ingvarsson, G. Xiao, Y. Lu, P. L. Trouilloud, A. Gupta, R. A. Wanner, W. J. Gallagher, P. M. Rice and S. S. P. Parkin, *Néel "orange-peel" coupling in magnetic tunneling junction devices*, Appl. Phys. Lett. **77**, 2373 (2000).

[14] J. C. S. Kools, A. J. Devasahayam, K. Rook, C.-L. Lee and M. Mao, *Effect of microstructure on the oscillating interlayer coupling in spin-valve structures*, J. Appl. Phys. **93**, 7921 (2003).

[15] S. S. P. Parkin, N. More and K. P. Roche, *Oscillations in Exchange Coupling and Magnetoresistance in Metallic Superlattice Structures: Co/Ru, Co/Cr, and Fe/Cr*, Phys. Rev. Lett. **64**, 2304 (1990).

[16] S. S. P. Parkin, *Oscillatory Magnetic Exchange Coupling through Thin Copper Spacers*, Phys. Rev. Lett. **66**, 2152 (1991).

[17] J. Nogués and I. K. Schuller, *Exchange Bias*, J. Magn. Magn. Mater. **192**, 203 (1999).

[18] W. H. Meiklejohn and C. P. Bean, *New Magnetic Anisotropy*, Phys. Rev. **102**, 1413 (1956).

[19] C. M. Schneider, P. Bressler, P. Schuster, J. Kirschner, J. J. de Miguel and R. Miranda, *Curie Temperature of Ultrathin Films of fcc Cobalt Epitaxially Grown on Atomically Flat Cu(100) Surfaces*, Phys. Rev. Lett. **64**, 1059 (1990).

[20] X. Y. Lang, W. T. Zheng, and Q. Jiang, *Size and interface effects on ferromagnetic and antiferromagnetic transition temperatures*, Phys. Rev. B **73**, 224444 (2006).

[21] X. Y. Lang, Z. Wen, and Q. Jiang, *Dependence of Thermal Stability of Antiferromagnetic Nanocrystals on Size and Magnetic Proximity Effect*, J. Phys. Chem. C **112**, 4055 (2008).

[22] X. Y. Lang, W. T. Zheng, and Q. Jiang, *Dependence of the blocking temperature in exchange biased ferromagnetic/antiferromagnetic bilayers on the thickness of the antiferromagnetic layer*, Nanotechnology **18**, 155701 (2007).

[23] T. Ambrose and C. L. Chien, *Finite-Size Effects and Uncompensated Magnetization in Thin Antiferromagnetic CoO Layers*, Phys. Rev. Lett. **76**, 1743 (1996).

[24] Y. J. Tang, D. J. Smith, B. L. Zink, F. Hellman and A. E. Berkowitz, *Finite size effects on the moment and ordering temperature in antiferromagnetic CoO layers*, Phys. Rev. B **67**, 054408 (2003).

[25] E. N. Abarra, K. Takano, F. Hellman and A. E. Berkowitz, *Thermodynamic Measurements of Magnetic Ordering in Antiferromagnetic Superlattices*, Phys. Rev. Lett. **77**, 3451 (1996).

[26] P. J. van der Zaag, Y. Ijiri, J. A. Borchers, L. F. Feiner, R. M. Wolf, J. M. Gaines, R. W. Erwin and M. A. Verheijen, *Difference between Blocking and Néel Temperatures in the Exchange Biased Fe_3O_4/CoO System*, Phys. Rev. Lett. **84**, 6102, (2000).

[27] K. Takano, R. H. Kodama, A. E. Berkowitz, W. Cao and G. Thomas, *Interfacial Uncompensated Antiferromagnetic Spins: Role in Unidirectional Anisotropy in Polycrystalline $Ni_{81}Fe_{19}/CoO$ Bilayers*, Phys. Rev. Lett. **79**, 1130 (1997).

[28] D. Venus and F. Hunte, *Competition between magnetic relaxation mechanisms in exchange-coupled CoO/Co bilayers*, Phys. Rev. B **72**, 024404 (2005).

[29] K.-W. Lin, F.-T. Lin, Y.-M. Tzeng and Z.-Y. Guo, *Structural and magnetic properties of ion-beam deposited NiFe/Co-oxide bilayers*, Eur. Phys. J. B **45**, 237 (2005).

[30] W. L. Roth, *The magnetic structure of Co_3O_4*, J. Phys. Chem. Solids **25**, 1 (1964).

[31] J. C. Eckert, N. P. Stern, D. S. Snowden, J. G. Checkelsky, P. D. Sparks and M. J. Carey, *Effects of oxygen concentration in Co/CoO exchange-coupled spin valves*, J. Magn. Magn. Mat. 272-276, 1898 (2004).

[32] J. van Lierop, K.-W. Lin, J.-Y. Guo, H. Ouyang and B. W. Southern, *Proximity effects in an exchange-biased Ni_80Fe_20/Co_3O_4 thin film*, Phys. Rev. B **75**, 134409 (2007).

[33] A. Hubert and R. Schäfer, *Magnetic domains*, Springer-Verlag Berlin Heidelberg New York (1998).

[34] R. D. McMichael and M. J. Donahue, *Head to head domain wall structures in thin magnetic strips*, IEEE Trans. Magn. **33**, p. 4167–4169 (1997).

[35] Y. Nakatani, A. Thiaville and J. Miltat, *Head-to-head domain walls in soft nanostrips: a refined phase diagram*, J. Magn. Magn. Mater. **290-291**, 750 (2005).

[36] M. Kläui, C. A. F. Vaz, J. A. C. Bland, L. J. Heyderman, F. Nolting, A. Pavlovska, E. Bauer, S. Cherifi, S. Heun and A. Locatelli, *Head-to-head domain-wall phase diagram in mesoscopic ring magnets*, Appl. Phys. Lett. **85**, 5637 (2004).

[37] M. Kläui, *Head-to-head domain walls in magnetic nanostructures*, J. Phys. Cond. Matt. **20**, 313001 (2008).

[38] J. M. B. Ndjaka, A. Thiaville and J. Miltat, *Transverse wall dynamics in a spin valve nanostrip*, J. Appl. Phys. **105**, 023905 (2009).

[39] N. W. Ashcroft and N. D. Mermin, *Solid State Physics*, Thomson Learning (1976).

[40] J. Bass and W. P. Pratt Jr., *Spin-diffusion lengths in metals and alloys, and spin-flipping at metal/metal interfaces: an experimentalist's critical review*, J. Phys. Cond. Mat. **19**, 183201 (2007).

[41] N. F. Mott, *Electrons in transition metals*, Adv. Phys. **13**, 325 (1964).

[42] N. F. Mott, *The Electrical Conductivity of Transition Metals*, Proc. Roy. Soc. (London) A **153**, 699 (1936).

[43] N. F. Mott, *The Resistance and Thermoelectric Properties of the Transition Metals*, Proc. Roy. Soc. (London) A **156**, 368 (1936).

[44] A. Fert and I. A. Campbell, *Two-Current Conduction in Nickel*, Phys. Rev. Lett. **21**, 1190 (1968).

[45] A. Fert and I. A. Campbell, *Electrical resistivity of ferromagnetic nickel and iron based alloys*, J. Phys. F **6**, 849 (1976).

[46] S. Lepadatu, M. C. Hickey, A. Potenza, H. Marchetto, T. R. Charlton, S. Langridge, S. S. Dhesi and C. H. Marrows, *Experimental determination of spin-transfer torque nonadiabaticity parameter and spin polarization in permalloy*, Phys. Rev. B **79**, 094402 (2009).

[47] S. S. P. Parkin, *Systematic Variation of the Strength and Oscillation Period of Indirect Magnetic Exchange Coupling through the 3d, 4d, and 5d Transition Metals*, Phys. Rev. **67**, 3598 (1991).

[48] J. S. Moodera, L. R. Kinder, T. M. Wong and R. Meservey, *Large Magnetoresistance at Room Temperature in Ferromagnetic Thin Film Tunnel Junctions*, Phys. Rev. Lett. **74**, 3273 (1995).

[49] R. Meservey and P. M. Tedrow, *Magnetic Field Splitting of the Quasiparticle States in Superconducting Aluminum Films*, Phys. Rev. Lett. **25**, 1270 (1970).

[50] P. M. Tedrow and R. Meservey, *Spin-Dependent Tunneling into Ferromagnetic Nickel*, Phys. Rev. Lett. **26**, 192 (1971).

[51] M. Jullière, *Tunneling between ferromagnetic films*, Phys. Lett. A **54** (3), 225 (1975).

[52] S. Ikeda, J. Hayakawa, Y. Ashizawa, Y. M. Lee, K. Miura, H. Hasegawa, M. Tsunoda, F. Matsukura and H. Ohno, *Tunnel magnetoresistance of 604% at 300 K by suppression of Ta diffusion in CoFeB/MgO/CoFeB pseudo-spin-valves annealed at high temperature*, Appl. Phys. Lett. **93**, 082508 (2008).

[53] M. N. Baibich, J. M. Proto, A. Fert, F. Nguyen Van Dau, F. Petroff, P. Etienne, G. Creuzet, A. Friederich and J. Chazelas, *Giant Magnetoresistance of (001)Fe/(OO1)Cr Magnetic Superlattices*, Phys. Rev. Lett. **61**, 2472 (1988).

[54] G. Binasch, P. Grünberg, F. Saurenbach and W. Zinn, *Enhanced magnetoresistance in layered magnetic structures with antiferromagnetic interlayer exchange*, Phys. Rev. B **39**, 4828 (1989).

[55] P. Zahn and I. Mertig, *Enhanced Magnetoresistance* in in *Handbook of Magnetism and Advanced Magnetic Materials*, vol. 1, eds. H. Kronmüller and S. Parkin. John Wiley & Sons, Ltd. (2007).

[56] J. Bass and W. P. Pratt Jr., *Current-perpendicular (CPP) magnetoresistance in magnetic metallic multilayers*, J. Magn. Magn. Mat. **200**, 274 (1999).

[57] B. Dieny, *Giant magnetoresistance in spin-valve multilayers*, J. Magn. Magn. Mater. **136**, 335 (1994).

[58] T. Valet and A. Fert, *Theory of the perpendicular magnetoresistance in magnetic multilayers*, Phys. Rev. B **48**, 7099 (1993).

Chapter 2 – Spin-Transfer Torque and Domain-Wall Motion

[59] W. Döring, *Über die Trägheit der Wände zwischen Weißschen Bezirken (On the inertia of the walls between Weiss domains)*, Zeit. Naturforsch. **3a**, 373 (1948).

[60] A. A. Thiele, *Steady-State Motion of Magnetic Domains*, Phys. Rev. Lett. **30**, 230 (1973).

[61] N. L. Schryer and L. R. Walker, *The motion of 180° domain walls in uniform dc magnetic fields*, J. Appl. Phys. **45**, 5406 (1974).

[62] A. P. Malozemoff and J. C. Slonczewski, *Magnetic Domain Walls in Bubble Materials*, Academic Press, New York (1979).

[63] A. P. Malozemoff and J. C. Slonczewski, *Effect of Bloch Lines on Magnetic Domain-Wall Mobility*, Phys. Rev. Lett. **29**, 952 (1972).

[64] J. C. Slonczewski, *Theory of Bloch-line and Bloch-wall motion*, J. Appl. Phys. **45**, 2705 (1974).

[65] A. Thiaville, J. M. García and J. Miltat, *Domain wall dynamics in nanowires*, J. Magn. Magn. Mat. **242**, 1061 (2002).

[66] A. Thiaville and Y. Nakatani, *Domain-Wall Dynamics in Nanowires and Nanostrips* in *Spin Dynamics in Confined Magnetic Structures III*, eds. B. Hillebrands and A. Thiaville, Springer-Verlag Berlin Heidelberg (2006).

[67] G. S. D. Beach, M. Tsoi and J. L. Erskine, *Current-induced domain wall motion*, J. Magn. Magn. Mater. **320**, 1272 (2008).

[68] J.-Y. Lee, K.-S. Lee, S. Choi, K. Y. Guslienko, and S.-K. Kim, *Dynamic transformations of the internal structure of a moving domain wall in magnetic nanostripes*, Phys. Rev. B **76**, 184408 (2007).

[69] D. G. Porter and M. J. Donahue, *Velocity of transverse domain wall motion along thin, narrow strips*, J. Appl. Phys. **95**, 6729 (2004).

[70] K. J. Sixtus and L. Tonks, *Propagation of Large Barkhausen Discontinuities*, Phys. Rev. **37**, 930 (1931).

[71] K. J. Sixtus and L. Tonks, *Propagation of Large Barkhausen Discontinuities II*, Phys. Rev. **42**, 419 (1932).

[72] T. Ono, H. Miyajima, K. Shigeto, K. Mibu, N. Hosoito and T. Shinjo, *Propagation of a domain wall in a submicrometer magnetic wire*, Science **284**, 468 (1999).

[73] D. Atkinson, D. A. Allwood, G. Xiong, M. D. Cooke, C. C. Faulkner and R. P. Cowburn, *Magnetic domain-wall dynamics in a submicrometre ferromagnetic structure*, Nature Mater. **2**, 85 (2003).

[74] G. S. D. Beach, C. Nistor, C. Knutson, M. Tsoi and J. L. Erskine, *Dynamics of field-driven domain-wall propagation in ferromagnetic nanowires*, Nature Mater. **4**, 741 (2005).

[75] M. Hayashi, L. Thomas, C. Rettner, R. Moriya and S. S. P. Parkin, *Direct observation of the coherent precession of magnetic domain walls propagating along permalloy nanowires*, Nature Phys. **3**, 21 (2007).

[76] M. Hayashi, L. Thomas, C. Rettner, R. Moriya and S. S. P. Parkin, *Real time observation of the field driven periodic transformation of domain walls in Permalloy nanowires at the Larmor frequency and its first harmonic*, Appl. Phys. Lett. **92**, 112510 (2008).

[77] K. Weerts, P. Neutens, L. Lagae and G. Borghs, *Influence of pulse amplitude and rise time on field-induced domain wall propagation in NiFe nanowires*, J. Appl. Phys. **103**, 094307 (2008).

[78] F. Cayssol, D. Ravelosona, C. Chappert, J. Ferré and J. P. Jamet, *Domain Wall Creep in Magnetic Wires*, Phys. Rev. Lett. **92**, 107202 (2004).

[79] H. Barkhausen, *Two phenomena uncovered with help of the new amplifiers*, Berichte der Deutschen Physikalischen Gesellschaft, Z. Phys. 20, 401 (1919).

[80] G. Blatter, M. V. Feigel'man, V. B. Geshkenbein, A. I. Larkin and V. M. Vinokur, *Vortices in high-temperature superconductors*, Rev. Mod. Phys. **66**, 1125 (1994).

[81] P. Chauve, T. Giamarchi and P. Le Doussal, *Creep and depinning in disordered media*, Phys. Rev. B **62**, 6241 (2000).

[82] S. Lemerle, J. Ferré, C. Chappert, V. Mathet, T. Giamarchi and P. Le Doussal, *Domain Wall Creep in an Ising Ultrathin Magnetic Film*, Phys. Rev. Lett. **849**, (1998).

[83] P. J. Metaxas, J. P. Jamet, A. Mougin, M. Cormier, J. Ferré, V. Baltz, B. Rodmacq, B. Dieny and R. L. Stamps, *Creep and Flow Regimes of Magnetic Domain-Wall Motion in Ultrathin Pt/Co/Pt Films with Perpendicular Anisotropy*, Phys. Rev. Lett. **99**, 217208 (2007).

[84] T. A. Moore, I. M. Miron, G. Gaudin, G. Serret, S. Auffret, B. Rodmacq, A. Schuhl, S. Pizzini, J. Vogel and M. Bonfim, *High domain wall velocities induced by current in ultrathin Pt/Co/AlOx wires with perpendicular magnetic anisotropy*, Appl. Phys. Lett. **93**, 262504 (2008).

[85] M. Yamanouchi, D. Chiba, F. Matsukura, T. Dietl and H. Ohno, *Velocity of Domain-Wall Motion Induced by Electrical Current in the Ferromagnetic Semiconductor (Ga,Mn)As*, Phys. Rev. Lett. **96**, 096601 (2006).

[86] Y. Nakatani, A. Thiaville and J. Miltat, *Faster magnetic walls in rough wires*, Nature Mater. **2**, 521 (2003).

[87] J.-Y. Lee, K.-S. Lee, and S.-K. Kim, *Remarkable enhancement of domain-wall velocity in magnetic nanostripes*, Appl. Phys. Lett. **91**, 122513 (2007).

[88] S. Glathe, R. Mattheis and D. V. Berkov, *Direct observation and control of the Walker breakdown process during a field driven domain wall motion*, Appl. Phys. Lett.**93**, 072508 (2008).

[89] D. A. Allwood, G. Xiong, M. D. Cooke, C. C. Faulkner, D. Atkinson and R. P. Cowburn, *Characterization of submicrometer ferromagnetic NOT gates*, J. Appl. Phys. **95**, 8264 (2004).

[90] A. Kunz and S. C. Reiff, *Fast domain wall motion in nanostripes with out-of-plane fields*, Appl. Phys. Lett. **93**, 082503 (2008).

[91] S. Glathe, I. Berkov, T. Mikolajick and R. Mattheis, *Experimental study of domain wall motion in long nanostrips under the influence of a transverse field*, Appl. Phys. Lett. **93**, 162505 (2008).

[92] M. T. Bryan, T. Schrefl, D. Atkinson and D. A. Allwood, *Magnetic domain wall propagation in nanowires under transverse magnetic fields*, J. Appl. Phys. **103**, 073906 (2008).

[93] A. Kunz and S. C. Reiff, *Enhancing domain wall speed in nanowires with transverse magnetic fields*, J. Appl. Phys. **103**, 07D903 (2008).

[94] V. L. Sobolev, H. L. Huang and S. C. Chen, *Domain wall dynamics in the presence of an external magnetic field normal to the anisotropy axis*, J. Magn. Magn. Mat. **147**, 284 (1995).

[95] V. L. Sobolev, H. L. Huang and S. C. Chen, *Generalized equations for domain wall dynamics*, J. Appl. Phys. **75**, 5797 (1994).

[96] V. L. Sobolev, H. L. Huang and S. C. Chen, *Equations of Domain Wall Motion in Ferromagnet in External Magnetic Field Normal to the Anisotropy Axis*, Chin. J. Phys. **31**, 403 (1993).

[97] C.-Y. You, *Another method for domain wall movement by a nonuniform transverse magnetic field*, Appl. Phys. Lett. **92**, 152507 (2008).

[98] C.-Y. You, *Equation of motion for a domain wall movement under a nonuniform transverse magnetic field*, Appl. Phys. Lett. **92**, 192514 (2008).

[99] J. C. Slonczewski, *Current-driven excitation of magnetic multilayers*, J. Magn. Magn. Mater. **159**, L1 (1996).

[100] L. Berger, *Emission of spin waves by a magnetic multilayer traversed by a current*, Phys. Rev. B **54**, 9353 (1996).

[101] M. Tsoi, A. G. Jansen, J. Bass, W.-C. Chiang, M. Seck, V. Tsoi and P. Wyder, *Excitation of a Magnetic Multilayer by an Electric Current*, Phys. Rev. Lett. **81**, 493 (1998).

[102] J. A. Katine, F. J. Albert, R. A. Buhrman, E. B. Myers and D. C. Ralph, *Current-Driven Magnetization Reversal and Spin-Wave Excitations in Co/Cu/Co Pillars*, Phys. Rev. Lett. **84**, 3149 (2000).

[103] S. Zhang, P. M. Levy and A. Fert, *Mechanisms of Spin-Polarized Current-Driven Magnetization Switching*, Phys. Rev. Lett. **88**, 236601 (2002).

[104] C. Chappert, A. Fert, F. N. van Dau, *The emergence of spin electronics in data storage*, Nature Mater. **6**, 813 (2007).

[105] T. Taniguchi, S. Yakata, H. Imamura and Y. Ando, *Penetration Depth of Transverse Spin Current in Ferromagnetic Metals*, IEEE Trans. Magn. **44**, 2636 (2008).

[106] Y. Huai, F. Albert, P. Nguyen, M. Pakala and T. Valet, *Observation of spin-transfer switching in deep submicron-sized and low-resistance magnetic tunnel junctions*, Appl. Phys. Lett. **84**, 3118 (2004).

[107] J. Z. Sun and D. C. Ralph, *Magnetoresistance and spin-transfer torque in magnetic tunnel junctions*, J. Magn. Magn. Mat. **320**, 1227 (2008).

[108] M. D. Stiles and J. Miltat, *Spin Transfer Torque and Dynamics* in *Spin Dynamics in Confined Magnetic Structures III*, eds. B. Hillebrands and A. Thiaville, Springer-Verlag Berlin Heidelberg (2006).

[109] J. C. Slonczewski, *Electronic device using magnetic components*, U.S. Patent No. 5695864 (1997).

[110] J. A. Katine and E. E. Fullerton, *Device implications of spin-transfer torques*, J. Magn. Magn. Mat. **320**, 1217 (2008).

[111] M. Hosomi, H. Yamagishi, T. Yamamoto, K. Bessho, Y. Higo, K. Yamane, H. Yamada, M. Shoji, H. Machino, C. Fukumoto, H. Nagao and H. Kano, *Novel nonvolatile memory with spin torque transfer magnetization switching: spin-ram*, IEDM Tech. Dig., 459 (2005).

[112] T. Kawahara, R. Takemura, K. Miura, J. Hayakawa, S. Ikeda, Y. Lee, R. Sasaki, Y. Goto, K. Ito, I. Meguro, F. Matsukura, H. Takahashi, H. Matsuoka and H. Ohno, *2Mb Spin-Transfer Torque RAM (SPRAM) with Bit-by-Bit Bidirectional Current Write and Parallelizing-Direction Current Read*, ISSCC Dig. Tech. Papers, 480 (2007).

[113] R. Nebashi, N. Sakimura, H. Honjo, S. Saito, Y. Ito, S. Miura, Y. Kato, K. Mori, Y. Ozaki, Y. Kobayashi, N. Ohshima, K. Kinoshita, T. Suzuki, K. Nagahara, N. Ishiwata, K. Suemitsu, S. Fukami, H. Hada, T. Sugibayashi and N. Kasai, *A 90nm 12ns 32Mb 2T1MTJ MRAM*, ISSCC Dig. Tech. Papers, 462 (2009).

[114] S. I. Kiselev, J. C. Sankey, I. N. Krivorotov, N. C. Emley, R. J. Schoelkopf, R. A. Buhrman and D. C. Ralph, *Microwave oscillations of a nanomagnet driven by a spin-polarized current*, Nature **425**, 380 (2003).

[115] W. H. Rippard, M. R. Pufall, S. Kaka, S. E. Russek, T. J. Silva, *Direct-Current Induced Dynamics in* $Co_{90}Fe_{10}/Ni_{80}Fe_{20}$ *Point Contacts*, Phys. Rev. Lett. **92**, 027201 (2004).

[116] L. Thomas and S. Parkin, *Current Induced Domain-wall Motion in Magnetic Nanowires* in *Handbook of Magnetism and Advanced Magnetic Materials*, vol. 2, eds. H. Kronmüller and S. Parkin. John Wiley & Sons, Ltd. (2007).

[117] L. Berger, *Dragging of domains by an electric-current in very pure, noncompensated, ferromagnetic metals*, Phys. Lett. **46**, 3 (1973).

[118] L. Berger, *Prediction of a domain-drag effect in uniaxial, noncompensated, ferromagnetic metals*, J. Phys. Chem. Solids **35**, 947 (1974).

[119] L. Berger, *Low-field magnetoresistance and domain wall drag in ferromagnets*, J. Appl. Phys. **49**, 2156 (1978).

[120] P. Freitas and L. Berger, *Observation of s-d exchange force between domain walls and electric current in very thin Permalloy films*, J. Appl. Phys. **57**, 1266 (1985).

[121] L. Berger, *Exchange interaction between ferromagnetic domain walls and electric current in very this metallic films*, J. Appl. Phys. **55**, 1954 (1984).

[122] L. Berger, *Motion of a magnetic domain wall traversed by fast-rising current pulses*, J. Appl. Phys. **71**, 2721 (1992).

[123] Ya. B. Bazaliy, B. A. Jones and S. Zhang, *Modification of the Landau-Lifshitz equation in the presence of a spin-polarized current in colossal- and giant-magnetoresistive materials*, Phys. Rev. B **57**, R3213 (1998).

[124] Z. Li and S. Zhang, *Domain-Wall Dynamics and Spin-Wave Excitations with Spin-Transfer Torques*, Phys. Rev. Lett. **92**, 207203 (2004).

[125] Z. Li and S. Zhang, *Domain-wall dynamics driven by adiabatic spin-transfer torques*, Phys. Rev. B **70**, 024417 (2004).

[126] A. Thiaville, Y. Nakatani, J. Miltat and N. Vernier, *Domain wall motion by spin-polarized current: a micromagnetic study*, J. Appl. Phys. **95**, 7049 (2004).

[127] A. Thiaville, Y. Nakatani, F. Piéchon, J. Miltat and T. Ono, *Transient domain wall displacement under spin-polarized current pulses*, Eur. Phys. J. B **60**, 15 (2007).

[128] A. Thiaville, Y. Nakatani, J. Miltat and Y. Suzuki, *Micromagnetic understanding of current-driven domain wall motion in patterned nanowires*, Europhys. Lett. **69**, 990 (2005).

[129] G. S. D. Beach, C. Knutson, M. Tsoi and J. L. Erskine, *Field- and current-driven domain wall dynamics: An experimental picture*, J. Magn. Magn. Mat. **310**, 2038 (2007).

[130] A. Mougin, M. Cormier, J. P. Adam, P. J. Metaxas and J. Ferré, *Domain wall mobility, stability and Walker breakdown in magnetic nanowires*, Europhys. Lett. **78**, 57007 (2007).

[131] A. A. Thiele, *Steady-State Motion of Magnetic Domains*, Phys. Rev. Lett. **30**, 230 (1973).

[132] O. Tchernyshyov and G.-W. Chern, *Fractional Vortices and Composite Domain Walls in Flat Nanomagnets*, Phys. Rev. Lett. **95**, 197204 (2005).

[133] J. He, Z. Li, S. Zhang, *Current-driven vortex domain wall dynamics by micromagnetic simulations*, Phys. Rev. B **73**, 184408 (2006).

[134] A. Thiaville and Y. Nakatani, *Micromagnetics of Domain-Wall Dynamics in Soft Nanostrips* in *Nanomagnetism and Spintronics*, ed. T. Shinjo, Elsevier, Oxford (2009).

[135] Y. Tserkovnyak, A. Brataas and G. E. W. Bauer, *Theory of current-driven magnetization dynamics in inhomogeneous ferromagnets*, J. Magn. Magn. Mat. **320**, 1282 (2008).

[136] J. Mallinson, *On the damped gyromagnetic precession*, IEEE Trans. Magn. **23**, 2003 (1987).

[137] S. E. Barnes and S. Maekawa, *Current-Spin Coupling for Ferromagnetic Domain Walls in Fine Wires*, Phys. Rev. Lett. **95**, 107204 (2005).

[138] G. S. D. Beach, C. Knutson, C. Nistor, M. Tsoi and J. L. Erskine, *Nonlinear Domain-Wall Velocity Enhancement by Spin-Polarized Electric Current*, Phys. Rev. Lett. **97**, 057203 (2006).

[139] M. Hayashi, L. Thomas, Ya. B. Bazaliy, C. Rettner, R. Moriya, X. Jiang and S. S. P. Parkin, *Influence of Current on Field-Driven Domain Wall Motion in Permalloy Nanowires from Time Resolved Measurements of Anisotropic Magnetoresistance*, Phys. Rev. Lett. **96**, 197207 (2006).

[140] G. Meier, M. Bolte, R. Eiselt, B. Krüger, D.-H. Kim and P. Fischer, *Direct Imaging of Stochastic Domain-Wall Motion Driven by Nanosecond Current Pulses*, Phys. Rev. Lett. **98**, 187202 (2007).

[141] M. Hayashi, L. Thomas, C. Rettner, R. Moriya, Y. B. Bazaliy and S. S. P. Parkin, *Current Driven Domain Wall Velocities Exceeding the Spin Angular Momentum Transfer Rate in Permalloy Nanowires*, Phys. Rev. Lett. **98**, 037204 (2007).

[142] L. Heyne, J. Rhensius, A. Bisig, S. Krzyk, P. Punke, M. Kläui, L. J. Heyderman, L. Le Guyader and F. Nolting, *Direct observation of high velocity current induced domain wall motion*, Appl. Phys. Lett. **96**, 032504 (2010).

[143] M. D. Stiles, W. M. Saslow, M. J. Donahue and A. Zangwill, *Adiabatic domain wall motion and Landau-Lifshitz damping*, Phys. Rev. B **75**, 214423 (2007).

[144] Y. Tserkovnyak, H. J. Skadsem, A. Brataas and G. E. W. Bauer, *Current-induced magnetization dynamics in disordered itinerant ferromagnets*, Phys. Rev. B **74**, 144405 (2006).

[145] Y. Tserkovnyak, A. Brataas, G. E. W. Bauer and B. I. Halperin, *Nonlocal magnetization dynamics in ferromagnetic heterostructures*, Rev. Mod. Phys. **77**, 1375 (2005).

[146] N. Smith, *Comment on "Adiabatic domain wall motion and Landau-Lifshitz damping"*, Phys. Rev. B **78**, 216401 (2008).

[147] X. Waintal and M. Viret, *Current-induced distortion of a magnetic domain wall*, Europhys. Lett. **65**, 427 (2004).

[148] A. Vanhaverbeke and M. Viret, *Simple model of current-induced spin torque in domain walls*, Phys. Rev. B **75**, 024411 (2007).

[149] S. Zhang and Z. Li, *Roles of Nonequilibrium Conduction Electrons on the Magnetization Dynamics of Ferromagnets*, Phys. Rev. Lett. **93**, 127204 (2004).

[150] J. Xiao, A. Zangwill and M. D. Stiles, *Spin-transfer torque for continuously variable magnetization*, Phys. Rev. B **73**, 054428 (2006).

[151] G. Tatara and H. Kohno, *Theory of Current-Driven DomainWall Motion: Spin Transfer versus Momentum Transfer*, Phys. Rev. Lett. **92**, 086601 (2004).

[152] J. F. Gregg, W. Allen, K. Ounadjela, M. Viret, M. Hehn, S. M. Thompson and J. M. D. Coey, *Giant Magnetoresistive Effects in a Single Element Magnetic Thin Film*, Phys. Rev. Lett. **77**, 1580 (1996).

[153] P. M. Levy and S. Zhang, *Resistivity due to Domain Wall Scattering*, Phys. Rev. Lett. **79**, 5110 (1997).

[154] E. Šimánek, *Spin accumulation and resistance due to a domain wall*, Phys. Rev. B **63**, 224412 (2001).

[155] A. D. Kent, J. Yu, U. Rüdiger and S. S. P. Parkin, *Domain wall resistivity in epitaxial thin film microstructures*, J. Phys. Cond. Mat. **13**, R461 (2001).

[156] L. Berger, *Analysis of measured transport properties of domain walls in magnetic nanowires and films*, Phys. Rev. B **73**, 014407 (2006).

[157] J. Ohe and B. Kramer, *Dynamics of a Domain Wall and Spin-Wave Excitations Driven by a Mesoscopic Current*, Phys. Rev. Lett. **96**, 027204 (2006).

[158] Y. Le Maho, J.-V. Kim and G. Tatara, *Spin-wave contributions to current-induced domain wall dynamics*, Phys. Rev. B **79**, 174404 (2009).

[159] M. Thorwart and R. Egger, *Current-induced nonadiabatic spin torques and domain-wall motion with spin relaxation in a ferromagnetic metallic wire*, Phys. Rev. B **76**, 214418 (2007).

[160] R. A. Duine, A. S. Núñez, J. Sinova and A. H. MacDonald, *Functional Keldysh theory of spin torques*, Phys. Rev. B **75**, 214420 (2007).

[161] H. Kohno, G. Tatara and J. Shibata, *Microscopic Calculation of Spin Torques in Disordered Ferromagnets*, J. Phys. Soc. Jpn. **75**, 113706 (2006).

[162] I. Garate, K. Gilmore, M. D. Stiles and A. H. MacDonald, *Nonadiabatic spin-transfer torque in real materials*, Phys. Rev. B **79**, 104416 (2009).

[163] K. Obata and G. Tatara, *Current-induced domain wall motion in Rashba spin-orbit system*, Phys. Rev. B **77**, 214429 (2008).

[164] I. M. Miron, G. Gaudin, S. Auffret, B. Rodmacq, A. Schuhl, S. Pizzini, J. Vogel and P. Gambardella, *Current-driven spin torque induced by the Rashba effect in a ferromagnetic metal layer*, Nature Mater. **9**, 230 (2010).

[165] I. M. Miron, P.-J. Zermatten, G. Gaudin, S. Auffret, B. Rodmacq and A. Schuhl, *Domain Wall Spin Torquemeter*, Phys. Rev. Lett. **102**, 137202 (2009).

[166] Z. Li and S. Zhang, *Thermally assisted magnetization reversal in the presence of a spin-transfer torque*, Phys. Rev. B **69**, 134416 (2004).

[167] G. Tatara, N. Vernier and J. Ferré, *Universality of thermally assisted magnetic domain-wall motion under spin torque*, Appl. Phys. Lett. **86**, 252509 (2005).

[168] R. A. Duine, A. S. Núñez and A. H. MacDonald, *Thermally Assisted Current-Driven Domain-Wall Motion*, Phys. Rev. Lett. **98**, 056605 (2007).

[169] M. E. Lucassen, H. J. van Driel, C. Morais Smith and R. A. Duine, *Current-driven and field-driven domain walls at nonzero temperature*, Phys. Rev. B **79**, 224411 (2009).

[170] G. Tatara, T. Takayama, H. Kohno, J. Shibata, Y. Nakatani and H. Fukuyama, *Threshold Current of Domain Wall Motion under Extrinsic Pinning, β-term and Non-Adiabaticity*, J. Phys. Soc. Jpn. **75**, 064708 (2006).

[171] R. A. Duine and C. Morais Smith, *Creep of current-driven domain-wall lines: Effects of intrinsic versus extrinsic pinning*, Phys. Rev. B **77**, 094434 (2008).

[172] J.-V. Kim and C. Burrowes, *Influence of magnetic viscosity on domain wall dynamics under spin-polarized currents*, Phys. Rev. B **80**, 214424 (2009).

[173] C. Burrowes, A. P. Mihai, D. Ravelosona, J.-V. Kim, C. Chappert, L. Vila, A. Marty, Y. Samson, F. Garcia-Sanchez, L. D. Buda-Prejbeanu, I. Tudosa, E. E. Fullerton and J.-P. Attané, *Non-adiabatic spin-torques in narrow magnetic domain walls*, Nature Phys. **6**, 17 (2010).

[174] M. Eltschka, M. Wötzel, J. Rhensius, S. Krzyk, U. Nowak, M. Kläui, T. Kasama, R. E. Dunin-Borkowski, L. J. Heyderman, H. J. van Driel and R. A. Duine, *Nonadiabatic Spin Torque Investigated Using Thermally Activated Magnetic Domain Wall Dynamics*, Phys. Rev. Lett. **105**, 056601 (2010).

[175] H. Min, R. D. McMichael, M. J. Donahue, J. Miltat and M. D. Stiles, *Effects of Disorder and Internal Dynamics on VortexWall Propagation*, Phys. Rev. Lett. **104**, 217201 (2010).

[176] P. P. Freitas and L. Berger, *Observation of s-d exchange force between domain walls and electric current in very thin Permalloy films*, J. Appl. Phys. **57**, 1266 (1985).

[177] C.-Y. Hung and L. Berger, *Exchange forces between domain wall and electric current in permalloy films of variable thickness*, J. Appl. Phys. **63**, 4276 (1988).

[178] E. Salhi and L. Berger, *Current-induced displacements and precession of a Bloch wall in Ni-Fe thin films*, J. Appl. Phys. **73**, 6405 (1993).

[179] L. Gan, S. H. Chung, K. H. Aschenbach, M. Dreyer and R. D. Gomez, *Pulsed-Current-Induced Domain Wall Propagation in Permalloy Patterns Observed Using Magnetic Force Microscope*, IEEE Trans. Magn. **36**, 3047 (2000).

[180] J. Grollier, D. Lacour, V. Cros, A. Hamzić, A. Vaurès, A. Fert, D. Adam and G. Faini *Switching the magnetic configuration of a spin valve by current-induced domain wall motion*, J. Appl. Phys. **92**, 4825 (2002).

[181] J. Grollier, P. Boulenc, V. Cros, A. Hamzić, A. Vaurès, A. Fert and G. Faini, *Switching a spin valve back and forth by current-induced domain wall motion*, Appl. Phys. Lett. **83**, 509 (2003).

[182] N. Vernier, D. A. Allwood, D. Atkinson, M. D. Cooke and R. P. Cowburn, *Domain wall propagation in magnetic nanowires by spin-polarized current injection*, Europhys. Lett. **65**, 526 (2004).

[183] M. Tsoi, R. E. Fontana and S. S. P. Parkin, *Magnetic domain wall motion triggered by an electric current*, Appl. Phys. Lett. **83**, 2617 (2003).

[184] A. Yamaguchi, T. Ono, S. Nasu, K. Miyake, K. Mibu, T. Shinjo, *Real-Space Observation of Current-Driven Domain Wall Motion in Submicron Magnetic Wires*, Phys. Rev. Let. **92**, 077205 (2004).

[185] A. Yamaguchi, S. Nasu, H. Tanigawa, T. Ono, K. Miyake, K. Mibu and T. Shinjo, *Effect of Joule heating in current-driven domain wall motion*, Appl. Phys. Lett. **86**, 012511 (2005).

[186] M. Kläui, P.-O. Jubert, R. Allenspach, A. Bischof, J. A. C. Bland, G. Faini, U. Rüdiger, C. A. F. Vaz, L. Vila and C. Vouille, *Direct Observation of Domain-Wall Configurations Transformed by Spin Currents*, Phys. Rev. Lett. **95**, 026601 (2005).

[187] M. Kläui, M. Laufenberg, L. Heyne, D. Backes, U. Rüdiger, C. A. F. Vaz, J. A. C. Bland, L. J. Heyderman, S. Cherifi, A. Locatelli, T. O. Mentes and L. Aballe, *Current-induced vortex nucleation and annihilation in vortex domain walls*, Appl. Phys. Lett. **88**, 232507 (2006).

[188] L. Bocklage, B. Krüger, T. Matsuyama, M. Bolte, U. Merkt, D. Pfannkuche and Guido Meier, *Dependence of Magnetic Domain-Wall Motion on a Fast Changing Current*, Phys. Rev. Lett. **103**, 197204 (2009).

[189] L. Heyne, M. Kläui, D. Backes, T. A. Moore, S. Krzyk, U. Rüdiger, L. J. Heyderman, A. Fraile Rodríguez, F. Nolting, T. O. Mentes, M. Á. Niño, A. Locatelli, K. Kirsch and R. Mattheis, *Relationship between Nonadiabaticity and Damping in Permalloy Studied by Current Induced Spin Structure Transformations*, Phys. Rev. Lett. **100**, 066603 (2008).

[190] B. Krüger, M. Najafi, S. Bohlens, R. Frömter, D. P. F. Möller and Daniela Pfannkuche, *Proposal of a Robust Measurement Scheme for the Nonadiabatic Spin Torque Using the Displacement of Magnetic Vortices*, Phys. Rev. Lett. **104**, 077201 (2010).

[191] T. A. Moore, M. Kläui, L. Heyne, P. Möhrke, D. Backes, J. Rhensius, U. Rüdiger, L. J. Heyderman, J.-U. Thiele, G. Woltersdorf, C. H. Back, A. Fraile Rodríguez, F. Nolting, T. O. Mentes, M. Á. Niño, A. Locatelli, A. Potenza, H. Marchetto, S. Cavill and S. S. Dhesi, *Scaling of spin relaxation and angular momentum dissipation in permalloy nanowires*, Phys. Rev. B **80**, 132403 (2009).

[192] D. Ravelosona, D. Lacour, J. A. Katine, B. D. Terris and C. Chappert, *Nanometer Scale Observation of High Efficiency Thermally Assisted Current-Driven Domain Wall Depinning*, Phys. Rev. Lett. **95**, 117203 (2005).

[193] M. Zhu, C. L. Dennis and R. D. McMichael, *Temperature dependence of magnetization drift velocity and current polarization in $Ni_{80}Fe_{20}$ by spin-wave Doppler measurements*, Phys. Rev. B **81**, 140407(R) (2010).

[194] P. M. Haney and M. D. Stiles, *Magnetic dynamics with spin-transfer torques near the Curie temperature*, Phys. Rev. B **80**, 094418 (2009).

[195] M. Laufenberg, W. Bührer, D. Bedau, P.-E. Melchy, M. Kläui, L. Vila, G. Faini, C. A. F. Vaz, J. A. C. Bland and U. Rüdiger, *Temperature Dependence of the Spin Torque Effect in Current-Induced Domain Wall Motion*, Phys. Rev. Lett. **97**, 046602 (2006).

[196] I. M. Miron, T. Moore, H. Szambolics, G. Gaudin, L. D. Buda-Prejbeanu, S. Auffret, B. Rodmacq, S. Pizzini, J. Vogel, M. Bonfim and A. Schuhl, *Fast current-induced domain wall motion controlled by the Rashba effect*, to be published.

[197] C. Burrowes, D. Ravelosona, C. Chappert, S. Mangin, E. E. Fullerton, J. A. Katine and B. D. Terris, *Role of pinning in current driven domain wall motion in wires with perpendicular anisotropy*, Appl. Phys. Lett. **93**, 172513 (2008).

[198] T. Koyama, G. Yamada, H. Tanigawa, S. Kasai, N. Ohshima, S. Fukami, N. Ishiwata, Y. Nakatani and T. Ono, *Control of Domain Wall Position by Electrical Current in Structured Co/Ni Wire with Perpendicular Magnetic Anisotropy*, Appl. Phys. Express **1**, 101303 (2008).

[199] H. Tanigawa, T. Koyama, G. Yamada, D. Chiba, S. Kasai, S. Fukami, T. Suzuki, N. Ohshima, N. Ishiwata, Y. Nakatani and T. Ono, *Domain Wall Motion Induced by Electric Current in a Perpendicularly Magnetized Co/Ni Nano-Wire*, Appl. Phys. Express **2**, 053002 (2009).

[200] S. Fukami, Y. Nakatani, T. Suzuki, K. Nagahara, N. Ohshima and N. Ishiwata, *Relation between critical current of domain wall motion and wire dimension in perpendicularly magnetized Co/Ni nanowires*, Appl. Phys. Lett. **95**, 232504 (2009).

[201] O. Boulle, J. Kimmling, P. Warnicke, M. Kläui, U. Rüdiger, G. Malinowski, H. J. M. Swagten, B. Koopmans, C. Ulysse and G. Faini, *Nonadiabatic Spin Transfer Torque in High Anisotropy Magnetic Nanowires with Narrow Domain Walls*, Phys. Rev. Lett. **101**, 216601 (2008).

[202] M. Cormier, A. Mougin, J. Ferré, A. Thiaville, N. Charpentier, F. Piéchon, R. Weil, V. Baltz and B. Rodmacq, *Effect of electrical current pulses on domain walls in Pt/Co/Pt nanotracks with out-of-plane anisotropy: Spin transfer torque versus Joule heating*, Phys. Rev. B **81**, 024407 (2010).

[203] H. Tanigawa, K. Kondou, T. Koyama, K. Nakano, S. Kasai, N. Ohshima, S. Fukami, N. Ishiwata and T. Ono, *Current-Driven Domain Wall Motion in CoCrPt Wires with Perpendicular Magnetic Anisotropy*, Appl. Phys. Express **1**, 011301 (2008).

[204] S. Li, H. Nakamura, T. Kanazawa, X. Liu and A. Morisako, *Current-Induced Domain Wall Motion in TbFeCo Wires With Perpendicular Magnetic Anisotropy*, IEEE Trans. Magn. **46**, 1695 (2010).

[205] M. Feigenson, J. W. Reiner and L. Klein, *Efficient Current-Induced Domain-Wall Displacement in $SrRuO_3$*, Phys. Rev. Lett. **98**, 247204 (2007).

[206] M. Yamanouchi, D. Chiba, F. Matsukura and H. Ohno, *Current-induced domain-wall switching in a ferromagnetic semiconductor structure*, Nature **428**, 539 (2004).

[207] M. Yamanouchi, J. Ieda, F. Matsukura, S. E. Barnes, S. Maekawa and H. Ohno, *Universality Classes for Domain Wall Motion in the Ferromagnetic Semiconductor (Ga,Mn)As*, Science **317**, 1728 (2007).

[208] H. Ohno and T. Dietl, *Spin-transfer physics and the model of ferromagnetism in (Ga,Mn)As*, J. Magn. Magn. Mater. **320**, 1293 (2008).

[209] H. Ohno, *Properties of ferromagnetic III-V semiconductors*, J. Magn. Magn. Mater. **200**, 110 (1999).

[210] J.-P. Adam, N. Vernier, J. Ferré, A. Thiaville, V. Jeudy, A. Lemaître, L. Thevenard and G. Faini, *Nonadiabatic spin-transfer torque in (Ga,Mn)As with perpendicular anisotropy*, Phys. Rev. B **80**, 193204 (2009).

[211] W. C. Uhlig, M. J. Donahue, D. T. Pierce and J. Unguris, *Direct imaging of current-driven domain walls in ferromagnetic nanostripes*, J. Appl. Phys. **105**, 103902 (2009).

[212] S. Pizzini, V. Uhlíř, J. Vogel, N. Rougemaille, S. Laribi, V. Cros, E. Jiménez, J. Camarero, C. Tieg, E. Bonet, M. Bonfim, R. Mattana, C. Deranlot, F. Petroff, C. Ulysse, G. Faini and A. Fert, *High Domain Wall Velocity at Zero Magnetic Field Induced by Low Current Densities in Spin Valve Nanostripes*, Appl. Phys. Express **2**, 023003 (2009).

[213] C. K. Lim, T. Devolder, C. Chappert, J. Grollier, V. Cros, A. Vaurès, A. Fert and G. Faini, *Domain wall displacement induced by subnanosecond pulsed current*, Appl. Phys. Lett. **84**, 2820 (2004).

[214] M. Hayashi, L. Thomas, C. Rettner, R. Moriya, X. Jiang and S. S. P. Parkin, *Dependence of Current and Field Driven Depinning of Domain Walls on Their Structure and Chirality in Permalloy Nanowires*, Phys. Rev. Lett. **97**, 207205 (2006).

[215] Y. Jang, S. Yoon, K. Lee, S. Lee, C. Nam and B. K. Cho, *Current-induced domain wall nucleation and its pinning characteristics at a notch in a spin-valve nanowire*, Nanotechnology **20**, 125401 (2009).

[216] E. R. Lewis, D. Petit, L. Thevenard, A. V. Jausovec, L. O'Brien, D. E. Read and R. P. Cowburn, *Magnetic domain wall pinning by a curved conduit*, Appl. Phys. Lett. **95**, 152505 (2009).

[217] M.-Y. Im, L. Bocklage, P. Fischer and G. Meier, *Direct Observation of Stochastic Domain-Wall Depinning in Magnetic Nanowires*, Phys. Rev. Lett. **102**, 147204 (2009).

[218] J. Briones, F. Montaigne, D. Lacour, M. Hehn, M. J. Carey and J. R. Childress, *Magnetic domain wall propagation in a submicron spin-valve stripe: Influence of the pinned layer*, Appl. Phys. Lett. **92**, 032508 (2008).

[219] S. Lepadatu, A. Vanhaverbeke, D. Atkinson, R. Allenspach and C. H. Marrows, *Dependence of Domain-Wall Depinning Threshold Current on Pinning Profile*, Phys. Rev. Lett. **102**, 127203 (2009).

[220] S.-M. Ahn, K.-W. Moon, D.-H. Kim and S.-B. Choe, *Detection of the static and kinetic pinning of domain walls in ferromagnetic nanowires*, Appl. Phys. Lett. **95**, 152506 (2009).

[221] G. Nahrwold, L. Bocklage, J. M. Scholtyssek, T. Matsuyama, B. Krüger, U. Merkt and G. Meier, *Current-induced domain-wall depinning in curved Permalloy nanowires*, J. Appl. Phys. **105**, 07D511 (2009).

[222] L. Thomas, M. Hayashi, X. Jiang, R. Moriya, C. Rettner and S. S. P. Parkin, *Oscillatory dependence of current-driven magnetic domain wall motion on current pulse length*, Nature **443**, 197 (2006).

[223] E. Saitoh, H. Miyajima, T. Yamaoka and G. Tatara, *Current-induced resonance and mass determination of a single magnetic domain wall*, Nature **432**, 203 (2004).

[224] B. Krüger, D. Pfannkuche, M. Bolte, G. Meier and U. Merkt, *Current-driven domain-wall dynamics in curved ferromagnetic nanowires*, Phys. Rev. B **75**, 054421 (2007).

[225] E. Martinez, L. Lopez-Diaz, O. Alejos and L. Torres, *Resonant domain wall depinning induced by oscillating spin-polarized currents in thin ferromagnetic strips*, Phys. Rev. B **77**, 144417 (2008).

[226] D. Bedau, M. Kläui, S. Krzyk, U. Rüdiger, G. Faini and L. Vila, *Detection of Current-Induced Resonance of Geometrically Confined Domain Walls*, Phys. Rev. Lett. **99**, 146601 (2007).

[227] L. Bocklage, B. Krüger, R. Eiselt, M. Bolte, P. Fischer and G. Meier, *Time-resolved imaging of current-induced domain-wall oscillations*, Phys. Rev. B **78**, 180405(R) (2008).

[228] R. Moriya, L. Thomas, M. Hayashi, Y. B. Bazaliy, C. Rettner and S. S. P. Parkin, *Probing vortex-core dynamics using current-induced resonant excitation of a trapped domain wall*, Nature Phys. **4**, 368 (2008).

[229] S. Lepadatu, O. Wessely, A. Vanhaverbeke, R. Allenspach, A. Potenza, H. Marchetto, T. R. Charlton, S. Langridge, S. S. Dhesi and C. H. Marrows, *Domain-wall spin-torque resonators for frequency-selective operation*, Phys. Rev. B **81**, 060402(R) (2010).

[230] S. Laribi, V. Cros, M. Muñoz, J. Grollier, A. Hamzić, C. Deranlot, A. Fert, E. Martínez, L. López-Díaz, L. Vila, G. Faini, S. Zoll and R. Fournel, *Reversible and irreversible current induced domain wall motion in CoFeB based spin valves stripes*, Appl. Phys. Lett. **90**, 232505 (2007).

[231] A. V. Khvalkovskiy, K. A. Zvezdin, Ya. V. Gorbunov, V. Cros, J. Grollier, A. Fert and A. K. Zvezdin, *High Domain Wall Velocities due to Spin Currents Perpendicular to the Plane*, Phys. Rev. Lett. **102**, 067206 (2009).

[232] C. Boone, J. A. Katine, M. Carey, J. R. Childress, X. Cheng and I. N. Krivorotov, *Rapid Domain Wall Motion in Permalloy Nanowires Excited by a Spin-Polarized Current Applied Perpendicular to the Nanowire*, Phys. Rev. Lett. **104**, 097203 (2010).

[233] D. A. Allwood, G. Xiong, C. C. Faulkner, D. Atkinson, D. Petit and R. P. Cowburn, *Magnetic domain-wall logic*, Science **309**, 1688 (2005).

[234] D. A. Allwood, G. Xiong, M. D. Cooke, C. C. Faulkner, D. Atkinson, N. Vernier and R. P. Cowburn, *Submicrometer Ferromagnetic NOT Gate and Shift Register*, Science **296**, 2003 (2002).

[235] S. S. P. Parkin, *Shiftable Magnetic Shift Register and Method of Using the Same*, U.S. Patent No. 6834005 (2004).

[236] S. S. P. Parkin, M. Hayashi and L. Thomas, *Magnetic Domain-Wall Racetrack Memory*, Science **320**, 190 (2008).

Chapter 3 – Continuous Spin-Valve Films

[237] K. Shigeto, T. Ono, H. Miyajima and T. Shinjo, *GMR effect in a single trilayer wire with submicron width*, J. Magn. Magn. Mater. **198-199**, 58 (1999).

[238] V. Uhlíř, S. Pizzini, N. Rougemaille, J. Novotný, V. Cros, E. Jiménez, G. Faini, L. Heyne, F. Sirotti, C. Tieg, A. Bendounan, F. Maccherozzi, R. Belkhou, J. Grollier, A. Anane and J. Vogel, *Current-induced motion and pinning of domain walls in spin-valve nanowires studied by XMCD-PEEM*, Phys. Rev. B **81**, 224418 (2010).

[239] S. S. P. Parkin, *The magic of magnetic multilayers*, IBM J. Res. Develop. **42**, 3 (1998).

[240] H. Lüth, *Solid Surfaces, Interfaces and Thin Films*, Springer-Verlag Berlin Heidelberg New York (2001).

[241] K. Oura, V. G. Lifshits, A. A. Saranin, A. V. Zotov, M. Katayama, *Surface Science: An Introduction*, Springer-Verlag Berlin Heidelberg New York (2003).

[242] H. Brune, *Microscopic view of epitaxial metal growth: nucleation and aggregation*, Surface Science Reports **31**, 121 (1998).

[243] J. V. Barth, G. Constantini and K. Kern, *Engineering atomic and molecular nanostructures at surfaces*, Nature **437**, 671 (2005).

[244] B. Heinrich and J. F. Cochran, *Magnetic Ultrathin Films* in *Handbook of Magnetism and Advanced Magnetic Materials*, vol. 4, eds. H. Kronmüller and S. Parkin. John Wiley & Sons, Ltd. (2007).

[245] J. Birch, F. Eriksson, G. A. Johansson and H. M. Hertz, *Recent advances in ion-assisted growth of Cr/Sc multilayer X-ray mirrors for the water window*, Vacuum **68**, 275 (2003).

[246] J. Becker, *Ion-Beam Sputtering* in *Handbook of Optical Properties*, eds. R. E. Hummel and K. H. Guenther, CRC Press LLC, Boca Raton (1995).

[247] A. Zangwill, *Physics at surface*, Cambridge University Press (1988).

[248] E. Fullerton, M. J. Conover, J. E. Mattson, C. H. Sowers and S. D. Bader, *150% magnetoresistance in sputtered Fe/Cr(lOO) superlattices*, Appl. Phys. Lett. **63**, 1699 (1993).

[249] S. S. P. Parkin, Z. G. Li and D. J. Smith, *Giant magnetoresistance in antiferromagnetic Co/Cu multilayers*, Appl. Phys. Lett. **58**, 2710 (1991).

[250] J. C. Slonczewski, *Conductance and exchange coupling of two ferromagnets separated by a tunneling barrier*, Phys. Rev. B **39**, 6995 (1989).

[251] B. Dieny, V. S. Speriosu, S. S. P. Parkin, B. A. Gurney, D. R. Wilhoit and D. Mauri, *Giant magnetoresistance in soft ferromagnetic multilayers*, Phys. Rev. B **43**, 1297 (1991).

[252] T. Shinjo and H. Yamamoto, *Large Magnetoresistance of Field-Induced Giant Ferrimagnetic Multilayers*, J. Phys. Soc. Jpn. **59**, 3061 (1990).

[253] W. H. Butler, X.-G. Zhang, D. M. C. Nicholson and J. M. MacLaren, *Spin-dependent scattering and giant magnetoresistance*, J. Magn. Magn. Mater. **151**, 354 (1995).

[254] P. Zahn, J. Binder, I. Mertig, R. Zeller and P. H. Dederichs, *Origin of Giant Magnetoresistance: Bulk or Interface Scattering*, Phys. Rev. Lett. **80**, 4309 (1998).

[255] T. Valet and A. Fert, *Classical theory of perpendicular giant magnetoresistance in magnetic multilayers*, J. Magn. Magn. Mater. **121**, 378 (1993).

[256] W. P. Pratt Jr., S.-F. Lee, P. Holody, Q. Yang, R. Loloee, J. Bass and P. A. Schroeder, *Giant magnetoresistance with current perpendicular to the multilayer planes*, J. Magn. Magn. Mater. **126**, 406 (1993).

[257] S. S. P. Parkin, *Origin of Enhanced Magnetoresistance of Magnetic Multilayers: Spin-Dependent Scattering from Magnetic Interface States*, Phys. Rev. Lett. **71**, 1641 (1993).

[258] B. Dieny, V. S. Speriosu, S. Metin, S. S. P. Parkin, B. A. Gurney, P. Baumgart and D. Wilhoit, *Magnetotransport properties of magnetically soft spin-valve structures*, J. Appl. Phys. **69**, 4774 (1991).

[259] S. S. P. Parkin, A. Modak and D. J. Smith, *Dependence of giant magnetoresistance on Cu-layer thickness in Co/Cu multilayers: A simple dilution effect*, Phys. Rev. B **47**, 9136 (1993).

[260] T. Sun, B. Yao, A. P. Warren, K. Barmak, M. F. Toney, R. E. Peale and K. R. Coffey, *Surface and grain-boundary scattering in nanometric Cu films*, Phys. Rev. B **81**, 155454 (2010).

[261] B. Dieny, V. S. Speriosu and S. Metin, *Thermal Variation of the Magnetoresistance of Soft Spin-Valve Multilayers*, Europhys. Lett. **15**, 227 (1991).

[262] B. Dieny, B. A. Gurney, S. Metin, S. S. P. Parkin and V. S. Speriosu, *Magnetoresistive sensor based on the spin valve effect*, U.S. Patent No. 5159513 (1992).

[263] B. Dieny, P. Humbert, V. S. Speriosu, S. Metin, B. A. Gurney, P. Baumgart and H. Lefakis, *Giant magnetoresistance of magnetically soft sandwiches: Dependence on temperature and on layer thicknesses*, Phys. Rev. B **45**, 806 (1992).

[264] J. Barnaś, O. Baksalary and A. Fert, *Angular dependence of giant magnetoresistance in magnetic multilayers*, Phys. Rev. B **56**, 6079 (1997).

[265] H.-J. Kim, W.-C. Jeong, K.-K. Cho, Y.-K. Kim and S.-K. Joo, *Effects of Substrate Surface Topology on NiFe/Cu/Co Spin Valve Characteristics*, Jpn. J. Appl. Phys. **39**, 4767 (2000).

[266] X.-L. Tang, H.-W. Zhang, H. Su, Z.-Y. Zhong and Y.-L. Jing, *Effects of an underlayer on the sensitivity of top spin valves*, J. Appl. Phys. **102**, 043915 (2007).

[267] M. Erekhinsky, A. Sharoni, F. Casanova and I. K. Schuller, *Surface enhanced spin-flip scattering in lateral spin valves*, Appl. Phys. Lett. **96**, 022513 (2010).

[268] G. Betz and G. K. Wehner, *Sputtering of Multicomponent Materials* in *Sputtering by Particle Bombardment II (Sputtering of Alloys and Compounds, Electron and Neutron Sputtering, Surface Topography)*, ed. R. Behrisch. Springer-Verlag Berlin Heidelberg New York Tokyo (1983).

[269] XPS international, `http://www.xpsdata.com`, *Handbook of Monochromatic XPS Spectra, The Elements of Native Oxides*, Vol. 1, John Wiley & Sons, Inc. (2001).

[270] J. Čechal, *Surfaces and thin film analysis using x-ray photoelectron spectroscopy*, PhD thesis, Brno University of Technology (2006).

[271] J. M. Slaughter, E. Y. Chen and S. Tehrani, *Magnetoresistance of ion-beam deposited Co/Cu/Co and NiFe/Co/Cu/Co/NiFe spin valves*, J. Appl. Phys. **85**, 4451 (1999).

[272] E. E. Fullerton, D. M. Kelly, J. Guimpel, I. K. Schuller and Y. Bruynseraede, *Roughness and Giant Magnetoresistance in Fe/Cr Superlattices*, Phys. Rev. Lett. **68**, 859 (1992).

[273] V. S. Speriosu, J. P. Nozieres, B. A. Gurney, B. Dieny, T. C. Huang and H. Lefakis, *Role of interfacial mixing in giant magnetoresistance*, Phys. Rev. B **47**, 11579 (1993).

[274] T. C. Huang, J.-P. Nozieres, V. S. Speriosu, B. A. Gurney and H. Lefakis, *Effect of annealing on the interfaces of giant-magnetoresistance spin-valve structures*, Appl. Phys. Lett. **62**, 1478 (1993).

[275] M. Hecker, D. Tietjen, H. Wendrock, C. M. Schneider, N. Cramer, L. Malkinski, R. E. Camley and Z. Celinski, *Annealing effects and degradation mechanism of NiFe/Cu GMR multilayers*, J. Magn. Magn. Mater. **247**, 62 (2002).

[276] C. B. Ene, G. Schmitz, R. Kirchheim and A. Hütten, *Stability and thermal reaction of GMR NiFe/Cu thin films*, Acta Materialia **53**, 3383 (2005).

[277] L. C. C. M. Nagamine, A. Biondo, L. G. Pereira, A. Mello, J. E. Schmidt, T. W. Chimendes, J. B. M. Cunha and E. B. Saitovitch, *Effect of interface intermixing on giant magnetoresistance in NiFe/Cu and Co/NiFe/Co/Cu multilayers*, J. Appl. Phys. **94**, 5881 (2003).

[278] M. Menyhard, A. Sulyok, K. Pentek and A. M. Zeltser, *Demixing in spin valve structures: an Auger depth profiling study*, Thin Solid Films **366**, 129 (2000).

[279] A. Jesche, A. Gorbunoff, A. Mensch, H. Stöcker, A. A. Levin and D. C. Meyer, *Structure and giant magnetoresistance of granular Co–Cu nanolayers prepared by cross-beam pulsed laser deposition*, J. Appl. Phys. **107**, 023904 (2010).

[280] J. Szucs, T. O'Brien, D. K. Lottis, S. Gangopadhyay, S. Mao and E. Murdock, *Temperature variation of the magnetoresistance in cobalt-enhanced spin-valve structures*, J. Appl. Phys. **81**, 4014 (1997).

[281] M. Suzuki and Y. Taga, *Role of interfacial roughness in the giant magnetoresistance in Co/Cu superlattices*, Phys. Rev. B **52**, 361 (1995).

[282] D. J. Chakrabarti, D. E. Laughlin, S. W. Chen and Y. A. Chang, *Cu-Ni (Copper-Nickel)* in *Phase Diagrams of Binary Nickel Alloys*, ASM, p. 85-95 (1991).

[283] O. Kubaschewski, *Fe-Cu; Iron-Copper* in *Iron – Binary Phase Diagrams*, Springer-Verlag, p. 35-37 (1982).

[284] T. Nishizawa and K. Ishida, *The Co-Cu (Cobalt-Copper) System*, Bull. Alloy Phase Diagrams **5**(2), 161 (1984).

[285] M. Mitáš, *Analysis of GMR heterostructures by SIMS*, Master thesis, Brno University of Technology (2008).

[286] J. Langer, R. Mattheis, B. Ocker, W. Maaß, S. Senz, D. Hesse and J. Kräußlich, *Microstructure and magnetic properties of sputtered spin valve systems*, J. Appl. Phys. **90**, 5126 (2001).

[287] D. Lottis, A. Fert, R. Morel, L. G. Pereira, J. C. Jacquet, P. Galtier, J. M. Coutellier and T. Valet, *Magnetoresistance in rf-sputtered (NiFe/Cu/Co/Cu) spin-valve multilayers*, J. Appl. Phys. **73**, 5515 (1993).

[288] H.-J. Kim, B.-I. Lee and S.-K. Joo, *Development of unusual magnetic anisotropy in Co-based trilayers*, J. Appl. Phys. **81**, 3995 (1997).

[289] A. Paul, T. Damm, D. E. Bürgler, S. Stein, H. Kohlstedt and P. Grünberg, *Optimizing the giant magnetoresistance of NiFe/Cu/Co pseudo spin-valves prepared by magnetron sputtering*, Appl. Phys. Lett. **82**, 1905 (2003).

[290] A. R. Modak, D. J. Smith and S. S. P. Parkin, *Dependence of giant magnetoresistance on grain size in Co/Cu multilayers*, Phys. Rev. B **50**, 4232 (1994).

[291] A. Atkinson, R. I. Taylor and A. E. Hughes, *A quantitative demonstration of the grain boundary diffusion mechanism for the oxidation of metals*, Phil. Mag. A **45**, 823 (1982).

[292] D. W. Rice, P. B. P. Phipps and R. Tremoureux, *Atmospheric Corrosion of Cobalt*, Alkaline Solutions **126**, No. 9, 1459 (1979).

[293] H. G. Tompkins and J. A. Augis, *The Oxidation of Cobalt in Air From Room Temperature to 467°C*, Oxidation of Metals, Vol. **16**, Nos. 5/6, 355 (1981).

[294] W. F. Egelhoff, P. J. Chen, R. D. K. Misra, T. Ha, Y. Kadmon, C. J. Powell, M. D. Stiles, R. D. McMichael, C.-L. Lin, J. M. Sivertsen and J. H. Judy, *Low-temperature growth of giant magnetoresistance spin valves*, J. Appl. Phys. **79**, 282 (1996).

[295] W. E. Bailey, N.-C. Zhu, R. Sinclair and S. X. Wang, *Structural comparisons of ion beam and dc magnetron sputtered spin valves by high-resolution transmission electron microscopy*, J. Appl. Phys. **79**, 6393 (1996).

[296] J. J. Quan, S. A. Wolf and H. N. G. Wadley, *Low energy ion beam assisted deposition of a spin valve*, J. Appl. Phys. **101**, 074302 (2007).

Chapter 4 – Patterning of Magnetic Nanowires

[297] T. Taniyama, I. Nakatani, T. Namikawa, Y. Yamazaki, *Resistivity due to Domain Walls in Co Zigzag Wires*, Phys. Rev. Lett. **82**, 2780 (1999).

[298] T. Taniyama, I. Nakatani, T. Namikawa, Y. Yamazaki, *Control of domain structures and magnetotransport properties in patterned ferromagnetic wires*, Appl. Phys. Lett. **76**, 613 (2000).

[299] K. Shigeto, T. Shinjo and T. Ono, *Injection of a magnetic domain wall into a submicron magnetic wire*, Appl. Phys. Lett. **75**, 2815 (1999).

[300] T. Schrefl, J. Fidler, K. J. Kirk and J. N. Chapman, *Domain structures and switching mechanisms in patterned magnetic elements*, J. Magn. Magn. Mat. **175**, 193 (1997).

[301] A. A. Tseng, *Recent developments in nanofabrication using focused ion beams*, Small **1**, 924 (2005).

[302] J. Gierak, *Focused ion beam technology and ultimate applications*, Semicond. Sci. Technol. **24**, 043001 (2009).

[303] E. Kerr, S. van Dijken, R. M. Langford and J. M. D. Coey, *Effect of Ga^+ ion implantation on the magnetoresistive properties of spin valves*, J. Magn. Magn. Mater. **290/291**, 124 (2005).

[304] C. Park and J. Bain, *Local degradation of magnetic properties in magnetic thin films irradiated by Ga^+ focused-ion-beams*, IEEE Trans. Magn. **38**, 2237 (2002).

[305] N. Imanishi, *Interactions of ions with matter* in *Focused Ion Beam Systems: Basics and Applications*, ed. N. Yayo. Cambridge University Press, Cambridge (2007).

[306] W. J. MoberlyChan, T. E. Felter and M. A. Wall, *Surface rippling & ion etch yields of diamond using a focused ion beam: with or without enhanced chemistry, aspect ratio regulates ion etching*, Microsc. Today **14**, 28–34 (2006).

[307] J. Muñoz-García, L. Vázquez, R. Cuerno, J. A. Sánchez-García, M. Castro and R. Gago, *Self-organized surface nanopatterning by ion beam sputtering* in *Towards Functional Nanomaterials*, ed. Z. M. Wang. Springer Verlag, New York (2009).

[308] Y. Stark, R. Frömter, D. Stickler and H. P. Oepen, *Sputter yields of single- and polycrystalline metals for application in focused ion beam technology*, J. Appl. Phys. **105**, 013542 (2009).

[309] R. Levi-Setti, T. R. Fox and K. Lam, *Ion channeling effects in scanning ion microscopy with a 60 keV Ga^+ probe*, Nucl. Instrum. Methods **205**, 299–309 (1983).

[310] R. Spolenak, L. Sauter and C. Eberl, *Reversible orientation-biased grain growth in thin metal films induced by a focused ion beam*, Scr. Mater. **53**, 1291–6 (2005).

[311] S. Lipp, L. Frey, C. Lehrer, B. Frank, E. Demm and H. Ryssel, *Investigations on the topology of structures milled and etched by focused ion beams*, J. Vac. Sci. Technol. B **14**, 3996–9 (1996).

[312] M. Urbánek, V. Uhlíř, P. Bábor, E. Kolíbalová, T. Hrnčíř, J. Spousta and T. Šikola, *Focused ion beam fabrication of spintronic nanostructures: an optimization of the milling process*, Nanotechnology **21**, 145304 (2010).

[313] J. Gierak, E. Bourhis, M. N. Mérat Combes, Y. Chriqui, I. Sagnes, D. Mailly, P. Hawkes, R. Jede, L. Bruchhaus, L. Bardotti, B. Prével, A. Hannour, P. Mélinon, A. Perez, J. Ferré, J.-P. Jamet, A. Mougin, C. Chappert and V. Mathet, *Exploration of the ultimate patterning potential achievable with focused ion beams*, Microelectronic Engineering **78–79**, 266 (2005).

[314] J. Fassbender and J. McCord, *Magnetic patterning by means of ion irradiation and implantation*, J. Magn. Magn. Mater. **320** 579–96 (2008).

[315] J. A. Katine, M. K. Ho, Y. S. Ju and C. T. Rettner, *Patterning damage in narrow trackwidth spin-valve sensors*, Appl. Phys. Lett. **83**, 401 (2003).

[316] L. Thomas, C. Rettner, M. Hayashi, M. G. Samant, S. S. P. Parkin, A. Doran and A. Scholl, *Observation of injection and pinning of domain walls in magnetic nanowires using photoemission electron microscopy*, Appl. Phys. Lett. **87**, 262501 (2005).

Chapter 5 – Magnetic Imaging by XMCD-PEEM

[317] J. Vogel, W. Kuch, J. Camarero, K. Fukumoto, Y. Pennec, S. Pizzini, M. Bonfim, F. Petroff, A. Fontaine and J. Kirschner, *Interplay between magnetic anisotropy*

and interlayer coupling in nanosecond magnetization reversal of spin-valve trilayers, Phys. Rev. B **71**, 060404(R) (2005).

[318] H. A. Dürr and C. M. Schneider, *Ultrafast Magnetodynamics with Lateral Resolution: A View by Photoemission Microscopy* in *Handbook of Magnetism and Advanced Magnetic Materials*, vol. 3, eds. H. Kronmüller and S. Parkin. John Wiley & Sons, Ltd. (2007).

[319] M. Bolte, G. Meier, B. Krüger, A. Drews, R. Eiselt, L. Bocklage, S. Bohlens, T. Tyliszczak, A. Vansteenkiste, B. Van Waeyenberge, K. W. Chou, A. Puzic and H. Stoll, *Time-Resolved X-Ray Microscopy of Spin-Torque-Induced Magnetic Vortex Gyration*, Phys. Rev. Lett. **100**, 176601 (2008).

[320] V. Chembrolu, J. P. Strachan, X. W. Yu, A. A. Tulapurkar, T. Tyliszczak, J. A. Katine, M. J. Carey, J. Stöhr and Y. Acremann, *Time-resolved x-ray imaging of magnetization dynamics in spin-transfer torque devices*, Phys. Rev. B. **80** 024417 (2009).

[321] J. Vogel, W. Kuch, M. Bonfim, J. Camarero, Y. Pennec, F. Offi, K. Fukumoto, J. Kirschner, A. Fontaine and S. Pizzini, *Time-resolved magnetic domain imaging by x-ray photoemission electron microscopy*, Appl. Phys. Lett. **82**, 2299 (2003).

[322] G. Schütz, E. Goering and H. Stoll, *Synchrotron Radiation Techniques Based on X-ray Magnetic Circular Dichroism* in *Handbook of Magnetism and Advanced Magnetic Materials*, vol. 3, eds. H. Kronmüller and S. Parkin. John Wiley & Sons, Ltd. (2007).

[323] J. Stöhr, H. A. Padmore, S. Anders, T. Stammler and M. R. Scheinfein, *Principles of X-ray Magnetic Dichroism Spectromicroscopy*, Surf. Rev. Lett. **5**, 1297 (1998).

[324] N. V. Smith, C. T. Chen, F. Sette and L. F. Mattheis, *Relativistic tight-binding calculations of x-ray absorption and magnetic circular dichroism at the L_2 and L_3 edges of nickel and iron*, Phys. Rev. B **46**, 1023 (1992).

[325] P. Carra, B. T. Thole, M. Altarelli, and X. Wang, *X-Ray Circular Dichroism and Local Magnetic Fields*, Phys. Rev. Lett. **70**, 694 (1993).

[326] B. T. Thole, P. Carra, F. Sette, and G. van der Laan, *X-Ray Circular Dichroism as a Probe of Orbital Magnetization*, Phys. Rev. Lett. **68**, 1943 (1992).

[327] H. Wende, *Recent advances in x-ray absorption spectroscopy*, Rep. Prog. Phys. **67**, 2105–2181 (2004).

[328] J. Feng and A. Scholl, *Photoemission Electron Microscopy (PEEM) in Science of Microscopy*, eds. P. W. Hawkes and J. C. H. Spence. Springer New York (2007).

[329] B. P. Tonner and D. Dunham, *Sub-micron spatial resolution of a micro-XAFS electrostatic microscope with bending magnet radiation: performance assessments*

and prospects for aberration correction, Nucl. Inst. Methods Phys. Res. A **347**, 436 (1994).

[330] D. Preikszas and H. Rose, *Correction properties of electron mirrors*, J. Electr. Micr. **1**, 1 (1997).

[331] T. Schmidt, U. Groh, R. Fink and E. Umbach, *XPEEM with energy-filtering: Advantages and first results from the smart project*, Surf. Rev. Lett. **9**, 223 (2002).

[332] A. Locatelli, E. Bauer, *Recent advances in chemical and magnetic imaging of surfaces and interfaces by XPEEM*, J. Phys. Cond. Mat. **20**, 093002 (2008).

[333] R. Nakajima, J. Stöhr and I. Idzerda, *Electron-yield saturation effects in L-edge x-ray magnetic circular dichroism spectra of Fe, Co, and Ni*, Phys. Rev. B **59**, 6421 (1999).

[334] M. Bonfim, *Micro bobines à champ pulsé : applications aux champs forts et à la dynamique de renversement de l'aimantation à l'échelle de la nanoseconde par effet Kerr et Dichroïsme Circulaire Magnétique de rayons X*, Thèse, Université Joseph Fourier Grenoble 1, (2001).

Chapter 6 – Current-Induced Domain-Wall Motion in Spin-Valve Nanowires

[335] E. H. Sondheimer, *The mean free path of electrons in metals*, Adv. Phys. **50**, 499 (2001).

[336] M. Cormier, *Renversement d'aimantation dans des nanostructures par propagation de parois de domaines sous champ magnétique et courant électrique*, Thèse, Université Paris-Sud 11, (2008).

[337] J. Vogel, S. Cherifi, S. Pizzini, F. Romanens, J. Camarero, F. Petroff, S. Heun and A. Locatelli, *Layer-resolved imaging of domain wall interactions in magnetic tunnel junction-like trilayers*, J. Phys: Condens. Matter **19**, 476204 (2007).

[338] M. J. Donahue and D. G. Porter, *OOMMF User's Guide*, Version 1.0. Interagency Report NISTIR 6376 (NIST, Gaithersburg, 1999).

[339] D. Djuhana, H.-G. Piao, S.-C. Yu, S. K. Oh and D.-H. Kim, *Magnetic domain wall collision around the Walker breakdown in ferromagnetic nanowires*, J. Appl. Phys. **106**, 103926 (2009).

[340] A. Kunz and R. W. Rentsch, *Simulations of Field Driven Domain Wall Interactions in Ferromagnetic Nanowires*, IEEE Trans. Mag. **46**, 1556 (2010).

[341] `http://www.zurich.ibm.com/st/magnetism/spintevolve.html`, OOMMF extension for CIDWM, IBM Zürich, 2008.

[342] A. Vanhaverbeke, A. Bischof and R. Allenspach, *Control of Domain Wall Polarity by Current Pulses*, Phys. Rev. Lett. **101**, 107202 (2008).

[343] S. Yang and J. L. Erskine, *Spin-transfer-torque-driven domain-wall dynamics in Permalloy nanowires*, Phys. Rev. B **75**, 220403(R) (2007).

[344] J. Shibata, G. Tatara and H. Kohno, *Effect of Spin Current on Uniform Ferromagnetism: Domain Nucleation*, Phys. Rev. Lett. **94**, 076601 (2005).

[345] Y. Togawa, T. Kimura, K. Harada, T. Akashi, T. Matsuda, A. Tonomura and Y. Otani, *Current-Excited Magnetization Dynamics in Narrow Ferromagnetic Wires*, Japan. J. Appl. Phys. **45**, L1322 (2006).

[346] L. Thomas, M. Hayashi, X. Jiang, C. Rettner and S. S. P. Parkin, *Perturbation of spin-valve nanowire reference layers during domain wall motion induced by nanosecond-long current pulses*, Appl. Phys. Lett. **92**, 112504 (2008).

[347] D. Morecroft, I. A. Colin, F. J. Castaño, J. A. C. Bland and C. A. Ross, *Current-induced magnetization reversal in NiFe/Cu/Co/Au notched mesoscopic bars*, Phys. Rev. B **76**, 054449 (2007).

[348] K. Fukumoto, W. Kuch, J. Vogel, F. Romanens, S. Pizzini, J. Camarero, M. Bonfim and J. Kirschner, *Dynamics of Magnetic DomainWall Motion after Nucleation: Dependence on the Wall Energy*, Phys. Rev. Lett. **96**, 097204 (2006).

[349] L. Heyne, J. Rhensius, Y.-J. Cho, D. Bedau, S. Krzyk, C. Dette, H. S. Körner, J. Fischer, M. Laufenberg, D. Backes, L. J. Heyderman, L. Joly, F. Nolting, G. Tatara, H. Kohno, S. Seo, U. Rüdiger and M. Kläui, *Geometry-dependent scaling of critical current densities for current-induced domain wall motion and transformations*, Phys. Rev. B **80**, 184405 (2009).

[350] M. Hayashi, L. Thomas, R. Moriya, C. Rettner and S. S. P. Parkin, *Current-Controlled Magnetic Domain-Wall Nanowire Shift Register*, Science **320**, 209 (2008).

[351] T. Devolder, A. Tulapurkar, Y. Suzuki, C. Chappert, P. Crozat and K. Yagami, *Temperature study of the spin-transfer switching speed from dc to 100 ps*, J. Appl. Phys. **98**, 053904 (2005).

[352] Y. Acremann, J. P. Strachan, V. Chembrolu, S. D. Andrews, T. Tyliszczak, J. A. Katine, M. J. Carey, B. M. Clemens, H. C. Siegmann and J. Stöhr, *Time-Resolved Imaging of Spin Transfer Switching: Beyond the Macrospin Concept*, Phys. Rev. Lett. **96**, 217202 (2006).

[353] G. Schönhense, H. J. Elmers, S. A. Nepijko and C. M. Schneider, in *Advances in Imaging and Electron Physics*, vol. 42, Elsevier Academic Press Inc., San Diego, USA (2006).

[354] M. Bonfim, G. Ghiringhelli, F. Montaigne, S. Pizzini, N. Brookes, F. Petroff, J. Vogel, J. Camarero and A. Fontaine, *Element-Selective Nanosecond Magnetization Dynamics in Magnetic Heterostructures*, Phys. Rev. Lett. **86**, 3646 (2001).

[355] F. Sirotti, S. Girlando, P. Prieto, L. Floreano, G. Panaccione and G. Rossi, *Dynamics of surface magnetization on a nanosecond time scale*, Phys. Rev. B **61**, R9221 (2000).

[356] A. Aharoni, *Demagnetizing factors for rectangular ferromagnetic prisms*, J. Appl. Phys. **83**, 3432 (1998).

[357] R. Cowburn, D. Koltsov, A. Adeyeye and M. Welland, *Lateral interface anisotropy in nanomagnets*, J. Appl. Phys. **87**, 7067 (2000).

[358] W. Kim, S. Seo, T. Lee and K. Lee, *Oscillatory domain wall velocity of current-induced domain wall motion*, J. Magn. Magn. Mater. **310**, 2032 (2007).

[359] Y. Togawa, T. Kimura, K. Harada, T. Matsuda, A. Tonomura, Y. Otani and T. Akashi, *Current-excited magnetization reversal under in-plane magnetic field in a nanoscaled ferromagnetic wire*, Appl. Phys. Lett. **92**, 012505 (2008).

[360] C. Kittel, *On the Theory of Ferromagnetic Resonance Absorption*, Phys. Rev. **73**, 155 (1948).

[361] P. E. Wigen, *Dipole-Narrowed Inhomogeneously Broadened Lines in Ferromagnetic Thin Films*, Phys. Rev. **133**, A1557 (1964).

[362] H. W. Schumacher, C. Chappert, P. Crozat, R. C. Sousa, P. P. Freitas, J. Miltat, J. Fassbender and B. Hillebrands, *Phase Coherent Precessional Magnetization Reversal in Microscopic Spin Valve Elements*, Phys. Rev. Lett. **90**, 017201 (2003).

Appendix

[363] C. Kittel, *Introduction to Solid State Physics*, 7th edition, John Wiley & Sons, Inc., New York (1996).

[364] J. F. Watts and J. Wolstenholme, *An Introduction to Surface Analysis by XPS and AES*, John Wiley & Sons Ltd, Chichester (2003).

[365] J. Polčák, J. Čechal, P. Bábor, M. Urbánek, S. Průša and T. Šikola, *Angle-resolved XPS depth profiling of modeled structures: testing and improvement of the method*, Surf. Int. Anal. **42**, 649 (2010).

[366] Z. Chanbi, R. W. Paynter, *On the choice of the regularization parameter for the interpretation of ARXPS data using a multilayer model*, J. Electron Spectrosc. Relat. Phenom. **164**, 28 (2008).

[367] L. J. van der Pauw, *A Method of Measuring Specific Resistivity and Hall Effect of Discs of Arbitrary Shape*, Philips Res. Repts. **13**, 1 (1958).

[368] R. Erni, M. D. Rossell, C. Kisielowski and U. Dahmen, *Atomic-Resolution Imaging with a Sub-50-pm Electron Probe*, Phys. Rev. Lett. **102**, 096101 (2009).

[369] R. Schäfer, *Investigation of Domains and Dynamics of Domain Walls by the Magneto-optical Kerr-effect* in *Handbook of Magnetism and Advanced Magnetic Materials*, vol. 3, eds. H. Kronmüller and S. Parkin. John Wiley & Sons, Ltd. (2007).

LIST OF ACRONYMS AND ABBREVIATIONS

OD, 1D, 2D, 3D – zero-, one-, two-, three-dimensional, respectively
ac – Alternating current
AF – Antiferromagnet, Antiferromagnetic layer
AFM – Atomic Force Microscope
AMR – Anisotropic Magnetoresistance
AR-XPS – Angle-Resolved X-ray Photoelectron Spectroscopy
BCC – Body-Centered Cubic
CEA – Comissariat à l'Energie Atomique
CCD – Charge-Coupled Device
CIDWM – Current-Induced Domain-Wall Motion
CIP – Current-in-plane
CNRS – Centre national de la recherche scientifique
CPP – Current-perpendicular-to-plane
dc – Direct current
DFT – Density Functional Theory
DUV – Deep-Ultraviolet
DW – Domain Wall
EBL – Electron Beam Lithography
EHE – Extraordinary Hall Effect
ESRF – European Synchrotron Radiation Facility
FCC – Face-Centered Cubic
FIB – Focused Ion Beam
FIB-CVD – Focused Ion Beam - Chemical Vapour Deposition
FM – Ferromagnet, Ferromagnetic layer
FMR – Ferromagnetic Resonance
FWHM – Full Width at Half-Maximum
GMR – Giant Magnetoresistance
HCP – Hexagonal Close-Packed
IBS – Ion-Beam Sputtering
IBAD – Ion-Beam Assisted Deposition
IBE – Ion-Beam Etching
IN – Institut Néel
IPA – Isopropanol
IPE – Institute of Physical Engineering
LCP – Left-Circularly Polarized
LLG – Landau-Lifshits-Gilbert equation
LSDA – Local Spin-Density Approximation
MAA – Methacrylic Acid

MBE – Molecular Beam Epitaxy
MFM – Magnetic Force Microscope
MIBK – Methyl Isobutyl Ketone
ML – Monolayer
MOKE – Magneto-Optical Kerr Effect
MRAM – Magnetoresistive Random-Access Memory
MTJ – Magnetic Tunnel Junction
NM – Non-magnetic layer
OOMMF – Object-Oriented Micromagnetic Framework
PEEM – Photoemission Electron Microscope
PMA – Perpendicular Magnetic Anisotropy
PMMA – Polymethyl Methacrylate
PTA – Plateforme Technologique Amont
RAM – Random-Access Memory
RCP – Right-Circularly Polarized
RF – Radio-Frequency
RIE – Reactive Ion Etching
RKKY – Ruderman-Kittel-Kasuya-Yosida interaction
RMS – Root Mean Square
RT – Room Temperature
SEM – Scanning Electron Microscope
SEMPA – Scanning Electron Microscope with Polarization Analysis
SIMS – Secondary Ion Mass Spectroscopy
STT – Spin-Transfer Torque
SV – Spin Valve
TEM – Transmission Electron Microscope
TEMPO – Time resolved Experiments on Materials with Photoelectron Spectroscopy
TMR – Tunnel Magnetoresistance
TW – Transverse Wall
UV – Ultraviolet
UHV – Ultra-High Vacuum
VW – Vortex Wall
XAS – X-ray Absorption Spectroscopy
XMCD – X-ray Magnetic Circular Dichroism
XPS – X-ray Photoelectron Spectroscopy

LIST OF SYMBOLS

∇ – Hamilton operator
A – Exchange stiffness constant
α – Gilbert damping constant
B – Magnetic flux density
β – Non-adiabatic parameter for CIDWM description
c – Speed of light
γ_0 – Gyromagnetic ratio
d – Depth
d_{m} – Dimension of motion
D – Diffusion rate
δ_{s} – Skin depth
Δ – Domain-wall width parameter
Δ_{xc} – Ferromagnetic exchange splitting
e – Electron charge
$\vec{e_{\mathrm{q}}}$ – Unit polarization vector
E – Energy
E_{B} – Binding energy
E_{d} – Demagnetizing energy
E_{F} – Fermi energy
E_{K} – Kinetic energy
E_{Z} – Zeeman energy
f – Frequency
F – Particle flux
g – Landé factor
$h, \hbar$ – Planck's and reduced Planck's constant, respectively
H – Magnetic field
H_{a} – External (applied) field
H_{c} – Coercive field
H_{dep} – Depinning field
H_{K} – Anisotropy field
H_{Oe} – Oersted field
H_{W} – Walker field
$\mathcal{H}$ – Hamiltonian
ζ – Spin asymmetry parameter
η – Dynamic exponent for description of creep DW motion
θ – Magnetization azimuth angle
I – Electric current
j – Electric current density

J – Exchange constant (Exchange integral)
J_{m} – Magnetic polarization
k_{B} – Boltzmann constant
K – Anisotropy constant
l – length
ℓ – Mean free path
ℓ_{sf} – Spin diffusion length
L – Orbital momentum
λ – Landau-Lifshits damping constant
λ_{e} – Electron wavelength
Λ – Exchange length
Λ_{B} – Bloch's length
m – Mass
m_{e} – Electron mass
m_s^*, m_d^* – Effective electron masses (s- and d-band electrons)
m_l, m_s – Orbital and spin magnetic quantum numbers
$\mathbf{m}$ – Magnetization unit vector
M – Magnetization
M_{S} – Spontaneous magnetization
μ – Permeability
μ_0 – Permeability of vacuum
μ_{B} – Bohr magneton
μ_{c} – Chemical potential
μ_{w} – DW mobility
n – Electron density
$\mathbf{n}$ – Surface normal unit vector
N – Demagnetizing factor
N_{a} – Transmission spin asymmetry coefficient
ν_0 – Attempt frequency
ξ – Angle between the plane of a sample and an X-ray incidence direction
p – Specular reflection parameter
P – Spin polarization
P_{T} – Probability of a specular transmission
P_{D} – Probability of a diffusive transmission
q – DW position
Q – Electric charge
$\mathbf{r}$ – Position vector
R – Resistance
$R_{\square}$ – Resistance per square
R_{P} – Resistance of parallel magnetization configuration
R_{AP} – Resistance of antiparallel magnetization configuration
ρ – Resistivity
ρ_{m} – Density of magnetic volume charges
s_z – z spin component

S – Spin momentum
S_c – Cross-section surface
σ – Conductivity
σ_m – Density of magnetic surface charges
t – Time
t' – Thickness
T – Temperature
T_C – Curie temperature
T_dep – Depinning temperature
T_N – Néel temperature
T_B – Blocking temperature
τ – Relaxation time
τ_ex – Period of Larmor precession about the exchange field
τ_sf – Spin relaxation time
u – Spin-transfer efficiency (effective spin-current drift velocity)
U – Voltage
v – Velocity
v_w – DW velocity at the Walker field
V – Volume
w – Width
W_abs – Effective absorption cross-section
x, y, z – Cartesian coordinates
ϕ – Magnetization out-of-plane angle
ϕ_K – Kerr angle of polarization rotation
ϕ_w – Work function
Φ – Angle between magnetization and an X-ray incidence direction
$\Phi_\mathrm{i}, \Phi_\mathrm{f}$ – Initial and final state, respectively
φ_t – Magnetization tilt angle
ω – Angular frequency
ω_0 – Resonance angular frequency
ω_C – Cyclotron frequency

Vectors are indicated in **bold** in the text, except of figures.

LIST OF PUBLICATIONS

Papers

1. V. Uhlíř, S. Pizzini, N. Rougemaille, J. Novotný, V. Cros, E. Jiménez, G. Faini, L. Heyne, F. Sirotti, C. Tieg, A. Bendounan, F. Maccherozzi, R. Belkhou, J. Grollier, A. Anane and J. Vogel, *Current-induced motion and pinning of domain walls in spin-valve nanowires studied by XMCD-PEEM*, Phys. Rev. B **81**, 224418 (2010).

2. M. Urbánek, V. Uhlíř, P. Bábor, E. Kolíbalová, T. Hrnčíř, J. Spousta and T. Šikola: *Focused ion beam fabrication of spintronic nanostructures: an optimization of the milling process*, Nanotechnology **21**, 145304 (2010).

3. S. Pizzini, V. Uhlíř, J. Vogel, N. Rougemaille, S. Laribi, V. Cros, E. Jiménez, J. Camarero, C. Tieg, E. Bonet, M. Bonfim, R. Mattana, C. Deranlot, F. Petroff, C. Ulysse, G. Faini, A. Fert: *High domain wall velocity at zero magnetic field induced by low current densities in spin valve nanostripes*, Appl. Phys. Express **2**, 023003 (2009).

4. A. Manchon, C. Ducruet, L. Lombard, S. Auffret, B. Rodmacq, B. Dieny, S. Pizzini, J. Vogel, V. Uhlíř, M. Hochstrasser, G. Panaccione: *Analysis of oxygen induced anisotropy crossover in Pt/Co/MOx trilayers*, J. Appl. Phys. **104**, 043914 (2008).

5. A. Manchon, S. Pizzini, J. Vogel, V. Uhlíř, L. Lombard, C. Ducruet, S. Auffret, B. Rodmacq, B. Dieny, M. Hochstrasser, G. Panaccione: *X-ray analysis of oxygen-induced perpendicular magnetic anisotropy in Pt/Co/AlOx trilayers*, J. Magn. Magn. Mater. **320**, 1889 (2008).

6. R. Plšek, V. Uhlíř, M. Urbánek, J. Spousta, T. Šikola: *Měření magnetických vlastností tenkých vrstev pomocí magnetooptického Kerrova jevu*, Jemná mechanika a optika **52**(6), 184 (2008).

7. A. Manchon, S. Pizzini, J. Vogel, V. Uhlíř, L. Lombard, C. Ducruet, S. Auffret, B. Rodmacq, B. Dieny, M. Hochstrasser, G. Panaccione: *X-ray analysis of the magnetic influence of oxygen in Pt/Co/AlOx trilayers*, J. Appl. Phys. **103**, 07A912 (2008).

Presentations

1. V. Uhlíř: *Processing techniques, tools and novel devices: Top-down lithography techniques*, Invited lecture at the EuroTraining Course *Nanotechnology for Electronics* at Electronic Devices and Systems IMAPS CS Conference, Brno, September 2009, Course Program.

2. V. Uhlíř, S. Pizzini, J. Vogel, N. Rougemaille, V. Cross, S. Laribi, J. Camarero, E. Jiménez, C. Tieg, G. Faini: *High velocity domain wall motion in spin-valve nanostripes induced by spin polarized current*, Invited oral presentation at the conference SPIE Optics+Photonics – Conference on Nanoscience – Spintronics II (7398), San Diego (California, USA), August 2009, Technical Program, We-11, p. 70.

3. V. Uhlíř, M. Urbánek, L. Ranno, P. Bábor, J. Spousta, T. Šikola: *High GMR and low interlayer coupling in spin-valve multilayers prepared by ion beam sputtering*, Poster presentation at the conference International Conference on Magnetism (ICM 2009), Karlsruhe (Germany), July 2009, Program and abtracts, Mo-A-5.1-09, p. 48.

4. S. Pizzini, V. Uhlíř, J. Vogel, N. Rougemaille, V. Cross, E. Jiménez, J. Camarero, S. Laribi, C. Tieg, E. Bonet, M. Bonfim, R. Mattana, C. Deranlot, F. Petroff, C. Ulysse, G. Faini, F. Sirotti, A. Fert: *High velocity current-induced domain wall motion in spin-valve nanostripes*, Poster presentation at the conference International Conference on Magnetism (ICM 2009), Karlsruhe (Germany) July 2009, Program and abtracts, Tu-A-6.1-14, p. 164.

5. M. Urbánek, V. Uhlíř, J. Spousta, T. Šikola: *Fabrication of the spintronic nanostructures by FIB: optimization of the milling process*, Poster presentation at the conference International Conference on Magnetism (ICM 2009), Karlsruhe (Germany), July 2009, Program and abtracts, Tu-B-7.8-28, p. 179.

6. M. Urbánek, V. Uhlíř, J. Spousta, T. Šikola: *Fabrication of the spintronic structures by focussed ion beam*, Poster presentation at the conference EuroNanoForum 2009, Praha, June 2009, Programme, P-144, p. 181.

7. S. Průša, P. Bábor, M. Kolíbal, V. Uhlíř, T. Šikola: *Combined TOF-LEIS and SIMS techniques*, Oral presentation at the conference 14th International Conference on Solid Films and Surfaces (ICSFS14), Dublin (Ireland), June/July 2008, Programme, Fri-CL-8, p. 190.

8. P. Bábor, S. Průša, R. Duda, M. Urbánek, M. Kolíbal, V. Uhlíř, T. Šikola: *Parallel depth profilling of GMR multilayers by DSIMS and TOF-LEIS*, Poster presentation at the conference 14th International Conference on Solid Films and Surfaces (ICSFS14), Dublin (Ireland), June/July 2008, Programme, Tue-P-56, p. 312.

9. V. Uhlíř, S. Pizzini, J. Vogel, E. Bonet-Orozco, L. Ranno, M. Bonfim: *Time Resolved Observation of Domain Wall Propagation in Spin Valve Nanowires*, Oral presentation at the International School Magnetic Fields for Science, Cargèse (France), September 5, 2007, Abstracts, Wed05-2.

10. V. Uhlíř, S. Pizzini, J. Vogel, L. Ranno, M. Bonfim: *Time Resolved Observation of Domain Wall Depinning and Propagation in Spin Valve Nanowires*, Poster presentation at the International Symposium Spin Waves 2007, St. Petersburg (Russia), June 16-21, 2007, Symposium Abstracts, p. 55.

11. M. Urbánek, J. Neuwirth, V. Uhlíř, M. Hála, O. Tomanec, D. Škoda, L. Dittrichová, J. Spousta, T. Šikola: *Magnetic anisotropy of cobalt thin films prepared by IBAD*, Poster presentation at the conference European Conference on Surface Science ECOSS 24, Paris (France), September 2006, Final programme, CLU–Th–P–438, p. 254.

12. J. Neuwirth, V. Uhlíř, M. Hála, M. Urbánek, J. Calvar, M. Marquart, J. Spousta, T. Šikola: *Výzkum tenkých a ultratenkých vrstev Co využitím magnetooptického Kerrova jevu (A study of cobalt thin and ultrathin films using magneto-optical Kerr effect)*, Oral presentation at the conference Optické vlastnosti pevných látek v základním výzkumu a aplikacích: XI konference, Brno, June 2006, Abstrakty, p. 21.